Universidad de Valencia
Departamento de Astronomía y Astrofísica

Programa de Doctorado en Física

Relativistic Hydrodynamics and Spectral Evolution of GRB Jets

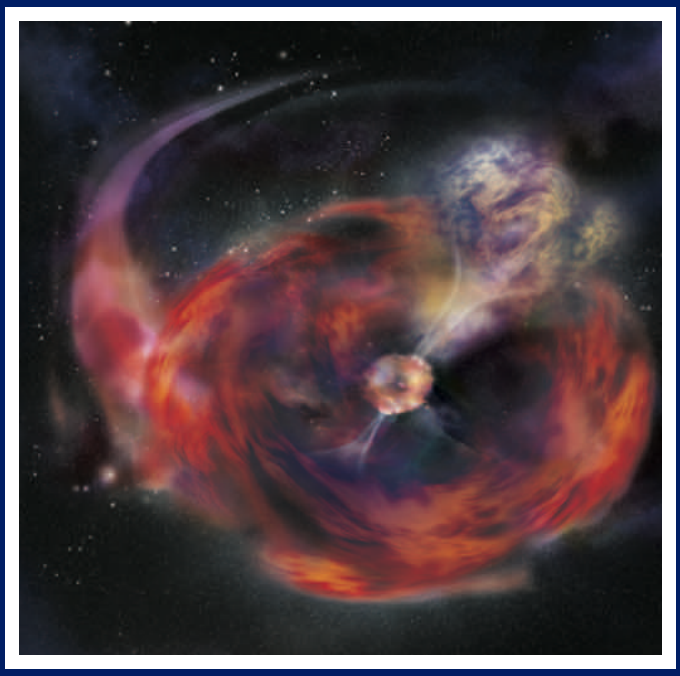

Tesis doctoral presentada por

Carlos F. Cuesta Martínez

y dirigida por

Miguel Ángel Aloy Torás y **Martin F. Obergaulinger**

Valencia, Mayo 2017

VNIVERSITAT DE VALÈNCIA

Departamento de Astronomía y Astrofísica

Facultad de Física

Tesis Doctoral

Programa de Doctorado en Física

Relativistic Hydrodynamics and Spectral Evolution of GRB Jets

May 29, 2017

Carlos F. Cuesta Martínez

Supervisors:

Miguel Ángel Aloy Torás

Martin F. Obergaulinger

Imagen Cubierta: Representación artística del modelo de fusión de un núcleo de helio con una estrella de neutrones en la "erupción de Navidad". Crédito: NASA, E/PO, Swift, Aurore Simonnet, Sonoma State Univ.

Cover Picture: Artistic representation of the helium core/neutron star merger model in the "Christmas burst". Credit: NASA, E/PO, Swift, Aurore Simonnet, Sonoma State Univ.

Miguel Ángel Aloy Torás, Profesor Titular del Departamento de Astronomía y Astrofísica de la Universitat de València

y

Martin F. Obergaulinger, Investigador Asociado al Departamento de Astronomía y Astrofísica de la Universitat de València

CERTIFICAN:

Que la presente memoria, titulada **Relativistic Hydrodynamics and Spectral Evolution of GRB Jets**, ha sido realizada bajo su dirección en el Departamento de Astronomía y Astrofísica de la Universitat de València por **Carlos F. Cuesta Martínez**, y constituye su Tesis Doctoral para optar al grado de Doctor en Física.

Y para que conste firman el presente certificado en Burjassot, a 29 de mayo de 2017.

Fdo: Miguel Ángel Aloy Torás

Fdo: Martin F. Obergaulinger

A María.
A mis padres.

Agradecimientos

No podría comenzar estas líneas de otra manera que no fuera agradeciendo en primer lugar a mis directores de tesis. A Miguel Ángel, por haberme dado esta oportunidad y haberme guiado durante los últimos (casi) 7 años. Creo que no conoceré a nadie más brillante. Y a Martin, por los buenos momentos en el despacho, que han sido muchísimos. Sin vosotros esta tesis no existiría.

Al resto de miembros del grupo CAMAP, comenzando por mis compañeros estudiantes y post-docs (Jesús Rueda, Jose Adsuara, Alejandro Torres, Vassilios Mewes, Nicolas DeBrye, Nicolás Sanchís, Jens Mahlmann, Tomasz Rembiasz, Bruno Peres y otros tantos que han pasado por el Departamento) con los que he vivido tantos y tantos momentos. A Petar Mimica y a Pablo Cerdá, por su infinita predisposición, pues parte de este trabajo ha sido fruto también de nuestra estrecha colaboración. A Carmen Aloy, por su infinita asistencia técnica. A José María Ibañez e Isabel Cordero, por sus infinitos ánimos. A Feli y Manel por su labor desde la secretaría. Y al resto de miembros del Departamento que en algún momento me hayan podido prestar su ayuda o dar algún consejo.

I would like to thank Christina Thöne and Antonio de Ugarte Postigo, as our collaboration has given rise to one of two publications on BBD-GRBs. Also, I would like to thank Elena Pian and Ewald Müller for their helpful comments which have served to improve this thesis.

Al Servicio de Informática, por su asistencia técnica en los supercomputadores *Lluis Vives* y *Tirant* que me ha salvado en más de una ocasión.

A la Consellería d'Educació, Cultura i Esport de la Generalitat Valenciana

y a VLC-Campus por su apoyo económico a través de las ayudas “VALi+d” (ACIF/2013/278) y “Atracció de Talents” (UV-INV-PREDOC13-110509), respectivamente.

Al resto de compañeros científicos con quiénes tantas horas he compartido en comidas y eventos varios. Algunos por desgracia ya os fuistéis hace tiempo, otros habéis estado hasta el momento final de esta tesis conmigo. De todos algo (bueno) he aprendido. No os menciono uno a uno porque vosotros ya sabéis quiénes sois.

Y en definitiva, a todos aquellos que habéis estado conmigo estos últimos 5 años.

A todos vosotros, amigos, gracias. Ha sido una experiencia increíble.

Ya cerrando estas líneas no me olvido de ti. Gracias, María, por estar siempre a mi lado y apoyarme en todo. La historia de este doctorado ha sido también nuestra historia.

Tampoco me puedo olvidar de mi familia (y de mi nueva familia), que siempre que han podido me han mandado muchos ánimos.

Y como no agradecer a mis padres, Fernando y Pilar, su apoyo incondicional. Gracias a ellos he llegado hasta aquí.

Abbreviations

This is a list of abbreviations used throughout the text:

AD accretion disc

BAT Burst Alert Telescope

BATSE Burst and Transient Source Experiment

BB blackbody

BBD blackbody-dominated

BH black hole

CB 'Christmas burst'

CD contact discontinuity

CE common envelope

EM external medium

FS forward shock

GRB gamma-ray burst

HN hypernova

LC light curve

llGRB low-luminosity gamma-ray burst

LGRB long gamma-ray burst

MHD magnetohydrodynamic

NS neutron star

PM proto-magnetar

PNS proto-neutron star

RHD relativistic hydrodynamic

RS reverse shock

SED spectral energy distribution

SMNS supramassive neutron star

SN supernova

SP spectrum

UV ultraviolet

UVOIR ultraviolet-optical-infrared

WR Wolf-Rayet

XRF X-ray flash

XRT X-ray Telescope

ZAMS zero-age main sequence

Contents

Resumen

En la presente tesis hemos estudiado los sistemas progenitores de las erupciones de rayos gamma (ERG) de larga duración mediante modelos numéricos de su evolución dinámica y emisión electromagnética. De todas las posibles clases de eventos, en particular nos centramos en aquellas que muestran una componente prominente de emisión térmica, la cual podría generarse por medio de la interacción de un chorro constituido por plasma relativista con el medio en el que se propaga.

Introducción

Las ERG son intensos destellos de radiación γ, muy luminosos (alrededor de 10^{51} erg liberados en unas decenas de segundo), que llegan esporádicamente a la Tierra desde cualquier dirección en el espacio. Al cabo de varios minutos u horas después de la ERG puede observarse la llamada post-luminiscencia que consiste en emisión que va desde los rayos X hasta las frecuencias en radio. Se cree que las ERG provienen de chorros relativistas altamente colimados que se formaron en el núcleo de estrellas masivas a punto de colapsar o en sistemas binarios en proceso de fusión. Mediante diferentes mecanismos físicos como puedan ser el calentamiento por neutrinos o las tensiones magneto-rotacionales, parte de la energía gravitacional del sistema puede ser extraída y empleada para acelerar chorros colimados a velocidades relativistas.

En el Capítulo 1 de la presente tesis presentamos, en primer lugar, un resumen de las características observacionales encontradas en las ERG desde su descubrimiento hace 50 años hasta el tiempo presente e introducimos el

marco general que satisfactoriamente explica la generación de radiación en ERG canónicas. Discutiremos los diferentes tipos de sistemas progenitores que se han propuesto para la formación de chorros relativistas y ERG, así como aquellas erupciones que han sido reciéntemente descubiertas y que difieren en su comportamiento del modelo canónico debido a la presencia de una componente térmica, nada despreciable, en su emisión temprana.

El modelo más aceptado sobre el origen y evolución de las ERG es el conocido como 'la bola de fuego'. Una bola de fuego es básicamente un cojunto de electrones, positrones, fotones y una cantidad pequeña de bariones que se mueven a velocidades relativistas. La bola de fuego se acelera al convertir parte de su energía interna en energía cinética. La energía cinética puede disiparse en los choques y ser convertida en radiación. Los fotones producidos pasan a formar parte de la bola de fuego y pueden quedar atrapados si la profundidad óptica es muy alta. Por un lado las observaciones muestran que las curvas de luz de las ERG son muy variables ($\Delta t \sim 10\,\mathrm{ms}$), de lo que se deduce que el motor central debe de ser un objecto muy compacto ($R \sim 3 \times 10^7\,\mathrm{cm}$). Por otro lado se espera que a estas escalas de longitud la opacidad originada por interacción de fotones sea muy alta, con lo cual, a priori, no se entiende que la radiación escape y sea observada. Esta paradoja, conocida como *el problema de compacidad*, puede resolverse si se supone que la fuente se expande a velocidades ultra relativistas.

La emisión de las ERG es principalmente de carácter no térmico, es decir, no depende de la temperatura de las partículas que componen los chorros. En particular las observaciones se ajustan razonablemente bien a leyes de potencias de lo cual se infiere que la radiación es del tipo sincrotrón. La generación de esta radiación se puede explicar mediante el modelo de choques internos y externos. Los chorros relativistas en su interacción con el medio externo desarrollan un par de choques, uno delantero y otro reverso, que pueden acelerar partículas una vez éstas cruzan de un lado al otro del choque. Este escenario puede explicar de manera adecuada la emisión a corto y largo plazo, sin embargo es necesario introducir la formación de choques internos en la bola de fuego para explicar las variabilidades observadas en las ERG.

La fenomenología observada es compatible con la existencia, al menos, de dos clases diferentes de ERG. Las de corta duración y las de larga duración (éstas últimas son el objeto de estudio de la presente tesis). Cada una de ellas ha sido asociada a un tipo diferente de progenitor. El modelo de la estrella colapsante (también denominado *colápsar*) da cuenta de las ERG de larga duración. En este modelo, una estrella masiva con rotación rápida colapsa sobre sí misma. El núcleo de la estrella puede colapsar a un agujero negro directamente o formar una proto-estrella de neutrones que posteriormente puede volver a colapsar, o no. En el caso de que se forme un agujero negro éste puede rodearse de un disco de acreción si el momento angular del sistema es alto. La acreción de masa por parte del agujero negro puede dar lugar al almacenamiento de grandes cantidades de energía que, mediante diversos procesos físicos previamente mencionados, pueden ser empleadas en la formación de chorros (bipolares) relativistas colimados. En el caso de que se forme una proto-estrella de neutrones en rotación rápida la energía puede ser extraída por procesos magneto-rotacionales debido a la presencia de campos magnéticos muy intensos ($B \sim 10^{15}\,\mathrm{G}$). Más recientemente, se ha propuesto que algunas ERG de larga duración también pueden ser generadas en sistemas binarios en proceso de fusión. Al contrario que las ERG de corta duración, cuyo sistema progenitor está basado en la fusión de dos objetos compactos como pueden ser los agujeros negros o las estrellas de neutrones, para las ERG de larga duración se ha argumentado que sistemas formados por un objeto compacto y una estrella masiva evolucionada pueden dar lugar a este tipo de emisiones. En este modelo la formación de un sistema agujero negro/disco de acreción se produce de manera natural tras la fusión, dando lugar además a emisiones muy duraderas (incluso más que la de una ERG típica de larga duración) gracias a la gran cantidad de masa existente en el sistema.

Durante el colapso de una estrella masiva puede originarse también lo que se conoce como explosión supernova (SN). En este caso las capas más externas de la estrella no llegan a colapsar y son expulsadas al exterior en forma de explosiones muy energéticas (aunque de menor luminosidad que las ERG típicas). Desde el descubrimiento de la SN 1998bw asociada a la ERG 980425

se han descubierto alrededor de una decena más de ERG asociadas a SN del Tipo Ibc. Esta asociación afianza el modelo de la estrella colapsante pues ambos fenómenos pueden generarse en el mismo sistema progenitor. Las SNs asociadas a ERG son de hecho más energéticas que las SNs típicas. Por otro lado la mayoría de estas ERG son de menor luminosidad que las ERG típicas. Lo que nos despierta un cierto interés en estas asociaciones de ERG con SN es la cantidad nada despreciable de este tipo de eventos en los que se observa una importante componente térmica en su espectro de emisión, difiriendo por tanto del comportamiento canónico observado en las ERG típicas.

La parte central de esta tesis se ha dedicado al modelado de ERG a partir de dos clases diferentes de progenitores: ERG ultra largas dominadas en su espectro de emisión por una componente térmica tipo cuerpo negro y ERG asociadas con explosiones supernovas originadas tras el colapso de una estrella masiva.

Metodología

En el Capítulo 2 describimos los códigos numéricos que hemos empleado para la realización de nuestro estudio. Primero comenzaremos explicando la física detrás de las simulaciones así como los métodos numéricos necesarios para su implementación en dichos códigos y las aproximaciones utilizadas en los sistemas astrofísicos objeto de esta tesis.

El estudio de los chorros que dan lugar a las ERG y de su emisión radiativa se ha dividido en dos etapas.

En primer lugar, mediante la aproximación de fluido seguimos la evolución dinámica de chorros relativistas que puede modelizarse mediante simulaciones hidrodinámicas relativistas multidimensionales. Estas simulaciones han sido realizadas con el código MRGENESIS, desarrollado en el seno de nuestro grupo, el cual se encarga de resolver las ecuaciones de la hidrodinámica relativista. Este conjunto de ecuaciones representa un sistema de leyes de conservación que, junto con la adición de una ecuación de estado, evalúa diversas propiedades hidrodinámicas del sistema como puedan ser la densidad de masa

en reposo, la velocidad, la energía, la presión o la temperatura. Las ecuaciones de la hidrodinámica relativista son demasiado complejas para poder obtener resultados analíticos y por tanto se necesita de diversos métodos numéricos para su resolución. En primer lugar el dominio físico se discretiza en una malla dividida en un gran número de celdas. El elemento básico en el que se fundamenta el método es la resolución del problema de Riemann que consiste en la interacción de dos fluidos. Los problemas de Riemann surgen de manera natural al discretizar las distribuciones (continuas) de las propiedades físicas del fluido entre celdas contiguas, dando lugar a la aparición de discontinuidades tales como choques o rarefacciones.

Para la elaboración de esta tesis hemos adaptado y calibrado el código de manera adecuada. Hemos incluido de manera aproximada las diversas condiciones iniciales que representan a los diferentes sistemas progenitores. Por ejemplo, dentro de la aproximación de fluido hemos considerado que éste es ideal y que por tanto puede ser tratado como un plasma electrón-protón. Esto nos permite describir la composición química del sistema en función de un único parámetro que es uniforme en todo el modelo. De esta manera reducimos la complejidad de los interiores estelares y los vientos que son generados ya que en realidad éstos están compuestos por diferentes metales además de hidrógeno y helio. Con ello despreciamos también cualquier tipo de efecto debido a la generación de reacciones nucleares.

En todas nuestras simulaciones hemos supuesto que nuestros sistemas tienen simetría ecuatorial y axial. La primera de las simetrías nos permite considerar la evolución de solo uno de los chorros bipolares en un único hemisferio, mientras que la segunda simetría nos permite modelizar esta evolución en dos dimensiones espaciales al considerar que el chorro tiene simetría de revolución en torno al eje de rotación del sistema.

Las dos principales componentes de la simulación, el chorro y el medio en el que se está propagando, dependen del sistema progenitor en consideración. La elaboración de un modelo completamente autoconsistente del motor central va más allá del alcance de esta tesis. Por tanto, los chorros han sido inyectados directamente en una malla numérica a una cierta distancia finita usando

parámetros prescritos como la luminosidad, el factor de Lorentz o la apertura angular del chorro. Las propiedades de los chorros y de su medio ambiente han sido escogidas de acuerdo a las propiedades generalizadas de las ERG a estudio.

En segundo y último lugar, hemos realizado el cálculo de la emisión de radiación por parte de dichos chorros. Para ello hemos supuesto diferentes procesos radiativos como sincrotrón o *bremsstrahlung* térmico. Como ya hemos mencionado previamente, la emisión sincrotrón puede ser originada en presencia de campos magnéticos por partículas que han sido aceleradas a velocidades relativistas. Por el otro lado, la emisión de tipo *bremsstrahlung* térmico, o libre–libre, es producida por la interacción de electrones libres que se aceleran o deceleran al pasar cerca de un ión positivo (por ejemplo, un protón) y principalmente depende de la densidad de partículas en el medio y de su temperatura. También hemos considerado procesos de absorción Thomson que pueden contribuir en gran medida a la opacidad si el medio resulta ser muy denso.

La parte del cálculo de la evolución radiativa puede ser separada de la evolución hidrodinámica gracias a la aproximación de que nuestros sistemas son adiabáticos. Esto significa que las pérdidas de energía del sistema por emisión de fotones son pequeñas. Por tanto este tratamiento puede realizarse a posteriori sin perder generalidad alguna en los resultados obtenidos de la simulación hidrodinámica.

La emisión sintética ha sido calculada con el código SPEV, también desarrollado por miembros de nuestro grupo. Este código se encarga de manejar la evolución temporal y espacial de la partículas, relativistas o no, susceptibles de emitir radiación. Estas partículas son inyectadas como trazas en la simulación hidrodinámica y son transportadas junto con el fluido. A lo largo de su evolución estas partículas pueden sufrir pérdidas y ganacias de energía por procesos adiabáticos o radiativos y radiar energía. En un último paso SPEV resuelve numéricamente la ecuación del transporte radiativo. Para ello se tienen en cuenta todas las contribuciones a la radiación habidas a lo largo de la línea de visión y se calcula la emisión total que observaría un hipotético observador.

Una parte del presente trabajo ha consistido en la extensión del código SPEV que incluía en su versión inicial solo procesos de carácter no térmico. Con el objetivo de dar cuenta de la señales térmicas que puedan originarse en algunas ERG, nuestra labor ha consistido en la incorporación de procesos térmicos como ha sido el de *bremsstrahlung* térmico y la implementación de métodos que permitan estimar de manera adecuada la temperatura en las diferentes regiones del sistema.

Hemos de destacar que las simulaciones numéricas realizadas en la presente tesis han necesitado de grandes volúmenes de cálculo y espacio en disco. Tanto MRGENESIS como SPEV están optimizados para ser utilizados en supercomputadoras de arquitectura paralela. La utilización de este tipo de supercomputadoras nos ha permitido elaborar estos modelos en alta resolución en un tiempo razonable.

Resultados

Los resultados de esta tesis han sido separados en dos capítulos diferentes en los que, como ya hemos mencionado, estudiamos la formación de chorros relativistas de ERG en dos tipos diferentes de progenitores.

En el Capítulo 3 hemos extendido el actual modelo teórico que intenta explicar la clase de ERG dominadas en su espectro de emisión por una componente térmica de cuerpo negro. Estos eventos se caracterizan por sus largas duraciones y la presencia de una notable componente térmica que sigue a las ERG, además de por su débil post-luminiscencia. La ERG 101225A, también conocida como la "erupción de Navidad" (ya que se observó el 25 de diciembre del año 2010), representa el miembro más notorio dentro de esta nueva clase de ERG. Dicha erupción fue detectada por el satélite *Swift* que observó una duración de la ERG de $\sim 7000\,\mathrm{s}$. Aparte de esta larga duración también se observó una inusual y prominente componente térmica de tipo cuerpo negro que se extendía en el espectro de emisión desde los rayos X hasta la banda óptica, dando lugar a una post-luminiscencia poco corriente. Además se ha estimado que la energía liberada en esta ERG es de $\gtrsim 1.2 \times 10^{52}\,\mathrm{erg}$. La emisión en

banda ultravioleta-óptica-infrarroja se ha modelado como un cuerpo negro en expansión cuyo radio evoluciona desde $\sim 2 \times 10^{13}$ cm (después de 0.07 días) hasta $\sim 7 \times 10^{13}$ cm (después de 18 días). El radio y la temperatura de la componente en rayos X es totalmente diferente sugiriendo que ambas emisiones no están causadas por el mismo proceso.

A la vista de dichas observaciones, se ha sugerido que la erupción de Navidad y, por extensión, las ERG dominadas por emisión de cuerpo negro pueden surgir de la fusión de un sistema binario formado por una estrella de neutrones y el núcleo de helio de una estrella masiva muy evolucionada. Este tipo de binarias atraviesa una fase en su evolución que se conoce como de envoltura común. La estrella de neutrones se ve envuelta por las capas externas de la estrella secundaria que son expulsadas debido a las fuerzas de marea ejercidas por la propia estrella de neutrones. Esta última comienza a caer en espiral sobre el núcleo de helio que queda al descubierto mientras por el camino va acretando grandes cantidades de materia. Una vez la estrella de neutrones se fusiona con el núcleo de helio puede formarse un sistema agujero negro/disco de acreción que daría lugar a la formación de un par de chorros muy energéticos de larga duración alineados con el eje de rotación del sistema. La principal ventaja de este modelo es que produce de manera natural un elemento que puede 'termalizar' el sistema, siendo éste la capa de hidrógeno que ha sido expulsada por la estrella masiva. Para cuando se formen los chorros productores de la ERG (en realidad la ERG que observamos así como su post-luminiscencia es producida únicamente por el chorro que apunta hacia nosotros) se espera que esta capa se encuentre situada a una distancia de unos $\sim 10^{13}$ cm del origen del sistema. La interacción de los chorros con esta envoltura es la que se espera que origine la emisión térmica.

Nuestro trabajo ha consistido en el modelado de simulaciones en 2 dimensiones (suponiendo simetría axial y ecuatorial) de la propagación de chorros ultra relativistas con diferentes propiedades en el medio generado tras la fusión de la binaria. Esta fusión no ha sido simulada en el presente estudio por lo que las condiciones iniciales del medio han sido aproximadas mediante una capa muy densa de geometría ligeramente toroidal que se parece a la envoltura de

hidrógeno expulsada en la binaria. Dichas condiciones en el medio concuerdan con simulaciones de binarias de este tipo realizadas por otros grupos. Hemos estudiado las consecuencias dinámicas más relevantes fruto de la interacción de uno de los chorros y esta capa densa y las hemos conectado con la generación de emisión térmica en la erupción de Navidad. En concreto hemos realizado un estudio paramétrico de la interacción chorro/medio ambiente que ha consistido en la variación de parámetros tales como la energía o el ángulo de apertura del chorro, y la geometría de la capa o su densidad así como también ésta última correspondiente a la del medio externo. También hemos jugado con los parámetros microfísicos relacionados con la emisión sincrotrón. Para ello hemos elaborado más de una decena de modelos hidrodinámicos y los hemos comparado entre sí.

Más adelante hemos comparado las curvas de luz resultantes con datos observacionales reales. Nuestros modelos permiten concluir que la emisión térmica se origina a raíz de la interacción entre el chorro y la envoltura de hidrógeno expulsada durante la fusión de la estrella de neutrones y el núcleo de helio. Hemos comprobado que nuestros modelos ajustan razonablemente bien las observaciones y reproducen los aspectos clave de la evolución radiativa como pueda ser el enrojecimiento del sistema.

En el Capítulo 4 hemos estudiado sistemas progenitores de ERG más canónicos, en particular equellos sistemas basados en una estrella masiva aislada al borde del colapso. Estos sistemas pueden generar tanto ERG como energéticas explosiones SN. No son muchas las asociaciones de ERG y SN que han sido observadas, por tanto este escenario genera muchas preguntas. Las ERG detectadas en la mayoría de estos eventos son de baja luminosidad mientras que las SN son muy energéticas. No restringiendo nuestro estudio a este escenario en particular, abordaremos el proceso de emergencia de la estrella por parte de chorros de ERG o de un choque de SN. Por desgracia, no existen actualmente datos observacionales que muestren la evolución de la radiación en estas fases tan tempranas, pero se ha teorizado que este tipo de emergencias puede producir una cantidad no despreciable de emisión térmica que debería

ser observada.

Así pues, hemos estudiado la propagación de chorros relativistas dentro de la estrella progenitora y el medio circunestelar, focalizándonos en el proceso de emergencia. Se ha prestado especial atención a la interacción de chorros con el choque originado por una SN lanzada instantes antes de que éstos comiencen a propagarse. El progenitor que hemos considerado consiste en una estrella Wolf-Rayet de $28M_{\odot}$ envuelta por una envoltura inflada que se extiende hasta unos pocos radios estelares. Con el objetivo de mantener el equilibrio hidrostático en la envoltura estelar, hemos implementado en MRGENESIS un potencial gravitatorio Newtoniano. La colocación de esta envoltura inflada ha venido motivada por recientes estudios sobre la evolución de vientos en estrellas Wolf-Rayet. Hemos seguido la evolución dinámica en una dimensión espacial del choque de la SN. Estas simulaciones en una única dimensión nos permiten acelerar el tiempo de cálculo en comparación con lo que hubieran costado si las mismas se hubieran realizado en 2 dimensiones espaciales y suponiendo simetría axial y ecuatorial. Las velocidades que hemos obtenido tras la emergencia del choque fuera de la estrella ($\sim 0.9c$) y 4 minutos más tarde ($\sim 0.7c$) han sido considerablemente mayores que las observadas en SN típicas e hipernovas. Hasta cierto punto, esto es un consecuencia de los parámetros utilizados en los modelos de pistón utilizados para inicializar la inyección de una SN en nuestro dominio computacional. Los antedichos parámetros nos son completamente libres pues están restringidos por la necesidad de considerar flujos supersónicos a través de la zona de inyección en la malla.

El modelo unidimensional de la SN en diferentes fases de evolución ha sido remapeado en dos dimensiones espaciales suponiendo simetría axial y ecuatorial. Desde este momento, hemos continuado la evolución hidrodinámica de estos sistemas en dos dimensiones. Hemos estudiado la evolución dinámica de uno de los chorros propagándose en el medio dejado atrás por el choque de la SN. Por completitud, se ha estudiado también un caso en el que la SN no se hubiera originado. Más alla de este análisis teórico, mostraremos que la presencia de un choque de SN puede alterar la propagación del chorro.

El objetivo principal de este capítulo ha consistido en el estudio de la

emisión sintética con SPEV durante y después de la emergencia por parte del chorro o del choque de la SN de la estrella progenitora. Sin embargo, esta parte ha experimentado diversos problemas técnicos y los resultados presentados en este apartado deben ser considerados preliminares. En particular, veremos que hemos sufrido de una excesiva difusión numérica causada por la falta de resolución en nuestra malla numérica.

Conclusiones

Del estudio en el Capítulo 3 de las ERG con una emisión dominada por una componente de cuerpo negro hemos obtenido las siguientes conclusiones.

Nuestras simulaciones explican de manera cualitativa la ausencia de una post-luminiscencia clásica y la aparición de una fuerte componente de carácter térmico. Esta componente térmica puede explicarse mediante la interacción de un chorro ultra relativista con una capa de alta densidad con forma toroidal cuyo eje coincide con el eje de rotación de la binaria. Hemos podido comprobar que la elección de parámetros en el chorro y la capa no es única, y que varias combinaciones de éstos pueden explicar las observaciones en las bandas de ultravioleta-óptico-infrarrojo de manera cualitativamente semejante. Por otro lado, solo hemos conseguido explicar parcialmente las observaciones en rayos X. Esta emisión la atribuimos a la región en forma de cuña situada en el radio interno de la capa y cuya extensión transversal depende principalmente de la geometría escogida en el modelo. Dicha extensión es mayor en nuestro caso ($\sim 8 \times 10^{11}$ cm) en comparación con el tamaño estimado de las observaciones ($\sim 10^{11}$ cm), por lo que proponemos mejorar el modelo en este aspecto. Encontramos también que la emisión sincrotrón del choque delantero del chorro domina la emisión en sus etapas tempranas, durante las cuales el choque es todavía moderadamente relativista. La contribución del choque reverso es de la misma magnitud que la del choque delantero durante los primeros 80 minutos después de la detección de la emisión de rayos gamma. Más adelante en la evolución, la emisión del choque reverso cesa pues éste desaparece debido a que el haz del chorro es estrangulado por su interacción con el medio.

Destacamos que, en concordancia con las observaciones, hemos obtenido curvas de luz planas durante los primeros 2 días después de la ERG y una evolución espectral que es consistente con el enrojecimiento observado en el sistema. Además, hemos obtenido que esta inversión espectral y enrojecimiento observados en la erupción de Navidad pueden relacionarse con el tiempo en el que la capa densa expulsada por el sistema progenitor en una fase temprana de envoltura común es completamente arrasada por el chorro ultra relativista.

Por tanto, como comentario final, subrayamos que nuestros modelos favorecen a los sistemas binarios compuestos por una estrella de neutrones y un núcleo de helio como posibles candidatos a originar ERG de ultra larga duración dominadas en su emisión por una componente de cuerpo negro. Aún así, no descartamos otras posibilidades mencionadas en la literatura como pueda ser la producción de este tipo de eventos en estrellas supergigantes azules.

Del estudio en el Capítulo 4 de ERG asociadas a explosiones SN producidas por estrellas masivas colapsantes hemos obtenido las siguientes conclusiones.

Basándonos en consideraciones analíticas que hemos podido verificar en nuestras simulaciones, hemos estimado el umbral de energía para la formación de chorros. Este límite inferior resulta del balance entre la presión dinámica ejercida por el progenitor y el empuje del chorro. Para un ángulo de semi-apertura fijo, $\theta_{\rm j}$, la luminosidad intrínseca mínima requerida para la existencia de chorros supersónicos depende de la posición radial dentro de la estrella progenitora. De manera sorprendente, a lo largo de una amplio rango de posibles localizaciones de la zona de inyección del chorro en el seno de la estrella (pero fuera de su núcleo) este umbral es uniforme y, en concreto para nuestro modelo estelar, se corresponde con $L_{\rm j}^{\rm th} \gtrsim 10^{49}\,{\rm erg\ s^{-1}}$. Traduciendo esta luminosidad en luminosidad isotrópica quivalente observada en rayos γ, $L_{\gamma,iso} \simeq 4\epsilon_\gamma L_{\rm j}/\theta_{\rm BO}^2$, obtenemos que depende del ángulo de apertura del chorro tras su emergencia, $\theta_{\rm BO}$, y de la eficiencia de conversión de la luminosidad intrínseca del chorro en radiación γ, ϵ_γ. Algunos profesionales en esta materia han apuntado que $\theta_{\rm BO} \sim \theta_{\rm j}$, en cuyo caso nuestros chorros tendrían una luminosidad unos pocos órdenes de magnitud mayor que la máxima observada para ERG de baja lu-

minosidad, a menos que una factor de eficiencia extremadamente pequeño sea considerado ($\epsilon_\gamma < 10^{-5}$). Sin embargo, la aparente contradicción puede ser resuelta. Chorros muy energéticos pueden producir eventos de baja luminosidad tanto si el ángulo de apertura de dichos chorros tras su emergencia de la estrella es grande, cosa que así observamos en nuestros modelos, como si la eficiencia de conversión de energía cinética e interna en radiación es baja.

Debido a las restricciones computacionales en el apartado del cálculo de la emisión tras la emergencia de la estrella, no hemos podido obtener curvas de luz y espectros durante un tiempo lo suficientemente largo para realizar un estudio adecuado de la emisión térmica. Por tanto, nuestras conclusiones deben de ser consideradas como preliminares.

Hemos obtenido luminosidades bastantes bajas sólo marginalmente consistentes con cálculos previos encontrados en la literatura. En concreto, encontramos que el destello de la SN simulada es $\lesssim 1000$ veces más tenue que uno de los prototipos de ERG/SN (ERG 060218/SN 2006aj) o que destellos de rayos X (DRX) asociados a SNs (DRX 080109/SN 2008D). Además, la luminosidad pico en banda de rayos X se produce al cabo de $\sim 6\,\mathrm{s}$ tras la emergencia del choque por la superficie estelar, siendo mucho más temprana que en el caso de los prototipos previamente mencionados. A pesar de ello, las observaciones de ERG/SN muestran propiedades heterogéneas, habiendo casos en los que la luminosidad bolométrica es órdenes de magnitud más pequeña que los ejemplos previos. Además, los tiempos necesarios para alcanzar el pico de luminosidad en rayos X (de alrededor de 10 s) son predichos teóricamente en progenitores compactos de WR (es decir, como los aquí considerados). Estos hechos hacen que nuestros modelos sean parcialmente consistentes con la fenomenología existente.

Nuestros modelos de chorro muestran una energía (tanto cinética como térmica) almacenada tras la emergencia muy grande. De los análisis del factor de Lorentz asintótico en la cavidad formada en los diferentes chorros, predecimos que los transitorios de alta energía que puedan producirse en nuestros modelos serán más similares a DRX que a ERG. De hecho, nuestros chorros muestran el pico de luminosidad específica en la banda ultravioleta extrema en vez de

en rayos X, y una luminosidad en rayos γ claramente menor ($\sim$ 2–4 órdenes de magnitud más pequeña que en la banda X).

Finalmente, hemos encontrado que la señal muy temprana observada en nuestros diferentes modelos de chorro (antes de que se alcance el pico en luminosidad) por debajo de la banda γ es muy similar entre chorros con similares luminosidades intrínsecas. Esto ocurre a pesar de la sustancial diferencia en la evolución hidrodinámica entre modelos de chorro que han interaccionado con un choque de SN previo y modelos de chorro que se han propagado en el modelo estelar sin modificar. Esperamos que esta similitud se mantenga, al menos, durante escalas de tiempo del orden del tiempo que tarda en cruzar transversalmente la luz esta región de emisión ($\sim$ 1–2 s). Por tanto, en un futuro continuaremos con el estudio de los modelos presentados en esta tesis siguiendo su evolución hasta tiempos más largos. Todos estos modelos además deberán de ser simulados empleando mallas numéricas de mayor resolución a las empleadas en este trabajo, o por otro lado puede ser interesante el desarrollo de métodos numéricos que impidan la difusión numérica observada.

Por último, hemos de mencionar que en la realización de esta tesis el tratamiento de la emisión ha sufrido de ciertas limitaciones. A pesar de que hemos supuesto que la radiación de tipo *bremsstrahlung* térmico es la contribución dominante, no debemos olvidar que otros procesos de emisión puede ser relevantes. Por ejemplo, en nuestros cálculos no hemos incluido los procesos de Comptonización que pueden ser influyentes a altas frecuencias. También en este último capítulo de la tesis no hemos podido incorporar a tiempo la emisión sincrotrón que puede ser relevante en algunas etapas de la evolución como se muestra en el primer capítulo de resultados. Aparte de las mejoras propuestas en cada uno los modelos hidrodinámicos elaborados para la presente tesis, todos estos procesos radiativos deberán ser incorporados en un futuro si se quiere obtener un cálculo de la emisión mucho más refinado.

Abstract

In this thesis we study the progenitor systems of long gamma-ray bursts (GRBs) using numerical models of their dynamics and the electromagnetic emission. Of all the possible classes of events, we focus on those showing a prominent component of thermal emission, which might be generated due to the interaction of a relativistic jet with the medium into which it is propagating.

Long GRBs are believed to arise from relativistic, highly collimated jets formed in the core of collapsing massive stars or in merging binary systems. By means of different physical mechanisms such as neutrino heating or magnetorotational stresses a fraction of the gravitational energy of the system can be extracted and employed to accelerate bipolar collimated jets to relativistic speeds. In Chapter 1, we present an overview of the observational features seen in GRBs since their discovery, 50 years ago, up to the present. We also introduce the canonical picture that successfully explains the generation of radiation in the relativistic jets of canonical GRBs. The observational signals vary strongly between different classes of inner engines of the GRB. We discuss several progenitor systems that have been argued for the formation of relativistic jets and GRBs as well as a few recently discovered bursts, which differ from the canonical behaviour by the presence of a non-negligible thermal component in their prompt emission.

The main part of the thesis is devoted to modelling GRBs from two different classes: ultra-long GRBs dominated by blackbody emission and GRBs associated with core-collapse supernovae (SNe). The study of GRB jets and

their radiative emission has been basically divided into two steps. First, the dynamical evolution of relativistic jets can be simulated by means of multidimensional special relativistic hydrodynamic simulations. In all our simulations we assume that our systems have equatorial and axial symmetry. The first of these symmetries allows us to consider the evolution of only one of the two bipolar jets in a single hemisphere, while the second symmetry allows us to model this evolution in two spatial dimensions (2D) considering that the jet has symmetry of revolution around the rotational axis of the system. The two main components of the simulations, the jet and the medium into which is propagating, depend on the different progenitor systems. A fully self-consistent modelling of the engine is beyond the scope of this thesis, and thus the jets have been injected into the numerical grid at a finite radius using prescribed parameters such as luminosity, Lorentz factor, and half-opening angle. The properties of the jet and its environment have been chosen according to generally assumed properties of the classes of GRBs of interest. Finally, the synthetic emission from such jets is computed in a post-processing stage assuming different radiative processes in which we follow the temporal and spectral evolution of the emitted radiation. In Chapter 2, we describe the numerical codes we have used for such propose. We explain the physics behind them as well as the numerical methods and the approximations used to simulate these astrophysical scenarios. The relativistic hydrodynamic simulations have been performed with the MRGENESIS code. For the realization of this thesis we have properly adapted and calibrated the code to include the progenitor systems considered here. The synthetic emission has been computed with the relativistic radiative transfer code SPEV, which deals with the temporal and spatial evolution of the radiating particles and solves the radiative transfer equation to evaluate the radiation received by observers at cosmological distances. An instrumental part of this project consisted in extending SPEV to include thermal processes, such as thermal bremsstrahlung, in order to account for the thermal signal that may arise in some GRBs.

In Chapter 3, we extend an existing theoretical model to explain the class of blackbody-dominated GRBs (BBD-GRBs), i.e., long lasting events char-

acterized by the presence of a notable thermal component trailing the GRB prompt emission, and a rather weak traditional afterglow. GRB 101225A, the "Christmas burst", is the most prominent member of this class. It has been suggested that BBD-GRBs could result from the merger of a binary system formed by a neutron star and the Helium core of an evolved, massive star. We model in 2D the propagation of ultrarelativistic jets through the environments created by such mergers. We outline the most relevant dynamical details of the jet propagation and connect them to the generation of thermal radiation in GRB events akin to that of the Christmas burst. A comprehensive parameter study of the jet/environment interaction has been performed and synthetic light curves are confronted with the observational data.

The thermal emission in our models originates from the interaction between the jet and the hydrogen envelope ejected during the neutron star/He core merger. We find that the lack of a classical afterglow and the accompanying thermal emission in BBD-GRBs can be explained by the interaction of an ultrarelativistic jet with a toroidally shaped ejecta whose axis coincides with the binary rotation axis. We also find that the synchrotron emission of the forward shock of the jet is dominant during the early phases of the evolution, along which that shock is still moderately relativistic. The contribution of the reverse shock is of the same magnitude as that of the forward shock during the first 80 minutes after the GRB. Later, it quickly fades because the jet/environment interaction chokes the ultrarelativistic jet beam and effectively dumps the reverse shock. We highlight that, in agreement with observations, we obtain rather flat light curves during the first 2 days after the GRB, and a spectral evolution consistent with the observed reddening of the system. Besides, we obtain that this spectral inversion and reddening happening at about 2 days in the Christmas burst can be related to the time at which the massive shell, ejected in an early phase of the common-envelope evolution of the progenitor system, is completely ablated by the ultrarelativistic jet.

In Chapter 4 we study more canonical progenitor systems of GRBs, namely single massive stars on the brink of collapse. Motivated by the many associations of GRBs with energetic SN explosions, we study the propagation of

relativistic jets within the progenitor star and the circumstellar medium. Particular attention is paid to the interaction between the jets and a SN shock wave launched briefly before the jets start to propagate. The progenitor considered here has been a Wolf-Rayet (WR) star of $28M_{\odot}$ of surrounded by an inflated envelope extending up to a few stellar radii. In order to maintain the hydrostatic equilibrium of the stellar envelope, we have implemented a *pseudo*-Newtonian gravitational potential in our numerical code. We have followed the dynamical evolution in one spatial dimension (1D) of the SN ejecta alone. These 1D runs constitute an ancillary step, which speeds up the computation. The velocities obtained for the SN ejecta at the breakout ($\simeq 0.9c$) and $\sim 4\,\mathrm{min}$ afterwards ($\sim 0.7c$) are considerably larger than typical velocities of SNe and even observed hypernovae velocities. To some extent, this is a result of the "piston" parameters employed in our models, which are constrained by the need of setting a supersonic inflow through the innermost radial boundary.

1D models in different evolutionary phases are subsequently mapped in 2D assuming axial and equatorial symmetry. From that point on, we continue the hydrodynamic evolution of the system in 2D. Employing axisymmetric relativistic hydrodynamic simulations we have explored the dynamical evolution of jets running into the medium left behind by the SN shock. For completeness, we have studied also the case in which no SN has formed. Based on analytic considerations and verified with an extensive set of simulations, we have estimated a threshold intrinsic jet luminosity, $L_{\mathrm{j}}^{\mathrm{th}}$. This threshold results from the balance between the progenitor ram pressure and the jet thrust. For a fixed jet injection half-opening angle, θ_{j}, the minimum intrinsic luminosity required for the well-posed initiation of supersonic jets depends on the radial position inside of the progenitor star. Quite surprisingly, over a broad range of possible locations of the jet nozzle (outside of the inner stellar core), the threshold is almost uniform and for the stellar model under consideration here it is $L_{\mathrm{j}}^{\mathrm{th}} \gtrsim 10^{49}\,\mathrm{erg\,s^{-1}}$. Translating this luminosity into the observed equivalent isotropic γ-ray luminosity, $L_{\mathrm{iso},\gamma} \simeq 4\epsilon_{\gamma} L_{\mathrm{j}}/\theta_{\mathrm{BO}}^2$, crucially depends on the jet opening angle after breakout, θ_{BO}, and on the efficiency in converting the intrinsic jet luminosity into γ-radiation, ϵ_{γ}. Some practitioners of the field

have pointed out that $\theta_{\rm BO} \sim \theta_{\rm j}$, in which case our jets would have a luminosity a few orders of magnitude above the highest observed ones in low-luminosity GRBs, unless an extremely small efficiency factor is applied (i.e., $\epsilon_\gamma < 10^{-5}$). The seeming contradiction between the high luminosity required for a successful jet initiation and the low ones observed can be resolved, though. Highly energetic jets can nevertheless produce low-luminosity events if either their opening angle after the breakout is large, which is found in our models, or if the conversion efficiency of kinetic and internal energy into radiation is low enough. Beyond these theoretical analysis, we show how the presence of a SN shock wave modifies the jet propagation. One of the main goals of this chapter was studying the emission with SPEV at the breakout of the jet or the SN ejecta. However this part suffered from technical problems, in particular excessive numerical diffusion caused by a lack of numerical resolution. Due to computing time restrictions, we could not properly obtain long-time light curves and spectra and could only compute the thermal emission. Therefore, our conclusions have to be considered preliminary.

We have obtained rather low luminosities inconsistent with previous calculations in the literature. We find that the SN flash of our models is $\lesssim 1000$ times dimmer than that of one of the prototype examples of GRB/SNe (GRB 060218/SN 2006aj) or X-ray flashes (XRF) associated to SNe (XRF 080109/SN 2008D). Moreover, the luminosity peak in the X-ray band happens at $\sim 6\,$s, i.e., much sooner than in the case of the previously mentioned observational prototypes. However, observations of GRB/SNe show heterogeneous properties, with cases in which the bolometric luminosity is orders of magnitude smaller than in the previous examples. Besides, X-ray peak times of $\sim 10\,$s are theoretically expected for compact WR progenitors. Both facts, make our models partly consistent with the existing phenomenology.

Our jet models display a large (kinetic plus thermal) energy reservoir after breakout. From the analysis of the asymptotic Lorentz factor in the whole cavity blown by the different jets, we foresee that the high-energy transients we may produce will be more similar to XRF than to GRBs. Indeed, our jet events display their peak specific luminosity in the extreme UV band, rather

than in the X-ray band, and clearly a fainter γ-ray luminosity ($\sim$ 2–4 orders of magnitude smaller than in the X-ray band).

Finally, we find that the very early observational signature of our different jet models (prior to the luminosity peak) below the $\gamma-$ray band is very similar comparing jets with the same intrinsic luminosity. This happens in spite of the substantially different hydrodynamic evolution of models which either interact with a pre-existing SN ejecta or propagate through the unmodified stellar progenitor. We expect this similarity lasting for time scales of the order of the light-crossing time of the transversal size of the emitting region ($\sim$ 1–2 s). Thus, we shall continue our models for even longer evolutionary times and, as argued above, employing a finer grid resolution. We are facing this challenge and the results will be reported in a forthcoming publication.

Chapter 1

Introduction

1.1 Gamma-ray bursts

Gamma-ray bursts (GRBs) are intense flashes of γ-rays, that arrive to Earth from unpredictable directions at random times, with inferred energies ($\sim 10^{51}$ erg released, typically, for tenths of seconds) that link them to the most extreme relativistic and compact objects of the Universe, namely with the formation of stellar mass black holes (BHs) or extremely magnetized neutron stars (NSs).

In the following, we try to summarize the GRB phenomenology and ennumerate the most stablished theories about their origin and nature that have been developed over the years thanks to the multiple missions on board of satellites carried out since their discovery. A very interesting and complete review about GRBs can be consulted in Vedrenne & Atteia's (2009) book, that can be updated and complemented with the review of Kumar & Zhang (2015).

1.1.1 50 years of observations

GRBs were discovered on 1967 by one of the military satellites *VELA*. These satellites were placed in orbit by the United States of America to ensure the Partial Test Ban Treaty signed with the Soviet Union and the United Kingdom in 1963 which prohibited the testing of nuclear bombs. Due to the low spatial resolution of the satellite, the first GRB was identified coming from the Moon

and suspicious arose that Soviets were testing nuclear bombs on the lunar surface. Once realized that no one was breaking the treaty, the observations were finally declassified for the scientific community and published by Klebesadel, Strong & Olson (1973) who reported the detection of 16 more bursts of this kind. Owing to the great expectation of these astrophysical events many efforts were done at that time in order to create burst catalogues (see, e.g., Mazets et al. 1981 –KONUS experiment–).

With the operationalization on 1991 of the Burst and Transient Source Experiment (BATSE; sensitive to photons in the range ∼25 keV–2 MeV) and the Energetic Gamma Ray Experiment Telescope (EGRET; sensitive to photons in the range 30 MeV–30 GeV) onboard the *Compton Gamma Ray Observatory*, the sensitivity of the detectors made a qualitative leap. The BATSE instrument counted on a system of alarms that, after several minutes to hours, alerted terrestrial telescopes to follow multiband GRB afterglows.

The afterglow is the emission that can be observed after the prompt gamma radiation. It is observed from X-rays to radio wavelengths and can last up to several months after the GRB itself. After a decade of BATSE observations it was concluded that the GRB distribution is isotropic (previously reported by, e.g., Atteia et al. 1987), but not homogenous as it can be seen from the deviation from the value of 0.5 in the so-called V/V_{max} test. In Euclidean space, each burst measured at a distance r defines a volume $V(r)$ enclosed within a larger volume, $V_{max}(r_{max})$ established by the most distant object of the sample. If the sample of bursts is distributed homogeneously the average is expected to be $\langle V/V_{max}\rangle = 0.5$. Recent studies have found values much smaller by more than 20σ (see, e.g., Guetta et al. 2005; $\langle V/V_{max}\rangle = 0.335 \pm 0.007$). As both the distance r and consequently $V(r)$ are unknown a priori, it is easier to use a procedure which relies on the number of counts registered in the detector. If P ($\propto r^{-2}$) is the count peak flux for each burst, a homogeneous distribution of bursts yields a relation $N \propto P^{-3/2}$. Hence, a deviation from a value of $-3/2$ in the $\log N$ – $\log P$ distribution as seen initially from BATSE data (Pendleton et al. 1996), implies that the distribution of GRBs is not homogeneous in an Euclidean sense.

On the basis of BATSE data two classes of GRBs can be differentiated (Kouveliotou et al. 1993): short events (with durations of less than 2 s) and the long ones (with durations of more than 2 s). The total duration is defined by the T_{90} parameter, i.e. the time in which the 90% of the total fluence has been registered. More precisely, $T_{90} = T_{95} - T_5$, where, T_5 and T_{95} refer to the times in which 5% and 95% of the fluence have been measured, respectively. The energy distribution, or hardness ratio, as a function of the duration seems to be different in both groups: in the long (short) ones more energy is received on the low (high) frequencies (see, e.g., Kouveliotou et al. 1993). In other terms is said that long (short) GRBs have softer (harder) spectra and then long (short) GRBs are often referred as 'long-soft' ('short-hard') GRBs. Likewise, BATSE data allows to establish that long GRBs are detected at a rate of 1 per day, approximately, while short GRBs at a low rate of ~ 0.3 per day. Furthermore, it is observed that GRB sources lack periodicity and do not repeat at the same place on the sky (Meegan et al. 1995).

Despite all these breakthroughs in our knowledge of GRBs, their origin –cosmological or galatic– was still a matter of debate in the mid-nineties. BATSE results seemed to favor cosmological models, but they were not confirmed until the arrival of *BeppoSAX*. Launched in 1996, *BeppoSAX* improved the precision on GRB location up to 4 arcminutes and brought the detection of the first multi-wavelength afterglow. The discovery was made by Costa et al. (1997) detecting an X-ray afterglow in GRB 970228. The study of the optical emission (van Paradijs et al. 1997) by terrestrial observatories allowed to confirm its cosmological nature[1] (redshift of $z = 0.695$; Bloom, Djorgovski & Kulkarni 2001). The first case of radio afterglows, predicted earlier for relativistic ejecta (Paczynski & Rhoads 1993), was detected by Frail et al. (1997; also in the GRB 970508).

Afterglow observations have made it possible to determine GRB distances and to detect host galaxies. The hosts of long GRBs have been identified with galaxies with high star-formation rates. The low luminosity and spectra

[1] Actually the first measurement was made for GRB 970508 at a redshift $z = 0.835$ (Metzger et al. 1997).

of these galaxies indicate low masses and low metallicities (10% of the solar metallicity in hosts with $z \lesssim 1$). They seem to favor the formation of (young) metal-poor massive stars, suggesting these as progenitors of GRBs. Despite these common features GRB hosts are not identified with any special population (Savaglio, Glazebrook & Le Borgne 2009). If the distance is known from observations, another important quantity of the system can be derived: the total energy released in the GRB. Assuming isotropic emission this energy turns out to be of the order of $M_{\odot}c^2$ (c being the speed of light in vacuum). However this energy is reduced if the emission is released from a collimated outflow (see Section 1.1.3).

Another remarkable achievement over these years of observations was the detection of SN1998bw (a Type Ib/c SN) in the error box of GRB 980425 (Galama et al. 1998), coming up with a possible GRB/SN connection that could provide important clues about the nature of GRBs. Since then a few more GRB/SN associations have been discovered (Iwamoto et al. 2000; Hjorth et al. 2003; Campana et al. 2006; Mazzali et al. 2006; Pian et al. 2006; Soderberg et al. 2006; Kaneko et al. 2007; Chornock et al. 2010; Starling et al. 2011; Cano et al. 2011; Fan et al. 2011; Margutti et al. 2013), making more evident the association of these two energetic events. The collapsar/hypernova model (see Section 1.2; Woosley 1993; Paczyński 1998; MacFadyen & Woosley 1999), in which the core of a massive star collapses to a BH surrounded by an accretion disc (AD), supports the association between long GRBs and SNe, in particular of Type Ib/c. However, the rate of GRB detections is much less than that of SN detections (by at least a factor of 100; see, e.g., Woosley & Bloom 2006), suggesting that GRBs are rare and that very special conditions must be fulfilled in the progenitor system in order to produce both events together.

At the beginning of the new millennium *HETE-2* and especially *Swift* (Gehrels et al. 2004) took the lead on GRB exploration. These satellites incorporated more than one instrument to monitor either γ and lower-frequency radiation, allowing for a quick follow-up of early multiband afterglows after the GRB detection (e.g., Fox et al. 2003). In particular *Swift* is well-equipped, carrying onboard several instruments which locate the burst within the first

1–2 minutes with a precision of 3 arcminutes. The Burst Alert Telescope (BAT; with a sensitivity range of 15–150 keV) initiates the detection process and starts automatically the afterglow search with the X-Ray Telescope (XRT; with a sensitivity range of 0.2–10 keV) and the Ultra-Violet/Optical Telescope (UVOT; with a sensitivity range of 170–600 nm). One of the main targets of *Swift* has been the early afterglow follow-up after the initial detection of the GRB. At least half of the observations of X-ray afterglows have demonstrated that the transition from the prompt emission is smooth (Gehrels, Ramirez-Ruiz & Fox 2009). *Swift* is also capable of detecting very distant GRBs which can be connected to Population III stars, formed in the early Universe. GRB 090429B is up to date the most distant GRB known with a redshift of $z = 9.4$ (Cucchiara et al. 2011). On its part, *HETE-2* made the important discovery of the first optical afterglow of a short GRB (GRB 050709; Villasenor et al. 2005).

Afterwards, the *Fermi Gamma-Ray Space Telescope* (with GBM and LAT instruments onboard) extended the spectral window up to ~ 300 GeV in the afterglow follow-up. It has been seen that the high-energy emission (> 100 MeV) comes after a delay of a few seconds with respect to the less energetic emission ($\sim 5\,\mathrm{keV} - 10$ MeV) and lasts up to $\sim 10^3$ s, i.e., around two orders of magnitude more than that of the latter (with durations of 10–30 s). This fact suggests different physical origins for each of these bands and that the > 100 MeV emission comes from synchrotron emission in the external FS (Kumar & Barniol Duran 2009; Ghisellini et al. 2010).

After almost 50 years of GRB observations there are still many open questions especially related with their formation and composition. New space missions are on their way for bringing us more light by means of early afterglow measurements (*SVOM*; Paul et al. 2011, and *UFFO* missions; Park et al. 2013) or polarization measurements (polarimeter POLAR; Produit et al. 2005) that together with ground-based observations at lower frequencies (e.g. with ALMA; ALMA Partnership et al. 2015) will give us more clues to understand the phenomenology and genesis of such intriguing events as the GRBs are.

1.1.2 Emission properties

The isotropic luminosity of a GRB can exceed that of the whole visible Universe for a few seconds. The typical total fluence, i.e. the integrated flux over the total duration of the burst, has been seen to be of the order of $\sim 10^{-7}$–10^{-3} erg cm^{-2}. Due to the cosmological origin of these sources, the isotropic energy is situated in the range 10^{48}–10^{55} erg. However, if the emission comes from an outflow collimated in a solid angle Ω, as presumed, the energy budget reduces a factor $\Omega/4\pi \sim 0.002$–0.01 and leads to values of 10^{49}–10^{52} erg, comparable to that of SN/hypernova (HN) explosions.

Prompt emission. The emission of the GRB prompt phase is mostly registered between the keV–MeV bands (γ-rays/hard X-rays) and lasts between a few milliseconds and a few minutes. They are also temporally highly variable (of the order of ~ 1 ms). The duration is detector-dependent since it depends, among other factors, on its sensibility and detection band, which makes that the temporal discrimination previously introduced has been described as inappropriate by some authors (see Section 1.2).

The spectrum (see, e.g., Pe'er 2015 for a review) is mainly non-thermal, for which optically thin synchrotron emission from relativistic electrons accelerated in internal shocks is the likeliest explanation. Furthermore, it has been found that the prompt emission can be modelled by different combinations of three possible components: a Band-function (Band et al. 1993), a quasi-thermal (blackbody) component and a power-law (non-thermal) component going up to high energies (Zhang et al. 2011). However, the presence of all these three components in a single burst has not been found. Only a combination of the quasi-thermal and the high energy non-thermal components has been identified (GRB 090902B). In fact, the classical Band-function alone has been observed to be the most common fit in the studied GRB sample. The Band-function consists of a broken power law characterized by a maximum or peak of energy E_p and the two spectral indices defining the low-energy (α) and

high-energy (β) power laws of the spectrum:

$$N(E) = \begin{cases} A \left(\frac{E}{100\,\mathrm{keV}}\right)^{\alpha} \mathrm{e}^{-E/E_0} & \text{for } E \leq (\alpha-\beta)E_0, \\ A \left[\frac{(\alpha-\beta)E_0}{100\,\mathrm{keV}}\right]^{\alpha-\beta} \mathrm{e}^{(\beta-\alpha)} \left(\frac{E}{100\,\mathrm{keV}}\right)^{\beta} & \text{for } E \geq (\alpha-\beta)E_0, \end{cases} \tag{1.1}$$

where $E_0 = E_p(2+\alpha)$ is the break energy and A the normalization parameter at 100 keV. Synchrotron self-absorption can be important at low energies as well as inverse Compton at high energies, so the Band-function can be modified in order to include these contributions. In the optically thin regime the index α of the spectral energy distribution has been predicted to take a value of $-2/3$, corresponding to an instantaneous synchrotron spectrum. On the other hand, radiation losses can be important as electrons cool on time scales shorter than the duration of a burst. For this reason the entire evolution of a cooling electron distribution should be followed in order to capture the whole emitted spectrum. The predicted value in this case is $\alpha = -3/2$.

The spectrum is also commonly represented as the variation of flux as a function of the frequency, $F_\nu \propto \nu^s$. The relation between the indices α and s is the following: $\alpha = s - 1$. The theory says that the instantaneous optically thin synchrotron spectrum is $F_\nu \propto \nu^{1/3}$ for $\nu < \nu_{\min}$, as a result of the sum of all the emission tails of the accelerated electrons (where $\nu_{\min}$ is the spectral peak delimited by the minimum Lorentz factor of the electron distribution), and $F_\nu \propto \nu^{-(q-1)/2}$ for $\nu > \nu_{\min}$ (where q is the electron power-law index; usually $q > 2$). Another segment in the optically thick regime is present at low frequencies due to self-absorption ($F_\nu \propto \nu^2$). In the optically thin regime $s \leq 1/3$ ($\alpha \geq -2/3$, the so-called 'line of death' of synchrotron emission). However, it has been observed that many GRBs show indices exceeding these values. Furthermore, $s = 0$ has been observed to be the most common value below the spectral peak (see, e.g., Kaneko et al. 2006), which requires additional processes beyond synchrotron.

In fact, apart from the Band-function additional components such as a thermal one have been inferred from observational fits of recent GRBs (Zhang et al. 2011). To connect both types of emission photospheric models have been invoked (Thompson 1994; Rees & Mészáros 2005; Giannios & Spruit

2007; Pe'er 2008; Lazzati, Morsony & Begelman 2009; Beloborodov 2010). The thermal emission from the photosphere, which can be Comptonized by electron/positron pairs created at internal shocks, could bring an alternative to the prompt emission. Indeed, some studies argue that the spectral peak could arise from Comptonized thermal photons (see, e.g., Rees & Mészáros 2005). Also it could explain the Amati and Ghirlanda correlations (see below).

Through the study of the spectral and temporal properties of the prompt emission correlations between parameters have been found over time. Amati et al. (2002) found that $E_{\rm p,i} \propto E_{\rm iso}^{1/2}$, a strong positive correlation between the intrinsic peak energy, $E_{\rm p,i}$ (where the spectrum peaks in the rest frame) and the isotropic energy, $E_{\rm iso}$, in a sample of 12 GRB spectra, in the range 2–700 keV, observed with *BeppoSAX*. This correlation is known as the Amati correlation. These results were lately confirmed in other observations (Lamb et al. 2004; Sakamoto et al. 2004, 2006) as well as the relationship between $E_{\rm p,i}$ and other parameters as $L_{\rm iso}$ (isotropic luminosity; Yonetoku relation: $E_{\rm p,i} \propto L_{\rm iso}^{1/2}$; Yonetoku et al. 2004), or E_γ (radiated energy; Ghirlanda relation: $E_{\rm p,i} \propto E_\gamma^{0.7}$; Ghirlanda et al. 2004), among others.

Afterglows. The temporal behaviour of GRB afterglows seems to follow a common pattern and Zhang et al. (2006) have been able to establish a canonical temporal evolution from observations of a large sample of X-ray afterglows. The flux evolution can be split in five phases (left panel of Figure 1.1). After the prompt emission (phase 0), and associated to that, (I) the initial steep decline is a rapid decay observed in the majority of bursts after a few tenths of seconds ($F_X \propto t^b$, with $b < -3$; Tagliaferri et al. 2005). It is followed after some minutes by (II) the shallow decay phase, a plateau interpreted as the late but continuous injection of energy by the central source, which is only observed in a few bursts, though ($b = -0.5$; Nousek et al. 2006; Zhang et al. 2006). At this point, the evolution of the afterglow connects with (III) the classical behaviour ($b = -1.2$), consistent with the external FS model and known before the identification of the early afterglow, followed by (IV) the post jet-break phase observed in the X-rays (and other bands) in, approximately,

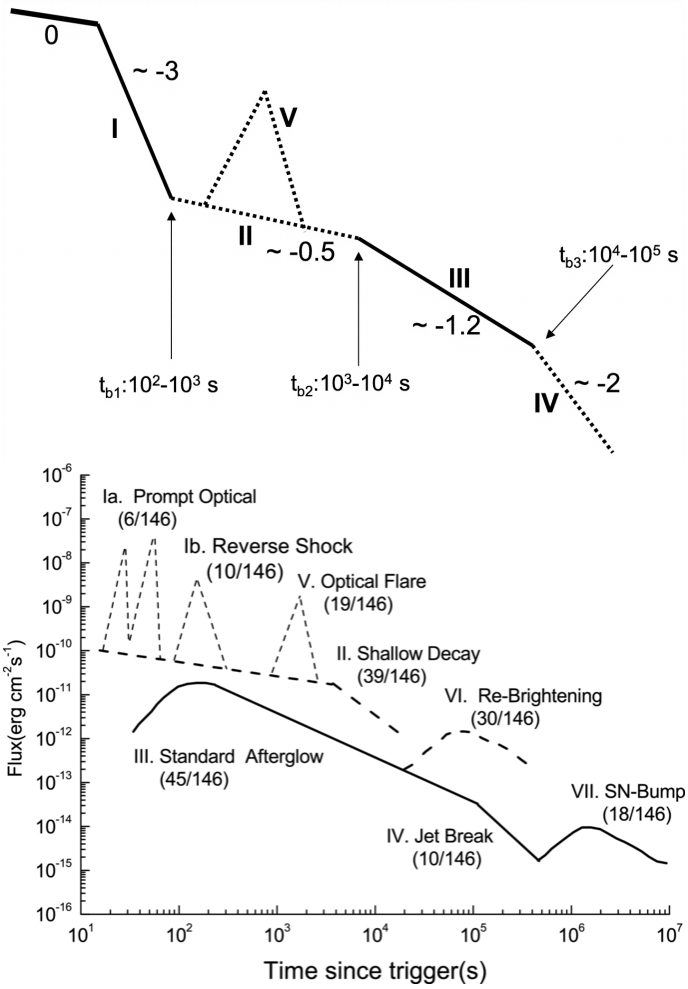

Figure 1.1: *Top*: Canonical X-ray afterglow light curve (from Zhang et al. 2006). Four power-law phases can be differentiated between the break points (t_b) after the prompt emission. See the text for a description. The temporal indices, b ($F_X \propto t^b$), are indicated for each power law. *Bottom*: Canonical optical afterglow light curve (from Li et al. 2012). In brackets are shown the number of GRBs in which have been identified each of these stages from a sample of 146 bursts.

20% of the events (Gehrels et al. 2009)[2]. This jet break is indicative of the

[2] Racusin et al. (2009) observed in their study of *Swift*-X-ray afterglows that this phase was present in at least 12% of the events of the studied sample.

likely collimation of the outflow. Besides, *Swift* has observed (V) late flares in the X-ray afterglow in half of the detected GRBs linked to the central engine activity (Burrows et al. 2005). These flares are less observed in the optical band, but still present.

Optical light curves show diverse behaviors in the first 500 s where indices can vary between $-1.17 < b < 0.21$, $F_O \propto t^b$. After this prompt phase, some light curves (LCs) show a single power-law with $-1.20 < b < -0.52$, or a broken power law consistent with an initial shallow phase ($-0.74 < b < -0.46$) before a classical afterglow ($-1.72 < b < -1.34$). By means of fitting a sample of 146 events, a study by Li et al. (2012) corroborates that the optical afterglow can be depicted also under a canonical behaviour (right panel of Figure 1.1) similar to that in X-rays. In a few events of the sample some flares have been observed during the prompt phase (Ia) as well as after its end (Ib, attributed to the reverse shock region). The (II) early shallow decay phase, with a flatter slope before the break compared to that of X-rays, and (III) the classical afterglow, preceded by an initial rise in some cases, are the most common features ($\sim 30\%$ of the events). By contrast, (IV) the jet-break point is observed only in the 7% of the events. (V) Flares at later times have been also observed, but in a small number of events. Up to here, and excluding the early flares (phase I), optical and X-ray bands show the same general behaviour. However, two more phases remain characteristic of the optical band: a (VI) re-brightening of the afterglow ($\sim 20\%$ of the events) and (VII) a SN bump observed only in a few cases (but suspected to be more common) after some days or weeks.

Besides flares, *Swift* has observed another discrepancy between the LCs of these two bands. While some breaks are commonly observed in most X-ray afterglows, they are not seen in the optical ones (or at a different time), showing a chromatic dependence of these breaks (Panaitescu et al. 2006). This threatens the external forward shock model for afterglows, consistent with pre-*Swift* observations, and suggests a more advanced modeling (Wang et al. 2015). The different evolution of these two bands in around 70% of the events (Melandri et al. 2014) suggests a different region or mechanism for these two

kind of emissions. Nevertheless, the remaining events display a consistency in the decay indices showing that a unique emitting region would be still possible.

1.1.3 The fireball model

There are still many open questions about the nature of GRBs. The most accepted model for its origin and evolution is the fireball model (Cavallo & Rees 1978; Paczynski 1986; Goodman 1986; Shemi & Piran 1990). A fireball is an ensemble of electron and positron pairs, photons and a small fraction of baryons moving at relativistic speeds. The fireball expands because of the huge radiation pressure. High speeds are achieved if this region is 'radiation-dominated', i.e., if $\eta \equiv E_0/M_0c^2 > 1$, where E_0 is the bulk energy of the fireball and M_0 its total mass. The fireball accelerates in this initial stage due to conversion of internal energy to kinetic energy. As long as the optical depth, τ, is large, the expansion is adiabatic. The bulk Lorentz factor increases as $\Gamma \propto R$ close to the central engine up to some saturation radius, R_s, from where $\Gamma = \Gamma_{max} \sim \eta$ remains constant in a coasting phase. The local (denoted as primed) temperature decreases as $T' \propto R^{-1}$ when $R < R_s$ and as $T' \propto R^{-2/3}$ when $R > R_s$ (see, e.g., Pe'er 2015). The fireball starts to decelerate once it encounters the resistance of the interstellar medium (see below for more details).

Kinetic energy is dissipated at shocks and (partially) converted into radiation. All the produced photons become part of the fireball and can interact with its constituent particles before eventually escaping. However they can be trapped if the mean free path between two scattering reactions of a photon is small compared to the size of the fireball (when the frequency of scattering events is high enough to absorb most of the energy of the photon), in which case we speak of an opaque or optically thick medium. The opaque region is delimited by the photosphere, $R_{\rm ph}$, defined as the location where the optical depth is unity, $\tau = 1$, and photons on average scatter a last time before escaping freely. Frequent scatterings couple photons and matter inside the photosphere tightly and enforce equal velocities and local thermal equilibrium, i.e. equal temperatures of radiation and matter. e^-e^+ pairs recombine below

a temperature $T' \sim 17$ keV and the fireball becomes transparent or optically thin at $R_{\rm ph} \sim 10^{12}$ cm (though this may happen earlier and below R_s). A small part of the energy is radiated from the photosphere with a luminosity $L_{ph} \propto R_{\rm ph}^2 T_{ph}'^4 \Gamma_{ph}^2$ (see, e.g., Kumar & Zhang 2015).

From the high temporal variability observed in LCs, $\Delta t \sim 10$ ms, it is inferred that the GRB sources are very compact, $R < c\Delta t \sim 3 \times 10^7$ cm (Paczynski & Rhoads 1993). Since the optical depth for $e^- e^+$ pair creation from the collision of two photons ($\gamma\gamma \rightarrow e^- e^+$) is $\tau_{\gamma\gamma} \propto R^{-2}$, at these distances the medium is still very opaque to the radiation ($\tau_{\gamma\gamma} \gg 1$) and an external observer should not see any photon. From the theoretical point of view this fact presents a conundrum as GRBs are actually observed from Earth. This *compactness problem* was solved considering relativistic expansion with bulk Lorentz factors $\Gamma > 100$. If the GRB source is moving relativistically, the latter condition relaxes to $R < c\Gamma^2 \Delta t$, increasing the emitting region by a factor of Γ^2 and decreasing the optical depth by a factor of Γ^4. Furthermore, GRB spectra reveal the presence of high energy photons above the 1 MeV threshold for pair creation by a single photon ($\gamma \rightarrow e^- e^+$) that should not be seen. However, this threshold is not violated since photons are actually blueshifted from the source due to the ultrarelativistic expansion, i.e. photons observed as γ-rays were actually emitted as X-rays in the restframe of the fireball. Also the photon energy is relaxed by a factor of Γ ($E_\gamma = E_{\gamma,obs}/\Gamma$) and only a small number of them will produce pairs. Even so, $e^- e^+$ pairs are in equilibrium within the fireball on the early stages and once it becomes transparent the radiation is quasi-thermal (Vedrenne & Atteia 2009) in contradiction to the observed non-thermal spectrum.

Collisionless shocks, in which electric and magnetic fields instead of particles dominate the interaction, are one of the solutions proposed to explain the existence of non-thermal spectra. Collisionless shocks in the rarefied plasma of an expanding ejecta are able to produce a non-thermal spectrum dissipating the kinetic energy of the fireball sufficiently far away from the source to explain the observed phenomenology (see, e.g., Piran 1999 for a review).

Internal & external shocks. The internal and external shock models were first introduced independently (although by the same authors), nevertheless both theories are combined nowadays to explain the non-thermal emission of a GRB from its early stages to the late ones (e.g., Sari & Piran 1995). The prompt γ radiation is produced by internal shocks while most of the fireball energy is released later in the afterglow by the external shock.

Any supersonic outflow that propagates into a finite density medium may form an external shock at its forward edge. Rees & Meszaros (1992) considered the external shock scenario in order to introduce the presence of a small fraction of baryons, with a typical mass of $M_{\rm bar} \sim 10^{-6} M_{\odot}$, that can help to create a non-thermal spectrum. This baryon 'contamination' is small enough to allow for Lorentz factors $\Gamma \geq 10^3$, consistent with relativistic motion in case the equivalent isotropic energy content of the fireball be $\gtrsim 2 \times 10^{51}$ erg. In this context, the interaction of a relativistic shell (the front part of the fireball) with the interstellar medium causes the formation of an external shock where highly relativistic electrons are accelerated producing synchrotron emission. Actually a pair of shocks separated by a contact discontinuity are formed: the forward (FS) and the reverse shock (RS), that divide the system into four regions (see, e.g., Fig. 4.4). The former advances relativistically into the circumburst medium (region 1) while the latter progresses subrelativistically[3] 'backwards' (with respect to the contact discontinuity) towards the relativistic material in the shell (region 4). The contact discontinuity situated between both shocks separates the shocked external medium (region 2) from the shocked shell (region 3).With the combined action of the FS and the RS the bulk kinetic energy of the ejecta can be converted again into thermal energy of the electrons and finally radiated away in the afterglow. The estimated radius at which this happens is $R_{\rm ext} \sim l^{3/4} \Delta^{1/4} \sim 10^{16} - 10^{17}$ cm (Sari & Piran 1995), where l is the Sedov length (defined as the distance traveled by the ejecta outside of which they have swept up an ISM mass exceeding its own) and Δ the width of the shell in the observer's frame. For a radius $R > R_{\rm ext}$ the fireball decelerates in a

[3]The RS is considered relativistic (Newtonian) in the thick (thin) shell models (see, e.g., Sari & Piran 1995; Gao et al. 2013).

self-similar way. If radiative losses are unimportant the expansion is considered adiabatic (Blandford & McKee 1976), i.e., $\Gamma \propto R^{-3/2}$. On the other hand, $\Gamma \propto R^{-3}$ in the radiative case (see, e.g., Rees & Meszaros 1992). The temporal dependence of the radius is $R \propto t^{1/4}$ in the adiabatic case (thus, $\Gamma \propto t^{-3/8}$) and $R \propto t^{1/7}$ in the radiative case (thus, $\Gamma \propto t^{-3/7}$).

At the Sedov length ($l \sim 10^{18}$ cm) the shell enters the Newtonian phase as the rest-mass energy of all the swept external medium becomes comparable to its energy.

The internal shock scenario (Rees & Meszaros 1994) was devised to explain the high temporal variability not adressed by external shocks. The variability is attributed to the random activity of a central engine which releases mildly relativistic *shells* with different Lorentz factors, leading to the interaction of fast shells with slower ones previously released. This mechanism reduces the ejecta Lorentz factor to values of ~ 100 and can dissipate a fraction of the kinetic energy at a distance $R_{\rm int} \sim 10^{14} - 10^{15}\,{\rm cm} < R_{\rm ext}$. Nevertheless its efficiency is low ($2-20\%$; see e.g., Piran 1999). The sum of the individual spectra produced in each of the collisions between shells shapes the total spectrum.

If $\Gamma < 100$ due to excessive mass-loading (for example, after breaking out a massive star), $R_{\rm int}$ may be smaller than $R_{\rm ph}$ and (non-thermal) γ-photons will be trapped leading to 'failed GRBs' and photospheric (thermal) emission in the UV/X-ray band followed by the typical afterglow (Xu et al. 2012).

Collimated outflows. It is assumed that GRBs result from $\gamma-$radiation released in ultrarelativistic bipolar jets with a high degree of collimation. Nevertheless, there are arguments for and against collimation. The most convincing argument in favor of collimated outflows or jets are the achromatic breaks found in some LCs, called for this reason 'jet breaks'. Due to relativistic Doppler boosting and aberration the radiation from a relativistic outflow is beamed into a narrow cone of half-oppening angle $\theta_b \sim 1/\Gamma$. If Γ is high, the observer only sees a small region of the source but once the outflow decelerates, i.e., Γ decreases, θ_b increases and a larger region of the source becomes visible. This effect is reflected in a monotonic decrease of the observed flux

since the emitting surface is larger. If the source were spherical and expanded isotropically, the slope of decline would remain constant. However, if it has a finite angular size θ_j, the flux breaks and changes its slope once $\theta_b > \theta_j$. This break of tendency is seen in many observed LCs suggesting collimated rather than spherical outflows (see Fig. 1.1). Once $\theta_j = \theta_b$ the observer receives the radiation from the whole surface of the outflow. From this point the flux decays faster than that of the spherical case and changes its slope of decline as the emitting surface does not increase anymore but the radiation cone does. Jet-breaks allow to estimate θ_j. Another indication for collimation is the clustering of jet energies around values of $\sim 10^{51}$ erg once isotropic energies are corrected assuming collimated sources (Frail et al. 2001). On the other hand, Fe lines in GRB X-ray afterglows (see, e.g., Piro et al. 1999) are indicative of a dense, iron-rich circumburst medium whose geometry may be contrary to the collimation idea. The iron-rich material must not be in front of the jet since an observer would see an absorption line instead of an emission line. Thus, the material should be located at the surroundings and being excited by photons coming from the jet. However, strong collimation prevents these photons from reaching the surrounding material. Nevertheless, photons from subrelativistic gas emitted alongside the jet or jets embedded in strong, dense winds (as numerical simulations suggest) might explain Fe lines in the context of relativistic jets.

Microphysical parameters. At shocks a fraction of the bulk kinetic energy is dissipated and distributed to particles and magnetic fields generated by compression behind the shock front. The parameters ϵ_e and ϵ_B define the ratios of energy given to electrons and magnetic fields ($B \propto \epsilon_\mathrm{B}^{1/2}$), respectively, to the energy dissipated. Equipartition for ϵ_e and ϵ_B is often considered, especially in internal shocks. Furthermore ϵ_e and ϵ_B are usually assumed to be constant throughout the whole evolution of the outflow, although have been suggested to vary with time (Panaitescu et al. 2006). Medvedev (2006) suggested that $\epsilon_\mathrm{e} \sim \sqrt{\epsilon_\mathrm{B}}$, from a theoretical study of the microstructure of collisionless shocks. This relation was further investigated on the basis of general spectral fits by

van Eerten & Wijers (2009), who could not reject Medvedev's relationship.

From a theoretical point of view, these parameters could be different in the FS and the RS. Different particle densities in the downstream region of both shocks lead to different electron distributions in the Lorentz factor space. Values of ϵ_B are expected to be much smaller than 1 for synchrotron radiation, but could be as large as 1 in the presence of instabilities (Piran 1999).

In general these parameters are chosen in such a way as to fit afterglow observations (Vedrenne & Atteia 2009). For ϵ_e, a narrow distribution has been found between 0.02 to 0.6, with a tendency for most GRBs to have $\epsilon_e < 1$, while for ϵ_B the estimation from X-ray and optical observations has established a wider distribution ($\epsilon_B \sim 10^{-8} - 10^{-3}$ for a uniform medium; $\epsilon_B \sim 10^{-9} - 10^{-3}$ for a wind medium), with a median of $\epsilon_B \sim 10^{-5}$ (Santana, Barniol Duran & Kumar 2014). However, we note from fittings of some GRB afterglows that ϵ_B can be comparable to ϵ_e (GRB 030329; GRB 050904; GRB 051221A) or even larger (GRB 980329; GRB 020405; GRB 060418; see Santana et al. 2014 and references therein).

Nowadays the origin of the prompt γ-ray emission in GRBs is still a matter of active debate (see, e.g., Zhang et al. 2011; Hascoët, Daigne & Mochkovitch 2013) but the internal–external shock scenario seems a likely model to explain the non-thermal spectrum in all temporal phases of a GRB. As an alternative, many authors have considered the possibility that the magnetic energy content of the flow may be dissipated (Usov 1992; Thompson 1994; Meszaros & Rees 1997; Lyutikov & Blandford 2003; Zhang & Yan 2011).

1.1.4 Afterglow modelling

The spectral energy distribution of the non-thermal emission produced by electrons in either internal or external shocks (see Section 1.1.3), as well as their temporal evolution, are commonly characterized by power laws. These electrons accelerate up to relativistic speeds and produce synchrotron and inverse Compton emission afterwards. In the simplest case these electrons are assumed

to follow a power law in Lorentz factor (γ) with a lower cut-off imposed by $\gamma_{\rm min}$ and an upper cut-off imposed by $\gamma_{\rm max}$ (determined by the magnetic field, B; see Eq. (2.63)). The general shape of the instantaneous spectra can be calculated on the basis of (assumed) intrinsic parameters of the shock and the electron distribution. However its temporal evolution depends on the shape of the outflow. Sari, Piran & Narayan (1998) assumed the expansion of a spherical shock of radius $R(t)$. Later Sari, Piran & Halpern (1999) showed that the FS of a collimated jet was more consistent with observations. In general, the flux can be described mainly by four characteristic quantities: the peak flux, $F_{\nu,\rm max}$, the typical synchrotron frequency (or peak frequency, determined by $\gamma_{\rm min}$), $\nu_{\rm m}$, the cooling frequency (for electrons which cool on the dynamical time scale of the system), $\nu_{\rm c}$, and the self-absorption frequency, $\nu_{\rm sa}$ (high-energy photons are absorbed via inverse Compton with low-energy photons; this frequency delimits the optically thick region of the spectrum and thus $\tau(\nu_{\rm sa}) = 1$). In the simplest models the instantaneous spectrum is calculated assuming synchrotron radiation from a power-law distribution of electrons accelerated at shocks (see, e.g., Sari et al. 1998). In principle all the three frequencies presented above can be ordered under all the possible combinations, however cases in which $\nu_{\rm sa} > \nu_{\rm c}$ are extremely rare (see, e.g., Gao et al. 2013). The typical situation is that $\nu_{\rm sa}$ be the smallest frequency. In this case, two regimes can be taken into account depending on whether the minimum Lorentz factor of the distribution, $\gamma_{\rm min}$, is larger or smaller than a critical value, $\gamma_{\rm c}$ (associated to the frequency $\nu_{\rm c}$), for those electrons which cool on the dynamical time scale of the system. If $\gamma_{\rm min} > \gamma_{\rm c}$ ('fast cooling' regime) the distribution of electrons cools up to $\gamma_{\rm c}$, while if $\gamma_{\rm min} < \gamma_{\rm c}$ ('slow cooling' regime) only electrons with Lorentz factors larger than $\gamma_{\rm c}$ will cool. The respective fluxes in the observer frame for both regimes are

$$F_\nu = F_{\nu,\rm max} \begin{cases} (\nu/\nu_{\rm sa})^2\,(\nu_{\rm sa}/\nu_{\rm c})^{1/3} & \text{if } \nu < \nu_{\rm sa}, \\ (\nu/\nu_{\rm c})^{1/3} & \text{if } \nu_{\rm sa} < \nu < \nu_{\rm c}, \\ (\nu/\nu_{\rm c})^{-1/2} & \text{if } \nu_{\rm c} < \nu < \nu_{\rm m}, \\ (\nu_{\rm m}/\nu_{\rm c})^{-1/2}\,(\nu/\nu_{\rm m})^{-q/2} & \text{if } \nu_{\rm m} < \nu, \end{cases} \tag{1.2}$$

if $\nu_{\rm a} < \nu_{\rm c} < \nu_{\rm m}$ (fast cooling) and

$$F_\nu = F_{\nu,\max} \begin{cases} (\nu/\nu_{\rm sa})^2\,(\nu_{\rm sa}/\nu_{\rm m})^{1/3} & \text{if } \nu < \nu_{\rm sa}, \\ (\nu/\nu_{\rm m})^{1/3} & \text{if } \nu_{\rm sa} < \nu < \nu_{\rm m}, \\ (\nu/\nu_{\rm c})^{-(q-1)/2} & \text{if } \nu_{\rm m} < \nu < \nu_{\rm c}, \\ (\nu_{\rm c}/\nu_{\rm m})^{-(q-1)/2}\,(\nu/\nu_{\rm c})^{-q/2} & \text{if } \nu_{\rm c} < \nu, \end{cases} \tag{1.3}$$

if $\nu_{\rm sa} < \nu_{\rm c} < \nu_{\rm m}$ (slow cooling), where q is the electron power-law index. The region $F_\nu \propto \nu^{1/3}$ is characteristic of the synchrotron radiation. The region where $\nu < \nu_{\rm sa}$ is a steep cut-off usually found in the afterglow due to the self-absorption being $F \propto \nu^2$ or even $\nu^{5/2}$ if the synchrotron frequency lies in this frequency range. A third case lying in the slow cooling regime is also possible when $\nu_{\rm m} < \nu_{\rm sa} < \nu_{\rm c}$, $\nu_{\rm sa}$ now being the intermediate frequency (Granot & Sari 2002). Granot et al. (2000) noted that for a non-homogeneous distribution of electrons (composed of hot and cold electrons within the shocked region) a new break frequency, $\nu_{\rm ac} < \nu_{\rm sa}$, appears in the fast cooling regime delimiting a new segment in the broken power-law spectrum with a slope of 11/8. In Figure 1.2 we show all five possible spectra for a non-homogeneous distribution of electrons. Note the new segment for $\nu_{\rm ac} < \nu < \nu_{\rm sa}$ in spectrum 5 and compare with Eq. (1.2). See the figure caption for more details.

The transition between the two regimes (from fast to slow cooling) may occur at some point between the prompt emission and the afterglow once the external shock becomes the main mechanism of particle acceleration. The temporal evolution of the four characteristic quantities, which in turn depend on the microphysical parameters of the system, depend explicitly on the hydrodynamics and therefore on the shape of the ejecta. Sari et al. (1998) studied the adiabatic (constant energy; if $\epsilon_{\rm e} \ll 1$) and radiative evolution (radiative energy loss is important; if $\epsilon_{\rm e} \sim 1$, i.e., all the internal energy is dissipated) of a relativistic spherical shock into a constant density ISM according to the solution of Blandford & McKee (1976). Note that a spherical expansion can only be considered valid at the initial stages of the evolution. When the relativistic shell has been decelerated to values of $\Gamma < 1/\theta_j$ the collimated structure of the fireball is uncovered and the 'edge effects' of the jet become relevant for

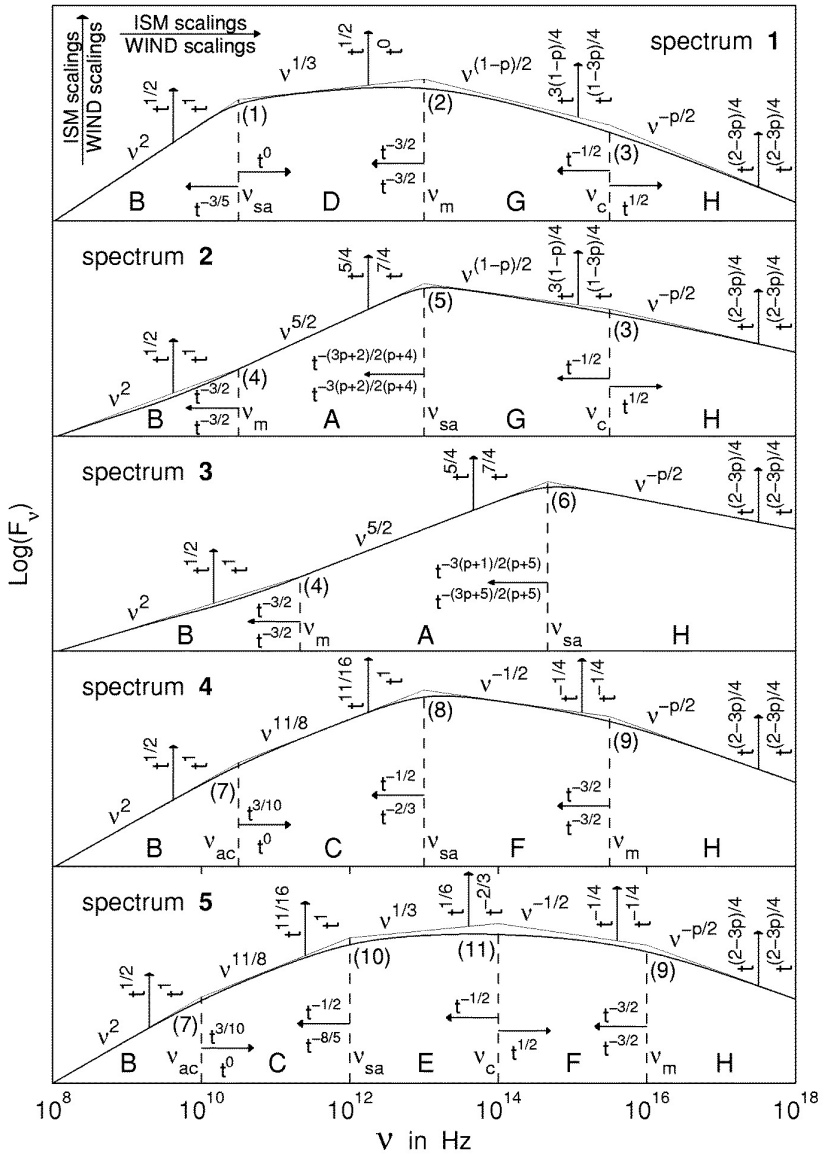

Figure 1.2: Possible spectra for a power-law distribution of electrons (from Granot & Sari 2002). Spectra 5 (canonical) and 4 are in the fast cooling regime. Spectra 1 (canonical) and 2 in the slow cooling. Spectrum 3 is valid for both slow and fast cooling. Thick lines represent the different segments of the power-law while thin lines an analytical fit by Granot & Sari (2002). Temporal dependences of each segment and each typical frequency are depicted for a constant density ISM and a wind density medium. The index p in Granot & Sari's figure corresponds to q in the text.

Table 1.1: Temporal indices, b ($\propto t^b$), of the four characteristic quantities considering different hydrodynamic evolutions in a constant density ISM.

b	$F_{\nu,\max}$	$\nu_{\rm m}$	$\nu_{\rm c}$	$\nu_{\rm sa}$
spherical	0	$-3/2$	$-1/2$	0
jet	-1	-2	0	$-1/5$

the dynamics of the system. This jet break is reflected in the afterglow LC as shown in the previous section. Sari et al. (1999) studied the adiabatic expansion of a jet, already in the slow cooling regime, which spreads laterally into a constant density ISM. It is remarkable that the edge effect does not change the expressions of the four characteristic quantities with respect to the spherical case (apart from an extra steepening correction factor; Gao et al. 2013), while its sideways expansion does. For comparison, in Table 1.1 we summarize the frequency and temporal dependences of the four characteristic quantities in the spherical and jet evolution phases. The expected flux in this phase is (compare with spectrum 1 in Figure 1.2)

$$F_\nu \propto \begin{cases} \nu^2\, t^0 & \text{if } \nu < \nu_{\rm sa}, \\ \nu^{1/3}\, t^{-1/3} & \text{if } \nu_{\rm sa} < \nu < \nu_{\rm m}, \\ \nu^{-(q-1)/2}\, t^{-q} & \text{if } \nu_{\rm m} < \nu < \nu_{\rm c}, \\ \nu^{-q/2}\, t^{-q} & \text{if } \nu_{\rm c} < \nu. \end{cases} \tag{1.4}$$

Here we have restricted the discussion to those reference models in which only the FS is assumed to radiate. The RS may have an strong influence at early times being responsible of producing strong optical flashes (Sari & Piran 1999a,b; Zhang, Kobayashi & Mészáros 2003b; Kumar & Panaitescu 2003; Giannios, Mimica & Aloy 2008; Mimica, Giannios & Aloy 2009a). Furthermore, in the discussion we have assumed that the ejecta expand into a uniform medium ($\rho \propto R^0$) in an adiabatic way (so that the energy of the outflow remains constant during the whole evolution). An electron spectral index $q > 2$ has been assumed as well in order to have finite electron energies. The reader is referred to the review of Gao et al. (2013; and references therein; see also

Leventis et al. 2012) where more advanced models are introduced accounting for all the dynamical phases within the fireball model and all the resulting LCs are shown.

Thanks to *Swift* and *Fermi* observations it has been possible to identify more clearly a thermal component in the prompt emission of a large number of bursts. Indeed, this component extends into the afterglow of some of them, since the best fit of the observed spectra consists in a BB component added to a power law.

The GRBs 060218 (Campana et al. 2006; $T_{90} = 2100\,\mathrm{s}$) and 100316D (Starling et al. 2011; Cano et al. 2011; $T_{90} > 1300\,\mathrm{s}$), both with $E_{iso} \simeq 4 \times 10^{49}$ erg and $T_{90} > 10^3\,\mathrm{s}$, show an unusual X-ray (and optical) afterglow with a thermal component which extends from a few hours to days. Both BBs evolve with a relatively constant temperature in the range of 0.1–0.2 keV from an initial distance larger than $10^{11}\,\mathrm{cm}$. The identification of another thermal component in the bright, more 'canonical' GRB 090618 (Page et al. 2011; $E_{iso} \sim 2.5 \times 10^{53}\,\mathrm{erg}$ and $T_{90} = 113\,\mathrm{s}$) show that this feature might not be restricted to ultra-long, low-luminosity GRBs (llGRBs). For this burst the BB component evolves in temperature from 1 to 0.3 keV and in radius from 5×10^{12} to $10^{13}\,\mathrm{cm}$. Starling et al. (2012) reported a detection in the X-ray afterglow of GRB 101219B (with similar spectral properties than GRB 090618) and the possible identification in another 4 bursts, showing that the thermal component can be observed in a broad range of GRB energies. Another interesting GRB is the ultra-long and energetic GRB 101225A (Thöne et al. 2011; Levan et al. 2014) which showed an anomalous afterglow with strong thermal component in both the X-ray and the optical band. The X-ray component is associated to a quiet hotspot located at $\sim 10^{11}\,\mathrm{cm}$, much smaller in radius than but similar in temperature as those BB components found in the already mentioned thermal GRBs. The optical emission is well fitted with an expanding, cooling BB with an inferred BB radius larger than $10^{14}\,\mathrm{cm}$.

All the aforementioned GRBs have been associated to spectroscopically confirmed core-collapse SNe (with the exception of GRBs 090618 and 101225A whose SNe have been reported only photometrically). This suggest that the

origin of the thermal signal in these bursts might arise from a shock breaking out of the progenitor star (Campana et al., 2006; Waxman, Mészáros & Campana 2007; Soderberg et al., 2008; Nakar & Sari 2012; Nakar 2015; Irwin & Chevalier 2016), which could be surrounded by a low-mass envelope extending up to $\sim 10^{14}$ cm. Other alternative mechanisms for thermal emission in prompt X-ray afterglows that can be found in the literature are emission from a relativistic cocoon during the expansion phase (Pe'er, Mészáros & Rees 2006; Starling et al. 2012) or Comptonization of shock breakout thermal photons in external shocks (Dai, Zhang & Liang 2006; Wang et al. 2007). Another scenario that was considered in order to explain the thermal features seen in X-ray and optical afterglows has been the interaction of the prompt emission and the GRB jet itself with a massive shell surrounding the progenitor star at a distance of $\sim 10^{16}$ cm (Badjin, Blinnikov & Postnov 2013). Even shells located at some tens of parsecs have been postulated to explain unusual (non necessarily 'thermal') X-ray afterglows (Holland et al. 2010; Evans et al. 2014; Zhao & Shao 2014; Margutti et al. 2015). For the particular case of GRB 060218, Irwin & Chevalier (2016) review emission models previously considered for this peculiar burst and propose a new one in order to cover all the afterglow phases. According to them, the prompt thermal X-rays would come from the jet's photosphere, the optical/UV thermal emission from the expanding SN shock that has interacted with a low-mass extended envelope at $\sim 10^{13}$ cm and the X-ray late emission from the light echo of the prompt emission from a dust shell at ~ 30 pc.

1.2 The progenitor system

The current phenomenology is compatible with the existence of, at least, two different classes of GRBs (but see, e.g., Horváth 1998, 2002; Mukherjee et al. 1998; de Ugarte Postigo et al. 2011), each of which likely linked to different progenitor systems. The typical timescales of both events constrain the size of the system. Long burst durations (LGRBs) are indicative of explosions generated by high-mass stars in which enough mass is available to power a

long-lasting outflow. Furthermore the increasing number of Type Ibc SNe associated to long GRBs point out to single massive stars as progenitors. The short timescales of short GRBs suggest more compact systems such as mergers of NS-NS or NS-BH binaries (Paczynski 1986; Goodman 1986; Eichler et al. 1989; Narayan et al. 1992; see Berger 2014 for a review) after losing their orbital energy in form of gravitational waves, more pronouncedly in the last milliseconds of the process. Regardless of the scenario it is more or less clear that the remnant of all of these systems will be a compact object: likely a BH or even a proto-magnetar (PM).

1.2.1 Mechanisms of energy extraction

Different extraction mechanisms have been enumerated to tap the rotational and gravitational binding energy of the BH-AD system and power a bipolar, collimated relativistic jet along the rotational axis of the system. First, neutrinos may be produced in the hot disc and annihilated (creating electron-positron pairs, $\nu\bar{\nu} \rightarrow e^{-}e^{+}$; Eichler et al. 1989), depositing an energy of the order of $\sim 10^{51}$ erg (Woosley 1993) close to the rotational axis. By means of numerical simulations of accreting BHs, Birkl et al. (2007) show that the released energies they obtain by neutrino annihilation could be enough to power GRB jets. On the other hand, magnetohydrodynamic (MHD) simulations by Nagataki et al. (2007) have shown that neutrino heating seems not very effective as a jet launching mechanism. Another possible sources of energy extraction involve magnetic fields supported by external currents in the disc. They may be strong enough for the vacuum to become unstable to production of $e^{-}e^{+}$ pairs. These pairs will form a force-free magnetosphere that can extract energy and angular momentum from a rotating BH by electromagnetic braking (Blandford & Znajek 1977). The energy released is used to accelerate relativistic electrons at large distances and can be beamed depending on the magnetic field geometry. An alternative model suggest that field lines may extract the energy and angular momentum from discs and carry out to large distances to power and collimate relativistic jets (Blandford & Payne 1982). General Relativistic MHD simulations of accreting BHs show that is possible to launch

magnetically dominated jets (Tchekhovskoy, Narayan & McKinney 2011). For large values of the BH spin, it has been found that rotational energy can be extracted from the BH in order to accelerate powerful outflows. Previous simulations of Tchekhovskoy, McKinney & Narayan (2008) showed that these jets are capable to reach Lorentz factors > 100 when they are breaking out the progenitor star. Furthermore, the energies and opening angles are consistent with those in long GRBs.

1.2.2 Collapsars

Nowadays, the paradigm within which we explain the origin of most LGRBs is the collapsar model (Woosley 1993; MacFadyen & Woosley 1999). Initially termed as 'failed (Type Ib) supernova' by Woosley (1993), a collapsar is basically a collapsing, massive star endowed with rapid rotation. The gravitational collapse of a carbon-oxygen/iron core of a massive star fulfills two of the requirements to harbor the central engine of a LGRB. First, the dynamical timescale of the collapse is of the order of tenths of seconds and, second, the potentially usable energy is of the order of $\sim 10^{51}$ erg. In this model, a stellar mass BH results from the collapse of core of the massive progenitor star. The BH must be surrounded by a thick AD (actually, an accretion torus), the accretion of which feeds both the BH and, depending on the dominant mechanism to tap the energy of the central engine (Sect.1.2.1), an ultrarelativistic jet. Stellar cores with a specific angular momentum, j, in the iron core within certain interval (e.g., $3 \lesssim j_{16} \lesssim 20$, where $j_{16} = j/(10^{16}\,\mathrm{cm^2\,s^{-1}})$) are more favored to form an AD and then a LGRB jet (MacFadyen & Woosley 1999). Retaining a large specific angular momentum in the core of massive stars is difficult because of the action of magnetic torques and the ejection of stellar winds. To ameliorate the problem, low-metallicity stars which tend to have weaker mass loss have been traditionally considered as precursors of collapsars (Woosley & Heger 2006). Among massive stars, the most compact ones, such as Wolf-Rayet (WR) stars, are considered the most probable progenitors, whereas extended stellar envelopes such as those of red supergiants ($R_\star \sim 10^{13}\,\mathrm{cm}$) are inconsistent with the data (e.g., Campana et al. 2006).

The original picture has suffered variations over the years, but the collapsar model can still be valid even when a BH does not form promptly, but only after a delay of many dynamical times. In the following, we enumerate a few variations of the collapsar picture.

Type I collapsars consist of a proto-neutron star (PNS) collapsing to a BH without launching a successful SN explosion. In contrast, in Type II collapsars (MacFadyen et al. 2001), an outgoing SN shock is launched, but so weak that is unable to eject all the helium and heavy elements. This provokes a reimplosion of this matter onto the PNS. This fallback gives place to the accretion of a few solar masses and then leads to BH formation. The leftover matter shells cannot directly be swallowed by the BH due to the large angular momentum they possess. Thus, a hot disc may form. At this time, the accretion rate is $\sim 0.001 - 0.01 M_\odot$ s^{-1}, which is 1–2 orders of magnitude less than in Type I collapsars. This rate favors electromagnetic or MHD-based energy extraction mechanisms (Sect. 1.2.1). This scenario is called the "delayed BH" version of the original collapsar scenario since the accretion timescale is larger. This leads to longer high energy transients. Though considerable uncertainty remains, the calculations of Fryer (1999) suggest the progenitor masses for BH formation by fallback (Type II) and prompt BH formation (Type I) to be in the range 20–40 $M_\odot$ and above 40 $M_\odot$, respectively. However, red supergiant progenitors do not favor relativistic outflows since most of the jet matter is braked on its way through the star envelope. Helium stars are more viable candidates to power relativistic jets.

In Type III collapsars, the PNS does not form and the progenitor collapses to a massive BH (Heger et al. 2003). An outgoing shock may develop initially but is only able to eject a small fraction of the surface layers of the progenitor star, leaving back a large part of the stellar matter to form an AD (Woosley & Heger 2012). Estimations of the accretion rate for a massive BH of $\sim 140 M_\odot$ are of the order of $\dot{M} \sim 1 M_\odot$ s^{-1} (Fryer, Woosley & Heger 2001). Candidates for Type III collapsars are single and binary stars. Possible scenarios among single stars involve low-metallicity stars with low mass-loss rates as well as stars of very high masses ($\sim$ 100–140 $M_\odot$) undergoing pair-creation instability

after having lost their hydrogen envelope. We note that the conditions for binaries are much more uncertain. The collapse timescale is of the order of days to months, leading to lengthy events with luminosities of 10^{47} erg s^{-1} (Woosley & Heger 2012).

Heger et al. (2003) argue that Type I and II collapsars can make standard GRBs, and that Type II and III collapsars can power very long GRBs. Among the most important restrictions to be fulfilled by any kind of LGRB progenitor model is the absence of hydrogen in the progenitor (as assumed in the original collapsar model, or Type I collapsars). Besides, Type III collapsars have the highest energy available due to their massive progenitors. Mass loss is of crucial importance to strip the hydrogen envelope, and then to make a GRB, and it depends on the stellar mass and metallicity (Figure 1.3).

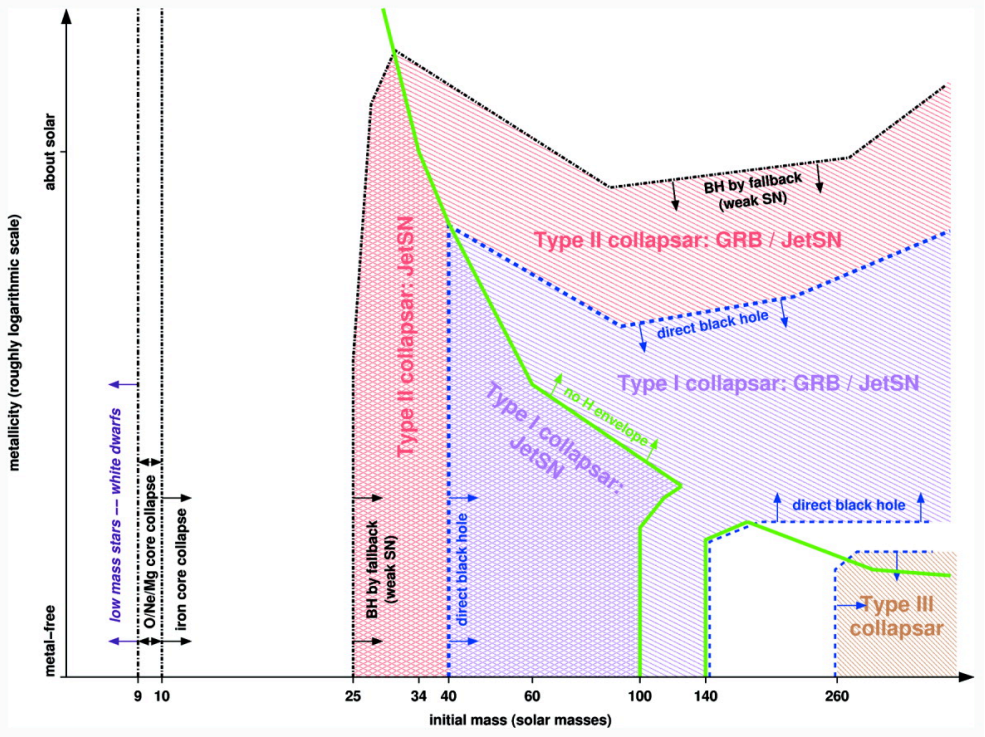

Figure 1.3: Collapsar formation as a function of mass and metallicity of the progenitor star (from Heger et al. 2003). JetSN refer to asymmetric SN in which most of the energy comes from bipolar outflow (jets) from the central object.

A GRB jet can be launched if a suitable physical mechanism, which so far is not well understood, extracts sufficient energy from the BH/AD system. The jet will propagate subrelativistically within the star and eventually will break out of the star relativistically after a time $t_{\rm b}$ (e.g., Aloy et al. 2000), before giving rise to the γ-ray emission. To do so the central engine must be active a time $t_{\rm e} > t_{\rm b}$ to compensate for the energy dissipated in the jet in its way through the star. Many numerical studies have been carried out investigating the propagation of relativistic jets in collapsars, either in 2D (MacFadyen & Woosley 1999; Aloy et al. 2000; MacFadyen et al. 2001; Zhang et al. 2003a, 2004; Mizuta et al. 2006; Morsony et al. 2007, 2010; Lazzati & Begelman 2010; Mizuta & Aloy 2009; Lazzati et al. 2009; Nagakura et al. 2011; Lazzati et al. 2013; López-Cámara et al. 2014; Ito et al. 2015) and more recently in 3D (López-Cámara et al. 2013). Once the central engine channels a fraction of the gravitational energy above the poles of the newborn compact object, a relativistic jet begins its way through the stellar interior until it reaches the outskirts of the progenitor star. As it has been shown by numerical simulations, the jet penetrates the stellar mantle and breaks out through the stellar surface, all the while maintaining a high degree of collimation and low baryon loading. The numerical studies mentioned above mostly work in the framework of the fireball model based on elements of hot plasma containing radiation in local thermal equilibrium that propagate at highly relativistic speeds and in which shock waves convert kinetic energy into the energy of thermal and non-thermal populations of particles. The radiation generated by these particles is finally radiated observable during the various phases of a GRB. The shocks responsible for particle acceleration can be either produced by the interaction of the relativistic ejecta and the external medium (external shocks) of by the interaction between shells of different speeds in the ejecta (internal shocks). Generally, the latter type of shocks is considered as the explanation for the early GRB emission, whereas the afterglows are thought to be created by external shocks.

Despite the fact that GRBs are mainly classified by the duration of their prompt emission, Bromberg et al. (2012, 2013) have shown that this criterion

cannot be applied strictly to discriminate if a burst comes from a collapsar or a non-collapsar progenitor. They argue, on the basis of probabilistic considerations, that the identification of a flat region in the duration distributions of the prompt GRB emission (at times much shorter than $t_{\rm b}$) from BATSE, *Swift* and *Fermi* data is characteristic of collapsars and proves that most of the soft GRBs with durations < 2 s come from this kind of progenitors. In the same way they also find that bursts longer than 10 s could have a non-collapsar origin. However, this particular result is detector-dependent and depends on the observational window since the 2 s limit seems to behave fine for BATSE GRBs. The plateau would appear for bursts with durations $t_\gamma = t_{\rm e} - t_{\rm b} \lesssim t_{\rm b}$ showing that it is a direct evidence of the jet/star interaction and then of the collapsar model (Bromberg et al. 2012). They also conclude that GRBs with known high redshifts ($z > 1$) likely come from collapsars (Bromberg et al. 2013).

1.2.3 Proto-magnetars

In most cases, core collapse first leads to the formation of a PNS. Whether or not a BH forms later, depends on a number of factors. BH formation by accretion could be prevented in case of high rotation, i.e., if the rotational energy is larger than the binding energy of the stellar envelope, and a rapidly spinning, strongly magnetized PNS could form behind the SN shock. The amplification of the initial progenitor magnetic field is a very active matter of debate and there is no consensus on the which is the dominant mechanism amplifying it. Among the most likely possibilities, we outline dynamo effects, the magneto-rotational instability (MRI), magneto-convection and adiabatic compression. Whatever is the magnetic field amplification mechanism the PM model requires magnetic fields in excess of $B \sim 10^{15}\,{\rm G}$ to release powers consistent with the observations of LGRBs. These high powers can only be obtained if, additionally, the spin period of the PNS is very short, say, $P \sim 1\,{\rm ms}$. For this reason they are also known as 'millisecond magnetars' or PMs (Usov 1992; Thompson 1994; Blackman & Yi 1998; Wheeler et al. 2000; Zhang & Mészáros 2001; Thompson, Chang & Quataert 2004; Bucciantini et al. 2007,

2008, 2009; Metzger, Thompson & Quataert 2007; Metzger et al. 2011). The rotational energy available in a magnetar is large, $E_{\rm rot} \sim I\Omega^2/2 \sim 10^{52}\,{\rm erg}$ ($I \sim 0.35MR^2$ being the moment of inertia of the PNS; Lattimer & Prakash 2001, and $\Omega = 2\pi/P \sim 6 \times 10^3$ rad s^{-1} its rotational velocity), and compatible with HNe. Such a high rotational energy can contribute strongly to the shock revival and the explosion, if it is extracted and transmitted to the shock by a centrifugally driven, magnetized wind that collimates as it, propagates within the star and becomes relativistic once it emerges from the stellar surface. Energetics and timescales inferred from PM winds are compatible with those observed in GRB explosions and the production of large amounts of ^{56}Ni leads to very bright SNe.

1.2.4 Supranovae

Unless the mass of the progenitor star is extremely high, the implosion of the iron core does not directly produce a BH, but instead, it forms first a PNS that later collapses to a BH by accretion of the surrounding layers of matter (e.g., most recently, O'Connor & Ott 2011; DeBrye et al. 2013; Cerdá-Durán et al. 2013). An alternative for collapse was considered by Vietri & Stella (1998) in their supranova model.

Its center is a supramassive NS (SMNS), i.e., a NS stabilised by centrifugal forces at a mass exceeding the limit for non-rotating stars (Baumgarte et al. 2000) by a factor of up to $\sim 14-21\%$ for rigidly rotating (see Cook, Shapiro & Teukolsky 1994) and $\sim 50\%$ for differentially rotating objects (Morrison et al. 2004). We note that the exact numerical values depend on the stiffness of the EoS (see, e.g., Galeazzi et al. 2013; Kaplan et al. 2014). If a supramassive NS (SMNS) formed in the core collapse of a rapidly rotating star loses most of its angular momentum by, e.g., dipole radiation, it becomes unstable against self-gravity and collapses to a BH.[4]

[4]Vietri & Stella (1999) later proposed an alternative channel with respect to the original supranova version, via mass and angular momentum transfer to the SMNS from a companion in a low-mass X-ray binary phase. As it involves a secondary star, we do not focus on this scenario.

The main advantage of this model is that it naturally provides a baryon-clean environment (estimates for the baryonic mass give values around $10^{-4} M_{\odot}$), in contrast to the collapsar model (massive stars can develop strong winds that *pollute* with baryonic matter the surrounding medium). The timescale of energy loss and subsequently collapse to BH for the SMNS is of the order of years, i.e., there is enough time for the SN explosion to clean the environment.

This GRB progenitor model has generated several criticisms. Among them we outline that supranovae may more likely produce short GRBs than long ones, or that the SN/GRB delay plays against the already observed SN/GRB associations (see Königl 2004 and references therein).These associations imply that GRBs and their accompanying SNe are nearly simultaneous. However, as pointed by Guetta & Granot (2003), the SN/GRB delay time may span a wide range of values, from near coincidence (similar to the collapsar model)[5] to even years. This broad range of delays may reconcile the supranova model with SN/GRB almost simultaneous detections, as well as with cases in which a SN counterpart is not observed together with a GRB event (Woosley & Bloom 2006).

In this way, the supranova model can be understood as a particular case of the collapsar model under very concrete conditions of the progenitor and for BH formation mechanism. In comparison with Type II collapsars, a SN is expected to form first after BH collapse. In this case, the SN may be weak or even absent and unable to clean sufficiently the environment since time delay between SN and GRB is supposed to be of the order of minutes to hours (MacFadyen et al. 2001), rather than years in supranovae (Vietri & Stella 1998).

1.2.5 Merging binary systems

Another plausible scenario to produce long GRBs is the merger of a binary system composed of a helium star and a NS or a BH (Fryer & Woosley 1998; Zhang & Fryer 2001; Barkov & Komissarov 2010, 2011). In this He/NS or He/BH

[5]Rigidly rotating stars can collapse in about one orbital period (Shibata, Baumgarte & Shapiro 2000).

mergers a compact object spirals into is massive companion as it transferres angular momentum. The outer layers of the He star can be expelled, engulfing the compact object and starting a common envelope phase. If the compact remnant is a NS it can quickly become a BH after accreting a few solar masses during the spiral in. Eventually the NS/BH and He core will merge, likely producing a BH surrounded by an AD as it happens in the collapsar model as well. Thus, even if the progenitor initially consists of a binary stellar system, in its intermediate state it looks very much like a standard collapsar, i.e., from the modeling point of view, it looks like a single stellar progenitor system once the binary has merged. This model has been proposed for GRB 101225A, in part because it provides a natural way to justify the existence of a dense, extended shell up to $\sim 10^{14}$–10^{15} cm which may give an explanation to the thermal signal observed in the X-ray afterglow of this particular GRB (see Chapter 3).

One argument in favour of binary systems is that they contain plenty of angular momentum that can be transferred to the core of the He star, making the existence of fast rotating iron cores much more easy than in single star systems. The large angular momentum of the outer layers also leads to a prolonged accretion of matter on the central engine. Furthermore, the AD is formed much sooner than in a typical collapsar. For neutrino-powered GRBs the rotation of the progenitor is critical since it sets the accretion rate onto the BH. Neutrino luminosities are low for typical accretion rates in collapsars (Popham, Woosley & Fryer 1999), but in He mergers they can be large enough to power GRBs. Indeed, the mass of the He star is critical. Zhang & Fryer (2001) show that the merger of a $2M_\odot$ compact remnant with a $4M_\odot$ He star produces a explosion of 10^{47} erg for ~ 500 s while the merger with a He star more massive than the previous one produces more than 10^{52} erg for ~ 65 s. Thus, magnetic mechanisms seem more likely in the case of small He star masses (see Chapter 3 for further discussion). In the context of magnetically driven GRB jets, Barkov & Komissarov (2010) argue that binaries involving a WR and compact remnant could sustain long accretion periods up to $\sim 10^4$ s that may explain both the shallow phase and flares observed by Swift in the

X-ray LCs.

1.3 GRB/SN association

The observed SNe accompanying GRBs have been catalogued as broad-lined Type Ic (Type Ic-bl). The first ever detection of an association of this kind was GRB 980425/SN 1998bw (Galama et al. 1998).

The SNe reliably associated with GRBs are also referred to in the literature as HNe (Paczyński 1998; Iwamoto et al. 1998) since their inferred explosion energies are at least ten times larger ($E_{\rm HN} > 10^{52}$ erg) than those of typical SNe (see, e.g., Woosley & Bloom 2006). Different studies of HN properties have suggested that HNe explode very aspherically (see, e.g., Maeda & Nomoto 2003), which could be due to the interaction of bipolar jets with the progenitor star. As they propagate along the rotational axis, the jets push stellar material towards the side and backwards and create a hot cocoon surrounding the jet beam. The lateral propagation of the cocoon eventually disrupts and ejects all the star in this jet-driven explosion. This scenario differs substantially from the standard spherical, delayed, neutrino-driven SN explosions.

The GRB/SN association can be observationally confirmed at low redshifts (typically, $z \lesssim 0.1$), where the accompanying SN becomes visible after ~ 10 d (GRB 101219B/SN 2010ma has the highest measured redshift, $z = 0.55$; Sparre et al. 2011). A good number of the confirmed events have GRBs classified as low luminosity events (llGRBs), because they show equivalent isotropic luminosities in the range $L_{\gamma,\rm iso} \sim 10^{46} - 10^{48}\,{\rm erg\,s^{-1}}$ (to be compared with typical values of $L_{\gamma,\rm iso} \sim 10^{50} - 10^{53}\,{\rm erg\,s^{-1}}$ for LGRBs; see, e.g., Hjorth 2013). In addition to being less luminous than regular LGRBs, llGRBs also seem to be less energetic than standard LGRBs (holding equivalent isotropic energies $E_{\gamma,\rm iso} \sim 10^{48} -$ few $\times\, 10^{49}\,{\rm erg}$; i.e., two to three orders of magnitude smaller than LGRBs), display relatively smooth (non-variable) LCs, and show no evidence for a high-energy power-law tail (e.g., Bromberg, Nakar & Piran 2011a). Up to date, the number of observed events that have been spectroscopically confirmed hardly exceeds ten (Modjaz et al. 2016), although there exist a larger

number of candidates in which SN-like features have been observed as well (see Hjorth & Bloom 2012). The small number of observed llGRBs (and broadly speaking of nearby GRB/SN associations) is due to the small volume in which we can observe them due to their low luminosity. However, there are observational hints that point towards the possibility that their event rate is much larger than that of LGRBs (Coward 2005; Cobb et al. 2006; Pian et al. 2006; Soderberg et al. 2006; Liang et al. 2007; Guetta & Della Valle 2007; Fan et al. 2011).

All three models sketched in the previous subsections, namely, collapsars, supranovae and PMs, are compatible with the existence of GRB/SN associations. Though it is very difficult to obtain direct observational evidence in favor of one or the other, Mazzali et al. (2014) argue that the upper energy limit of observed in the GRB/SN events ($\sim 2 \times 10^{52}\,\mathrm{erg}$) is an evidence of the presence of a millisecond magnetar as a central engine since the rotational energy available in such an object is of the same order. Indeed, they suggest that these events are mainly powered by the SN and not by the GRB jet as the kinetic energy of the SN is much larger than that of the GRB. Greiner et al. (2015) support the millisecond magnetar model based on observation analysis of a superluminal SN associated to the ultra-luminous GRB 111209A.

The SN launched before the GRB is generated can be either "engine-driven" or "jet-driven". Within this context, canonical SNe are referred to as engine-driven. In this class of events, the shock wave launched at the formation of the PNS and stalled inside the inner core is revived by the deposition of energy by neutrino heating in a layer around the PNS (for a review, see, e.g., Janka et al. 2007). Though the symmetry of this gain layer is broken by hydrodynamic instabilities, it nevertheless possesses a roughly spherical shape in the sense that no preferred axis along which the explosion develops can be found.

This scenario differs strongly from that of a core where rapid rotation causes the formation of a collimated relativistic outflow along the rotational axis driven by either highly anisotropic neutrino heating or by magnetocentrifugal forces. Despite the different initial geometry, such an event may, as a byproduct, lead to the expulsion of matter that, by its more spherical shape

and slower speeds than the jet resembles a standard SN (Ramirez-Ruiz, Celotti & Rees 2002). The origin of this matter forming a jet-driven SN is the cocoon of hot, shocked material surrounding the jet. This hot cocoon expands sideways quickly due to the drop in ram pressure, both in the outer layers of the progenitor star (namely in the He envelope), as well as in the external medium. Furthermore, the jet cocoon is surrounded by a shocked cavity where the stellar matter (first) and the external medium (later) are heated up and totally or partly unbound from the progenitor star. As the shocked jet cavity grows sideways from the polar regions towards the equator, eventually the whole star is swept and the outer layers disrupted. The result is similar to a rather prolate SN explosion.

A non-negligible fraction of GRBs/SNe have shown an 'unusual' thermal component in their X-ray (and optical) afterglows (Thöne et al. 2011). The fact that GRBs have been associated to SN Ic-bl plays in favor of the collapsar model and points towards WR stars with masses $> 10 M_{\odot}$ as the likeliest candidates (Woosley 1993; Kumar & Zhang 2015). Even so, the large BB radii ($> 10^{11}$ cm) and the low isotropic energies ($< 10^{50}$ erg) measured for those 'thermal' GRB/SN associations may be indicative of different progenitors. Nonetheless, WR stars are prone to generate dense winds and Campana et al. (2006) and Waxman et al. (2007) already suggested that the BB emission from these bursts would arise once the shock became optically thin during its propagation within this extended wind. The wide GRB energy ranges observed could be explained on the basis of progenitor-dependent wind properties that might give rise to jets with different conditions, with the relativistic ones as those that would produce the most energetic bursts. Low luminosity GRBs may be generated by mildly relativistic or even almost 'failed' jets (see Chapter 4 for further discussion). Heavy WR winds result in a great stellar mass reduction favoring the loss of the outer hydrogen (and even the helium) envelope. The lack of this element is characteristic of Type Ic SNe (furthermore they show little or no helium). Mass loss, related to metallicity, is crucial for the evolution and fate of single massive stars (Heger et al. 2003). In this regard, SN explosions reveal many properties of their progenitors. Stellar models of

Georgy et al. (2012) estimate that single stars may account for $\sim 60\%$ of the observed WR stars at solar metallicity. Besides, they say that these single WR stars would lead to $\sim 50\%$ of the Type Ib/c SNe. These estimation rates are uncertain since stellar core collapse at the threshold between ordinary SNe and BH formation are not properly well understood (e.g., Obergaulinger & Aloy 2017). On the other hand, Type Ic SNe could originate as well in close binary systems with low-mass progenitor stars ($\lesssim 20 M_\odot$), since binary interaction allows to lose the hydrogen envelope. Eldridge et al. (2013) suggest that this scenario could take place in the majority of Type Ic SN progenitors since such ejecta masses seem to be more consistent than that of massive WR stars.

Due to the lack of prompt observations in GRB/SN detection it is poorly understood how an outgoing shock (relativistic or not) punches out its progenitor star. In the collapsar model a relativistic jet must successfully break out of its progenitor in order to produce a canonical LGRB. Before the typical non-thermal radiation associated to the flash in γ/X-rays caused by the breakout, the SN shock breakout may produce some sort of thermal signal (Campana et al., 2006; Waxman, Mészáros & Campana 2007; Soderberg et al., 2008; Nakar & Sari 2012; Nakar 2015; Irwin & Chevalier 2016). Observations in the last ten years are pointing towards this direction. In particular GRB 060218, associated to SN 2006aj, has shown a thermal component in X-rays which cools as it moves to optical frequencies (Campana et al. 2006). The analysis of the observations suggest that the progenitor is a WR star. The inferred shock radius after $\sim 200\,\mathrm{s}$ is $5.2 \times 10^{11}\,\mathrm{cm}$ and increases above $10^{12}\,\mathrm{cm}$ at the end of the burst, while its temperature remains around $0.17\,\mathrm{keV}$. The estimated BB radii agrees with the case of a WR surrounded by an extended wind. As atmospheric models show the presence of a wind can raise the photospheric radius of a WR up to several $R_\odot$ due to its high opacity, being much larger than the actual hydrostatic radius obtained by stellar models (see, e.g., Crowther 2007). Cui et al. (2010) found in their *Swift* GRB sample that the inferred progenitor radii ($\sim 10^{10}$–10^{12} cm) are, in general, smaller than the photospheric radii of observed WRs ($\sim 10^{11}$–10^{13} cm). Recent studies (see, e.g., Gräfener, Owocki & Vink 2012) consider that, instead of a wind, WR

stars may develop very dilute 'inflated' envelopes that can extend far beyond ($R_e \sim 10^{12}$ cm) the location of the core ($R_c \lesssim 10^{11}$) and increase the opacity, reconciling the large WR radii observed with the idea of compact WR cores as GRB progenitors.

The analyses of individual events as well as studies of the statistics of larger samples gives interesting hints on the detailed nature of the SNe associated to GRBs, but do net yet conclusively settle the issue. Modjaz et al. (2016) analyzed the optical spectra of SNe Ic-bl with and without associated GRBs. They observed interesting features with important implications for GRB progenitors. Modjaz et al. (2016) point out that GRB stellar progenitors are possibly different from those of SN Ic. They noticed that the lack of He lines implies that progenitors of GRB/SN are not only hydrogen-free but helium-free as well. Since stellar models of single massive stars with low metallicities are not very likely to lose the helium layer, binary interaction seems a more plausible mechanism in order to get rid of the He layer. Thus, they conclude that short-period binaries are more likely candidates of SNe Ic-bl than singles massive stars. Furthermore, they argue that the larger kinetic energies measured in GRB/SNe mean larger jet energies, in comparison with SNe without associated GRBs.

Soderberg et al. (2006) calculate that the rate of broad-lined Ibc SNe is about the same as that of llGRBs, implying that llGRBs cannot be significantly beamed. Indeed, it is likely that llGRBs are even isotropic and the result of "failed" jets (e.g., Bromberg et al. 2011a), i.e., jets which become partly chocked in the stellar envelope. Attending to the peculiarities differentiating llGRBs from typical LGRBs some authors (e.g., Bromberg et al. 2011a) claim that these events have a non-collapsar origin, unless an engine-driven SN, that modified the conditions of the external environment, occurred before the GRB. More recently, Nakar (2015) has suggested that both kinds of bursts may have a similar origin. The similar properties inferred from the associated SNe in both kind of bursts suggest the existence of similar progenitors with modified environments. The optical LCs of the llGRB 060218, with a two peak structure, suggest the presence of an extended low-mass envelope at a

distance of 10^{13}–10^{14} cm that could also explain the observable differences at high energies (see also Irwin & Chevalier 2016). This envelope would brake the incipient relativistic jet and would dissipate part of the energy choking the jet that would emerge at much lower speeds without producing a typical burst signal.

1.4 Methodology and assumptions

The goal of this thesis is to probe the physics of the relativistic outflows produced by newly formed compact objects in core-collapse SN, collapsars and other interesting GRB progenitor scenarios. We will focus on the dynamical effects that result from the jet/stellar progenitor interaction and, as a consequence, on the emission properties that may result on those systems. In particular, and motivated by recent GRB observations by *Swift*, we will pay special attention to the production of thermal emission.

Once generated, a jet will propagate through the envelope of the star and through the surrounding medium. If at that moment a successful SN explosion has already been triggered by other mechanisms (neutrino heating and hydrodynamic instabilities), a relativistic jet may eventually overtake the SN shock wave. The jet will be affected by the progenitor density profile it is crossing. Furthermore, it may be prone to several instabilities, e.g., Kelvin-Helmholtz and current-driven kink instabilities that may even disrupt the outflow. In this thesis we investigate this phase of the evolution. Our main interest will be the breakout of the outflow from the stellar surface and its propagation into the external medium. For that we will model the electromagnetic emission processess taking place in the fluid flow in order to construct detailed LCs and spectra. This allows us to connect the observed phenomenology to the properties of the astrophysical flows producing it.

Our numerical models are based upon some approximations. First of all we assume that the stellar interiors, the surrounding media and the plasma constituting any outflow from these systems can be model as a fluid. Indeed, the fluid can be considered to be collisionless since small scale (dynamically

negligible) magnetic fields provide the necessary coupling among the plasma constituents on scales much smaller than the size of a numerical cell in our simulations. This approximation is good enough if one considers that the plasma will be fully ionized because of the high temperatures of the stellar interiors and their surrounding medium.

We assume that the fluid is an ideal gas that for modelling purposes can be treated as an electron-proton plasma. This allows us to deal with the complexity derived from the fact that stellar interiors are composed by different metal contents in addition to hydrogen and helium. Also, as nuclear reactions are expected to at most marginally affect the jet dynamics, we have not considered all the different elements that conform the different stellar layers. Hence, the only input we use from the realistic simulations of stellar evolution are the hydrodynamic profiles of the progenitors (density, pressure and radial velocity). Even so, the ratio of the relative abundance of hydrogen over heavier elements ($X_{\rm h}$) must be specified for calculations of the thermal emission. The same chemical composition is assumed for the circumburst medium, which in practice basically consists of ionized matter. We assume that its density and pressure profiles follow either a decaying power-law (ρ, $p \propto r^{-\alpha}$, α being a positive or a null exponent) or that there exist a more complex stellar environment including the possibility of extended envelopes.

As equation of state (EoS) we use the *TM* approximation (Mignone et al. 2005), which introduces an effective, temperature-dependent, adiabatic index which distinguishes between "hot", relativistic regions (e.g., the jet) and "cold", non-relativistic regions (e.g., the stellar interior or the external medium). Like the ideal EoS, the *TM* EoS also considers a single component. Another point to take into account is that the *TM* EoS is only valid if effects due to radiation pressure, electron degeneracies and neutrino physics can be neglected. Other dynamical effects that could arise from a more complex EoS are also neglected.

We do not focus on the jet formation mechanism but on how the jet propagates into the progenitor system. In our simulations the jet injection is made *ad hoc* by imposing inflow conditions through a nozzle located at the inner radial boundary of our numerical grid.

As we have seen in previous sections, synchrotron radiation from external/internal shocks is believed to be the main source of radiation in the GRB prompt emission. However, recent observations points towards a prominent thermal component. As we assume that all the plasma is ionized due to high temperatures ($T \sim 10^4$–10^6 K), we assume that the dominant process responsible of the thermal emission is thermal (free–free) bremsstrahlung. In this context electrons constituting the plasma will radiate as they accelerate/decelerate when interacting electromagnetically with positive ions (in our case protons). The velocity of these electrons follows a Maxwellian distribution. The thermal bremsstrahlung emissivity depends on intrinsic properties such as the temperature, the density or the composition of the emitting plasma. The total intensity is set in order to obtain the classical BB intensity ($I_\nu = B_\nu$) from an optically thick plasma. Nevertheless, Thomson opacity is also considered as it can become dominant for large densities and temperatures (where thermal-bremsstrahlung absorption may become small), modifying the specific intensity in optically thick regions. A quantum approach is necessary in order to calculate properly the free-free emission and absorption coefficients. However, the coefficients we have used have been calculated under the classical approximation (which remains valid in some regimes) considering only a quantum correction gathered in the Gaunt factor. The thermal emission is coupled with the non-thermal one as synchrotron radiation can be absorbed by the medium via thermal or Thomson absorption. For simplicity of the thermal emission treatment Comptonization has not be considered in the framework of this thesis. Photons from the photosphere can be Comptonized and the thermal spectrum of the prompt emission can be modified at high energies. Although it should be incorporated into a proper treatment of the radiation mechanisms, it can be ruled out for the temperature and density conditions considered here for the emitting plasma. Besides, its influence to the low energy bands is not dominant.

In those systems where gravitational and magnetic fields are dynamically unimportant and that can be modeled as fluids, special relativistic hydrodynamics (RHD) provides a good description of the fluid motion. RHD states

a close relation between the most relevant (thermodynamical) quantities that govern the evolution of a system in space and time. These quantities are coupled by partial differential equations closed with an EoS that may be solved numerically. The equations of RHD are too complex to be solved analytically and a practical method is the finite volume approach, i.e., splitting the whole physical domain into small zones/cells for solving the problem numerically. The basic problem for solving them resides in the solution of the well-known Riemann Problem which consists in the interaction of two fluids with different physical states that gives rise to the appearance of discontinuities such as shocks, or rarefactions. In numerical simulations, the same situation arises for two neighboring cells containing different physical states. In practice, each numerical cell will be surrounded by more than two contiguous cells (e.g., in 2D, the number of contiguous cells would be 8). At this point one has the same number of Riemann problems as pairs of neighboring cells. For this reason, as first approach one samples the distribution of the hydrodynamic variables by functions that are constant within each cell and discontinuous at cell interfaces. Using numerical techniques such as the method of lines, the discretization of time can be split off from the spatial discretization and treated independently.

In hydrodynamics, it is usually assumed that the gas consists of particles in local thermal equilibrium. This assumption is, strictly speaking, violated in our case because the shock waves caused by the interaction of a jet with its environment generate a non-thermal population of particles. Light particles making up the jet matter can be accelerated up to relativistic speeds with respect to the co-moving frame if the shocks are strong enough. Besides, plasma instabilities at the shocks give rise to the formation of small-scale, random magnetic fields which help to accelerate relativistic particles. The relativistic particles emit radiation, thus losing part of their energy. Nevertheless, the hydrodynamic evolution is considered adiabatic. That means that the fluid only loses its energy due to its expansion work and the effect of radiative losses on the fluid flow is neglected. The emitting particles and their radiation are instead treated in a postprocess phase, i.e., after computing the RHD evolution. Their evolution is governed by the kinetic equation, which takes into account

either adiabatic and radiative losses (and gains). If particles are relativistic, they can emit synchrotron radiation. The synchrotron emission and absorption coefficients are based on involved integrals. To save time, we use look-up tables of these coefficients generated numerically rather than a direct integration at run-time. If particles are not relativistic and in thermal equilibrium, they can emit thermal bremsstrahlung. A proper calculation of the temperature by means of an iterative procedure and the calculation of the Gaunt factor (also tabulated) is necessary to obtain the right emission and absorption coefficients. Once the coefficients of all the emission and absorption processes are known, the total emission is calculated by integrating the radiative transport equation along the line of sight of a fictitious observer.

The equations of RHD are solved using the code MRGENESIS (Aloy et al. 1999; Leismann et al. 2005; Mimica et al. 2009b), which has been modified appropriately to simulate our astrophysical systems. In order to avoid computationally intractable three dimensional simulations, we assume that these systems and the jets which propagate through them have equatorial and axial symmetry, i.e., we follow jet evolution in two spatial dimensions in only one of the two hemispheres assuming symmetry of revolution around the rotational axis of the system. The creation and kinetic evolution of the emitting particles, as well as the spectral evolution and emission are modelled with the SPEV code (Mimica et al. 2009b) which has also been modified to include thermal emission. SPEV is able to track the spectral evolution of populations of non-thermal particles (e.g., relativistic electrons and positrons) as they are advected by a background, magnetized, thermal fluid, and experience radiative (synchrotron) losses. SPEV is also equipped with ray-tracing routines that allow the users to produce not only light curves but also synchrotron maps of radiating plasmas. Implementing new local emission mechanisms (i.e., additional loss terms) in SPEV is conceptually simple (though technically involved). Thus, we have improved the coupling between MRGENESIS and SPEV, which has allowed us to follow the complete evolution of a relativistic jet from its propagation in its progenitor and the external medium to its energy release in form of radiation.

If it is not explicitly written in some equations, the reader should be aware that hereafter we will use natural units, i.e., the speed of light, c, and the gravitational constant, G, are equal to the unity ($c = G = 1$). Regarding the index notation, unless specified in the text, be aware that greek indices run from 0 to 3, i.e., $\mu, \nu = 0, 1, 2, 3$, while latin indices run from 1 to 3. Einstein summation convention is applied.

Chapter 2

Numerical method

2.1 Ideal RHD

Let us consider a relativistic fluid described by its physical or *primitive* variables: rest-mass density, ρ, pressure, p, four-velocity, u^μ, the first two measured in the comoving frame while the latter is measured in the laboratory frame. The specific enthalpy then reads

$$h = 1 + \varepsilon + \frac{p}{\rho}, \tag{2.1}$$

where ε is the specific energy (i.e., the energy per mass).

Given a spacetime metric ($g^{\mu\nu}$) the energy-momentum tensor describing an ideal fluid is

$$T^{\mu\nu} = \rho h u^\mu u^\nu + p g^{\mu\nu}. \tag{2.2}$$

The conservation in space and time of this tensor, together with the conservation of mass during the whole evolution, tells how a fluid behaves. More concretely, the evolution of the system is governed by the conservation laws for energy-momentum and mass,

$$\nabla_\mu T^{\mu\nu} = 0, \tag{2.3}$$

$$\nabla_\mu (\rho u^\mu) = 0, \tag{2.4}$$

where ∇_μ is the covariant derivative with respect to the metric tensor $g_{\mu\nu}$. We need to solve the Relativistic Euler equations, which form a hyperbolic system of conservation laws. The mathematical character of the latter equations determines the choice of the numerical methods we need to use for the time evolution of the systems at hand.

In this thesis, we study jets in axisymmetric systems. Therefore, we use spherical coordinates in 2 dimensions, or polar coordinates[1], $\mathbf{x} = (r,\ \theta)$. In these coordinates the metric tensor is diagonal and reads $g = (-1, 1, r^2)$, and the governing equations of the fluid motion (Eqs. (2.3)–(2.4)) become:

$$\frac{\partial \mathbf{U}}{\partial t} + \frac{1}{r^2}\frac{\partial r^2 \mathbf{F}}{\partial r} + \frac{1}{r\sin\theta}\frac{\partial \sin\theta \mathbf{G}}{\partial \theta} = \mathbf{S}_\mathbf{U}. \tag{2.5}$$

The vector of conserved quantities, $\mathbf{U}$, and the r- and θ- components of the momentum, $\mathbf{F}$ and $\mathbf{G}$ respectively, are defined as

$$\mathbf{U} = \begin{pmatrix} D \\ S^r \\ S^\theta \\ \tau \end{pmatrix}, \tag{2.6}$$

$$\mathbf{F} = \begin{pmatrix} Dv^r \\ S^r v^r + p \\ S^\theta v^r \\ (\tau + p)v^r \end{pmatrix} \text{ and} \tag{2.7}$$

$$\mathbf{G} = \begin{pmatrix} Dv^\theta \\ S^r v^\theta \\ S^\theta v^\theta + p \\ (\tau + p)v^\theta \end{pmatrix}, \tag{2.8}$$

where D, $\mathbf{S} = (S^r, S^\theta)$ and τ are the relativistic mass density, the momentum density and the energy density, respectively, all of them measured in the

[1]Then, greek indices $\mu = 1$ and 2 correspond to r and θ coordinates, respectively.

laboratory frame and defined as a function of the primitive variables:

$$D = \rho\Gamma, \tag{2.9}$$

$$\mathbf{S} = \rho h \Gamma^2 \mathbf{v}, \tag{2.10}$$

$$\tau = \rho h \Gamma^2 - p - D. \tag{2.11}$$

The velocity is also measured in the laboratory frame, $\mathbf{v} = (v^r, v^\theta)$, and relates to the four-velocity as

$$u^\mu = \Gamma(1, \mathbf{v}), \tag{2.12}$$

where

$$\Gamma \equiv \frac{1}{\sqrt{1 - \mathbf{v}^2}} \tag{2.13}$$

is the fluid (bulk) Lorentz factor.

In the absence of physical sources, the source term, $\mathbf{S_U}$, only contains all the geometrical factors in 2D spherical coordinates:

$$\mathbf{S_U} = \begin{pmatrix} 0 \\ \frac{1}{r}\left(2p + S^\theta v^\theta\right) \\ \frac{1}{r}\left(\frac{\cos\theta}{\sin\theta} p - S^\theta v^r\right) \\ 0 \end{pmatrix}. \tag{2.14}$$

Together with the conservation laws, one more relation between the primitive variables is needed to close the system. This is the EoS, which establishes a relationship between thermodynamic variables such as pressure, rest-mass density and specific energy of the fluid. It is usually written as $p = p(\rho, \varepsilon)$.

The simplest case considers the ideal gas approach given by

$$p = (\gamma - 1)\rho\varepsilon \tag{2.15}$$

where the constant γ is the adiabatic index defined as the ratio of specific heats ($\gamma = c_p/c_V$). However, since hot and cold physical regions can coexist in the same system, it may be necessary to consider a more realistic EoS where γ may vary between these different regions.

Mignone, Plewa & Bodo (2005) proposed a new, approximate EoS (see also De Berredo-Peixoto, Shapiro & Sobreira 2005), much simpler than the Synge EoS for a relativistic perfect gas: the *TM* EoS. Introducing first a thermodynamic quantity proportional to the temperature, $\Theta = p/\rho$, the *TM* EoS stems from Taub's inequality,

$$(h - \Theta)(h - 4\Theta) \geq 1, \tag{2.16}$$

which is a relation for the specific enthalpy that is consistent with the kinetic-relativistic theory (Taub 1948), but taking the equal sign of Eq. (2.16).

The use of the *TM* EoS has many advantages. It is computationally cheap and the solution only differs by less than 4% from the theoretical value given by the Synge EoS (see Mignone et al. 2005).

As a function of Θ, the specific enthalpy is given by

$$h = \frac{5}{2}\Theta + \sqrt{\frac{9}{4}\Theta^2 + 1}\,, \tag{2.17}$$

and solving for pressure one obtains that

$$p = \frac{\rho}{8}\left(5h - \sqrt{9h^2 + 16}\right). \tag{2.18}$$

Using Eq. (2.1) it is also useful to leave pressure as a function of the specific energy (Mignone & McKinney 2007):

$$p = \frac{\rho\varepsilon}{3}\frac{\varepsilon + 2}{\varepsilon + 1}\,. \tag{2.19}$$

With the *TM* EoS an effective adiabatic index can be defined:

$$\gamma_{\rm ef} = \frac{h - 1}{h - 1 - \Theta}, \tag{2.20}$$

ranging between 4/3 and 5/3, so that distinguishes between hot, relativistic regions and cold, non-relativistic regions, respectively.

2.2 MRGENESIS

MRGENESIS is a high-resolution shock-capturing RHD code that has been developed by some of the members of our group (Aloy et al. 1999; Leismann

et al. 2005; Mimica et al. 2009b). As any numerical code based on the finite-volume approach, MRGENESIS discretizes a physical domain into a numerical grid composed of several control volumes, or numerical cells.

We can recast Eq. (2.5) as

$$\frac{\partial \mathbf{U}}{\partial t} + \nabla \mathbf{F} = \mathbf{S}_{\mathbf{U}}, \tag{2.21}$$

where now $\mathbf{F}$ encompasses all the fluxes present in Eq. (2.5). Applying the finite-volume method, this set of partial differential equations are discretized by performing volume integrals over each small discrete numerical cell with volume ΔV:

$$\frac{1}{\Delta V}\left(\int_V \frac{\partial \mathbf{U}}{\partial t}\,\mathrm{d}V + \int_V \nabla \mathbf{F}\,\mathrm{d}V\right) = \frac{1}{\Delta V}\int_V \mathbf{S}_{\mathbf{U}}\,\mathrm{d}V. \tag{2.22}$$

The volume integral of the convective term, $\nabla \mathbf{F}$, can be converted into a surface integral by means of the divergence theorem. Then the fluxes are computed at the interfaces of the control volumes. The last part of discretization is to consider that the conserved variables, $\mathbf{U}$, are evaluated as their averaged values, $\tilde{\mathbf{U}}$,

$$\tilde{\mathbf{U}} \equiv \frac{1}{\Delta V}\int_V \mathbf{U}\,\mathrm{d}V, \tag{2.23}$$

inside each zone,

$$\frac{\partial \tilde{\mathbf{U}}}{\partial t} + \frac{1}{\Delta V}\left(\oint_S \mathbf{F}\cdot\mathbf{n}\,\mathrm{d}S\right) = \tilde{\mathbf{S}}_{\mathbf{U}}, \tag{2.24}$$

where $\tilde{\mathbf{S}}_{\mathbf{U}}$ are the volume averaged sources and $\mathbf{n}$ is the unitary vector normal to the surface of the control volume.

As already said, we are interested in using 2D spherical coordinates. Therefore, the numerical grid extends in radial (r) and angular (θ) directions. Latin letters i and j will label a particular cell. We specify the position (r, θ) of its center by $(r_i, \theta_j) \equiv (i, j)$. Its volume has been denoted by $\Delta V \equiv \Delta V_{i,j}$. Under this coordinates, control volumes are actually control areas and the volume integrals are only performed over r and θ directions, whereas the ϕ integration

can be ignored. At the same time the surface integral needed to compute the numerical fluxes is actually an integration along the interfaces of the bidimensional cell. Finally, to obtain the solution the code uses the method of lines (LeVeque 1992) which allows us to treat the spatial variation and temporal evolution using two independent discretizations. If $\mathbf{U}_{i,j}^n$ is the solution within the cell (i,j) at a time t^n, where the subscript n refers to the n-time step, the final discretization of equations reads (we omit the *tilde* over variables to avoid cumbersome notation),

$$\frac{\mathrm{d}\mathbf{U}_{i,j}}{\mathrm{d}t} = -\frac{3(r_{i+1/2}^2\mathbf{F}_{i+1/2,j}^n - r_{i-1/2}^2\mathbf{F}_{i-1/2,j}^n)}{\Delta r^3} + \frac{3}{2}\frac{\Delta r^2}{\Delta r^3}\frac{(\mathbf{G}_{i,j+1/2}^n \sin\theta_{i,j+1/2} - \mathbf{G}_{i,j-1/2}^n \sin\theta_{i,j-1/2})}{\Delta\cos\theta} + \mathbf{S}_{\mathbf{U},i,j}^n \equiv L(\mathbf{U}), \tag{2.25}$$

where $L(\mathbf{U})$ is the spatial operator.

The numerical fluxes $\mathbf{F}_{i\pm1/2,j}^n \equiv \mathbf{F}(r_{i\pm1/2}, \theta_j, t^n)$ and $\mathbf{G}_{i,j\pm1/2}^n \equiv \mathbf{G}(r_i, \theta_{j\pm1/2}, t^n)$ are defined at the interfaces[2] between adjacent cells and are calculated with the appropriate Riemann solver or flux formula. In our case, Marquina's flux formula (Donat & Marquina 1996) has been chosen for computing both numerical fluxes,

$$\mathbf{F}^{\mathrm{M}}(\mathbf{U}_l, \mathbf{U}_r) = \sum_{p=1}^{m} (\psi_+^p \mathbf{r}^p(\mathbf{U}_l) + \psi_-^p \mathbf{r}^p(\mathbf{U}_r)), \tag{2.26}$$

where m is the number of eigenvalues and $\mathbf{r}^p(\mathbf{U}_l)$ and $\mathbf{r}^p(\mathbf{U}_r)$ are the right (normalized) eigenvectors of the Jacobian matrices of the left, $\mathbf{U}_l$, and right, $\mathbf{U}_r$, states on the interface. The coefficients $\psi_\pm^p$ depend on the local eigenvalues and characteristic variables and fluxes. See Donat & Marquina (1996) for more details.

For time integration a Total Variation Diminishing (TVD) third order Runge–Kutta method (Shu & Osher 1988) is performed in three steps (we

[2] E.g., the interface between the cells (i,j) and $(i\pm1,j)$ is $(i\pm1/2,j)$ and the interface between the cells (i,j) and $(i,j\pm1)$ is $(i,j\pm1/2)$.

omit the subscripts (i, j) for clarifying the notation),

$$\mathbf{U}^{(1)} = \mathbf{U}^n + \Delta t L(\mathbf{U}^n), \tag{2.27}$$

$$\mathbf{U}^{(2)} = \frac{1}{4}(3\mathbf{U}^n + \mathbf{U}^{(1)} + \Delta t L(\mathbf{U}^{(1)})), \tag{2.28}$$

$$\mathbf{U}^{n+1} = \frac{1}{3}(\mathbf{U}^n + 2\mathbf{U}^{(2)} + 2\Delta t L(\mathbf{U}^{(2)})). \tag{2.29}$$

For spatial intercell reconstruction a third order piecewise parabolic method (PPM; Colella & Woodward 1984) scheme has been used. This scheme is divided into 4 steps following the extension of Martí & Müller (1996) and is applied to reconstruct p, ρ, u^r and u^θ. The first one is the interpolation procedure, which in the original PPM algorithm is purely one-dimensional. Let j denote the location of a cell center and $j-1/2$ and $j+1/2$ its left and right boundaries (interfaces). The reconstructed values at the cell boundaries are obtained using a quartic polynomial constructed with the zone-averaged values of cells $j-2$, $j-1$, j, $j+1$ and $j+2$. In the case of a uniformly spaced grid the value of the polynomial at the interface $j+1/2$ is

$$a_{j+1/2} \equiv a_{R,j} \equiv a_{L,j+1} = \frac{1}{2}(a_j + a_{j+1}) + \frac{1}{6}(\delta_m a_j - \delta_m a_{j+1}) \tag{2.30}$$

where $\delta_m a_j = \min(\frac{1}{2}|a_{j+1} - a_{j-1}|, 2|a_j - a_{j-1}|, 2|a_{j+1} - a_j|)\,\mathrm{sign}(a_{j+1} - a_{j-1})$ if $(a_j - a_{j-1})(a_{j+1} - a_j) > 0$, or 0 otherwise. Steps two (contact steepening) and four (monotonization) are applied as in Martí & Müller (1996; see appendix I therein).

However, the third step has been slightly modified. This step states that some flattening is necessary in the presence of strong shocks in order to avoid spurious postshock oscillations. The criterion for detecting a shock in cell j is based on two conditions: (1) the existence of a large pressure jump (larger than a parameter ε_p),

$$\frac{|p_{j+1} - p_{j-1}|}{\min(p_{j+1}, p_{j-1})} > \varepsilon_p, \tag{2.31}$$

and (2) a negative divergence of the 3-velocity, $\nabla \mathbf{v} < 0$. While the first condition is purely phenomenological (based on the fact that pressure is discontinuous across a shock), the second one posesses a physical upper bound that

the divergence of the flow velocity crossing a shock must satisfy (the shock must be compressive). The sign of the velocity divergence is approximated by evaluating the undivided velocity difference in the coordinate direction along which we perform the reconstruction step (see also App. A for an alternative approximation that has been used in polar coordinates), namely

$$v_{j+1} - v_{j-1} < 0\,. \tag{2.32}$$

If the cell j fulfills conditions (2.31) and (2.32) the following *flattening* procedure is applied for a variable a (density, pressure, or 4-velocity):

$$\begin{aligned} a_{L,j} &\to a_j f_j + a_{L,j}(1 - f_j), \\ a_{R,j} &\to a_j f_j + a_{R,j}(1 - f_j). \end{aligned} \tag{2.33}$$

The flattening parameter is $f_j \in [0, 1]$ and given by $\max(\tilde{f}_j, \tilde{f}_{j+s_j})$ where

$$\tilde{f}_j = \min\left(1, w_j \max\left(0, \left(\frac{p_{j+1} - p_{j-1}}{p_{j+2} - p_{j-2}} - \omega_j\right)\omega^{(2)}\right)\right). \tag{2.34}$$

Here s_j is $+1$ if $p_{j+1} - p_{j-1} > 0$ or -1 if $p_{j+1} - p_{j-1} < 0$. In order to numerically account for strong transonic rarefactions in the flow, which may develop nearly "vacuum" conditions[3], we have considered applying to the aforementioned rarefactions a recipe similar to the shock flattening. In this case, we lift the restriction of compressive flow (Eq. (2.32)) and apply the flattening procedure expressed in Eq. (2.33) to regions where only condition (2.31) is fulfilled. For the practical implementation of this procedure, the parameter w_j is set to 1 when condition (2.31) is satisfied and 0 otherwise. The parameter $\omega^{(2)} = 10$ (Martí & Müller 1996) is common for shocks and rarefactions while

$$\omega_j = \begin{cases} \omega^{(1)} & \text{if } j \in \text{ shock}, \\ \omega^{(3)} & \text{if } j \in \text{ rarefaction}. \end{cases} \tag{2.35}$$

[3]These situations happen, e.g., after switching off inflow jet conditions through a nozzle. The fluid injected at the end of the injection phase pulls matter behind it at ultrarelativistic velocities, resulting in an depletion of the matter near the jet nozzle. Therefore, extra dissipation is needed there to prevent the appearance of numerical artifacts.

In principle $\omega^{(1)} \neq \omega^{(3)}$ and the flattening for these two waves can be set independently by the user. Note that the larger ω_j is, the larger is the flattening parameter. For shocks $\omega^{(1)} = 0.52$ (Martí & Müller 1996). For rarefactions we set $\omega^{(3)} = 10$. However, if the fluid is highly variable it might be convenient to set $\omega^{(3)} = \omega^{(1)}$.

At the end of each substep of the time loop, the code recovers the primitive variables by solving a nonlinear equation with a Newton–Raphson method. The case of the ideal EoS is described in the appendix C of Aloy et al. (1999).

For the *TM* EoS the recovery procedure has to be slightly modified. In this case we have to find the solution to Eq. (2.19), i.e., to find the root of the function:

$$f(p) = \frac{\varepsilon_* + 2}{\varepsilon_* + 1}\frac{\rho_*\varepsilon_*}{3} - p = p_* - p, \tag{2.36}$$

where (Aloy et al. 1999)

$$\rho_* = \frac{D}{\Gamma_*},\ \varepsilon_* = \frac{\tau + [D + p(1+\Gamma_*)][1-\Gamma_*]}{D\Gamma_*},$$

$$\Gamma_* = \frac{1}{\sqrt{1 - |\mathbf{v}_*|^2}},\ \text{and}\ \mathbf{v}_* = \frac{\mathbf{S}}{\tau + D + p}.$$

The derivative of the solvant function $f(p)$ is approximated by $f'(p) = |\mathbf{v}_*|^2 c_{s*}^2 - 1$, where now the sound speed is (Mignone et al. 2005)

$$c_{s*} = \sqrt{\frac{\Theta_*}{3h_*}\frac{5h_* - 8\Theta_*}{h_* - \Theta_*}} \tag{2.37}$$

where $\Theta_* = p_*/\rho_*$ and h_* is given by Eq. (2.17) using the '$*$' variables.

2.2.1 Jet initialization

In our simulations jets are injected imposing inflow conditions through the radial inner boundary of the numerical grid (R_0). The (radial) velocity of the flow is set up fixing an initial Lorentz factor, Γ_j, i.e., $v_\mathrm{j} = \sqrt{1 - \Gamma_\mathrm{j}^{-2}}$, while the initial rest-mass density, $\rho_{0,\mathrm{j}}$, and pressure, $p_{0,\mathrm{j}}$, are obtained as detailed below.

The luminosity of the jet, with a half-oppening angle $\theta_{\rm j}$, can be calculated by means of the energy flux (last row of Eq. (2.7)) that crosses the nozzle of injection (of surface $S_0 = 2\pi R_0^2(1-\cos\theta_{\rm j})$):

$$L_{\rm j} = \rho_{\rm j}\Gamma_{\rm j}(h_{\rm j}\Gamma_{\rm j} - 1)vc^3 S_0\,, \tag{2.38}$$

so that the energy carried by the jet is calculated as

$$E_{\rm j} = \int L_{\rm j}{\rm d}t\,, \tag{2.39}$$

where an integration over the total injection time has to be done. Our jets have a constant luminosity up to the injection time, $t = t_{\rm inj,j}$, however, for numerical reasons, are not shut down abruptly at this time. Beyond $t_{\rm inj,j}$, density and pressure decay as $\propto (t/t_{\rm inj,j})^{-4}$. Performing the integral over the two injection phases, the total energy of the jet is

$$E_{\rm j} = \frac{4}{3}L_{0,\rm j}t_{\rm inj,j}\,. \tag{2.40}$$

From the last equation, and assuming that the jet energy can be expressed in terms of its equivalent isotropic energy, $E_{\rm j} = (1-\cos\theta_{\rm j})E_{\rm iso}/2$, the initial rest-mass density of the jet is obtained as

$$\rho_{0,\rm j} = \frac{3}{4}\frac{E_{\rm iso}}{4\pi\Gamma_{\rm j}(h_{\rm j}\Gamma_{\rm j}-1)vc^3R_0^2t_{\rm inj,j}}\,. \tag{2.41}$$

Finally, the pressure is computed by means of Eq. (2.18) for the *TM* EoS.

2.3 Radiative transfer

Matter emits radiation by different processes that can be classified as either thermal or non-thermal. A body in thermal equilibrium with a temperature T radiates following Planck's law,

$$B_\nu(\nu,T) = \frac{2h_{\rm P}\nu^3}{c^2}\frac{1}{{\rm e}^{h_{\rm P}\nu/kT}-1}, \tag{2.42}$$

where B_ν is the BB intensity, $h_{\rm P}$ is the Planck constant, ν is the frequency of the radiation, k is the Boltzmann constant, and c is the speed of light in vacuum.

Non-thermal radiation is a type of radiation whose properties do not depend on the temperature of the particles (if it can even be defined), but rather on their other properties. The emitting particles are often not in thermal equilibrium (thus their temperature cannot be defined) and in many cases can yield spectra which are piecewise power-law functions of frequency. Synchrotron radiation, emitted by accelerated particles in a magnetic field, is of this kind.

A light ray can be considered as a beam of photons propagating through a medium. New photons can be created by molecules, atoms or particles in the medium and incorporated to the ray, and by the inverse reactions can be absorbed and removed from it. The radiative transfer equation (also known as the radiation transport equation, Rybicki & Lightman 1979) describes how the total intensity per unit frequency, I_ν (erg s^{-1} cm^{-2} Hz^{-1}), changes because of emission and absorption of different processes specified through the coefficients j_ν (emissivity) and α_ν (absorptivity), respectively, along the path, λ, of the ray:

$$\frac{\mathrm{d}I_\nu}{\mathrm{d}\lambda} = -\alpha_\nu I_\nu + j_\nu. \tag{2.43}$$

The coefficients j_ν and α_ν add up all the different contributions from different radiation processes.

In an optically thin medium, absorption is negligible, and the total intensity can be calculated as the sum of all the independent contributions alone, i.e., $I_\nu = \sum_m I_\nu^m$ for a number of m processes. Besides, it is worth mentioning that in the optically thick case thermal radiation, which fulfills $S_\nu \equiv j_\nu/\alpha_\nu = B_\nu$ (Kirchhoff's law), becomes blackbody radiation, $I_\nu = B_\nu$ (Rybicki & Lightman 1979).

2.3.1 Synchrotron emission

The observed radiation flux, $\mathbf{F}$, depends on the electric field, $\mathbf{E}$, produced by an electron of charge $-e$, located at a position x, moving with a velocity $\mathbf{v}$ (in

units of c) in a constant homogeneous magnetic field, $\mathbf{B}$, (Jackson 1962)

$$\begin{aligned}\mathbf{F}(w, w_B) &= 2\pi c\mathbf{n}|\mathbf{E}(w, w_B)|^2 = \\ &= \mathbf{n}\frac{w_B e^2 w^2}{4\pi c x^2}\left|\int_{\text{orbit}}[\mathbf{n}\times(\mathbf{n}\times\mathbf{v})]\exp\left(\mathcal{I}w(t-\mathbf{n}\ \mathbf{r}(t)/c)\right)dt\right|^2,\end{aligned} \tag{2.44}$$

where $w_B \equiv eB/\gamma m_\mathrm{e}c$ is the relativistic gyro-frequency, w is the emission angular frequency and, m_e and γ are the mass and the Lorentz factor of the electron, respectively, while $\mathbf{n}$ is the unit vector from the observer to the electron and $\mathcal{I} = \sqrt{-1}$.

From the manipulation of $\mathbf{n}\times(\mathbf{n}\times\mathbf{v})$, the flux can be split in two components, one parallel and one perpendicular to the projection of the magnetic field. Restricting to the case of relativistic particles ($\gamma \gg 1$) and high frequencies ($w \gg w_B$), the total emitted power per unit frequency is

$$\begin{aligned}\frac{\mathrm{d}P}{\mathrm{d}w} &= \frac{1}{2\pi}\int \mathrm{d}\Omega\mathbf{n}\mathbf{F}(w, w_B)x^2 = \\ &= \frac{\sqrt{3}e^3 B|\mathbf{v}|^2\sin\alpha}{2\pi m_\mathrm{e}c}\gamma F\left(\frac{2m_\mathrm{e}c}{3e\gamma^2 B\sin\alpha}\right),\end{aligned} \tag{2.45}$$

where α is the angle between the particle trajectory and $\mathbf{B}$, and

$$F(X) \equiv X\int_X^\infty \mathrm{d}y\, K_{5/3}(y), \tag{2.46}$$

with $K_{5/3}(y)$ being the modified Bessel function of index 5/3.

The power emitted per unit frequency, unit solid angle and unit volume is given by

$$\frac{\mathrm{d}P}{\mathrm{d}w\mathrm{d}\Omega\mathrm{d}V} = \int_1^\infty \mathrm{d}\gamma n(\gamma)\left(\frac{\mathrm{d}P}{\mathrm{d}w}\right). \tag{2.47}$$

where $n(\gamma)$ is the number density of the emitting particles with Lorentz factors within $[\gamma, \gamma+\mathrm{d}\gamma]$. Substituting the angular frequency, w, by the linear frequency, $\nu = w/2\pi$, we obtain the emissivity

$$j_\nu^{\text{syn}} = \frac{\mathrm{d}P}{\mathrm{d}\nu\mathrm{d}\Omega\mathrm{d}V} = \frac{\sqrt{3}e^3 B\sin\theta}{4\pi m_\mathrm{e}c^2}\int_1^\infty \mathrm{d}\gamma\, n(\gamma)F\left(\frac{\nu}{\nu_0\gamma^2}\right), \tag{2.48}$$

where

$$\nu_0 \equiv \frac{3eB\sin\theta}{4\pi m_\mathrm{e}c} \tag{2.49}$$

is the characteristic linear frequency and θ is the angle between $\mathbf{B}$ and $\mathbf{n}$.

The same population of particles is able to self-absorb and re-emit its own synchrotron radiation. The self-absortion coefficent reads (its proof can be found in, e.g., Rybicki & Lightman 1979)

$$\alpha_\nu^{\rm syn} = \frac{\sqrt{3}e^3 B\sin\theta}{8\pi m_{\rm e}^2 c^2 \nu^2}\int_1^\infty {\rm d}\gamma\,\gamma^2\left[-\frac{\rm d}{{\rm d}\gamma}\left(\frac{n(\gamma)}{\gamma^2}\right)\right]F\left(\frac{\nu}{\nu_0\gamma^2}\right). \tag{2.50}$$

For a power law distribution of particles, which lie between a minimum and a maximum energy, i.e., a minimum and maximum Lorentz factors ($\gamma_{\rm min}$ and $\gamma_{\rm max}$ respectively)

$$n(\gamma) = n(\gamma_{\rm min})\left(\frac{\gamma}{\gamma_{\rm min}}\right)^{-q}\mathcal{S}(\gamma;\gamma_{\rm min},\gamma_{\rm max}), \tag{2.51}$$

where q is the power-law index of the electron energy distribution, and $\mathcal{S}$ is the interval function, $\mathcal{S}(x;a,b) = 1$ if $a \leq x \leq b$ or $\mathcal{S} = 0$ otherwise, the synchrotron emissivity and self-absorption are given by (Mimica 2004)

$$j_\nu^{\rm syn} = \frac{\sqrt{3}e^3 B\sin\theta}{8\pi m_{\rm e}c^2}n(\gamma_{\rm min})\gamma_{\rm min}^q\left(\frac{\nu}{\nu_0}\right)^{(1-q)/2}H_1\left(\frac{\nu}{\nu_0\gamma_{\rm min}^2},q,\frac{\gamma_{\rm max}}{\gamma_{\rm min}}\right), \tag{2.52}$$

$$\alpha_\nu^{\rm syn} = \frac{\sqrt{3}e^3 B\sin\theta}{16\pi m_{\rm e}c^2}n(\gamma_{\rm min})\gamma_{\rm min}^q\left(\frac{\nu}{\nu_0}\right)^{-q/2}\left(\frac{q+2}{\nu^2}\right)H_1\left(\frac{\nu}{\nu_0\gamma_{\rm min}^2},q+1,\frac{\gamma_{\rm max}}{\gamma_{\rm min}}\right), \tag{2.53}$$

where H_1 is the integral

$$H_1(x,q,\gamma_{\rm max}/\gamma_{\rm min}) = \int_{x\left(\frac{\gamma_{\rm min}}{\gamma_{\rm max}}\right)^2}^{x} d\xi\,\xi^{(q-3)/2}F(\xi)\,. \tag{2.54}$$

2.3.2 Thermal emission

For the development of this thesis, we have implemented the algorithm for computing (thermal) bremsstrahlung-BB radiation with SPEV (Cuesta-Martínez et al. 2015a,b). Since we are using a simplified EoS (the *TM* approximation), we also need to provide a method to compute the temperature in every cell considering its local thermodynamic properties (pressure and rest-mass density), as well as the optical depth (Section 2.4.3).

In the following, we describe the emission and absorption coefficients (Rybicki & Lightman 1979) of free–free thermal bremsstrahlung. First of all, we define the useful dimensionless variable

$$x = \frac{h_{\rm P}\nu}{kT}, \tag{2.55}$$

where ν is the frequency of the radiation, and T is the temperature of the fluid in the comoving frame. For a plasma with a Maxwellian distribution of velocities the emission coefficient per unit of frequency takes the form

$$j_\nu^{\rm th} = 5.4\times10^{-39}\frac{Z^2}{\mu_{\rm e}\mu_{\rm i}}\frac{\rho^2}{m_{\rm p}^2}T^{-1/2}{\rm e}^{-x}\bar{g}_{\rm ff}(\nu,T)\,{\rm erg\ s^{-1}\ cm^{-3}\ Hz^{-1}}, \tag{2.56}$$

Following Kirchhoff's law, the absorption coefficient per unit frequency is determined by the relation $\alpha_\nu^{\rm th} = j_\nu^{\rm th}/B_\nu$, where B_ν is the BB intensity. Therefore

$$\alpha_\nu^{\rm th} \simeq 4.1\times10^{-23}\frac{Z^2}{\mu_{\rm e}\mu_{\rm i}}\frac{\rho^2}{m_{\rm p}^2}T^{-7/2}x^{-3}(1-{\rm e}^{-x})\bar{g}_{\rm ff}(\nu,T)\,{\rm cm^{-1}}. \tag{2.57}$$

In the previous two expressions, ρ is the rest-mass density, m_p the proton mass, $\bar{g}_{\rm ff}$ the Maxwellian averaged Gaunt factor for free–free transitions and $Z = \mu_{\rm i}/\mu_{\rm e}$, where $\mu_{\rm e} = 2/(1+X_{\rm h})$ and $\mu_{\rm i} = 4/(1+3X_{\rm h})$. The variable X_h is the relative abundance of hydrogen and we have chosen a typical value $X_h = 0.71$ for main sequence stars and $X_{\rm h} = 0.02$ for Wolf-Rayet stars.

The Maxwellian averaged free–free Gaunt factor has been obtained by interpolation of the values computed by van Hoof et al. (2014, 2015), who updated and extend the earlier tables constructed by Sutherland (1998; be aware that labels in his table 2 are transposed; see Appendix B). In the case of $X_{\rm h} = 0.71$ ($X_{\rm h} = 0.02$) we take the tables of $\bar{g}_{\rm ff}$ for $Z = 1$ ($Z = 2$) as we assume that the medium is mostly composed of hydrogen (helium). The inputs to obtain the Gaunt factor are the variables x and $\gamma^2 = Z^2{\rm Ry}/kT$, where Ry is the Rydberg energy. In our range of temperatures and frequencies the Gaunt factor is close to unity, $\bar{g}_{\rm ff}(\nu,T) \sim 1$. As an alternative to the table interpolation chosen here, we could have approximated by 1 the Gaunt factor at low temperatures and take the expression proposed by Anderson et al. (2010) for high

temperatures ($T > 10^5\,\mathrm{K}$). It should be remarked that Anderson et al.'s expression (9) contains a typo since x is used as $kT/h_{\mathrm{P}}\nu$ instead of its initial definition given by their equation (6), in which $x = h_{\mathrm{P}}\nu/kT$ (compare with our Eq. (2.55)). Interested readers can check equation (8) in Shapiro & Knight (1978), for comparison with equation (9) in Anderson et al. (2010).

2.4 SPEV

SPEV, also developed by members of our group (Mimica et al. 2009b), is the numerical code which allows us to follow the evolution of non-thermally radiating particles (i.e., relativistic electrons) and, after the newest upgrade, thermally radiating particles (i.e., non-relativistic electrons and baryons) in any outflow and compute their electromagnetic emission: synchrotron radiation[4] by non-thermal particles and thermal bremsstrahlung by thermal particles. Under the fluid approximation the constituent particles are not considered individually in the hydrodynamic evolution. Thermally radiating particles are assumed to be in thermal equilibrium, while non-thermally radiating particles are not, since they are generated, e.g., by acceleration processes near shocks. Energy losses in the fluid due to radiation from these particles are not fed back into our RHD code. To properly account for this effect one must perform coupled radiative RHD simulations (Mimica et al. 2004, 2005, 2007). However, in our problem radiative losses are negligibly small and, hence they do not induce substantive changes in the hydrodynamic evolution. This justifies treating radiation separately from the dynamics in a post-processing step performed with SPEV.

First, SPEV reads the numerical data of the RHD simulations and stores the local variables of each cell of the grid in order to initialize and evolve particles that are injected and advected as tracers by the jet fluid. Non-thermal and thermal radiating particles are discriminated at this point (see Sects. 2.4.1 and 2.4.2). Each tracer represents a family of particles (e.g., a particle energy

[4]SPEV can deal also with inverse Compton radiation, but it is not considered in the framework of this thesis.

distribution), which is initialized based on the local properties of the injection place (i, j). Its evolution is followed along its trajectory within the fluid, using a Lagrangian description. During the advection, tracers may experience adiabatic changes that, together with the radiative losses assumed, will modify the particle spectra. As we assume that the particles do not diffuse during the advection, i.e., they remain in the same fluid element between two consecutive times, their spatial and temporal evolution can be treated separately. We highlight the fact that the hydrodynamic evolution is computed in the laboratory frame, while the observed emission must be evaluated in the observer frame.

Second, we obtain synthetic observations in a virtual detector from the radiation emitted by the tracers. The radiation arriving at time $t_{\rm det}$ at a certain detector position comes from a large range of retarded emission times. As we shall see, that's an important point in relativistic flows and also presents a considerable technical difficulty since it makes it necessary to evaluate as many hydrodynamic outputs as is computationally feasible to extend the temporal observational window as well as to obtain a sufficiently accurate and fine time coverage of the emitted radiation. Due to the finite value of the speed of light, photons emitted from different hydrodynamic snapshots (from position z at a time t as seen in the laboratory frame) will contribute to the same observing time,

$$t_{\rm det} = t - z/c\,. \tag{2.58}$$

The issue can be explained in terms of the photons emitted by the head of an ultrarelativistic jet moving with at Lorentz factor $\Gamma_{\rm h}$ towards the observer, which can be produced over a large temporal window in the laboratory frame, Δt, but only contribute into a tiny observational range, $\Delta t_{\rm det} \simeq \Delta t/\Gamma_{\rm h}^2$. The head moves approximately at (almost) the speed of light, all the while continuously emitting photons for all t. As a result all these photons will travel (almost) together with the jet's head concentrating all the emission into a window $\Delta t_{\rm det} \to 0$ if $\Gamma_{\rm h} \gg 1$ (see Fig. 2.1). Thus, in order to evaluate the observed radiation over a sufficiently large time interval $\Delta t_{\rm det}$, it is necessary to compute the hydrodynamic evolution of the most relativistic models up to extremely long laboratory-frame times.

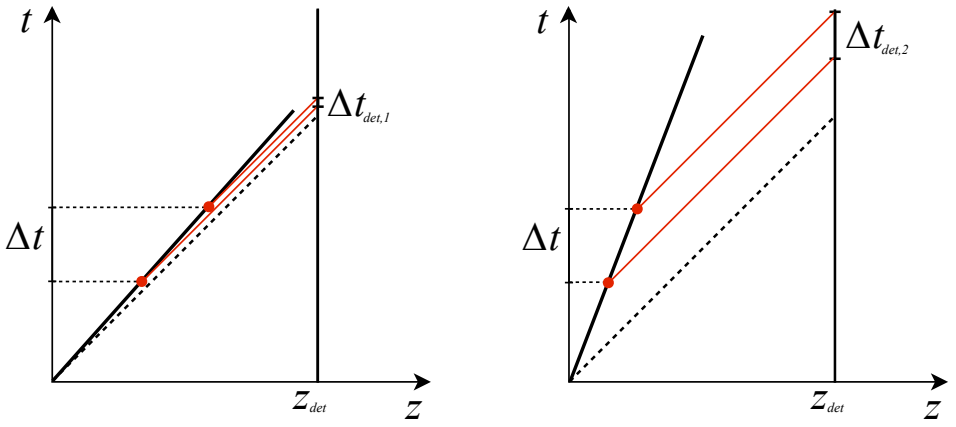

Figure 2.1: Space-time diagrams of two photons (red lines) emitted at the same lab-frame times (with a delay between them of Δt) by two different bodies (black diagonal lines) moving with different velocities: $v_1 \lesssim c$ (left; c is represented with a diagonal dashed line), and $v_2 \ll c$ (right). The temporal window in which they are detected, at $z_{\rm det}$, is larger in the case in which the body has a larger velocity, i.e, $\Delta t_{\rm det,1} < \Delta t_{\rm det,2}$. Also note that the photons are collected at later times on the right-hand case.

2.4.1 Non-thermal particles

For the initialization of the non-thermal particle population we closely follow Mimica & Aloy (2012). As it is commonly done (e.g., Bykov & Meszaros 1996; Daigne & Mochkovitch 1998; Mimica et al. 2004; Bošnjak et al. 2009; Böttcher & Dermer 2010), we assume that a fraction $\epsilon_{\rm e}$ of the dissipated kinetic energy at the forward (and reverse) shock is used to accelerate electrons in the vicinity of the shock front. The properties of the particles are given by the post-shock state of the fluid.

Shock detection. Shocks are detected in the fluid along the radial direction (by simplicity, as the jet is axisymmetric) using an slightly modified PPM criterion (Colella & Woodward 1984) already presented in Eqs. (2.31)–(2.32). We modify the detection criterion so that only the strongest shocks in the flow are captured. In the case of relativistic jets, our detection criterion is able to

capture both the FS and the RS, but neglects the contribution of other much weaker shocks. These shocks are assumed to contribute negligibly to the overall non-thermal emission in the problems we set up. For the current purposes, a shock is detected between cells i (pre-shock state) and $i \mp \Delta_{\rm sh}$[5] (the "$-$" and "$+$" signs in the latter expression identify the post-shock state of the FS and of the RS, respectively), where $\Delta_{\rm sh}$ is the shock width[6]. We typically take $\Delta_{\rm sh} = 10\,({\rm FS}), 5\,({\rm RS})$. In this case, we use $\varepsilon_p = 0.5$ in Eq. (2.31).

We have checked that this criterion is enough to detect the FS but sometimes is not able to properly identify the RS. The identification of the RS can be hindered by the presence of other shock waves (oblique/lateral recollimation shocks) and the perturbations inflicted to the head by the ejection of vortices feeding the jet back-flow or by the interaction with a non-smooth EM. All these effects have the consequence that the jump in pressure across the RS reduces below the typical threshold with which the FS can be detected. Lowering this threshold (i.e., lowering the parameter ϵ in Eq. (2.31)), leads to the detection of many other (weak) shocks, in addition to the RS (something we aim to avoid). Therefore, for a better identification of the RS, we use an additional variable, proportional to the entropy, S, defined as $S = k \log \sigma$, with k being a constant and

$$\sigma = \frac{p}{\rho^{5/3}}(h - \frac{p}{\rho}) \tag{2.59}$$

for the *TM* EoS (Mignone & McKinney 2007). The specific enthalpy, h, is given by Equation (2.17). As the pressure, the entropy must show a jump at shocks, fulfilling

$$\frac{\sigma_{i+\Delta} - \sigma_i}{\sigma_i} > \kappa, \tag{2.60}$$

where we chose a value of $\kappa = 100$. The entropy must be smaller in the non-shocked region of the jet, i.e., behind the RS, and for this reason we are ensuring that $\sigma_i < \sigma_{i+\Delta}$.

[5]Instead of between cells $i-1$ and $i+1$ as in Eq. (2.31).

[6]Strictly speaking a shock has no transverse extent, but due to numerical diffusion shocks are smoothed out and cannot be identified as sharp jumps in the simulation leading to a transition region between the pre- and post-shock states.

Initialization. We assume that the energy spectrum of the injected relativistic particles is a power-law in the electron Lorentz factor γ, with a power-law index q:

$$\frac{\mathrm{d}n_{\rm inj}}{\mathrm{d}t'\,\mathrm{d}\gamma} = Q_0 \gamma^{-q} \mathcal{S}(\gamma;\ \gamma_{\rm min}, \gamma_{\rm max})\ , \tag{2.61}$$

where $n_{\rm inj}$ is the number density of the injected electrons, Q_0 is a normalization factor, $\gamma_{\rm min}$ and $\gamma_{\rm max}$ are the lower and upper injection cut-offs (computed below) and $\mathrm{d}t'$ is the time interval. All the quantities are measured in the shocked fluid rest frame. The reference value for the power-law index of the electron energy distribution is $q = 2.3$.

We assume that the upper cut-off for the electron injection ($\gamma_{\rm max}$) is obtained by assuming that the acceleration time-scale is proportional to the gyration time-scale. Then, the maximum Lorentz factor is obtained by equating this time-scale to the cooling time-scale,

$$\gamma_{\rm max} = \left(\frac{3 m_{\rm e}^2 c^4}{4\pi a_{\rm acc} e^3 B_{\rm st}} \right)^{1/2} . \tag{2.62}$$

where $a_{\rm acc} \geq 1$ is the acceleration efficiency parameter (Böttcher & Dermer 2010) and $B_{\rm st}$ is a stochastic magnetic field, measured in the shocked fluid rest frame, created by the action of shocks. We typically take here $a_{\rm acc} = 1$. The stochastic magnetic field strength is assumed to be a fraction $\epsilon_{\rm B}$ of the internal energy density of the shocked fluid $u_{\rm S}$:

$$B_{\rm st} = \sqrt{8\pi \epsilon_{\rm B} u_{\rm S}}\,. \tag{2.63}$$

The minimum Lorentz factor cut-off ($\gamma_{\rm min}$) is obtained numerically (using the Newton-Raphson method) by assuming that the number of accelerated electrons is a fraction $\zeta_{\rm e}$ of the electrons accelerated into the power-law distribution, so that (see Mimica & Aloy 2012 for details)

$$\frac{\int_{\gamma_{\rm min}}^{\gamma_{\rm max}} \mathrm{d}\gamma\ \gamma^{1-q}}{\int_{\gamma_{\rm min}}^{\gamma_{\rm max}} \mathrm{d}\gamma\ \gamma^{-q}} = \frac{\epsilon_{\rm e}}{\zeta_{\rm e}} \frac{u_{\rm S}}{\Gamma_0' n_0 m_{\rm e} c^2}\,, \tag{2.64}$$

where Γ_0' is the bulk Lorentz factor of the initially unshocked medium measured in the frame of the contact discontinuity between the initial states (up-

and down-stream the shock front), and n_0 is the number density of the initially unshocked plasma measured in its fluid rest frame. Finally, to be consistent with our approximations for the calculation of the synchrotron emission, we only consider as synchrotron emitting those electrons whose Lorentz factor $\gamma_{\rm min} \geq 2$. Below this threshold we assume that electrons are purely thermal and that they only contribute to the free–free bremsstrahlung emission. The condition $\gamma_{\rm min} < \gamma_{\rm max}$ must be fulfilled in every moment, including the initialization.

The distribution of Lorentz factors is discretized logarithmically in $N_{\rm b} = 32$ bins:

$$\gamma_k = \gamma_{\rm min,0} \left(\frac{\gamma_{\rm max}}{\gamma_{\rm min,0}} \right)^{\frac{k-1}{N_{\rm b}}}, \quad k = 1, N_{\rm b}+1 \tag{2.65}$$

and

$$\gamma_{\rm min,0} = \max\left(1, \frac{\gamma_{\rm min}}{1 + eB^2\gamma_{\rm min}\Delta t'}\right), \tag{2.66}$$

$$\gamma_{\rm max,0} = \frac{\gamma_{\rm max}}{1 + eB^2\gamma_{\rm max}\Delta t'}, \tag{2.67}$$

where $\Delta t' = \Delta t/\Gamma_{ij}$ is the interval of proper time for the injected particles at the cell labeled with the indices (i, j), whose bulk Lorentz factor is Γ_{ij}. Δt is the time between the snapshot during which the injection takes place and the next one. The number density of particles per unit Lorentz factor in the shocked fluid rest frame is initialized in every snapshot taken in the laboratory frame ($t = t^0$) as a single power-law, thus in each γ-bin (k) the power-law index is $s_k = s$, $\forall k$ (Mimica et al. 2009b):

$$n_k^0 = Q_0 \gamma_k^{-s} \begin{cases} 1 & \text{if } \gamma_k < \max(\gamma_{\rm min}, \gamma_{\rm max,0}), \\ \max(\gamma_{\rm min}, \gamma_{\rm max,0}) & \text{if } \gamma_k > \max(\gamma_{\rm min}, \gamma_{\rm max,0}), \end{cases} \tag{2.68}$$

where the normalization factor is

$$Q_0 = \zeta_{\rm e} \frac{\rho}{m_p} \begin{cases} \dfrac{1}{\frac{\left(\gamma_{\rm min,0}^{1-q} - \gamma_{\rm max,0}^{1-q}\right)}{q-1} + \frac{\left(\gamma_{\rm max,0}^{-q} - \gamma_{\rm max}^{-q}\right)}{q\,\gamma_{\rm max,0}}} & \text{if } \gamma_{\rm min} \leq \gamma_{\rm max,0}, \\ \dfrac{1}{\frac{1}{\gamma_{\rm max,0}} - \frac{1}{\gamma_{\rm min}} + \gamma_{\rm min}^{q-1}\left(\gamma_{\rm min}^{1-q} - \gamma_{\rm max}^{1-q}\right)} & \text{if } \gamma_{\rm min} > \gamma_{\rm max,0}. \end{cases} \tag{2.69}$$

Therefore the initial number density of particles within the interval $[\gamma_k, \gamma_{k+1}]$ in the shocked fluid rest frame is (Mimica et al. 2009b)

$$\mathcal{N}_k = \frac{n_k^0}{s-1}\gamma_k \left[1 - \left(\frac{\gamma_{k+1}}{\gamma_k}\right)^{1-q}\right] \tag{2.70}$$

Depending on the case, the power-law index can take the following values:

$$s = \begin{cases} 2 & \text{if } \gamma_k < \gamma_{\rm min}, \\ q & \text{if } \gamma_k < \gamma_{\rm max,0}, \\ q+1 & \text{if } \gamma_k \geq \max(\gamma_{\rm min}, \gamma_{\rm max,0}). \end{cases} \tag{2.71}$$

Evolution. The tracers move with the fluid. In the time-step between two consecutive snapshots in the laboratory frame (n and $n+1$), $\Delta t^n = t^{n+1} - t^n$, we consider that a family of particles moves from its current position, $(r_i(t^n), \theta_j(t^n)) \equiv (r_i^n, \theta_j^n)$, to its new one, $(r_i^{n+1}, \theta_j^{n+1})$, with a velocity, $\mathbf{v}(t^n) = (v_i^r, v_i^\theta)$, equal to that of the jet fluid at (r_i^n, θ_j^n):

$$\begin{pmatrix} r_i^{n+1} \\ \theta_j^{n+1} \end{pmatrix} = \begin{pmatrix} r_i^n + v^r \Delta t^n \\ \theta_j^n + \dfrac{v_i^\theta}{r_i^n} \Delta t^n \end{pmatrix}. \tag{2.72}$$

Along the path between (r_i^n, θ_j^n) and $(r_i^{n+1}, \theta_j^{n+1})$ the properties of the particle distribution such as their energy and Lorentz factor also change. The temporal evolution in the local fluid comoving frame of the particle distribution is determined by the kinetic equation (Kardashev 1962),

$$\frac{\partial n(\gamma, t')}{\partial t'} + \frac{\partial}{\partial \gamma}(\dot{\gamma} n(\gamma, t')) = Q(\gamma)\,, \tag{2.73}$$

where the energy of the particles changes as

$$\dot{\gamma} \equiv \frac{{\rm d}\gamma}{{\rm d}t'} = k_a \gamma - k_s \gamma^2\,. \tag{2.74}$$

due to adiabatic expansion or compression (decreasing or increasing the particle energy at a rate determined by k_a, respectively) and radiative processes (always

decreasing γ at a rate determined by k_s), in this case synchrotron process:

$$\begin{aligned} k_a &= \frac{1}{3\Delta t'^n} \ln\left[\frac{\rho(t^{n+1})}{\rho(t^n)}\right], \\ k_s &= eB^2. \end{aligned} \tag{2.75}$$

The number density of particles evolves as (Mimica et al. 2009b)

$$n_k^0(t^{n+1}) = n_k^0(t^n)\,\mathrm{e}^{2k_a\Delta t'^n}\left[1+\frac{k_s}{k_a}\gamma_k(t^n)\left(\mathrm{e}^{k_a\Delta t'^n}-1\right)\right]^2 \tag{2.76}$$

$$\mathcal{N}_k(t^{n+1}) = \mathcal{N}_k(t^n)\mathrm{e}^{3k_a\Delta t'^n}. \tag{2.77}$$

The new power-law index, $s_k(t^{n+1})$, is obtained at t^{n+1} by solving iteratively the integral in the γ-space of the total power-law electron distribution (Mimica et al. 2009b),

$$\mathcal{N}_k(t^{n+1}) = \int_{\gamma_k}^{\gamma_{k+1}} n_k^0(t^{n+1})\left(\frac{\gamma}{\gamma_k}\right)^{-s_k(t^{n+1})}\mathrm{d}\gamma. \tag{2.78}$$

Finally, the Lorentz factor evolves as (Mimica et al. 2009b)

$$\gamma_k(t^{n+1}) = \gamma_k(t^n)\,\frac{\mathrm{e}^{k_a\Delta t'^n}}{1+\gamma_k(t^n)\left(\mathrm{e}^{k_a\Delta t'^n}-1\right)k_s/k_a}. \tag{2.79}$$

The latter variables that characterize the particle distribution are re-evaluated, for practical purpose, at the laboratory frame time t^{n+1}, however, we emphasize that they are calculated and evolved in the proper time of the particle distribution. It holds that $t'^{n+1} = t'^n + (t^{n+1}-t^n)/\Gamma^n \equiv t'^n + \Delta t'^n$, where $\Delta t'^n = \Delta t/\Gamma^n$.

In the course of the temporal evolution, it is possible that the initially logarithmically distributed Lorentz factor bins are compressed (since particles loose energy), so that the distance between the maximum and the minimum Lorentz factors of the distribution $\Delta\gamma = \gamma_{\max}/\gamma_{\min}$ decreases. For numerical reasons, we limit the value of $\Delta\gamma$ to be larger than a minimum threshold Δ_γ. If during the evolution $\Delta\gamma < \Delta_\gamma$, the tracers from this distribution are eliminated from the calculation. Tracers are also removed from the simulation when they have exited the numerical grid.

2.4.2 Thermal particles

Thermal particles are injected in every cell of the moving jet or in opaque regions such as the progenitor star itself or dense winds and shells. In the latter two cases, they do not emit thermal radiation, but act as absorbers.

The temperature of the electrons present in the fluid has been computed assuming that matter is coupled to radiation when the optical depth, τ, is large enough. In that case the equilibrium temperature can be obtained numerically (using Newton–Raphson method) from the following equation for the total pressure, which takes into account contributions of electrons, baryons and radiation pressure,

$$p = p_{\rm bar} + p_{\rm rad} = \frac{k}{\mu m_{\rm H}} \rho T + \frac{1}{3} a_{\rm R} T^4 \,. \tag{2.80}$$

Here $m_{\rm H}$ ($\approx m_{\rm p}$) is the mass of the hydrogen atom, $\mu = (1/\mu_{\rm e} + 1/\mu_{\rm i})^{-1} \approx 4/(3{+}5X_{\rm h})$ is the mean molecular weight in units of $m_{\rm H}$, and $a_{\rm R}$ is the radiation constant.

The initial number of electrons and baryons is $n_e = \rho/\mu_e m_p$ and $n_i = \rho/\mu_i m_p$, respectively.

2.4.3 Emission

A Cartesian virtual detector, which is discretized in a large number of pixels, is defined at a certain distance from the numerical grid with a given orientation with respect to the z-axis. SPEV is able to replicate tracers around the z-axis and build a 3D structure of the system whose emission is collected by a 2D virtual detector (Tabik et al. 2012). However, in order to increase the computation speed and reduce the memory usage, we take the axisymmetry of our systems and the location of the observer on the z-axis (i.e., the z-axis is parallel to the detector) to only consider tracers on the x–z plane and collect their emission in a 1D detector (see Fig. 2.2). The total emission is computed in a last step by replicating each pixel as an annulus around the z-axis. For algebraic simplicity, the position of all the particles is converted into Cartesian coordinates. The normal projection of each particle onto the detector can

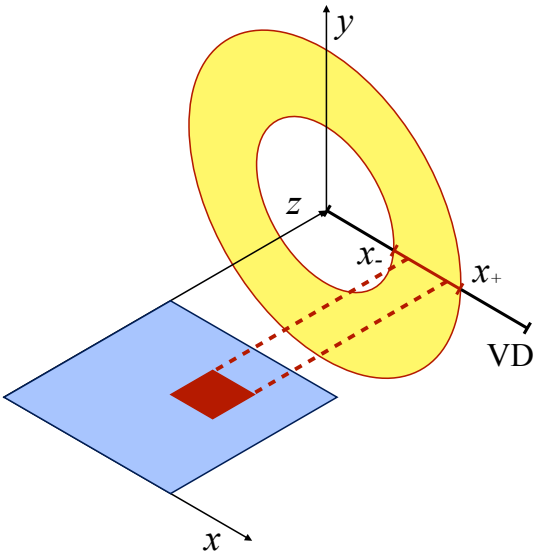

Figure 2.2: A 1D virtual detector (VD) is perpendicular to the z-axis (i.e., the symmetry axis) of the system. The blue area represents (a piece of) the physical domain, in the x–z plane, in which the red cell is considered to contribute to the emission. The red dashed lines represent the normal projection of the boundaries of intersection (in the x-direction) of this cell with a given pixel of size $\Delta x = x_+ - x_-$. As our systems are axisymmetric the intensity collected by the pixel is lately replicated around the z-axis (in the form of a yellow annulus) to take into account the true emitting volume.

intersect one or more pixels so that the contribution to a single pixel will be given by particles whose projections overlap with that pixel. Thus, the intensity at a certain detection time, $t_{\rm det}$, is given by photons emitted along the line of sight of the pixel at different laboratory frame times, t. In our particular problem Eq. (2.58) needs to include additional terms since we define $t_{\rm det} = 0$ for those photons emitted at $t = 0$ and $z = R_0$. Thus, we must consider the jet's flight time, $t_{\rm off}$, from $r = 0$ to R_0, so that

$$t_{\rm det} = t - z/c + R_0/c + t_{\rm off}\,. \tag{2.81}$$

The value $t_{\rm off}$ is calculated assuming that the jet was moving with velocity $v = v_i = c\sqrt{1-\Gamma_i^{-2}}$ until that time. Hence, $t_{\rm off} = R_0/v_i = R_0/(c\sqrt{1-\Gamma_i^{-2}})$.

Note that Eq. (2.81) does not include any cosmological correction due to the redshift.

Now, for the understanding of the problem we focus on a given pixel. As we consider a flat spacetime, photons will follow straight lines. Then, the intensity at a given frequency along the line of sight of the pixel suffers variations as photons are emitted and absorbed by the particles on its path. SPEV calculates its evolution integrating the radiative transport equation along each line of sight and computing the final intensity in the pixel. In the integration, both non-thermal and thermal particles are distinguished since their emission and absorption coefficients are different.

Before integration, the temperature of the thermal fluid is recomputed since Eq. (2.80) might not be fulfilled in optically thin regions (i.e., in regions where the radiation is not in equilibrium with matter) leading to erroneous thermal coefficients. In optically thin fluid regions, i.e., in those where the optical depth is small, we assume that radiation is partially decoupled from matter. Thus, in a simple generalization of Eq. (2.80), the total pressure is computed as

$$p = p_{\rm bar} + p_{\rm rad}(1 - {\rm e}^{-\tau_{\rm t}}). \tag{2.82}$$

Here $\tau_{\rm t}$ is the total optical depth of the system, along the line of sight, restricting the length of the integration path to the size of each single numerical cell of the hydrodynamic simulation along the line of sight (l_τ). Explicitly, the optical depth in a single cell is $\tau = \tau(T, \nu) = \alpha_\nu(T, \nu) l_\tau$, where α_ν is the sum of the thermal and non-thermal absorption coefficients.

As τ depends on the temperature, and for computing properly the temperature we must know the overall optical depth of our model, we need to perform an iterative process, which is repeated until a desired convergence is reached. For the initial guess of the temperature we assume that matter and radiation are coupled (Eq. (2.80)). We remark that the temperature depends on frequency, so we have different temperatures for different frequency bands.

We note that using this method for computing the temperature, in regions where there is a large gradient in optical depth, we may find also a very large temperature gradient, so that optically thick regions are much cooler than

optically thin ones.

In order to compute both the thermal and non-thermal specific intensity, SPEV integrates independently the radiation transport equation for both cases. We properly account for the emissivity of thermal bremsstrahlung and synchrotron processes, as well as for the corresponding absorption processes in each fluid element along the line of sight. In the following we will use the superscripts 'th' and 'nt' to refer to either thermal or non-thermal radiation properties. For the computation of the total specific intensity, we should consider a unique absorption coefficient that includes bremsstrahlung absorption, synchrotron self-absorption (both from synchrotron photons and from thermal photons), as well as absorption of synchrotron photons by the baryonic medium. However at the ultraviolet–optical–infrared (UVOIR) and X-ray frequencies under consideration here, synchrotron self-absorption is negligible (Mimica, Giannios & Aloy 2010).

The total specific intensity can be computed as the sum of the thermal and non-thermal contributions, $I_\nu = I_\nu^{\rm th} + I_\nu^{\rm nt}$, each of which changes along a photon path parametrized by the parameter λ, as

$$\frac{{\rm d}I_\nu^{\rm nt}}{{\rm d}\lambda} = j_\nu^{\rm nt} - (\alpha_\nu^{\rm th} + \alpha_\nu^{\rm nt}) I_\nu^{\rm nt}, \tag{2.83}$$

$$\frac{{\rm d}I_\nu^{\rm th}}{{\rm d}\lambda} = j_\nu^{\rm th} - \alpha_\nu^{\rm th} I_\nu^{\rm th}, \tag{2.84}$$

where $j_\nu^{\rm nt}$ and $\alpha_\nu^{\rm nt}$ are the synchrotron emission (Eq. (2.52)) and absorption coefficients (Eq. (2.53)), and $j_\nu^{\rm th}$ and $\alpha_\nu^{\rm th}$ are the free–free bremsstrahlung emission (Eq. (2.56)) and absorption coefficients (Eq. (2.57)).

Finally, to consider the whole ('true') emitting volume each 1D pixel, whose upper and lower edges are represented by x_+ and x_-, respectively, is replicated around the z-axis in the form of an annulus. The total intensity is calculated by adding up the individual contributions of every pixel multiplied by a factor of $\pi(x_+^2 - x_-^2)$ (the area of its associated annulus; Fig. 2.2).

Chapter 3

Blackbody-dominated GRBs

The work presented in the following chapter has been published in the scientific journal 'Monthly Notices of the Royal Astronomical Society' in two complementary publications. The correspoding titles are 'Numerical models of blackbody-dominated gamma-ray bursts – I. Hydrodynamics and the origin of the thermal emission' (Cuesta-Martínez, Aloy & Mimica 2015a) and 'Numerical models of blackbody-dominated gamma-ray bursts – II. Emission properties' (Cuesta-Martínez et al. 2015b). Both papers have been properly arranged and restructured in this thesis for better comprehension of the work. However, the reader must be aware that part of the published results have been modified since publication due to an error we found in the tables used for computing the Gaunt factor (Sutherland 1998). For this reason, we have recalculated and updated in this thesis all light curves and spectra from both papers employing a new and corrected version of the Gaunt factor table. Nevertheless it is important to remark that the error made only truly affects to the X-ray band results and therefore our main conclusions on both papers still remain valid (see Appendix B for details).

3.1 Introduction: The 'Christmas burst'

Most of the detected GRBs can be classified in one of the two standard classes proposed by Kouveliotou et al. (1993). However, as the number of observed

events increases, outliers to the basic division between short and long duration GRBs appear. Beyond their phenomenological characterization, the most interesting question that such outliers rise is whether they are typical events with atypical intrinsic and environmental physical parameters, or whether they are different types of events, perhaps associated with different channels of producing ultracompact stellar mass objects. Among them we point out the superlong and ultra-long GRBs (see, e.g., Tikhomirova & Stern 2005; Gendre et al. 2013; Levan et al. 2014, hereafter L14) with durations of about $\sim 10^3$ and $\sim 10^4$ s. These durations are much longer than those of typical long bursts. Many progenitor scenarios have been proposed for the newly discovered bursts, such as tidal disruption events (e.g., Lodato & Rossi 2011; MacLeod et al. 2014), core collapse leading to a long-lasting source (e.g. Toma et al. 2007; Nakauchi et al. 2013) or stellar mergers (e.g., Barkov & Komissarov 2010; Thöne et al. 2011, hereafter T11).

For some GRBs associated with SNe, an additional thermal component in the X-ray afterglow has been found and attributed to the SN shock breaking out of the star or the circumstellar wind (Campana et al. 2006; Soderberg et al. 2008). Nevertheless, recent observations of bursts, associated with faint SNe, appear with a thermal component not only in X-rays but also in optical bands. This is the case of GRB 101225A (also called the 'Christmas burst', CB; T11) which, apart from lasting more than a typical burst, shows an unusually strong blackbody (BB) component in both its X-ray and its optical spectrum. The initial observed duration was longer than 2000 s. This duration is only a lower bound, since before and after its detection it was out of the field of view of *Swift*. It was also active in the subsequent *Swift* orbit, suggesting a duration in excess of $\sim$ 7000 s (L14). GRB 101225A does not possess a classical afterglow. Rather, the X-ray emission following the GRB (0.38 h $< t_{\rm obs} <$ 18 d) is well fitted with an absorbed power-law spectrum in addition to a BB component, i.e., assuming a thermal hotspot with a characteristic temperature $T \sim 1$ keV (it should be noted that other fits are also possible for describing the early X-ray evolution, see e.g., L14). The ultraviolet–optical–infrared (UVOIR) light curve and SED also display a very peculiar behaviour.

During the first 10 d they are best fit as if corresponding to a cooling process of an expanding BB (T11). From the spectral fits to a simple model which assumes that the observed emission originates from an expanding sphere of a uniform surface temperature one infers that the radius of the BB-emitting component grows from 13 AU (0.07 d after the burst) to 45 AU (18 d after). During the same time interval the BB temperature decreases from 43000 to 5000 K. The radius and temperature evolution of the UVOIR data are radically different from that of the X-ray hotspot, suggesting that they are not caused by the same process. After 10 d there is a flattening of the light curve, suggestive of an associated SN, whose light curve would peak at ~ 30 d. The most recent redshift estimate for the CB is $z = 0.847$, and has been obtained by L14 thanks to the identification of [O II], [O III] and Hβ spectral lines. The measured redshift sets a lower bound for the energy of $E_{\rm iso} \gtrsim 1.20 \times 10^{52}$ erg. To account for the observational peculiarities of the CB, T11 propose that the progenitor system of this event is a merger of a neutron star with the helium core of an intermediate-mass star. Beyond the subtleties of whether the merger process results in a GRB central engine consisting of a hyperaccreting stellar mass black hole or of a powerful magnetar, the bottom line of the model is the ejection of a fraction of the hydrogen envelope of the secondary star of the binary system as a result of a quick phase of common envelope (CE) evolution of both binary members. The ejecta debris shapes the circumburst medium in such a way that the associated GRB does not display a typical afterglow and it is the reason behind the appearance of a strong thermal component in the optical bands during the first $\sim 5 - 10$ d after the burst. We note that this scenario is not incompatible with the possibility of having additional sources of thermal emission like, e.g., the X-ray emission expected in some GRBs with associated supernovae (SNe) resulting from the supernova shock breakout (Campana et al. 2006; Soderberg et al. 2008). However, this X-rays contribution might be heavily modified by the absorption of the breakout flash in the ejected CE.

Other bursts, such as GRB 100316D (Starling et al. 2011), GRB 090618 (Page et al. 2011) or GRB 060218 (Campana et al. 2006), also exhibit a BB

component, implying we may be starting to see a new (sub)-class of non-standard GRBs. They are characterized by some thermal element heating the environment, and their central engine may be, in some cases, active for very long time (not the case of GRB 090618). GRB 101225A probably constitutes one of the most prominent examples of the so-called blackbody-dominated GRBs (BBD-GRBs). Thus, it pays off to understand the particularities that differentiate GRB 101225A from other more standard cases.

In the present chapter, we refine the theoretical model proposed in T11 by performing multidimensional numerical relativistic hydrodynamic (RHD) simulations of jets interacting with an assumed ejecta debris, and further computing the emission from such numerical models. We will characterize the different thermal signatures to be expected in terms of different physical parameters of our models. We also compute the non-thermal (synchrotron) emission produced by our jet models in addition to the pure thermal emission. The synthetic light curves (LCs) and spectra obtained are compared with the observational data. This allows us to infer the true event energy, radiative efficiency and the origin of the thermal and non-thermal radiation from the CB. It also serves us for the purpose of assessing that the lack of a classical afterglow in our models is directly linked to the atypical jet/environment interaction, which produces the deceleration of the jet by mass entrainment in the beam, instead of the typical mechanism consisting of plowing mass of the external medium (EM) in front of the GRB ejecta. The main objective of this work is to explain the thermal component observed during the first 5 d of UVOIR observations that, as we shall see, can be chiefly associated with the jet/CE ejecta interaction. Furthermore, we shall see that the non-thermal emission is dominant during the early phases of the evolution, when the forward shock is moderately relativistic. After 5 d a SN signal (T11) adds a new spectral component that we do not model in this work. At this point it is important to stress that our goal is not to 'fit' the observations with our simulations, but rather to attempt to show that, qualitatively and quantitatively, observations can be explained with reasonable and sound combinations of the physical parameters that characterize an ultrarelativistic jet and its environment.

The outline of the chapter is as follows. In Section 3.2, we discuss the possible progenitor scenarios of BBD-GRBs. In Section 3.3, we set the initial conditions of our hydrodynamic models and we introduce the microphysical parameters needed to compute the non-thermal emission. In Section 3.4, we present the dynamics of the 'reference model' (RM; the model that better explains the observational data) and assess the robustness of our results by considering suitable variations of the main parameters defining the jet, the ejecta and the external medium (EM). In Section 3.5, we show that the likely origin of the thermal component (observed in the optical observations of GRB 101225A up to the first 5 d) is the interaction between the ultrarelativistic jet and the ejecta. In Section 3.6, we show the origin of the non-thermal emission and its contribution to the total emission in comparation with the thermal one. In Section 3.7, we present a parametric scan of both the non-thermal emission and the hydrodynamic model parameters whose aim is to obtain the best explanation for the optical observations of GRB 101225A. In Section 3.8, we show the study made in order to look for the best trade off between resolution and quality of our models. In Section 3.9, we summarize the main results of our simulations and underline the strengths and weaknesses of our models. We also discuss the possible improvements in the radiative transport algorithm.

3.2 Progenitor models

There are two basic alternative progenitor models that could explain (most of) the phenomenology associated with the CB and, by extension, the BBD-GRBs. On the one hand, Nakauchi et al. (2013) have proposed that the direct collapse of the envelope of a blue supergiant star may provide the fuel for a very prolonged central engine activity. In this model, the photospheric emission of the cocoon blown by a relativistic jet may be released once the jet breaks out of the surface of the star. This photospheric emission would create a SN-like bump at longer times, but the spectral inversion of the system at about ~ 2 d after the GRB is difficult to explain with such model. A plausible alternative

is that the CB resulted from an evolved He star and a neutron star (NS) forming a binary system (Fryer & Woosley 1998; Zhang & Fryer 2001; Barkov & Komissarov 2010, 2011).

In this model, a compact object, either a BH or an NS acquires a massive accretion disc by merging with the helium core of its red giant companion. The compact primary enters the helium core after it first experiences a common envelope (CE) phase that carries it inward through the hydrogen envelope (see, e.g., Fryer, Rockefeller & Young 2006; Chevalier 2012). The spiral-in process is accompanied by the accretion of several solar masses of helium on a time-scale of minutes and provides a neutrino luminosity, which is very sensitively depending on the mass of the helium core.[1] However, the amount of energy released by neutrinos might not be enough to power a long-lasting jet unless a rather massive He core is invoked, namely, with a mass $\gtrsim 10\,M_\odot$ (Fryer et al. 2013). If the He core mass is relatively small, it is plausible that the BH–disc interaction, mediated by magnetic fields is the primary source of energy of the central engine. In this case, a simplified estimate of the Blandford–Znajek power yields luminosities of $\sim 10^{51} - 10^{52}\,\mathrm{erg\,s^{-1}}$. Longer time-scales to power an outflow shall result if the merger remnant is a magnetar, in which case the initial NS does not turn into a BH due to an insufficient amount of accreted mass, resulting from a low accretion rate (see, e.g., Ivanova et al. 2013). NS–He core mergers might occur at a rate comparable to that of merging NSs and BH–NS binaries (Belczynski, Bulik & Fryer 2012). The main advantage of this model is that it can account for the observed long duration, and the fact that it provides a simple explanation for the presence of a structured, high-density circumburst environment. The reason is that during the travel of the NS in the CE phase, a fraction of the hydrogen envelope is tidally ejected away from the He core in the form of a thick, dense shell. We refer to it as the CE shell in the rest of this work. According to recent numerical simulations (e.g., Passy et al. 2012; Ricker & Taam 2012; Fryer et al. 2013), the dynamic phase of the

[1] One obtains $L_{\nu\bar{\nu}} \sim 2 \times 10^{38} (M_{\rm He}/M_\odot)^{9.5}\,\mathrm{erg\,s^{-1}}$ for the neutrino–antineutrino annihilation luminosity ($L_{\nu\bar{\nu}}$) of He cores with masses $M_{\rm He} > 4M_\odot$ from the fig. 6 of Fryer et al. (2013)

CE evolution lasts for 3–5 orbits at the initial binary separation. Taking such a time-scale as a reference, and assuming the debris is ejected at 1–2 times the escape velocity, we can estimate the maximum distance at which it will be located before the merger happens as $R_{\rm debris} \approx (3\text{–}5) \times t_{\rm orbit} v_{\rm escape} \approx (27\text{–}45) \times R_{\rm orbit}$, where $R_{\rm orbit}$ is the semimajor axis of the orbit. The helium-merger model provides a numerically tested explanation for a complex circumburst medium, which roughly resembles a torus or shell located at $\sim 10^{14}\,{\rm cm}$ (which one associates to the debris location after a travel time of $\sim 1.5\,{\rm yr}$, for an initial orbital separation $R_{\rm orbit} \simeq 30\text{–}100 R_{\odot}$, which roughly coincides with the radius of the secondary, evolved, massive star of the binary). The debris distribution is expected to be non-uniform: most of the mass is ejected along the equator and a low-density funnel is likely to exist, aligned with the rotational axis of the system. Once the two stars merge, an accretion disc and jets are formed leading to a GRB-like event.

In T11, the authors sketched a theoretical model according to which only a small part of the jet escapes through the funnel giving rise to the detected gamma-ray emission while most of it interacts with the previously ejected material. The outflowing matter interacting with the boundary of the ejecta closer to the rotational axis leads to a hotspot, producing the persistent X-ray emission. The jet/CE ejecta interaction along the ejecta funnel loads with baryons the relativistic beam of the jet, resulting in a quick deceleration of the jet to mildly relativistic speeds, and thus diminishing any standard afterglow signature. As soon as the jet material breaks out of the shell, it can expand sideways almost freely, forming a hot bubble. The emission from this bubble may account for the UVOIR BB emission before it is finally outshone by the observed SN.

Fryer et al. (2013) point out that the BB component observed in the CB, in the X-ray flare 060218 and, perhaps, in other low-redshift bursts, is an observational signature of the shell (or torus) of merger ejecta surrounding the burst. The density structure of the medium around the secondary star and, thus, the environment in which the hydrogen envelope is ejected can only be constrained with detailed simulations of He/NS mergers. Zhang & Fryer

(2001) simulations are the only ones which may map the progenitor system that T11 assume for GRB 101225A with sufficiently high numerical resolution. Unfortunately, these models span a typical region of less than 10^{12} cm, and, thus, do not include the evolution of the hydrogen envelope. It is not unlikely that, after the SN explosion of the primary (initially most massive) star, the system suffers a 'kick' causing that the final merger occurs out of its initial location. Depending on the magnitude of the kick and the time elapsed from the first SN explosion to the final merger, the latter may happen either very close to the original location or very far away from it. If the merger happens close to its original place, the GRB jet may have to drill its way through the young SN remnant and then through the wind of the secondary star (Fryer et al. 2006). In the alternative scenario, the merger may take place beyond the termination shock of the wind of the secondary star, in a medium which will be rather uniform if the mass of the secondary star is not too large (< 15–$20 M_{\odot}$; Fryer et al. 2006). In any case, the structure of the circumburst medium depends (among other factors) on the exact mass of the He core. As noted in Fryer et al. (2013), the spectrum of masses of He cores for solar metallicity models spans the range from a few solar masses to a bit more than $25 M_{\odot}$. If the metallicities are subsolar, He core masses can be found up to $\sim 45 M_{\odot}$. With such a range of He core masses, the mass of the hydrogen envelope can be rather large (perhaps tens of solar masses), and hence, the amount of mass ejected from the original secondary (massive) star, both prior to the merger with the compact remnant and as a result of it is extremely uncertain. For instance, it is known that sufficiently massive stars (e.g., $\gtrsim 40 M_{\odot}$) may develop luminous blue variable eruptions during which masses of the order of $1\,M_{\odot}$ may be ejected at speeds of the order of the escape velocity of the star. If such a catastrophic event happens a few years before the binary begins its final approach, by the time of merger, this ejecta may have travelled a few $\times 10^{15}$ cm, and filled the environment with mass densities $\sim 10^{-14}\,\mathrm{g\,cm^{-3}}$. We also point out that late unstable burning may generate gravity waves that deposit their energy and momentum in the outer parts of the star, driving strong mass-loss (e.g., Quataert & Shiode 2012), and contributing to raise the

density of the immediate circumburst medium of the merger. As we shall see, our models accommodate better the observational data if the GRB-jet (true) energy is $\lesssim 10^{52}$ erg. In order to tap so much energy in the outflow, we need to consider models where the He core mass is larger than $\sim 10 M_{\odot}$, if the jet is neutrino-powered or $\gtrsim 3 M_{\odot}$ if it is magnetically powered according to the results of Fryer et al. (2013).

Another important factor shaping the structure of the medium surrounding the merger is the location of the binary system. It is very likely that a merger among evolved massive stars happens inside of molecular clouds. These molecular clouds may have rather high number densities (e.g., $\sim 10^5\,\mathrm{cm}^{-3}$ for G353.2+0.9; Giannetti et al. 2012, or $\sim 10^7\,\mathrm{cm}^{-3}$ for the molecular cloud against which Cas A is colliding; Fryer et al. 2006). Therefore, we foresee that the environment surrounding some mergers may be rather massive. As a matter of fact, and as we shall see in Sections 3.4 and 3.7, our models suggest that high-density media accommodate better the observational data. We point out that the interaction of a GRB jet with a dense molecular cloud is not within the scope of our work. We refer the interested reader to Barkov & Bisnovatyi-Kogan (2005a,b) for a detailed discussion of the effects that such interaction may have on the resulting optical afterglow of "standard" GRBs. We note that, differently from our model, the optical afterglow in the previous papers results from the reprocessing of the γ-rays and X-rays produced by the GRB jet in the high-density molecular cloud in which the jet moves (this idea was originally suggested by Bisnovatyi-Kogan & Timokhin 1997).

3.3 The numerical model

In order to test the physical model sketched in the previous section, we carry out numerical simulations focusing on the interaction of a relativistic jet with a simple model for the circumburst medium. We have employed the finite volume, high-resolution shock-capturing, RHD code MRGENESIS, in 2D spherical coordinates – assuming that the system is axisymmetric – to solve the RHD equations. The code uses a method of lines, which splits the spatial variation

and temporal evolution with two independent discretizations. A Total Variation Diminishing third order Runge–Kutta method and a third order PPM (Colella & Woodward 1984) scheme have been used for both time integration and spatial intercell reconstruction, respectively. Marquina's flux formula (Donat & Marquina 1996) has been chosen for computing the numerical fluxes at the cell interfaces. For the models of interest in this work, a high order scheme is essential to ameliorate the fine grid needed to resolve both the initial ultrarelativistic jet, as well as the jet/CE-shell interaction. We have produced all our models employing the *TM* approximation (Mignone et al. 2005) as an equation of state.

For simplicity, we do not consider general relativistic (GR) effects. This is justified since we begin our jet simulations sufficiently far away from the central engine of the GRB (where a GR gravitational field is important). In the rest of this work, we consider flat space–time in the whole numerical domain. Furthermore, magnetic fields are assumed to be dynamically unimportant, so that a pure hydrodynamic approach is used.

In order to post-process our hydrodynamic models and compute detailed LCs and spectra, we have improved the radiative transport code SPEV to include thermal emission processes, which can account for the BB component in the observations of GRB 101225A. We assume that the thermal radiation is produced by free–free thermal bremsstrahlung. For simplicity in the treatment of the thermal emission, Comptonization is ignored. For the temperatures ($T \lesssim 2 \times 10^5\,\mathrm{K}$) and number densities ($n \lesssim 10^{14}\,\mathrm{cm}^{-3}$) of the emitting plasma, thermal bremsstrahlung is the dominant contribution. However, there are (relatively small) emitting regions where Comptonization may be dominant. Ideally, the sum of the contributions of both processes should be considered when computing the total thermal emission. However, we are only including one of them, so that our calculation of the thermal emission should be regarded as a lower bound to the total thermal emission for the proposed model. A rough estimate based on the bolometric power in both free–free bremsstrahlung and Comptonization processes allows us to conclude that the radiative fluxes we compute considering only free–free bremsstrahlung are cor-

rect (within a factor $\sim$ 2–3) during the first 5 d of the system evolution. We also consider non-thermal emission (synchrotron radiation). In the rest of this chapter we refer to the two emission processes included in the radiative code as non-thermal (synchrotron) and thermal (free–free thermal bremsstrahlung or bremsstrahlung-BB) emission.

To compare with observations we compute the observed flux in the r, $W2$ and X bands, corresponding to frequencies of 4.68×10^{14} Hz, 1.56×10^{15} Hz and 2.42×10^{18} Hz, respectively. Because the GRB prompt emission *has been* observed, and due to the probable geometry of the CE shell (with a low-density, narrow funnel along the axis), we assume that the line of sight is aligned with the rotational axis of the system, and that the GRB was observed exactly head-on (i.e., the viewing angle is assumed to be $\theta_{\rm obs} = 0^{\circ}$).

Since we cannot directly infer from observations all the physical parameters which are necessary to set up the dynamics of an ultrarelativistic jet as well as the environment in which it propagates, we first fix the parameters for the RM, and afterwards we perform a broad parametric scan by varying the properties both of the jet and of the ambient medium. We are not performing consistent numerical simulations of the merger of a He core with a compact remnant. Therefore, we set up the environment and the ejecta debris in an idealized way. For simplicity of the model initialization, we assume that the RM has a uniform medium outside of the He core (which is much smaller than the innermost radius of our computational domain). We will also alternatively consider external media which are stratified according to different rest-mass density gradients. Furthermore, since the non-thermal emission also depends on a number of microphysical parameters, we consider variations of those parameters to more reliably assess the quality of our numerical results.

3.3.1 Setup of the reference model

The radial grid of all of our simulations begins at $R_0 = 3 \times 10^{13}$ cm, where an ultrarelativistic jet is injected.[2] This means that, differently from other jet

[2]It is desirable to use a value for R_0 as small as possible, to prevent possible numerical 'pathologies' related with the start of the jet injection and, later, its switch off. However,

simulations addressing the propagation of the jet inside of the progenitor star (e.g., Aloy et al. 2000; Zhang, Woosley & MacFadyen 2003a; Zhang, Woosley & Heger 2004; Mizuta et al. 2006; Morsony, Lazzati & Begelman 2007, 2010; Mizuta & Aloy 2009; Mizuta, Nagataki & Aoi 2011; Nagakura et al. 2011; Nagakura, Suwa & Ioka 2012; López-Cámara et al. 2013), our models assume a collimated jet outside of the stellar envelope, which is consistent with the results of the former models as well as with the fact that the jet is injected for a very long time in our case. For (almost) all models the radial grid ends at $R_{\rm f} = 3.27 \times 10^{15}\,{\rm cm}$, and consists of 5400 uniform radial zones.[3] The polar grid spans the range $[0°, 90°]$, with a resolution of 270 uniform zones (i.e., three zones per degree). We arrived at this particular resolution after performing a convergence study: we performed simulations using progressively finer grids and found that the gross morphodynamical properties of the jet, and the shape of the light curves and spectra have converged (see Section 3.8). Reflecting boundary conditions are imposed at R_0, at the rotational axis and at the equator. Outflow boundary conditions are set at $R_{\rm f}$. The grid is initially filled with a cold, static, dense, uniform medium of density $\rho_{\rm ext} = 8 \times 10^{-14}\,{\rm g\,cm^{-3}}$. With this value of $\rho_{\rm ext}$, the total mass in the computational domain is $\sim 6 M_\odot$. As we pointed out in Section 3.2, this relatively high mass of the environment can only be attained under somewhat extreme conditions, namely, that the progenitor system is embedded in a high-density molecular cloud, and/or that the He star undergoes episodes of violent mass-loss a few years before the merger takes place. In Section 3.4, we will assess more thoroughly how this assumption shapes our main findings by considering lower density environments too.

much smaller values of R_0 than the one we use here would reduce the time step of our models so much to make them computational unfeasible.

[3]Except for the models which are set up with a larger radial grid boundary $R_{\rm f}$ (see Table 3.1), namely M2, G0, S1 and S2, where we use 8500, 8500, 13000 and 18000 radial zones, respectively.

3.3.1.1 CE-shell parameters

Starting at a distance $R_{\rm CE,in} = 4.5 \times 10^{13}\,{\rm cm}$ we place a high-density shell that extends out to $R_{\rm CE,out} = 1.05 \times 10^{14}\,{\rm cm}$ (see Fig. 3.1). This structure is a simplified model of the ejecta produced during the spiralling of the compact object towards the core of the He star. The gap between the inner radial shell boundary and the radial innermost boundary of the computational domain at R_0 is somewhat artificial and its main purpose is to let the jet accelerate smoothly within the computational grid by converting a fraction of its initial thermal energy into kinetic energy (see Section 3.3.1.2). As we will see, this gap has a negligible influence in the resulting light curves, and on the qualitative results we obtain.

Since the CE shell moves at approximately the escape velocity, its speed is negligible compared to that of any relativistic jet. Thus, we are justified in our assumption that the shell is at rest during the several days that the dynamical jet/shell interaction lasts. The CE shell is uniform in density and pressure, and we assume it is mostly composed of ionized hydrogen ($X_{\rm h} = 0.71$). Our model of the CE shell contains a low-density funnel (made of EM) around the symmetry axis with an opening angle of $\theta_{\rm f,in} = 1^\circ$ at $r = R_{\rm CE,in}$. The funnel width grows exponentially up to $\theta_{\rm f,out} = 30^\circ$ at $r = R_{\rm CE,out}$ to reproduce a toroidal-like shape (see Fig. 3.1). In T11 we attributed the X-ray hotspot (observed to be a stationary feature for a few hours after the prompt GRB emission) to the fingerprint of the jet/CE-shell interaction close to the radial innermost boundary of the shell. For such a X-ray hotspot, a fixed size of a few $\sim 10^{11}\,{\rm cm}$ would correspond to the transversal radius of the funnel until it is ablated by the jet beam. With the choice of $R_{\rm CE,in}$ and $\theta_{\rm f,in}$ given above, the minimum cross-sectional radius of the funnel is $R_{\rm CE,in} \sin\theta_{\rm f,in} \sim 8 \times 10^{11}\,{\rm cm}$. This is somewhat larger than the size of the X-ray hotspot inferred from observational fits. This means that our models will not reproduce the observational signature of the X-ray hotspot very well, since we lack the appropriate numerical resolution (especially in the transversal direction; see Section 3.5.2).

For the CE-shell density, we take the value $\rho_{\rm CE,sh} = 1.2 \times 10^{-10}\,{\rm g\,cm^{-3}}$, so that $\rho_{\rm CE,sh} = 1500\rho_{\rm ext}$ and $p_{\rm CE,sh}/\rho_{\rm CE,sh} \approx 6.7 \times 10^{-9} c^2$ (c being the speed of

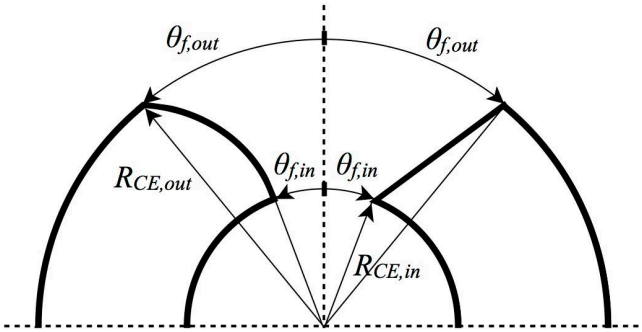

Figure 3.1: Different geometries considered for the CE-shell model: toroidal-like (left) and linear funnel (right). The funnel extends from $\theta_{\rm f,in}$ to $\theta_{\rm f,out}$ (measured, from the rotational axis of the system) in the angular direction, and from $R_{\rm CE,in}$ to $R_{\rm CE,out}$ in the radial direction.

light in vacuum). This density corresponds to an ejecta mass $\sim 0.26\,M_\odot$. The mass of the CE shell is linked to the mass and metallicity of the secondary star in the binary. However, we do not have exact values for the mass ejection in systems composed of a compact binary and a massive star undergoing to CE phase. From the models of Zhang & Fryer (2001) it is difficult to estimate the mass ejected from the system beyond a few 10^{11} cm. More massive secondary stars will have larger hydrogen envelopes, which tend to be less gravitationally bound. This means that if the secondary is very massive, one shall expect a large mass in the CE shell. For instance, Terman, Taam & Hernquist (1995), who simulate systems with companions of 16 and 24 $M_\odot$ (with a poor numerical resolution), show that most of the CE shell is ejected during the later spiral-in phase. Nevertheless, it is not unlikely that a sizable fraction of the hydrogen envelope is ejected before the CE-shell phase begins. In this case, the amount of mass left on top of the He core will be the most gravitationally bound part of the envelope and the fraction of such mass tidally ejected could be relatively modest. After an extended numerical experimentation, we consider here relatively low reference values of the CE-shell mass (see Section 3.4.2.3).

The pressure in the circumburst medium and in the CE shell is uniform ($p_{\rm ext} = p_{\rm CE,sh}$) and we set it low enough to assure that the plasma is cold (non-

relativistic) and has negligible influence on the jet dynamics during the initial 5 d of evolution. We choose $p_{\rm ext}/\rho_{\rm ext} = 10^{-5}c^2$. At later times the pressure in the cavity blown by the jet decreases until it matches that of the EM. From that point on, the influence of the EM pressure cannot be neglected, but our simulations are stopped well before such pressure matching happens.

We point out here that, in contrast to Badjin, Blinnikov & Postnov (2013), who apply a sophisticated radiation transport code to the purpose of estimating the thermal signature of the interaction of both afterglow ejecta and of the prompt radiation emitted by the afterglow ejecta with massive structures in the EM, our shell density ($n_{\rm CE,sh} \sim 10^{14}\,{\rm cm}^{-3}$) is much larger than theirs ($n \sim 10^{10}\,{\rm cm}^{-3}$), and the inner shell radius of our models ($R_{\rm CE,in} = 4.5 \times 10^{13}\,{\rm cm}$) is much smaller than that of Badjin et al. ($\simeq 10^{16}\,{\rm cm}$), resulting in rather different physical conditions in the massive shell. In addition, we set the ratio $p_{\rm CE,sh}/(\rho_{\rm CE,sh}c^2)$ such that the temperature of the shell is above $10^4\,{\rm K}$, which allow us to avoid dealing with the possible hydrogen ionization processes in the shell (a microphysical effect which is considered by Badjin et al. 2013).

3.3.1.2 Jet parameters

For the RM, we have chosen a jet opening angle of $\theta_{\rm j} = 17^\circ$ (i.e. $\theta_{\rm j} \gg \theta_{\rm f,in}$), ensuring that the beam of the jet spans a wedge wider than the funnel when it hits the innermost radial boundary of the CE shell. The jet has an initial Lorentz factor $\Gamma_i = 80$, and its specific enthalpy is set to $h_{\rm i} = 5$, so that it can potentially accelerate to an asymptotic Lorentz factor $\Gamma_\infty \approx 400$, by virtue of the relativistic Bernoulli's law. Indeed, we set up the inner 'gap' between the CE shell and the jet injection nozzle (see previous section) for numerical convenience. In this way, we let the jet speed up smoothly and within the grid to Lorentz factors above 100 before it collides with the CE shell. In order to set a reference value for the total jet energy we consider that it is constrained by the observed lower bound of $E_{\rm iso,\gamma+X} > 1.2 \times 10^{52}\,{\rm erg}$ (L14). The isotropic equivalent total energy of the jet will be larger than this value, since we do not exactly know the radiative efficiency in gamma- and X-rays of the jet ($\epsilon_{\rm R}$), namely, $E_{\rm iso,\gamma+X} = \epsilon_{\rm R} E_{\rm iso}$. We choose $E_{\rm iso} = 4 \times 10^{53}\,{\rm erg}$

Table 3.1: Summary of the most important properties that define the different hydrodynamic models in this work. The equivalent isotropic energy is expressed in units of 10^{53} erg ($E_{\rm iso,53}$). The rest-mass density contrast $\rho_{\rm CE,sh}/\rho_{\rm ext}$ specified in the third row, refers to the innermost radius ($R_{\rm CE,in}$) of the CE shell. The row 'Geometry' refers to the geometrical shape of the CE shell, and models where the shell has a toroidal shape are annotated with 'T', and those in which the funnel are linear with 'L'. We indicate in bold which parameter of each model is different from RM. We list the innermost radius of the CE shell in units of 10^{13} cm ($R_{\rm CE,in,13}$). In the penultimate row, models with a uniform EM are annotated with 'U' ('U1' denotes a density $\rho_{\rm ext} = 8 \times 10^{-14}\,{\rm g\,cm^{-3}}$ and 'U2' a density $\rho_{\rm ext} = 8 \times 10^{-15}\,{\rm g\,cm^{-3}}$), and models with a stratified medium with 'S'. In the last row, we list the outermost radius of our computational domain in units of 10^{15} cm ($R_{\rm f,15}$).

Model	RM	T14	T20	E53	D2	D3	GS	G2	G3	M2	G0	S1	S2
$\theta_{\rm j}$	17°	**14°**	**20°**	17°	17°	17°	17°	17°	17°	17°	17°	17°	17°
$E_{\rm iso,53}$	4	4	4	**2**	4	4	4	4	4	4	4	4	4
$\rho_{\rm CE,sh}/\rho_{\rm ext}$	1500	1500	1500	1500	**817**	**15000**	**4304**	1500	1500	**15000**	**15000**	1500	1500
Geometry	T	T	T	T	T	T	**T**[a]	**L**	T	T	T	T	T
$\theta_{\rm f,out}$	30°	30°	30°	30°	30°	30°	30°	30°	**15°**	30°	30°	30°	30°
$R_{\rm CE,in,13}$	4.5	4.5	4.5	4.5	4.5	4.5	4.5	4.5	4.5	4.5	**3**	4.5	4.5
Ext. medium	U1	U1	U1	U1	U1	U1	U1	U1	U1	**U2**[b]	**U2**[b]	**S**[c]	**S**[d]
$R_{\rm f,15}$	3.27	3.27	3.27	3.27	3.27	3.27	3.27	3.27	3.27	**5.13**	**5.13**	**7.83**	**10.83**

[a] In model GS, the CE-shell rest-mass density and pressure are not uniform but decay with r^{-2}.

[b] In the models M2 and G0, the pressure in the EM and CE shell is $p_{\rm ext}/\rho_{\rm ext} = 10^{-4}c^2$.

[c] In model S1, the EM has a rest-mass density and pressure that decay with r^{-1}.

[d] In model S2, the EM has a rest-mass density and pressure that decay with r^{-2}.

for our reference model. This means that our reference jet model has a true energy $E_{\rm j} = E_{\rm iso}(1-\cos\theta_{\rm j})/2 = 8.7\times10^{51}\,{\rm erg}$, which is a likely fraction of the available rotational energy (few times $10^{52}\,{\rm erg}$) if the central engine is a protomagnetar (Metzger et al. 2011). We also note that this jet energy could be in reach in neutrino-powered jets if the mass of the He core is sufficiently large (Fryer et al. 2013).

On the other hand, observations provide us with a lower bound for the burst duration. We take it as a reference for setting the total injection time, $t_{\rm obs,inj} = 7000\,{\rm s}$ (see L14). Also, as we can see from the fig. 1 of the supplementary material in T11, the jet injection luminosity can be assumed to be constant only up to $t_{\rm obs,1} = 2000\,{\rm s}$, and then decreasing until $t_{\rm obs,2} = t_{\rm obs,inj}$. More specifically, and taking into account that when setting-up a jet a suitable transformation of $t_{\rm obs,1}$ and $t_{\rm obs,2}$ to the laboratory frame (attached to source) shall be done (namely, $t = t_{\rm obs}/(1+z)$), we consider a two-phase injection:[4] (1) constant up to t_1 and (2) variable both in ρ and p (so that p/ρ is constants) with a dependence $t^{-5/3}$, similar to that expected from tidal disruption events, up to t_2. With the known redshift $z = 0.847$ we obtain $t_1 \simeq 1100\,{\rm s}$ and $t_2 \simeq 3800\,{\rm s}$. It is numerically convenient for $t > t_2$ to progressively switch off the jet by reducing both the injected rest-mass density and pressure as $\propto t^{-4}$, rather than switching it abruptly off.

3.3.1.3 Non-thermal microphysical parameters

The non-thermal microphysical parameters for the calculation of the synchrotron emission have been chosen so that the sum of the thermal and the non-thermal emission is consistent with the observations. Behind the forward shock a fraction of the fluid internal energy is carried by relativistic electrons ($\epsilon_{\rm e} = 10^{-3}$) and by stochastic magnetic fields ($\epsilon_B = 10^{-6}$). For a large number of GRB afterglows, observations suggest a value $\epsilon_B \lesssim 10^{-4}$ (Kumar et al. 2012). We choose an even smaller value for ϵ_B for several reasons. On the one hand, ϵ_B can grow from the lower values in the interstellar medium (ISM)

[4] In Aloy et al. (2013) we assumed a unique constant injection interval with duration equal to $t_{\rm inj}$.

to $\epsilon_B \sim 0.1$ due to the amplification of the magnetic field by the two-stream instability (Medvedev & Loeb 1999). However, this field quickly decays away from the shock in a few plasma scales (e.g., Sironi & Spitkovsky 2011), and it is difficult to estimate its value far from the shock front. Sironi & Spitkovsky (2011) find in their PIC models that the far field strength should be of the order of the shocked ISM field strength assuming flux freezing. Provided that our typical grid size is $\sim 10^{11}$–10^{12} cm, over the first post-shock numerical cell the stochastic magnetic field may have decayed to the compressed ISM field values estimated by Sironi & Spitkovsky (2011). Since our ISM is assumed to be unmagnetized, a value $\epsilon_B \sim 10^{-5}$–10^{-6} is a plausible 'average' of ϵ_B in the post-shock state. On the other hand, to be consistent with the assumption that the magnetic field be dynamically negligible (i.e. to be consistent with our fluid dynamical approach), we require that $\epsilon_B < 10^{-2}$ (e.g., Mimica, Aloy & Müller 2007). And, finally, large values of ϵ_B yield very high stochastic magnetic fields ($B_{\rm st} \gtrsim 10^4$ G) that would cause superfast synchrotron cooling of the electrons. Such short cooling time-scales cannot be resolved using our simulations, because we would need to resolve in our explicit hydrodynamic models time-scales which are shorter than the synchrotron cooling time of the electrons contributing to radiation in the observing bands, which is $t_{\rm cool} \propto \epsilon_B^{-3/4}$. For the numerical resolutions employed in this work, the typical time step is $\simeq 10$ s. With the value $\epsilon_B = 10^{-6}$, the cooling time of electrons contributing to the radiation in the X-ray band is $\simeq 500$ s. Increasing ϵ_B by a factor of 100 lowers that cooling time to $\simeq 20$ s. This time-scale could be resolved by the hydrodynamical time resolution of our simulation, but only if we would post-process and record *every* time step. Unfortunately, at present this is not feasible since we would need to record more than 4×10^4 files per 2D model. Of course, if we limit ourselves to the evaluation of the non-thermal flux density at optical frequencies, we could safely consider values $\epsilon_B \lesssim 10^{-3}$. Beyond these technical limitations, ϵ_B could be different for different shocks, but we assume, for simplicity, that it is the same in all cases.

The number of relativistic electrons accelerated by the shock is a fraction, $\zeta_{\rm e} = 0.1$, of the total number of electrons in the pre-shocked state. The power-

Table 3.2: Summary of the non-thermal microphysical parameters that describe the models. For each model, we indicate in bold the parameter that is different from the RM.

Model	RM	P4	P5	P6	EE2	EB5	ZE2	A6
q	2.3	**2.4**	**2.5**	**2.6**	2.3	2.3	2.3	2.3
$\epsilon_{\rm e}/10^{-3}$	1	1	1	1	**10**	1	1	1
$\epsilon_B/10^{-6}$	1	1	1	1	1	**10**	1	1
$\zeta_{\rm e}$	0.1	0.1	0.1	0.1	0.1	0.1	**0.01**	0.1
$a_{\rm acc}$	1	1	1	1	1	1	1	$\mathbf{10^6}$

law index of the electron energy distribution is $q = 2.3$, and the acceleration efficiency parameter, $a_{\rm acc} = 1$ (see Section 2.4.1). We can define an effective fraction of internal energy employed to energize non-thermal electrons, $\epsilon'_{\rm e} = \epsilon_{\rm e}/\zeta_{\rm e}$. With such definition, $\epsilon'_{\rm e} \approx 0.01$, i.e. closer to the 'typical' values of $\epsilon_{\rm e}$ commonly used in other studies in which the $\zeta_{\rm e}$ parameter is absent. A similar parameterization can be found in Bošnjak, Daigne & Dubus (2009).

3.4 Hydrodynamic evolution

In this section, we describe the morphology and the dynamics of the RHD jet simulations performed with MRGENESIS. We first discuss the results for the RM (Section 3.4.1) and then consider variations of the parameters in Section 3.4.2. A summary of the most salient parameters of the models presented here is given in Table 3.1, where also the names of each of the models are listed.

3.4.1 Reference model

In Fig. 3.2, we show four snapshots of the RM evolution. Shortly after the start of the jet injection, within the first few seconds, the jet starts to hit the inner boundary of the CE shell (Fig. 3.2, upper-left panel). As a result a pair of shocks form that rapidly heat the plasma to temperatures of up to $\sim$ few $\times\, 10^6\,$K. The properties of these shocks are not the standard ones

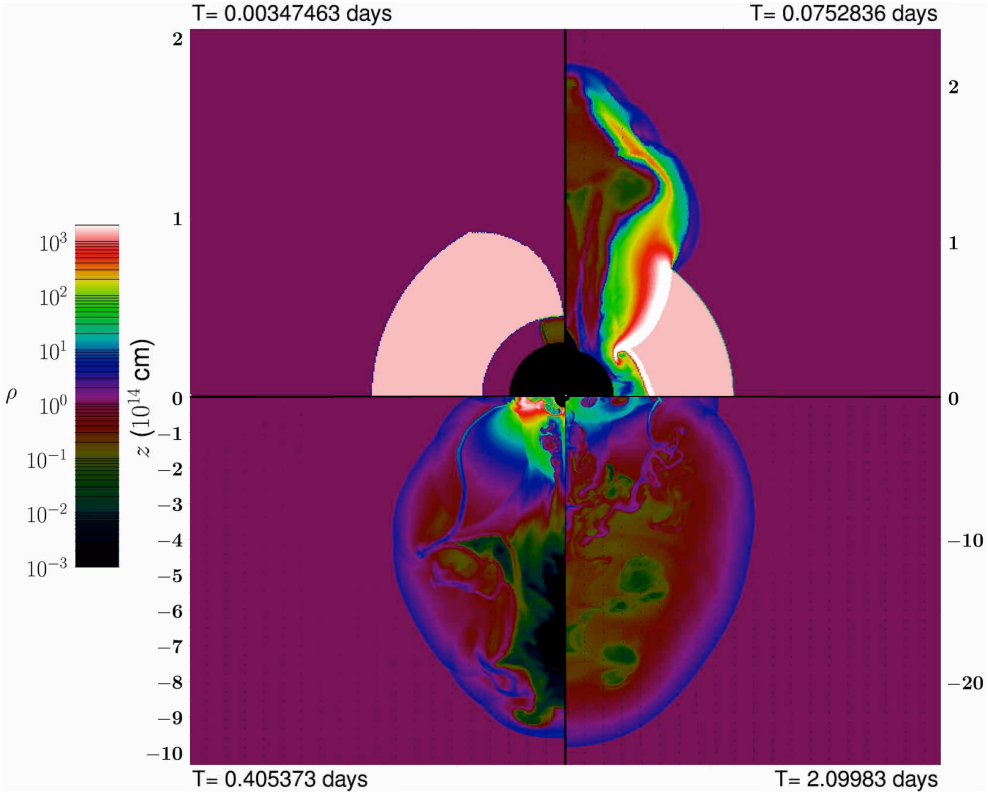

Figure 3.2: Four snapshots of the rest-mass density evolution of the RM. The rest-mass density is normalized to the EM density $\rho_{\rm ext} = 8 \times 10^{-14}\,{\rm g\,cm^{-3}}$. The time displayed in each panel refers to the laboratory frame time. In the upper-left panel, we show the geometry of the shell before the jet impacts it. The upper-right panel shows the jet penetrating the shell. The lower-left panel displays the jet having developed a quasi-spherical bubble after interacting with the shell. Finally, in the lower-right panel it can be seen the self-similar expansion of the hot bubble through the circumburst medium after $\sim 2\,{\rm d}$.

expected for the forward and reverse shocks in relativistic ejecta associated with GRB afterglows. Instead, they are propagating at Newtonian speeds, starting at the funnel walls and moving laterally towards the jet axis. In the process, the shocks are also penetrating the CE shell and moving sideways, in a direction almost perpendicular to the jet propagation and, hence, to the line of sight (the shock can be seen as white shades in Fig. 3.2, upper-right panel).

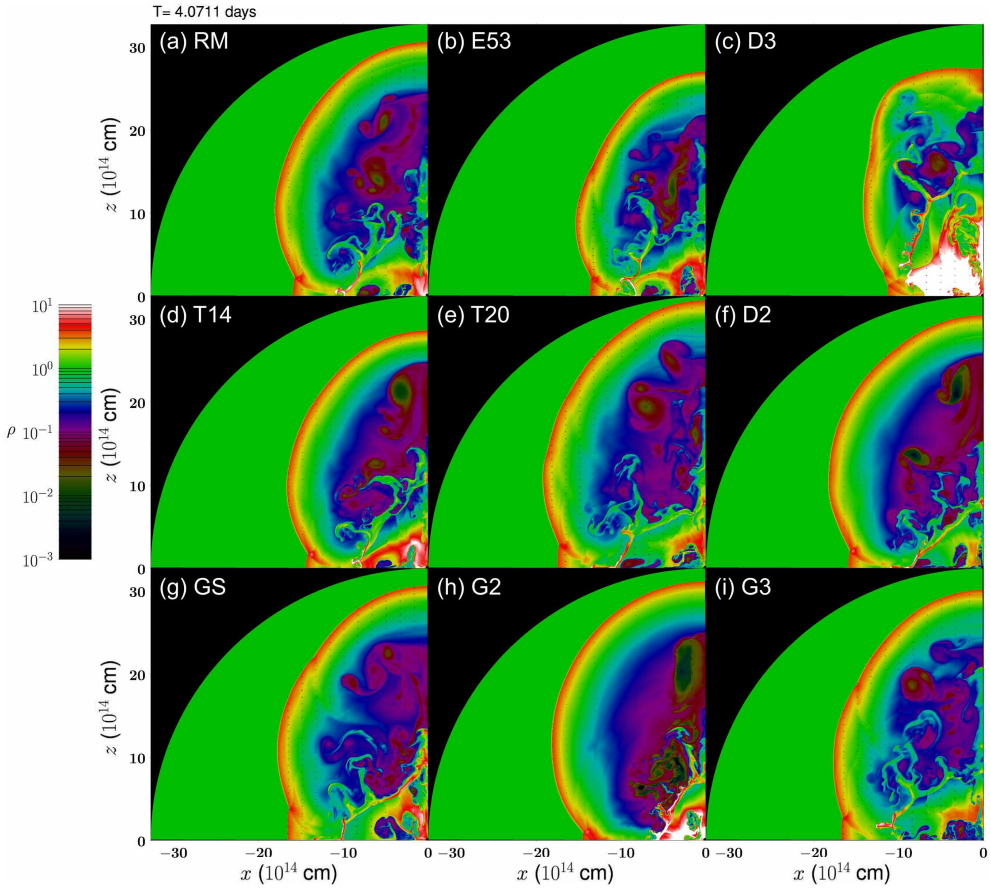

Figure 3.3: Snapshots of the rest-mass density of all the models with a uniform, high-density EM at the end of the computed evolution ($T = 4.0711$ d): (a) RM, (b) E53, (c) D3, (d) T14, (e) T20, (f) D2, (g) GS, (h) G2 and (i) G3 (see Table 3.1). The rest-mass density is in the same units as in Fig. 3.2.

During the time in which we keep the jet injection conditions through the inner boundary of our computational domain, a fraction of the jet close to the axis (its innermost core) flows with a negligible resistance. However, the jet is broader than the narrow CE-shell funnel and, hence, a major fraction of the jet volume impacts on the inner radial edge of the CE shell. Since the CE shell is much denser than the jet, the result of the CE-shell/jet interaction is the jet baryon loading, which quickly (within hours) decelerates it to subrelativistic

speeds. After about 0.1 d, most of the mass of the CE shell originally located in the angular region $[\theta_{\rm f,in}, \theta_{\rm j}]$ is incorporated into the jet beam and surrounding cocoon.

The subsequent jet evolution is determined by the balance between the injected jet energy and the mass ploughed by the cavity blown by the jet from the EM. As we shall see, all models propagating into a uniform circumstellar medium pile up ~ 1–$2\,M_\odot$ of EM and tend to develop a spherical shape in the long term.

3.4.2 Parametric scan

We have presented the RM as a prototype of the evolution of an ultrarelativistic jet piercing a massive shell that results from the ejection of the envelope of the stellar progenitor. In the following, we will show how changes in the assumed parameters of our models shape the resulting dynamics and also we will assess the robustness of the results. Along the way, we will show that the generic long-term evolution of all the models we have explored is such that they behave almost self-similarly. In Table 3.1, we show the parameters of the RM subject to variation in the parametric scan. The rest of the models are produced changing only one or two of the parameters with respect to the RM. On the basis of these results, we will assess the origin of the thermal emission in Section 3.5.

3.4.2.1 Isotropic energy of the jet, $E_{\rm iso}$

We have evolved two models with different isotropic energies $E_{\rm iso} = 4 \times 10^{53}$ (RM, Fig. 3.3a) and 2×10^{53} erg (E53, Fig. 3.3b). The rest of the parameters are the same, especially the jet half-opening angle, $\theta_{\rm j} = 17°$. The size of the bubble blown by the jet is proportional to the equivalent isotropic energy of the models. We see that bubbles in more energetic models propagate faster, reach larger distances, and have a more spherical shape.

In both models (RM and E53) the mass of the CE shell is $0.26 M_\odot$, but the

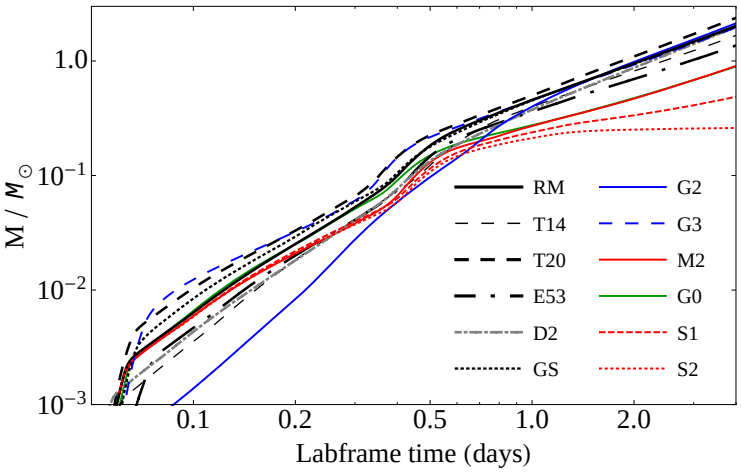

Figure 3.4: Time evolution (in the laboratory frame) of the rest mass enclosed by the bubble blown by each of the models. The mass accounts for the contribution of the Northern and Southern hemispheres.

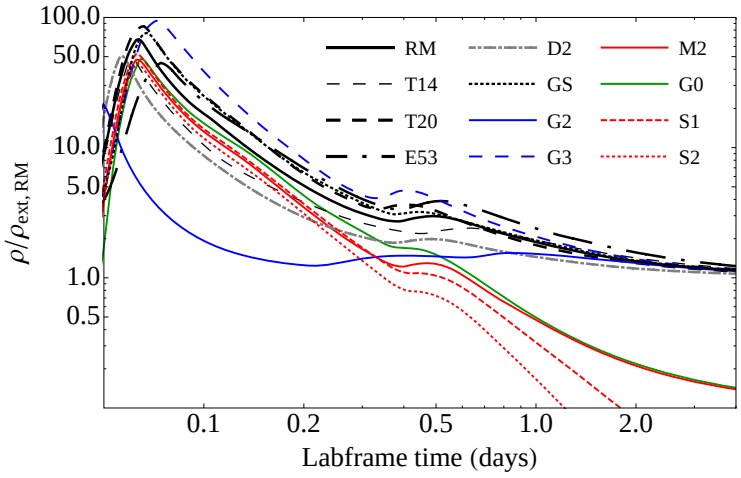

Figure 3.5: Time evolution (in the laboratory frame) of the average bubble density of the bubble blown by each of the models in units of the EM density of the RM ($\rho_{\rm ext,RM} = 8 \times 10^{-14}\,{\rm g\,cm^{-3}}$).

total bubble mass exceeds that value by $\simeq 1$ d (Fig. 3.4).[5] Only a fraction of the

[5]We note that the time axis in Figs 3.4 and 3.5 corresponds to the lab-frame time, i.e.,

rest mass of the bubble comes from the matter dragged from the jet/CE-shell interaction region during the early phases of the evolution. Indeed, all models end up fully ablating the CE shell, which is incorporated into the bubble. A major fraction of the mass, however, comes from the EM which is swept up by the external shock and piles up along the bubble surface. The mass enclosed by the bubble grows with the energy of the jet. More energetic models expand faster and, as a consequence, sweep up matter of the EM more rapidly. After about 0.5 d, the rate of mass growth decreases. This is the time at which a major fraction of the CE shell is ablated by the jet.

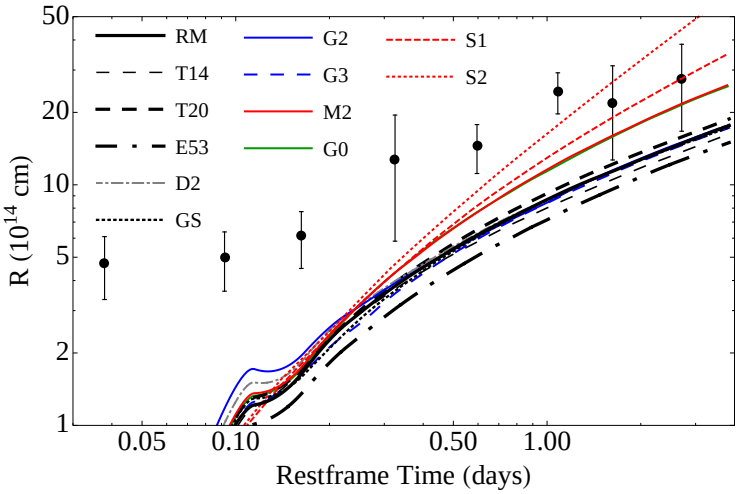

Figure 3.6: Time evolution (in the rest frame of the source) of the transversal radius of different numerical models. The circles with error bars display the data obtained in T11 from fits to the observed flux assuming a simple BB spherical expansion of an emitting source. To convert the values of the radius to the rest frame, we employ a redshift $z = 0.847$. Model G0 lies almost exactly below model M2.

Because of its more rapid expansion, the average density of the bubble in

the time of an observer attached to the source. This time should not be confused with the 'rest-frame' observer time shown in, e.g., Fig. 3.6 which is the time, $t_{\rm det}$, measured by a distant observer. That observer receives the information from the source by means of photons, but is assumed to be sufficiently close so that cosmological effects are unimportant. See the precise definition of $t_{\rm det}$ in Section 3.5.

RM is smaller than in model E53 (compare the dash-dotted and solid black lines in Fig. 3.5). Thus, the average density of the bubble becomes smaller as we increase $E_{\rm iso}$. We also note that the generic evolution of the average density displays a fast rise up to a maximum at times $\lesssim 2\,{\rm h}$, and then a slower decrease. The time at which the maximum average density is reached increases as $E_{\rm iso}$ decreases. This behaviour is connected to the fact that the jet/CE-shell interaction is stronger initially, when the jet is more relativistic and is either still being injected at constant rate or decaying as $t^{-5/3}$ (note that $t_1 = 1100\,{\rm s}$ and $t_2 = 3800\,{\rm s}$; Section 3.3.1.2). Hence, mass from the CE shell is quickly incorporated into the jet cocoon, causing the average bubble density to grow as well. Soon after the moment at which jet injection power is decreased ($t_2 = 3800\,{\rm s}$), the rate of mass loading of the bubble from the CE shell decreases and produces the slow decline observed for $t \gtrsim 0.1\,{\rm d}$.

We have also computed the time evolution of the cross-sectional radius of the bubble and found that both models display a similar transversal expansion if the EM is uniform. For reference in Fig. 3.6 we also display the evolution of the cross-sectional radius obtained from the simple model of T11, in which the observed flux is fit to an expanding BB with radius R and effective temperature T. As we shall demonstrate in Section 3.5, in our case most of the thermal emission is originated from a relatively small region compared with the cross-sectional radius of the bubble. In contrast, the results of T11 assume that the size of the emitting region is that of the expanding BB fit. Our models provide a typical size (estimated by its cross-sectional radius) which is similar to (but typically smaller than) that obtained with the (over) simplified physical model of T11 for the emitting region.

3.4.2.2 Half-opening angle, $\theta_{\rm j}$

Fixing the isotropic equivalent jet energy to the value in the RM, $E_{\rm iso} = 4 \times 10^{53}\,{\rm erg}$, we have varied the jet half-opening angle, and considered three cases for $\theta_{\rm j}$: 14° (T14, Fig. 3.3d), 17° (RM, Fig. 3.3a) and 20° (T20, Fig. 3.3e). In all three cases, we set up the jet injection half-opening angles to be much wider than the innermost half-opening angle of the funnel ($\theta_{\rm j} \gg \theta_{\rm f,in} = 1°$;

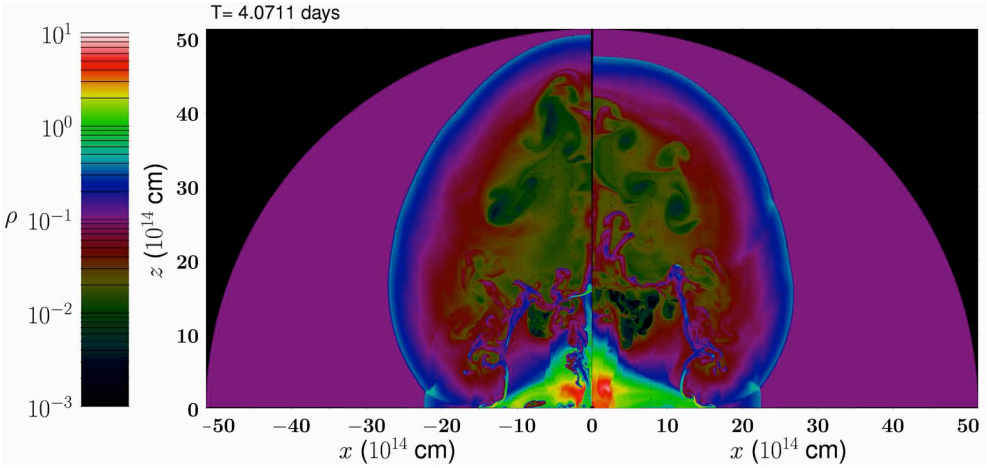

Figure 3.7: Final distribution of the rest-mass density for the models with uniform, low-density EM ($\rho_{\rm ext} = 8 \times 10^{-15}$ g cm^{-3}). Left-hand panel: model M2. Right-hand panel: model G0 (same as M2 but without the 'gap' between R_0 and $R_{\rm CE,in}$). The rest-mass density is in the same units as in Fig. 3.2.

see Fig. 3.1). This is a basic ingredient of our model, since a very narrow jet would minimize the interaction with the CE shell, while an excessively broad jet would be incompatible both with the theoretical expectations of the jet half-opening angle and with the typical estimates based on observations connecting light-curve breaks with the jet angular size.

In order to understand how the variation of $\theta_{\rm j}$ affects the dynamics, we first note that the true jet energy, $E_{\rm j}$, depends on $E_{\rm iso}$ and $\theta_{\rm j}$ so that by changing the jet injection half-opening angle the true injected jet energy is modified, although the amount of energy per unit solid angle remains constant. We note that the true jet energy of model T20 ($E_{\rm j}$(T20) $= 1.21 \times 10^{52}$ erg) is the largest among of all our models. We can appreciate that bubbles in models with larger jet half-opening angles have a larger radius in both longitudinal and transversal direction, and a more oblate structure. This is a consequence of increasing the jet energy as $\theta_{\rm j}$ is increased, since then the jet/CE-shell interaction region is larger, and it results in more massive bubbles (Fig. 3.4).

Compared with the evolution of jets with smaller opening angles we observe

that the mass growth rate of model T20 is qualitatively similar to that of the T14 and the RM models, but the transition to a smaller mass growth rate happens earlier. Indeed, the smaller the jet half-opening angle, the later such transition happens (Fig. 3.4). Coupled to this transition, we can see that the bump in the average rest-mass density of the bubble (around 0.4–0.7 d; Fig. 3.5) happens later for smaller values of $\theta_{\rm j}$.

The cross-sectional radii of models with increasing jet half-opening angles are very similar (Fig. 3.6). However, in the long term, jets with larger half-opening angles exhibit slightly larger cross-sectional radii. This is in large part due to the larger true jet energy of models with larger $\theta_{\rm j}$.

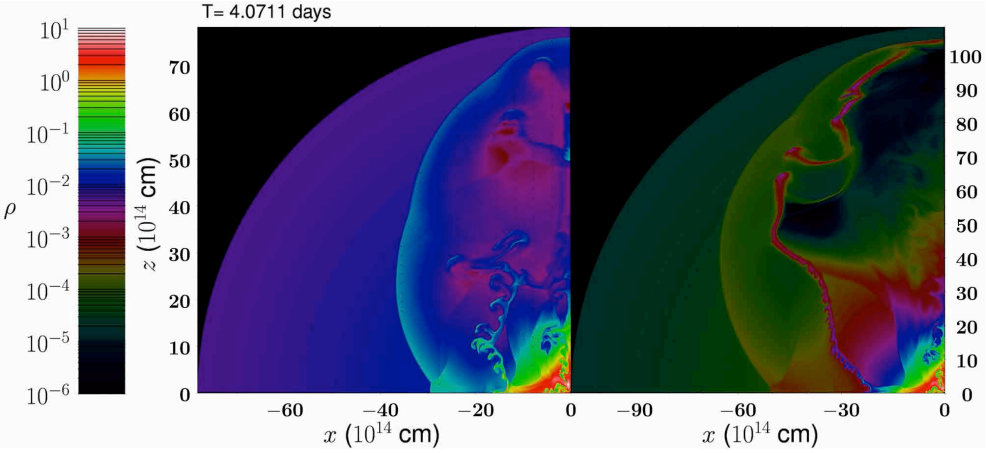

Figure 3.8: Final distribution of the rest-mass density for the models with stratified EM. Left- (right)-hand panel: model S1 (S2), with a radial distribution of rest-mass density and pressure proportional to r^{-1} (r^{-2}). Note the difference in the z-scales shown to the left and to the right of the corresponding panels, and the difference with respect to Fig. 3.3 in the range displayed by the colour palette. The rest-mass density is in the same units as in Fig. 3.2.

3.4.2.3 CE-shell density contrast with respect to the external medium, $\rho_{\rm CE,sh}/\rho_{\rm ext}$

The ratio of rest-mass density of the CE shell to the EM density also plays an important role in shaping the dynamics. We have tested three different

CE-shell densities, $\rho_{\rm CE,sh}/\rho_{\rm ext} = 1500$ (RM, Fig. 3.3a), 817 (D2, Fig. 3.3f) and 15000 (D3, Fig. 3.3c) corresponding to masses of $M_{\rm CE,sh} \sim 0.26$, 0.14, and $2.6 M_\odot$, respectively. As we shall see in Section 3.5, the model with the most massive CE shell (D3), yields a thermal signature incompatible with the observations and, thus, we will not consider it in this section for further discussion.

In the D2 model, the bubble is less dense than in the RM and also less dense than most of the rest of the models in this parametric study (Fig. 3.5). Since the volume of the bubble blown by the jet of model D2 is quite similar to that of the RM, its bubble mass is also smaller (Fig. 3.4). As we have seen in the RM, the mass of the bubble includes that of the swept EM as well as that accumulated during the CE-shell/jet interaction. The former contribution is roughly similar in the RM and in the D2 model. However, the contribution to the bubble mass from the shell is substantially smaller, because of the lower CE-shell rest-mass density. In Fig. 3.3(b), we can observe that the RM displays a larger density in the central part of the bubble (close to the axis and to the origin, extending for about 10^{15} cm) than model D2 (panel (f)).

Since the mass incorporated from the CE shell is smaller in model D2, it initially ($t_{\rm det} \lesssim 0.3$ d) expands faster than the RM (Fig. 3.6). After that, the cross-sectional radius evolution is dominated by the mass incorporated to the cavity from the EM in relation to the energy supplied by the jet to the cavity (which is the same in both models) and, hence, the cross-sectional size of models D2 and RM become almost indistinguishable.

For completeness, we have tested a simple stratification of the CE shell in which the rest-mass density and pressure decrease as $\propto r^{-2}$ (model GS, Fig. 3.3g). We have set the rest-mass density $\rho_{\rm CE,sh,0}/\rho_{\rm ext} = 4304$ at $r = R_{\rm CE,in}$ in order to have, approximately, the same mass in the CE shell as in RM. The pressure at $r = R_{\rm CE,in}$ is the same as in the EM, i.e., $p_{\rm CE,sh,0} = p_{\rm ext} = 10^{-5} c^2 \rho_{\rm ext}$. The global hydrodynamical properties like the bubble mass (Fig. 3.4), average cavity density (Fig. 3.5), and cross-sectional radius (Fig. 3.6) are very similar in this model to those of the RM. However, as we shall see in Section 3.5.1, the stratification of the CE shell modifies jet/CE-shell interaction

and imprints substantial changes in the computed thermal emission.

3.4.2.4 External medium

In the previous sections, we have always considered a uniform EM (i.e., isopycnic and isobaric). However, the environment of massive stars is certainly more complicated than in our simple model (see Section 3.2). Such complex environments can also have rather complicated density profiles. A suitable simplification that helps us disentangling the many different effects that show up in the dynamics of our jets is to consider first that the EM is a uniform medium. Later, we will parametrize the EM assuming that the rest-mass density decays as a power law of the distance.

The fiducial value of $\rho_{\rm ext}$ for our RM, yields an EM mass of $\sim 6 M_\odot$ within the numerical domain. This value is a balance between what we realistically expect in the environment around the secondary star of the merger (likely, a lower value of the EM mass; Section 3.2) and the numerical difficulty posed by the very large density jump between the CE shell and the EM, together with very low pressure-to-density ratios in the RM ($p_{\rm ext}/\rho_{\rm ext} = 10^{-5} c^2$). In order to assess the effects on the dynamics and on the light curves of a less dense environment we have reduced the density of the EM by one order of magnitude in models M2 and G0 ($\rho_{\rm ext} = 8 \times 10^{-15}\,{\rm g\,cm^{-3}}$; Table 3.1). To easy the numerical difficulty of reducing the EM density, while keeping the same mass in the CE shell (which means that the density contrast $\rho_{\rm CE,sh}/\rho_{\rm ext}$ is 10 times larger in the M2 and G0 models than in the RM), we increase the ratio pressure-to-rest-mass density everywhere in the domain (i.e. for models M2 and G0 we have $p_{\rm ext}/\rho_{\rm ext} = 10^{-4} c^2$). The only difference between both models is that in G0 we have extended the inner radius of the CE shell until the innermost boundary at R_0. Therefore, the cavity blown by the jet in model M2 has a more prolate shape while the cavity of model G0 is a bit more spherical since the jet has to pull the extra initial mass where the 'gap' was located. As we can see in Fig. 3.7, the jets of models M2 and G0 are able to reach larger distances in the same evolutionary time than the jet of the RM. Thus, in order to properly compute the late light curves and spectra, we have

extended the computational domain up to $R_{\rm f} = 5.13 \times 10^{15}\,{\rm cm}$, so that the EM in models M2 and G0 encloses a mass of $2.3 M_\odot$. We note that up to the same outer boundary than in the RM, the mass of the EM of both models is only of $\sim 0.6 M_\odot$.

The evolution of mass ploughed by the bubble (red solid line in Fig. 3.4) is similar to that of RM until 0.5 d, where the evolution is still dominated by the interaction with the CE shell. The average rest-mass density (Fig. 3.5) also displays a similar behaviour until this time and takes similar values as that RM. At longer times the average density becomes obviously smaller by a factor of ~ 10, as expected because of the 10 times smaller EM density of model M2 with respect to the RM. The cavity blown by the jet in the M2 model is not only longer, but also has a factor of ~ 2 larger transversal radius than the RM (Fig. 3.6). As a concluding remark in the case of models with uniform EM, and as it is expected, a smaller EM rest mass modifies the long-term evolution (i.e. the evolution after about 0.5 d), but the initial CE-shell/jet interaction does not change appreciably. We advance that a uniform medium cannot be extended to arbitrarily large distances from the progenitor since it would bring an unrealistically large mass in the EM.

We now turn to models with a non-uniform EM and consider two simple parameterizations of stratified external environments. We assume that the rest-mass density and pressure decrease with the distance as r^{-1} (model S1) or r^{-2} (model S2) from $r = R_{\rm CE,in}$. Below the CE shell, i.e. in the region $R_0 < r < R_{\rm CE,in}$ we impose a uniform medium with the same rest-mass density as the in the uniform ambient medium models, but with a larger pressure $p_{\rm ext}/\rho_{\rm ext} = 10^{-3} c^2$. The pressure in the CE shell is the same as in the RM. We note that, differently from De Colle et al. (2012), with this initialization, any potential jet break (which would occur if the CE shell was absent), would happen at very different distances depending on the rest-mass density gradient.

Jets propagating in wind-like media tend to develop more elongated cavities than the same jets moving through a uniform, high-density medium in the long term (Fig. 3.8). Likewise, the sideways expansion is also larger compared to jets propagating in a isopycnic/isobaric medium (Fig. 3.6). Since the interaction

at early times is determined mostly by the conditions in the CE shell, the average rest-mass density and total mass of the jet approaches the RM values until $\sim 0.4\,\mathrm{d}$. But, as the jet proceeds through the stratified medium, both quantities differ at later times (see Figs. 3.4 and 3.5). The mass of the bubble grows slowly and its average density, which decreases as t^{-2} in the S1 model and as t^{-3} in the S2 model, is also smaller compared with the RM.

3.4.3 Long-term evolution

In the long term, all models moving in a uniform, high-density ambient medium develop a quasi-spherical cavity (Fig. 3.3). However, a simple (spherically symmetric) Blandford–McKee blastwave is not adequate to describe the dynamics during the first days of evolution, and the reason is the jet/shell interaction. Since both the EM and the CE shell are much denser than the jet, it develops a mildly relativistic bow (forward) shock and a non-relativistic reverse shock. The jet/shell interaction causes the jet to decelerate and produce a 'hot bubble' in which the original jet is disrupted. Even if this kind of scenario would yield a typical afterglow, no signs of jet break would have been observed, since there is no jet anymore.

After an initial phase dominated by the CE-shell/jet interaction dynamics (lasting for $\sim 1\,\mathrm{d}$), the cross-sectional diameter of the bubble expands faster than the longitudinal jet dimension. This happens when the cavities travel a distance of the order of the Sedov length,

$$l_{\mathrm{Sedov}} = \left(\frac{(17-4k)E_{\mathrm{j}}}{8\pi\rho_{\mathrm{ext}} R_{CE,in}^{k} c^2} \right)^{1/(3-k)} , \tag{3.1}$$

(k being the index of the power-law decay of the rest-mass density) for each model.[6] In Fig. 3.9, we quantify the aspect ratio of each model, defined as the ratio between the cross-sectional diameter and the longitudinal (along the z-axis) jet length. After ~ 1 d and until 4 d the aspect ratio grows, becoming $\simeq 0.5$–0.6. Extrapolating the rate of increase of the aspect ratio between 1

[6] For the RM and most of our models endowed with a uniform, high-density medium the Sedov length is $\sim 4 \times 10^{14}\,\mathrm{cm}$.

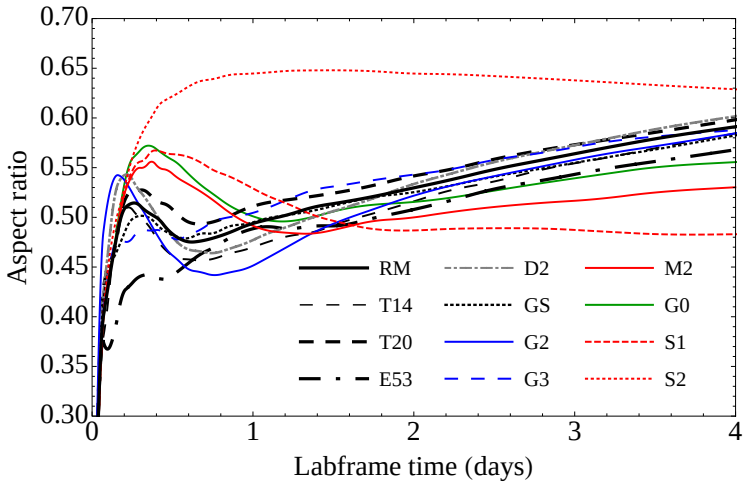

Figure 3.9: Evolution of the aspect ratio of different models in the laboratory time. This aspect ratio is defined as the ratio between the cross-sectional diameter and the longitudinal (along the z-axis and including the Northern and Southern hemispheres) extent of the jet.

and 4 d, we estimate that our models propagating in a uniform, high-density circumburst medium will become spherical (aspect ratio equals one) in approximately 12 to 18 d. This estimate is rather robust, since models enter a quasi-self-similar regime after $\simeq 1\,\mathrm{d}$. The rate of growth of the aspect ratio $\simeq 0.03\,\mathrm{units\,d^{-1}}$ is a generic feature, only weakly dependent on the jet parameters and properties of the CE shell. Thus, we find that this transition to sphericity roughly coincides with the time at which T11 find that a SN contribution is needed to explain the flattening of the light curves in the optical bands. Since the EM is less massive in models M2 and G0, the transition to sphericity is delayed and the shape of the blown cavity displays a slightly smaller aspect ratio than in other uniform models with larger EM rest-mass density.

In contrast to the long-term evolution of jets propagating in a uniform medium, jets travelling along a stratified EM tend to develop prolate cavities. This feature is reflected in the decrease after 0.5 d of the aspect ratio (Fig. 3.9). Eventually, the aspect ratio tends to settle to a roughly uniform value, since

the jet encounters less resistance in all directions as it expands across the EM. We also note that the S2 model experiences a rapid transversal expansion after 1 d associated with the rapid initial decrease of rest-mass density and pressure in the EM. In case the evolution could be extrapolated forward in time, these cavities will take much longer time to become spherical.

3.5 Origin of the thermal emission

In this section, we compute the thermal signature of a number of models (and specifically of the RM) with the goal of uncovering the provenance of the thermal emission. To do so, we post-process the output of our RHD simulations (using MRGENESIS) with our radiative transport code SPEV. Throughout the computational domain we assume that only fluid elements above a certain threshold in temperature, $T_{\rm th} = 25000\,{\rm K}$, or above a certain threshold in velocity, $v_{\rm th} \simeq 0.00045c$, emit thermal radiation. At least one of these conditions is fulfilled in every fluid element inside the relativistic jet and inside the interaction region between the jet and the CE shell. However, imposing the former thresholds, we avoid computing the emission from the *cold* CE shell itself, where $T_{\rm CE,sh} \sim 19900\,{\rm K} < T_{\rm th}$. The velocity threshold, avoids including the absorption of the EM, which we have ignored here for simplicity. The CE shell is, however, very important because of its absorption properties. In the density/temperature conditions of the CE shell, it acts as a Thomson absorber, having a grey absorption coefficient $\alpha_{\rm t} = 0.2(1 + X_{\rm h})\rho\ {\rm cm}^{-1}$.

Using SPEV we can produce light curves and spectra accounting for or neglecting the absorption processes. We will refer to these two modes of computing the spectral properties of our models as 'thick' or 'thin', respectively. Comparing the thin and thick spectral properties we are able to better understand when the systems at hand become optically thin and where the emission and absorption dominantly take place.

For the RM (Fig. 3.10), we observe that the system is optically thick until about ~ 1 d after the burst[7] in the $W2$ band, and until ~ 2 d in the r band.

[7]Note that if the dashed and continuous lines overlap in Fig. 3.10 it means that absorption

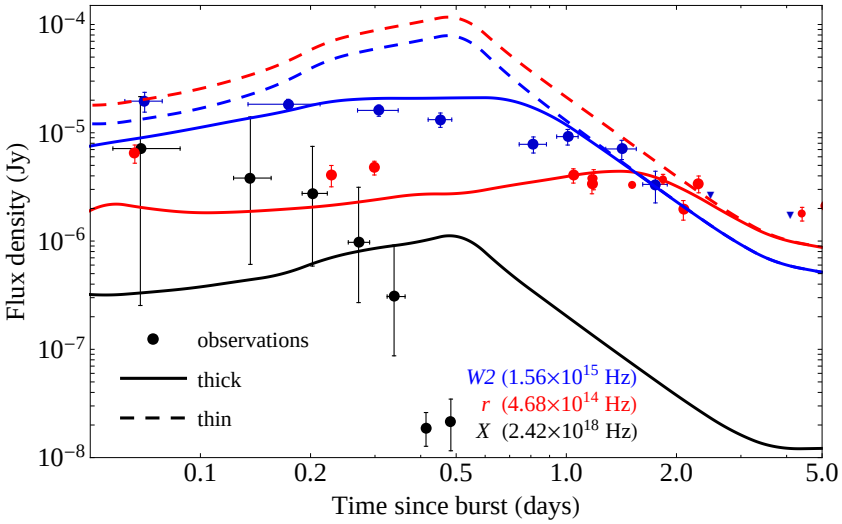

Figure 3.10: Light curves for the RM considering only the (thermal) bremsstrahlung-BB contribution. Both optically thick (solid lines) and thin (dashed lines) light curves are plotted, to better illustrate the transition from optically thick to optically thin emission. For the X-ray band (black lines), the optically thin and thick light curves coincide, since the X-ray emitting region is optically thin. For the representation of the X-ray data, we have clustered the data of each of the XRT observing cycles into a single point, with error bars showing the data dispersion.

In the X-ray band, the system is optically thin from the beginning of the observing time (note that the dashed black line overlaps with the solid black line in Fig. 3.10). It is evident that the computed thermal emission in the X-ray band peaks too late (at about 0.5 d) compared with the observational data, though the flux decline after the emission peak happens at a rate compatible with the observed data. As we will show (Section 3.5.1), these two facts are connected to a large extent to the *assumed* geometry and rest-mass distribution of the CE shell. Since the goal of this work is not obtaining a *perfect* fit of the data but understanding the basic properties of the system, we have not tuned the geometry of the channel to accurately describe the observations. Instead, we point out the qualitative fact that the time at which we find the maximum

does not influence the observed emission, i.e., the medium has become optically thin.

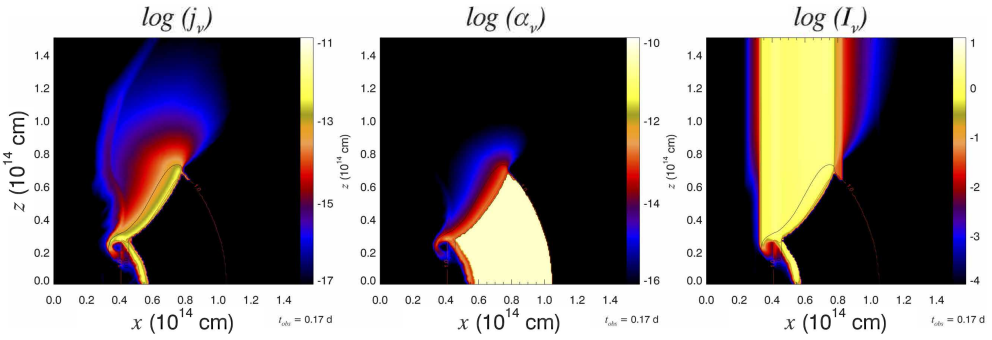

Figure 3.11: Emission, j_ν, (left) and absorption, α_ν, (centre) coefficients and evolution of the specific intensity, I_ν (right) along the line of sight. The observer is located in the vertical direction (towards the top of the page) at a viewing angle $\theta_{\rm obs} = 0°$. The emission is computed in the $W2$ band for band free–free (thermal) bremsstrahlung process, at an observational time $t_{\rm obs} = 0.17\,{\rm d}$. The units of j_ν, α_ν and I_ν are given the CGS system (see Section 2.3.2 for details). From the figures, one can realize that the main contribution of the thermal radiation comes from the interaction region jet/CE-shell, located at a distance from the symmetry axis of $\simeq 3 \times 10^{13}\,{\rm cm}$ and extending to $\simeq 8 \times 10^{13}\,{\rm cm}$. This emission region coincides with the locus of the section of the CE shell shocked by the relativistic jet.

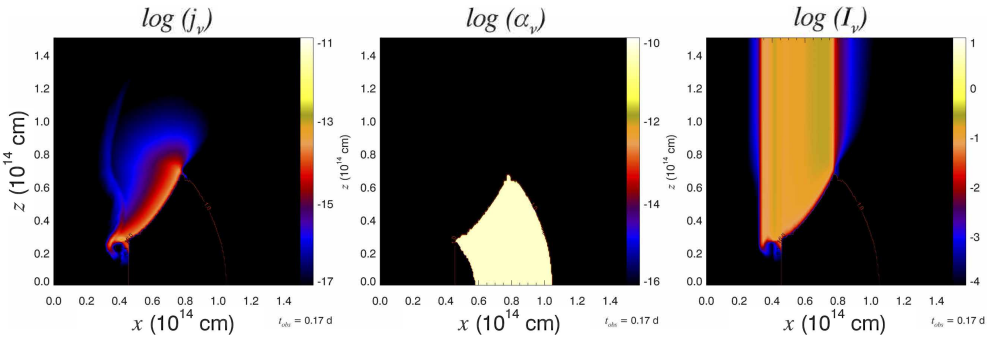

Figure 3.12: Same as Fig. 3.11 but in the X-ray band. The emissivity (left panel) and the specific intensity (right panel) have to be corrected with a factor of ~ 3 (see App. B for details).

flux density depends on frequency: the larger the frequency the earlier the flux density peak happens.

When the system becomes optically thin at all optical frequencies after

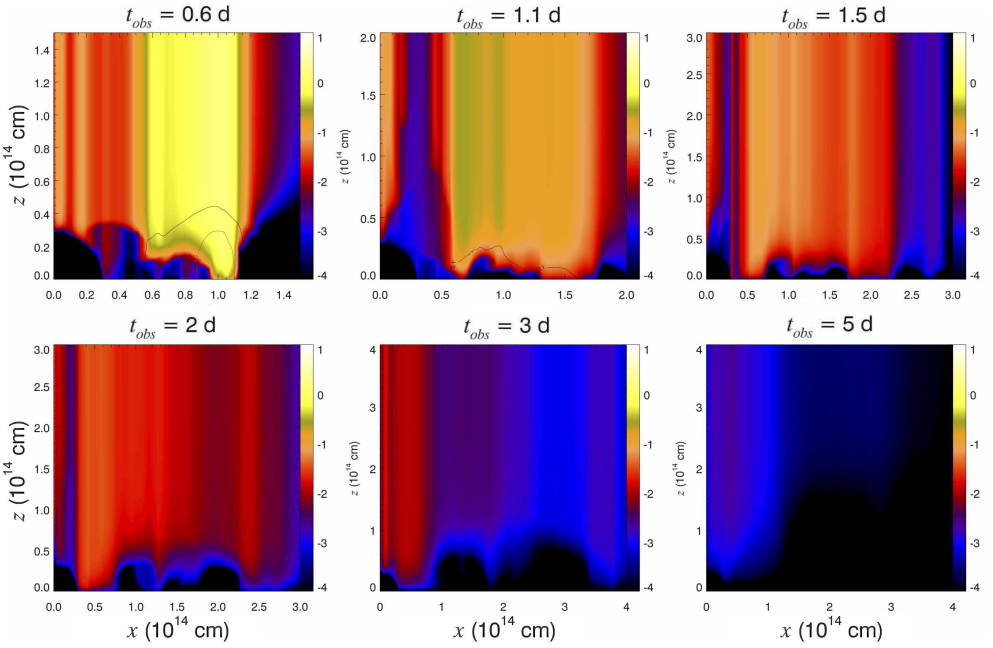

Figure 3.13: Evolution of the specific intensity, I_ν, in the $W2$ band (same as the right-hand panel in Fig. 3.11). The image is focused on the jet/CE-shell interaction region. Note that the transition from optically thick to optically thin at $\sim$ 1.5–2 d (top-right and bottom-left panels) is due to the ablation of the CE shell, which is absent after $\sim$ 2 d (bottom panels). The observational times are provided above of each of the panels.

$\sim$ 1.5–2 d, the thermal spectrum is inverted and we observe a larger flux in the r band than in the $W2$ band, i.e., the initially blue system becomes red as the observations in T11 suggest. This feature is related to the time by which the CE shell is fully ablated by the ultrarelativistic jet. To demonstrate this assessment, we have identified the location of the parts of the system from where thermal radiation is coming from. This is not a trivial task, since in our method, the contribution to the total flux of each computational cell can be strongly *blurred* because of the relativistic effects (e.g., time dilation, time delays, aberration). That means that for a given observed time, $t_{\rm obs}$, there will be contributions from different snapshots of the hydrodynamical evolution. We consider a virtual detector consisting of a screen oriented perpendicularly to

the symmetry axis (i.e., at an observing angle of 0°). For a given laboratory time in our hydrodynamical simulations, t, the photons coming from a fluid element located at a distance R (measured along the symmetry axis from the centre of the system) will arrive at the detector in a time $t_{\rm det} = t - R/c + t_{\rm offs}$, where $t_{\rm offs} = R_0/c\sqrt{1-\Gamma_{\rm i}^{-2}}$ is defined as the (laboratory frame) time spent by the jet to travel from $r = 0$ to $r = R_0$. The relation between $t_{\rm det}$ and the observer's frame time is given by $t_{\rm obs} = t_{\rm det}(1+z)$, where here z refers to the redshift. In Fig. 3.11 (left-hand and central panels), we depict the emission and absorption coefficients of free–free bremsstrahlung process at $t_{\rm obs} = 0.17\,{\rm d}$. We also show the specific intensity an observer looking head on at the jet would see. We note that the dominant contribution to the flux accumulated in our virtual detector is due to the region where the jet has interacted more strongly with the CE shell, namely, in regions which extend from 0.3 to $0.7 \times 10^{14}\,{\rm cm}$ in the z-direction and from 0.4 to $0.75 \times 10^{14}\,{\rm cm}$ in the x-direction. It is clear that the CE shell is not emitting but absorbing all the flux coming from regions with $z < 0.3 \times 10^{14}\,{\rm cm}$.

From the spatial distribution of the specific intensity in the X-ray band (Fig. 3.12, right-hand panel) and the distribution of the emissivity (Fig. 3.12, left-hand panel) we conclude that the X-ray detectable region is smaller than at optical frequencies. This region is concentrated very close to the surface of the CE shell facing the symmetry axis. The extent of the X-ray observable emitting region (facing up in Fig. 3.12, right-hand panel) is strongly dependent on the CE-shell geometry and mass distribution. A less dense shell closer to the symmetry axis would enhance the observed emission and, since this region would be dredged up by the jet faster than the current high-density CE shell, its emitted flux would decrease much sooner than in our models (see Section 3.5.1).

Figure 3.13 displays several snapshots of the evolution of the specific intensity in the $W2$ band for different observer's frame times, showing the process of ablation of the shell and the consequent reduction of emission. We notice that the CE shell is almost complete at 0.17 d (Fig. 3.11), while it is strongly disrupted (almost ablated) at 0.6 d (Fig. 3.13, upper-left panel). During the subsequent evolution the optical depth decreases drastically due to the ablation

process suffered by the CE shell, yielding a transition from an optically thick to an optically thin regime, as well as triggering a reddening of the observed system.

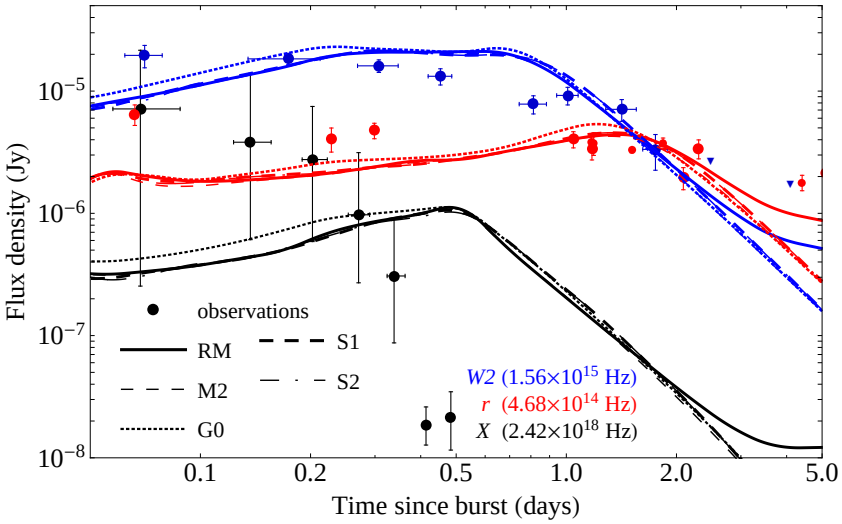

Figure 3.14: Light curves for the RM (solid lines), M2 (thin dashed lines), S1 (thick dashed lines), S2 (dot–dashed lines) and G0 (dotted lines) considering only the (thermal) bremsstrahlung-BB contribution. Optically thick light curves are plotted.

Though most of the thermal radiation is emitted before $t_{\rm obs} \simeq 2\,{\rm d}$ from the jet/CE-shell interaction, there is also a minor thermal contribution originating from the expanding jet bubble that lasts much longer than the dominant thermal component. This contribution will depend on the properties of the EM as, e.g., its rest-mass density. Initially in the RM, the contribution to the observed flux of the bubble is two to four orders of magnitude smaller than the flux emerging from the jet/CE-shell interaction region. However, at later times ($t_{\rm obs} \gtrsim 5\,{\rm d}$) the bubble emission still remains, and its thermal contribution tends to flatten the observed light curves. As we decrease the density in the EM we expect to have a less pronounced flattening, or even that the flattening does not show up during the time-scales of few days considered here. This is the case for model M2 where such flattening is absent after $\sim 3\,{\rm d}$ (Fig. 3.14).

For the stratified models S1 and S2, the flattening in the light curve is also absent. The reason is that the bubble density is smaller than in RM since the mass ploughed into the cavity at distances $R \sim 10^{15}$ cm is smaller. Therefore, the bubble emission is also expected to be weaker. The emission for models RM, M2, S1 and S2, in the three bands depicted in Fig. 3.14, is practically the same until $t_{\rm obs} \simeq 2\,{\rm d}$, since the main thermal contribution is determined only by the CE-shell/jet interaction region.

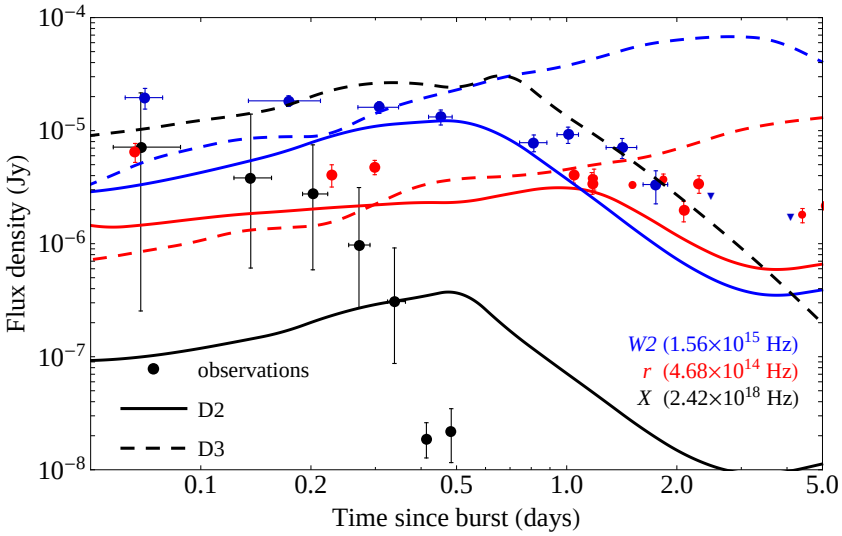

Figure 3.15: Light curves for D2 (solid lines) and D3 (dashed lines) models, considering only the (thermal) bremsstrahlung-BB contribution. Optically thick light curves are plotted.

The mass of the CE shell and the density contrast $\rho_{\rm CE,sh}/\rho_{\rm ext}$ play a key role shaping the emission properties of our models. As we have seen in Fig. 3.10 a CE-shell mass of $M_{\rm CE,sh} = 0.26 M_\odot$ suitably accommodates the observations (except at early times). We have tested two additional models with different CE-shell masses. One with half the mass of the RM (model D2) and another one with 10 times more mass (model D3). As we see in Fig. 3.15 the latter model (dashed lines) leads to an emission peak which is almost two orders of magnitude above the observational data (or the upper limits) in the $W2$ band,

and about three orders of magnitude above the observations in the X-rays band. Furthermore, the emission peak at all frequencies is shifted to very late times, clearly incompatible with the observations. In model D3 the spectral reddening, if it happens, may take place after 5 d, i.e., too late to explain the observations. Contrarily, model D2 (solid lines in Fig. 3.15) shows peak fluxes (at all frequencies) at earlier times than in the RM, and the spectral inversion happens earlier than indicated by the observations. We therefore conclude that CE-shell masses not much larger than $\sim 0.26 M_{\odot}$ may account better for the observational data.

3.5.1 CE-shell geometry

By analysing the results of our simulations we found that most of the thermal contribution comes from the interaction region between the CE shell and the jet. Therefore, the exact details of the shell and funnel geometry can significantly influence the jet dynamics as well as the thermal emission. Thus, we have tested four different geometries of the CE-shell funnel to find out how they affect the emission: a toroidal geometry (RM, G3 and G0) and a simpler, linear geometry for the funnel (G2). A sketch of the two funnel geometries is displayed in Fig. 3.1. The difference between models G3 and RM is that in G3 the funnel half-opening angle at $R_{\rm CE,out}$ is smaller than that of the RM. Model G0 differs from the RM in that it has a 10 times smaller rest-mass density in the EM, and the CE shell extends to the origin of the computational domain (i.e., there is no 'gap' between the CE shell and the innermost radial boundary at R_0). We are using the same shell density in all these models. Therefore, the shell mass in the wedge spanned by the jet ($\theta_{\rm j} = 17^{\circ}$ in the models considered here) is much smaller in model G2 than in the case of a toroidal-like shell (RM). Likewise, the shell mass in the wedge spanned by the jet is larger in the G3 and in the G0 models than in the RM. Due to different funnel geometries, the CE-shell/jet interaction proceeds also differently. The presence of a 'high'-density region close to the equator in model G2 (Fig. 3.3h) tells us that the CE-shell ablation process is not fully finished after $t \simeq 4$ d in this model. This high-density region is not present in the toroidal cases (Figs 3.3a and i).

As a consequence of the smaller amount of swept up mass in the CE shell, the average bubble density (Fig. 3.5) and mass (Fig. 3.4) are much smaller in the G2 model than in any of the other models presented here, at least, until $\sim 1\,\mathrm{d}$. The late evolution of G2 ($t \gtrsim 1\,\mathrm{d}$) is akin to that of the RM, since the dynamics is then determined by the circumstellar medium. The break in the slope of the mass growth rate of model G2 (Fig. 3.4) is delayed with respect to most of the other models (it happens at $\sim 1\,\mathrm{d}$).

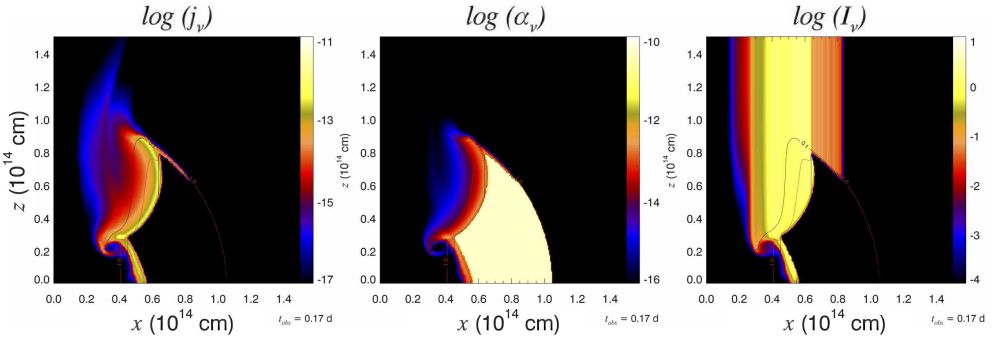

Figure 3.16: Same as Fig. 3.11 but for model G2.

We have also computed the emission, absorption and specific intensity maps associated with the G2 model in the $W2$ (Fig. 3.16) and in the X-ray (Fig. 3.17 upper panels) bands. It is evident that, initially, the shape of the region from where most of the thermal emission is produced differs substantially between the RM and the G2 model. In G2, the cross-sectional area of the thermally emitting region normal to the line of sight (0°) is smaller (Fig. 3.16 left panel and Fig. 3.17a) than in the RM. Such a shape is determined by the propagation of (forward and reverse) shocks sweeping the CE shell as the jet hits it. Because of the fact that, initially, the dominant emission region is much less inclined with respect to the line of sight in the case of model G2, the optical depth is also larger in such region, since radiation propagates upwards parallel to the symmetry axis and encounters denser parcels of the disrupted shell along the way. Indeed, we can observe the sharp cut-off in the specific intensity of the X-ray band of model G2 at about $6 \times 10^{13}\,\mathrm{cm}$ from the symmetry axis and at $z \gtrsim 5{\times}10^{13}\,\mathrm{cm}$ (Fig. 3.17c). This is associated with the very steep optical depth

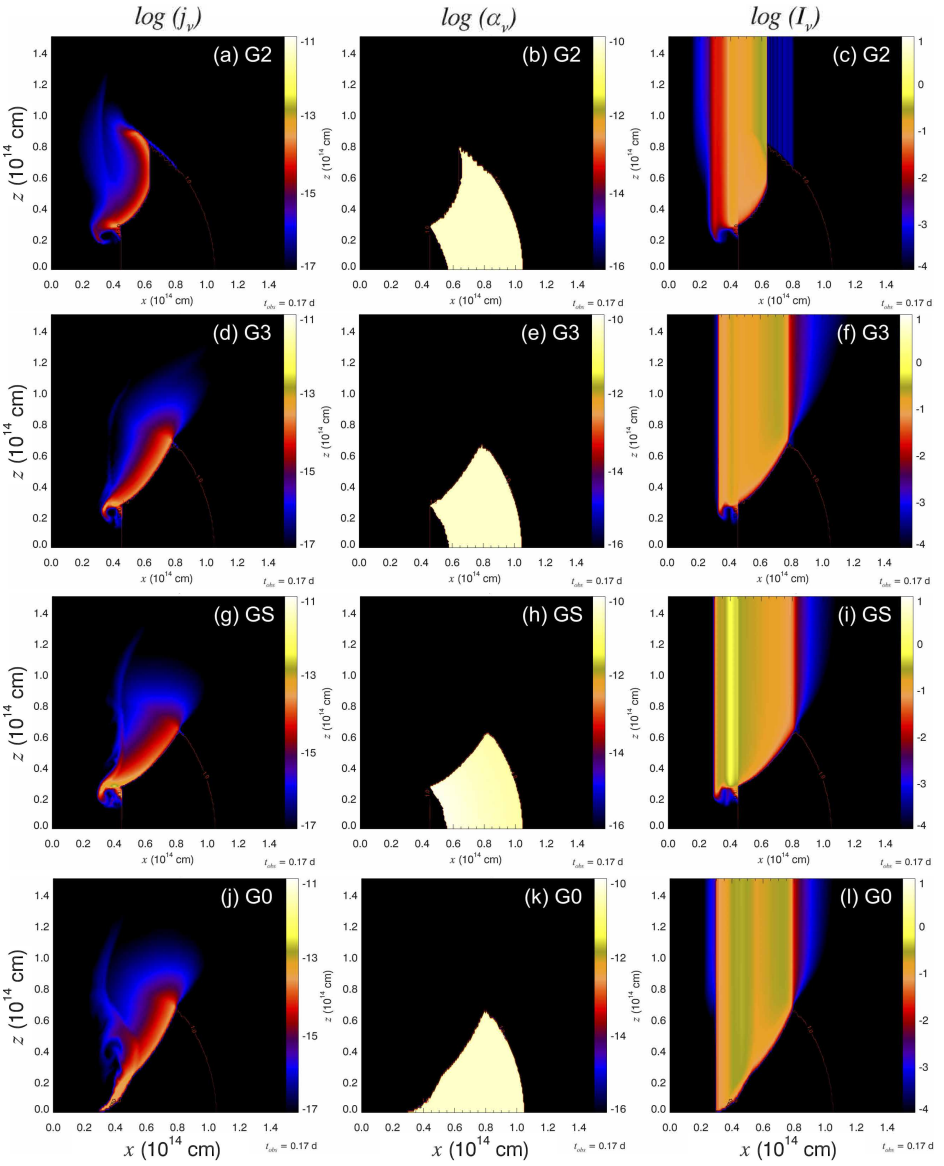

Figure 3.17: Emission, j_ν (left panels) and absorption, α_ν (central panels) coefficients and evolution of the specific intensity, I_ν (right panels) along the line of sight. The observer is located in the vertical direction (towards the top of the page) at $\theta_{\rm obs} = 0°$. The emission is computed in the X-ray band for free–free bremsstrahlung process, at $t_{\rm obs} = 0.17\,{\rm d}$. Models shown: G2 (top row), G3 (central upper row), GS (central bottom row) and G0 (bottom row). The emissivity (left panels) and the specific intensity (right panels) have to be corrected with a factor of ~ 3 (see App. B).

gradient in that region, as well as to a substantial decrease in the emissivity (Fig. 3.17a), because there the fluid temperature is smaller.[8] Later in the evolution, the inclination of the emitting region with respect to the vertical direction grows, as the shocks resulting from the CE-shell/jet interaction sweep the CE shell towards the equator. This change in the inclination of the emitting region tends to reduce the optical thickness above it and to increase the effective emitting area, contributing, in part, to explain the delay in the peak flux at all frequencies when comparing the optically thick light curves resulting from thermal processes for models G2 (Fig. 3.18) and RM (Fig. 3.10). Also, until $\sim 0.7\,\mathrm{d}$ the flux in all the frequencies is smaller than in the RM, and falls below the observational data. Furthermore, there is an obvious deficit of thermal energy flux at early times in model G2. As in the RM, the system of model G2 is initially optically thick in the $W2$ and r bands, but the transition to the optically thin regime happens later than in the former model (at $t_{\mathrm{obs}} \simeq 2\,\mathrm{d}$ in the $W2$ band and $t_{\mathrm{obs}} \simeq 4\,\mathrm{d}$ in the r band).

All these features in the thermal emission result from the smaller amount of mass of the CE shell with which the jet is initially interacting, namely, the sector of the CE shell spanning from $\theta_{\mathrm{f,in}}$ to θ_{j}. For later reference, we will name this piece of the CE shell the CE-early-interaction wedge. Since the energy and momentum fluxes of the jet are the same in both models, the time needed to push away the CE-early-interaction wedge is smaller in model G2 than in the RM. Once the jet path is cleared, the jet/shell interaction weakens and, consequently, the time the jet needs to ablate the whole CE shell increases. This explains why the peak of the light curves at different frequencies is delayed in model G2 with respect to the RM. It also explains why the initial thermal flux is smaller in model G2 than in the RM, since the emitting region is also smaller in G2. Finally, the lower rate at which the CE shell is ablated in model G2 leads to a delay in the transition to transparency in the $W2$ and r bands with respect to the RM.

Since the difference between the RM and model G3 is the cross-sectional

[8] This is a result of the model we have for the estimation of the fluid temperature from the total pressure including optical depth corrections (see Section 2.4.3).

radius of the central funnel (smaller in case of G3), the light curves of the RM (Fig. 3.10) display smaller flux at early times ($t_{\rm obs} < 0.1$ d) and a peak at later times than those of the G3 model (Fig. 3.18). In spite of this fact, light curves of models G3 and RM are qualitatively more similar between them than those of model G2. The differences in model G3, with respect to the RM, arise as a result of the larger mass of the CE-early-interaction wedge in the former case. We also note that the pattern of the X-ray intensity distribution (Fig. 3.17f) in G3 is roughly similar to that of RM (Fig. 3.12).

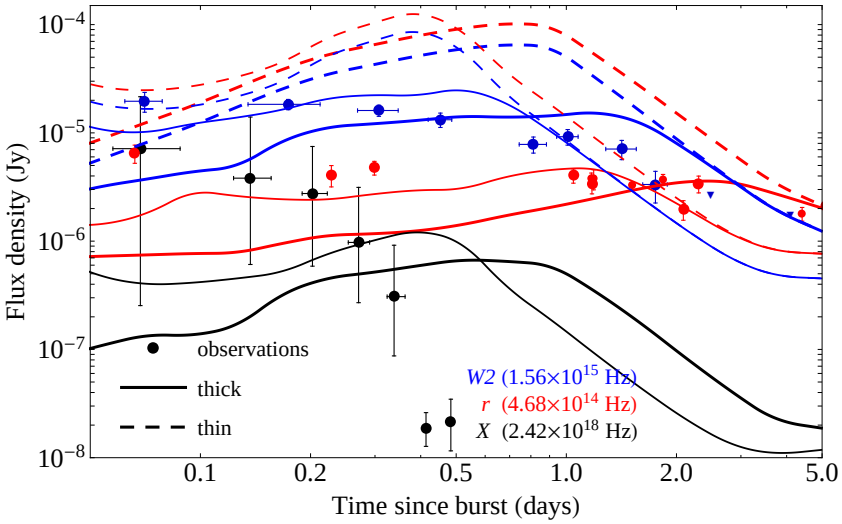

Figure 3.18: Same as in Fig. 3.10 but for model G2 (thicker lines) and model G3 (thinner lines).

From the comparison of the X-ray light curves in the RM (Fig. 3.10) with those in models G2 and G3 (Fig. 3.18), we note that our predicted flux in the X-ray band is very sensitive to the geometry and, more generally, to the physical conditions of the CE-early-interaction wedge. A higher CE-shell density close to the symmetry axis seems to *fit* the observational data better than a *wide* low-density funnel. We also note that the slope of the light curve after the X-ray maximum is very similar for all three models, and the same is true in the $W2$ band as well.

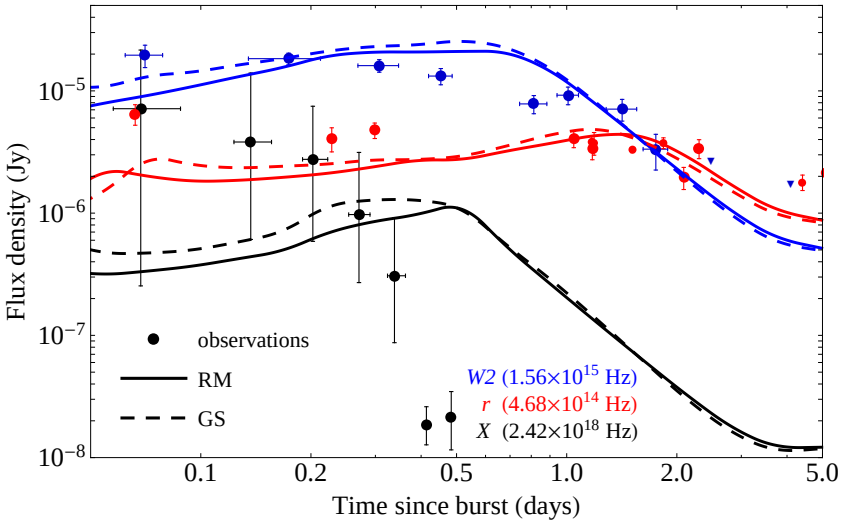

Figure 3.19: Same as in Fig. 3.10 but for model GS (dashed lines) compared to the RM (solid lines). Only optically thick light curves are considered.

To better explain the observations, a stronger emission at early times as well as a faster decrease after the maximum in the X-ray light curves is needed. This could be obtained by fine tuning the stratification of the CE shell. However, such a level of detail in the model set up is beyond the scope of this work. Here we consider a simple stratification of the CE shell in which the rest-mass density and pressure decrease as $\propto r^{-2}$ (model GS). Comparing Fig. 3.12 (right-hand panel; RM) and Fig. 3.17g (GS), we note that a stratified CE shell has a cross-sectional area of the X-ray emitting region which is similar to (though slightly larger than) that of the uniform CE shell of the RM. However, the specific intensity displays a stronger variation as we move away from the symmetry axis. In model GS, the specific intensity in X-rays is higher because of the contribution of (higher density) emitting regions which are closer to the symmetry axis. The change in the distribution of rest mass of the CE shell also yields small differences in the $W2$ and r-band light curves of model GS (Fig. 3.19). We note that the observed flux in these two bands integrated up to the peak frequency in each band is $\lesssim 10$ per cent larger than in the RM,

and that the peak at each frequency is shifted to a bit earlier times. After the maxima, the decay of the light curves is slightly faster than in the RM.

The differences between the RM and model G0 are very small, in spite of the fact that the CE shell in the latter model extends down to the innermost radial computational domain, i.e., we take $R_{\rm CE,in} = R_0 = 3 \times 10^{13}\,{\rm cm}$. We can observe that the emission region in this case extends up to the innermost radial boundary of the computational domain (Fig. 3.17j). However, in spite of the small changes in the emission and absorption regions, the overall light curve of model G0 is almost indistinguishable from that of model M2 (Fig. 3.14). G0 shows a slight increase of flux at early times, in the X-ray and $W2$ bands, since the jet/CE-shell interaction is a bit more extended. Provided that the only difference between the M2 and G0 models is the 'gap' between the CE shell and the jet injection nozzle, we conclude that the effects of our specific initialization of the jet is negligible. Once again, this is a result of the fact that the thermal emission originates from the jet/CE-shell interaction and the small mass difference added in the CE shell of G0 with respect to models M2 or RM does not change neither qualitatively, nor quantitatively our results.

3.5.2 X-ray emission

As we have seen in the previous section, the X-ray flux density in our models peaks too late with respect to the observations. In Fig. 3.20, we display the X-ray light curves of all the models (except D3) listed in Table 3.1. The time of peak flux is model dependent: broader jets (T20) peak earlier ($t_{\rm X,peak}({\rm T20}) \simeq 0.4\,{\rm d}$) than the RM ($t_{\rm X,peak}({\rm RM}) \simeq 0.5\,{\rm d}$) or narrower jets ($t_{\rm X,peak}({\rm T14}) \simeq 0.6\,{\rm d}$). The model which peaks latest is G2 (previously discussed in Section 3.5.1). The model D2 is the one with the lowest X-ray flux density. This is easy to understand since it is the model where the mass of the CE-early-interaction wedge is smaller, and where the CE-shell/jet interaction converts the smallest amount of kinetic into thermal energy. Changing only the stratification of the CE shell (compare models GS and RM in Fig. 3.20) we realize that a stratified CE shell only increases the flux by a factor of $\lesssim 2$ at early times, but after $\simeq 0.5\,{\rm d}$ the flux is very similar to that of the RM. Model

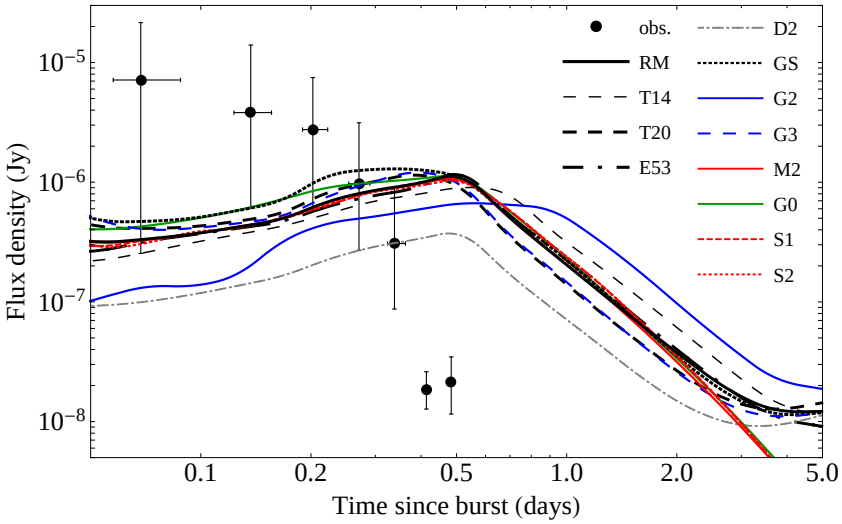

Figure 3.20: Light curves for all the models in this work (except D3) in the X-ray band. The X-ray data have been clustered as explained in Fig. 3.10.

G0 shows a similar behaviour at early times since we decreased the innermost radius of the CE shell (keeping the opening angle of the funnel constant). Thus, as we have increased the CE-early-interaction wedge, the emission grows at early times. However, even more important than the small increase of the X-ray flux at early times is the fact that at late times, the X-ray light curve of model G0 (also of model M2; Fig. 3.20) does not flatten, as a result of the 10 times smaller EM rest-mass density than in the RM.

In all the models, the flux density in X-rays until $\simeq 0.3$ d is lower than the observations by approximately 1–2 orders of magnitude. Integrating until 0.3 d the total flux density amounts to ~ 10 per cent of the observed flux. This result is compatible with the analysis of T11, since they conclude that the X-ray hotspot displays a thermal component which accounts for ~ 20 per cent of the X-ray flux.

We note that all of the models display an excess of X-ray flux density after ~ 0.4 d. This can be improved by more sophisticated funnel geometries, since the geometry of the CE-shell funnel has an important influence on the X-ray

peak time. However, we have not considered more complex funnel geometries to avoid increasing the number of free parameters in our models. Of course, the CE shells considered here are an oversimplified model of the very complex structures resulting from NS–He star mergers.

3.6 Origin of the non-thermal emission

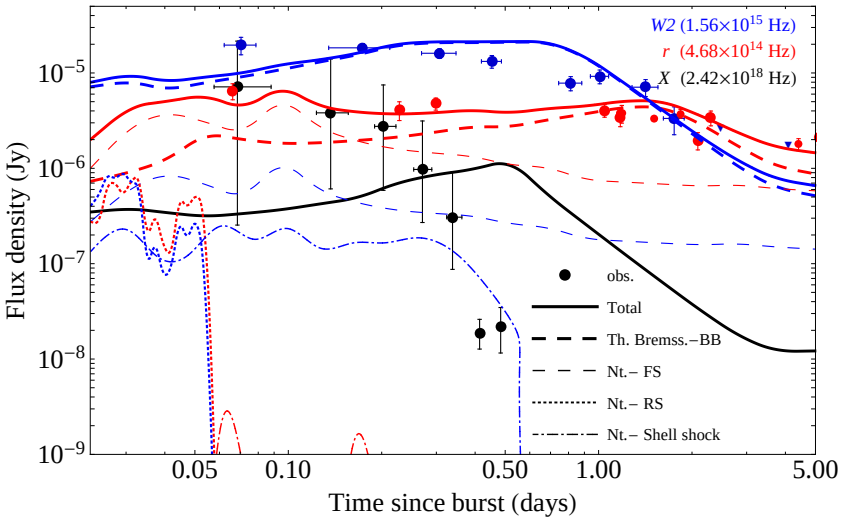

Figure 3.21: Synthetic LCs during the first 5 d for RM. We show the total emission (solid lines) and the individual contribution of the thermal (thick dashed lines) and various non-thermal radiation sources. For the latter case, we distinguish the contributions arising from the shocks resulting from the jet/CE-shell interaction (thin dot–dashed lines), the forward shock (thin dashed lines) and the reverse shock (short-dashed lines). The observational data have been taken from T11 and references therein (large solid circles), and from L14 (small solid circles). Upper observational limits are represented as triangles. Red, blue and black colours are used to display data in the r, $W2$ and X-ray bands, respectively. The non-thermal X-ray band flux arising from shocks resulting from the jet/CE-shell interaction is very absorbed and cannot be shown on the scale we are representing in the figure.

In our models the non-thermal emission is produced by particles accelerated at (strong) shocks. As in any weakly magnetized or unmagnetized jet

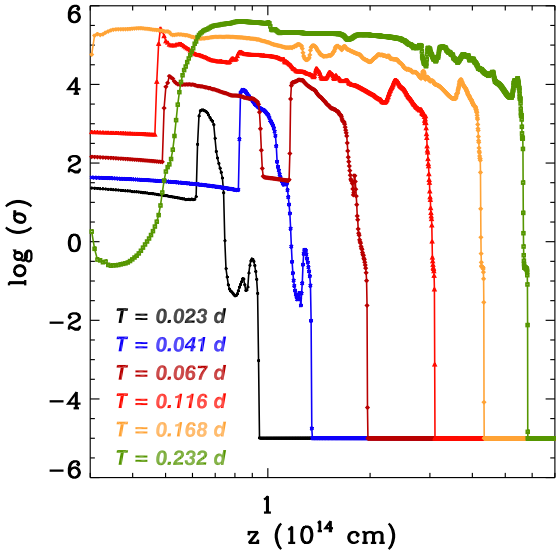

Figure 3.22: Profiles of the logarithm of the specific entropy along the symmetry axis at different evolutionary lab-frame times (see legends). Since $\sigma \propto p/\rho^{\gamma}$ (γ being the adiabatic index, which in our case runs between 4/3 and 5/3), and since we keep p/ρ =constant at the injection nozzle, the specific entropy will grow in time in the switch off phase, namely, after $t = 0.023\,\mathrm{d}$ as $\sigma(t) \propto t^{5(\gamma-1)/3}$.

model, there are at least two main shocks produced by the jet/medium interaction. These are the forward (FS) and reverse shocks (RS) or, using a terminology more common in jet hydrodynamics, the bow shock and the Mach disc. Since the jet is not pressure matched, the beam of the jet may also develop a number of bi-conical shocks where the flow is pinched. In the specific scenario we are considering, the jet blasts the CE shell and drives two main shocks, qualitatively similar to the FS and RS, but moving towards the jet axis (thus, shocking the jet beam) and away from it (compressing the CE shell). Though in principle all of these shocks may accelerate non-thermal electrons and thereby contribute to the synchrotron emission of our models, we will justify in the following that the dominant synchrotron flux arises the observer from the FS.

Bi-conical (recollimation) shocks are much weaker than the FS or the RS,

and the efficiency of shock acceleration in such oblique shocks is smaller than that of shocks perpendicular to the fluid motion. Thus, we can safely ignore them when accounting for the non-thermal emission.

Regarding the shocks driven by the jet/CE-shell interaction, they move in a high-density medium at a relatively small angle with respect to the jet axis. This part of the system is opaque to the synchrotron radiation during most of the evolution considered here. We note that the shell density is so high that the optical depth of the fluid through which the shocks are propagating is $\tau_\nu \gtrsim 10$ for all frequencies under consideration. To completely assess the contribution of shocks resulting from the jet/CE-shell interaction, we have included them in the computation of the non-thermal emission of the RM. As can be seen in Fig. 3.21 (dot–dashed lines), their contribution is only significant (but still subdominant) until $t_{\rm obs} \lesssim 0.4\,{\rm d}$, and only in the $W2$ band. After $t_{\rm obs} \sim 0.6\,{\rm d}$ we are no longer able to detect these shocks, since they are mixed with a much distorted and partly ablated CE shell. In the r band, and specially in the X-ray band (which cannot be seen on the scale of the figure), their contribution to the total flux density is absolutely negligible.

During the time interval when the injected jet power is sufficiently high (e.g., until 0.058 d) we see a distinct specific entropy jump of more than two orders of magnitude on both the FS and the RS (Fig. 3.22). These shocks are located at $z_{\rm FS} \simeq 9.2 \times 10^{13}\,{\rm cm}$ and $z_{\rm RS} \simeq 6.2 \times 10^{13}\,{\rm cm}$ at $t \simeq 0.023\,{\rm d}$, and at $z_{\rm FS} \simeq 1.3 \times 10^{14}\,{\rm cm}$ and $z_{\rm RS} \simeq 8 \times 10^{13}\,{\rm cm}$ at $t \simeq 0.041\,{\rm d}$ (Fig. 3.22, black and blue lines). However, not long after the jet head leaves the outer edge of the CE shell, two oppositely moving shocks driven by the jet/CE-shell interaction travel towards the jet axis and eventually met. The brown line in Fig. 3.22 corresponds to a time ($t \simeq 0.067\,{\rm d}$) at which these two shocks have reached the jet beam. We note the rise of the specific entropy in the unshocked tail of the jet (i.e., the part of the jet trailing RS that is free expanding; $5 \times 10^{13} \lesssim z \lesssim 9 \times 10^{13}\,{\rm cm}$). As a result of the jet/CE-shell interaction the jet beam is choked, strongly baryon loaded and the RS is smeared so much that its strength is greatly decreased. In practical terms there is effectively no entropy jump across the locus of the RS after $t = 0.116\,{\rm d}$ (when the RS is situated at

$z \simeq 2.3 \times 10^{14}$ cm; Fig. 3.22, red line). Instead, we find a steep positive specific entropy gradient. Progressively, the high entropy of the matter coming from the shocked CE shell fills the unshocked jet tail, eventually reaching the inner grid boundary (Fig. 3.22; $t = 0.168$ d). In short, the jet/CE-shell interaction effectively blurs the RS after a lab-frame time $t \simeq 0.07$ d. Hence, any radiative signature of the RS may only influence our emission results at early times. Indeed, we have computed the non-thermal flux associated with the RS until a bit after the time in which we can still identify in our models a RS, and we notice that, in the $W2$ band, the RS signature is up to one order of magnitude below that of the FS (Fig. 3.21; blue short-dashed line). The situation in the r band is quantitatively different. In this band, the RS non-thermal flux emission is comparable to that of the FS. The relative contribution of the RS is more relevant at smaller frequencies. Unfortunately, the observational data in the z band is scarce, and available only after $\simeq 0.3$ d after the burst (T11). Hence, we cannot constrain our models with observational data in a band where the RS would be dominant over the FS.

Turning now to Fig. 3.23 we clearly see that the production sites of the observed non-thermal and thermal radiation are distinct. The main contribution to the total thermal intensity is due to radiation originating from the jet/CE-shell interaction region, located at a distance from the symmetry axis of $\simeq 3 \times 10^{13}$ cm and extending to $\simeq 8 \times 10^{13}$ cm. In the specific intensity maps in Fig. 3.23 (panels a, d and g) such a dominant contribution is clearly seen as a light (yellow or orange) fringe emerging from the jet/CE-shell interaction region. This is the case in all the three bands considered here. On the other hand, the non-thermal emission comes from the bow (forward) shock of the jet (Fig. 3.23, panels b, e and h). We also can see the contribution of the shocks driven in the CE shell as a set of intense vertical fringes in the range $4 \times 10^{13} < x < 8 \times 10^{13}$ cm. In spite of its large intensity density, the contribution of these CE-shell shocks to the total flux is smaller than that of the FS at almost any time. Furthermore, we note that non-thermal radiation coming from these shocked regions and places where $r < R_{\rm CE,in}$ is strongly absorbed by the CE shell, and thus $\alpha_\nu^{\rm th} \gg \alpha_\nu^{\rm nt}$. Likewise, bremsstrahlung absorption is

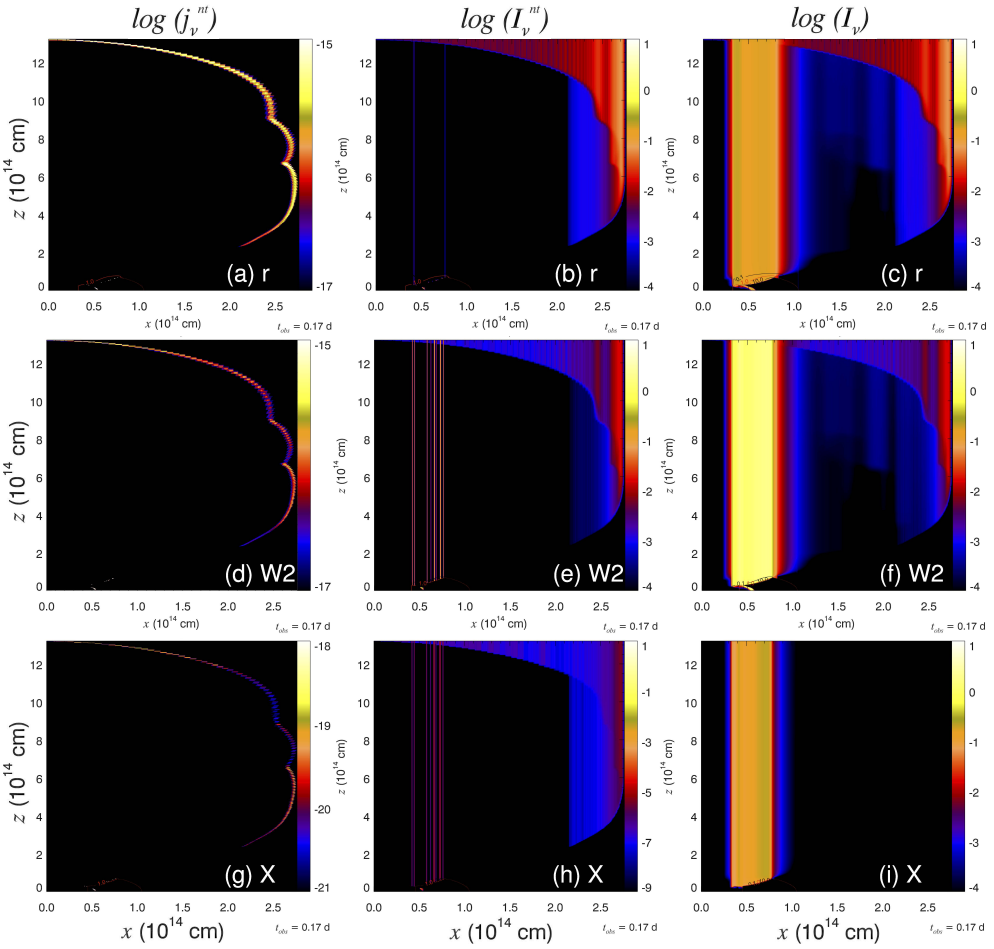

Figure 3.23: Synchrotron emissivity, j_ν (left-hand column), and evolution of the specific intensity, I_ν, along the line of sight considering only non-thermal processes (central column) or both (thermal and non-thermal) processes simultaneously (right-hand column). The observer is located in the vertical direction (towards the top of the page) at a viewing angle $\theta_{\rm obs} = 0°$. The emission is computed in the r (upper row), $W2$ (middle row) and X-rays (bottom row) bands at an observational time $t_{\rm obs} = 0.17\,{\rm d}$. Note that, while the colour scales are the same for the total specific intensity (right-hand column), they are different for the lower left and central panels, since the non-thermal X-ray emission is much fainter than in the other two bands displayed in the figure. The units of j_ν and I_ν are given in the CGS system (see Section 2.4 for details). The thermal intensity in the X-ray band (panel i) should be corrected a factor of ~ 3 (see App. B).

almost negligible in the FS and RS, since the rest-mass density at those shocks is much smaller than at the CE shell ($\rho_{\rm shocks} \ll \rho_{\rm CE,sh}$), and the temperature is, conversely, larger ($T_{\rm shocks} \gg T_{\rm CE,sh}$).

Since also the synchrotron self-absorption is very low at these frequencies, the forward shocked region is optically thin to the non-thermal radiation and, hence, the observed non-thermal specific intensity follows closely the locus of the forward shock in the observer's frame (Fig. 3.23, panels b, e and h). We point out that in the maps displayed in Fig. 3.23, we have not considered the contribution of the RS, which is negligible at $t_{\rm obs} = 0.17\,{\rm d}$. As a result of the jet/CE-shell interaction, the forward shock is not perfectly spherical. Instead, even at 0.17 d, we can still see a number of kinks in the shocked emission surface between 2.4×10^{14} and $2.7 \times 10^{14}\,{\rm cm}$. Furthermore, we also note that since the non-thermal emission results from the outer (geometrically thin) skin of the cavity, the non-thermal emission region appears limb brightened for the observer. We also observe that the thermal and non-thermal contributions to the total flux are much more evenly distributed in the r band than in the $W2$ band.

3.7 Spectral evolution

In this section we examine the synthetic LCs and spectra obtained for the different models. Both thermal and non-thermal contributions have been included. We first discuss the results for the RM (Sect. 3.7.1) and then consider variations of the parameters in Sect. 3.7.2. A summary of the most relevant parameters of the models is given in Tables 3.1 and 3.2.

3.7.1 Reference model

As we have already shown in the previous section, the synthetic LCs computed in the $W2$ and r bands are very close to the observational points (Fig. 3.21). As anticipated in Sect. 3.1, our models are not a 'perfect fit' of the observations, not even for the RM, though they qualitatively and quantitatively agree with them. At early times, the $W2$ band is more energetic than the r band,

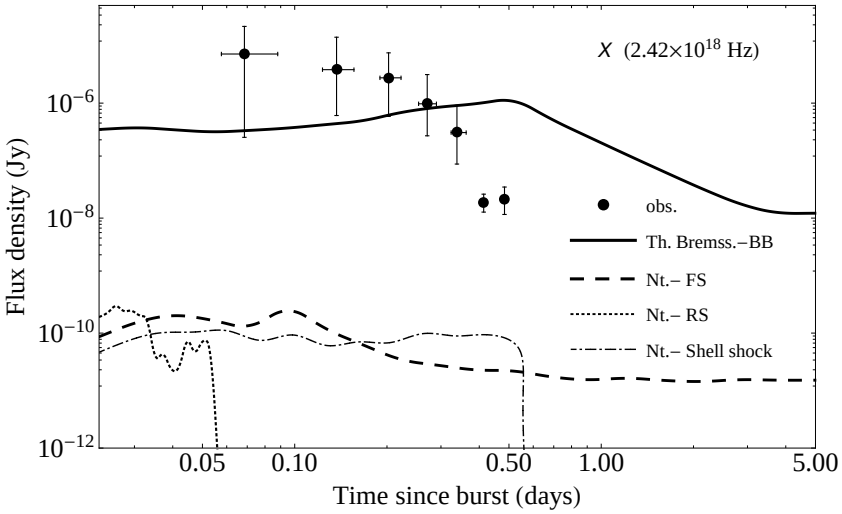

Figure 3.24: Synthetic LC in X-ray band during the first 5 d for RM. We show the thermal (solid lines) and the non-thermal (dashed lines) radiation. For the representation of the X-ray data we have clustered the data of the X-Ray Telescope (XRT) observing cycle into a single point, with error bars showing the data dispersion.

in agreement with observational data. The contribution of the non-thermal emission to the total LC is significant at early times ($t_{\rm obs} \lesssim 0.5\,{\rm d}$; Fig. 3.21), and is more relevant at lower frequencies. It is dominant, by a factor of < 2, in the r band until $\approx 0.15\,{\rm d}$. Looking at the distribution of the specific intensity in the r band (Fig. 3.23c), this fact is not due to a much larger specific (synchrotron) intensity at the FS, but to the fact that the FS surface is larger than the thermally emitting region. In the $W2$ band, the thermal emission is larger at any time than the non-thermal one and, indeed, the thermal flux density is more than one order of magnitude larger than the non-thermal one after $t_{\rm obs} = 0.17\,{\rm d}$ (Fig. 3.21). The bremsstrahlung-BB contribution represents 96 and 73 per cent of the total received flux in the $W2$ and in the r band, respectively.

In the X-ray band, the non-thermal flux is much smaller than the thermal one at $t_{\rm obs} = 0.17\,{\rm d}$ (Fig. 3.24), which is due to the fact that the X-ray emission of the FS is extremely weak (note the difference in the scales on the left-

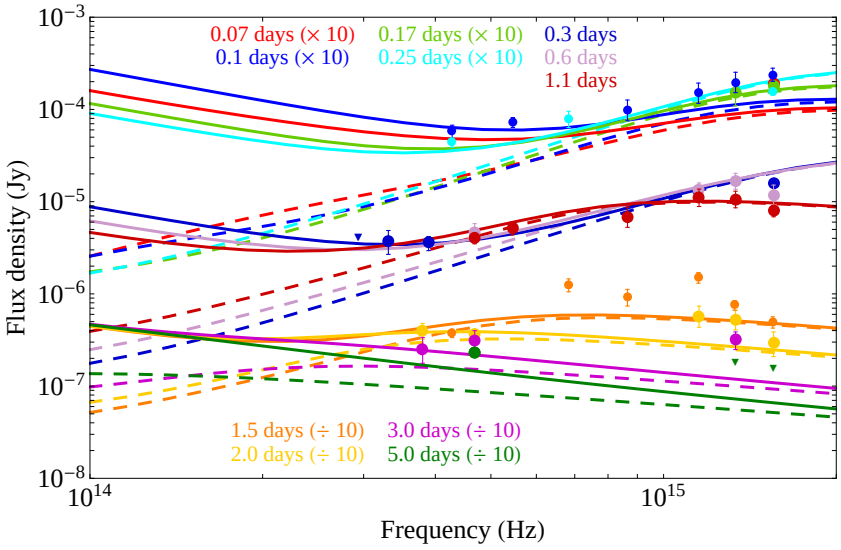

Figure 3.25: Fitted spectrum at different observing times (colours denote observations at different times, see legend; detections at 0.1, 0.25 and 1.5 d are taken from L14; rest of data taken from T11) for the RM. The total contribution (non-thermal plus thermal) is represented as solid lines and the thermal contribution as dashed lines. Note that for visualization convenience some of the data have been multiplied or divided by a factor of 10 (see the plot legends).

hand panels of Fig. 3.23). This happens because the FS is only moderately relativistic at this time of the jet evolution. In many regards, the emission of the FS resembles that of the very late afterglow in a standard GRB.

At late times, our models suggest that the non-thermal emission might eventually be relevant. In the r band, the non-thermal flux can be comparable in magnitude to the thermal one after $t_{\rm obs} \gtrsim 4\,{\rm d}$. The same qualitative feature may happen much later in the $W2$ band, since the difference between the thermal and non-thermal contributions to the flux density decreases progressively until there is only a factor of ~ 4 at $t_{\rm obs} = 5\,{\rm d}$.

The agreement between our model and the observations is not limited to the LC, but also extends to the spectral data (Fig. 3.25) for the first 5 d after the burst. The agreement between observed spectra and the synthetic ones computed for our RM is much better at early and intermediate times than

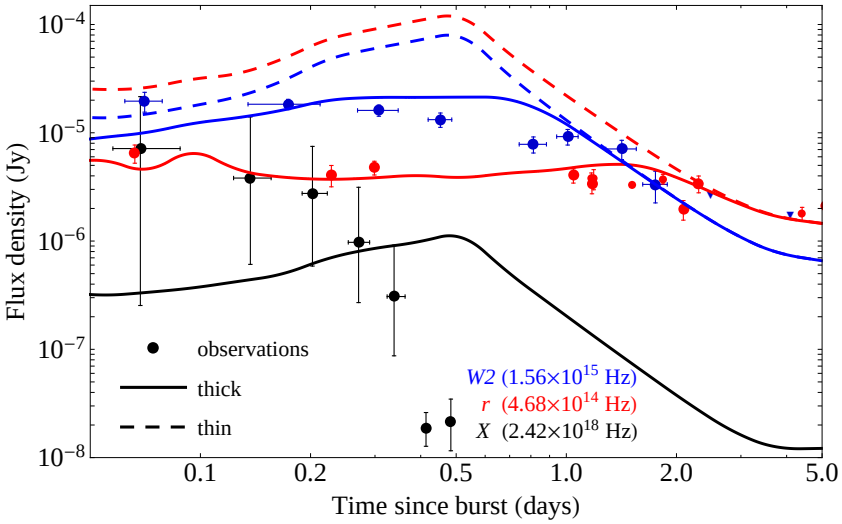

Figure 3.26: Optically thick (solid lines) and thin (dashed lines) total light curves in the $W2$, r and X-ray band are plotted to illustrate the transition from optically thin to optically thick emission. It is useful to compare this figure with Fig. 3.10, where only the thermal contribution is considered. Observational data is marked with symbols (see Fig. 3.21).

after $\sim 3\,\mathrm{d}$. The thermal contribution is clearly dominant for frequencies $\gtrsim 6 \times 10^{14}\,\mathrm{Hz}$. In the X-ray band the non-thermal contribution is practically negligible (Fig. 3.24). Even when we include the non-thermal contributions to the emitted radiation, the system is optically thick until $\sim 1\,\mathrm{d}$ after the burst in the $W2$ band, and until $\sim 2\,\mathrm{d}$ in the r band (Fig. 3.26). As we also saw in Fig 3.10 the system is optically thin in the X-ray band at all times.

3.7.2 Parametric scan

We have found that the parameters of the RM are an appropriate fit to the observations, but it turns out that this combination of the parameters is not the only one able to satisfactorily explain them. As we have pointed out in Section 3.7.1, at lower frequencies the non-thermal contribution is more relevant, so any modification in any of the non-thermal microphysical parameters

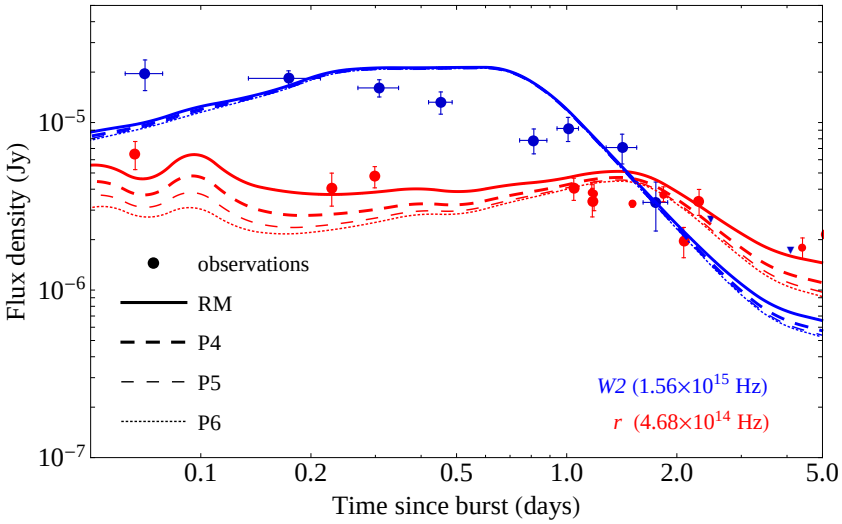

Figure 3.27: Synthetic LCs for different values of the electron energy distribution index q: 2.3 (RM, solid lines), 2.4 (P4, thick dashed lines), 2.5 (P5, thin dashed lines) and 2.6 (P6, dotted lines). Observational data are marked with symbols (see Fig. 3.21).

will be reflected to a greater degree in the r band than in $W2$. We have shown in Sect. 3.7.1 for the RM that the X-ray non-thermal contribution can be neglected since it is $\sim$ 3–4 orders of magnitude smaller than the thermal contribution. This conclusion can be extended to the rest of the models in this work since, as pointed out in Section 3.5.2, the thermal X-ray emission in all our models displays a (thermal) flux deficit at early times that cannot be compensated by the non-thermal X-ray flux. Furthermore, the duration of the X-ray emission is also too long to accommodate the observational data (see Fig. 3.20). We concluded that to reproduce the observations we shall tune the properties of the CE shell (e.g., the density gradient both in the radial and angular directions), something which would require also much more numerical resolution and prohibitively long computing times to perform a broad parametric scan of sufficiently representative models. Therefore, we will not focus the parametric scan in this band in the rest of the work.

Tables 3.1 and 3.2 lists the parameters of all the models we are considering

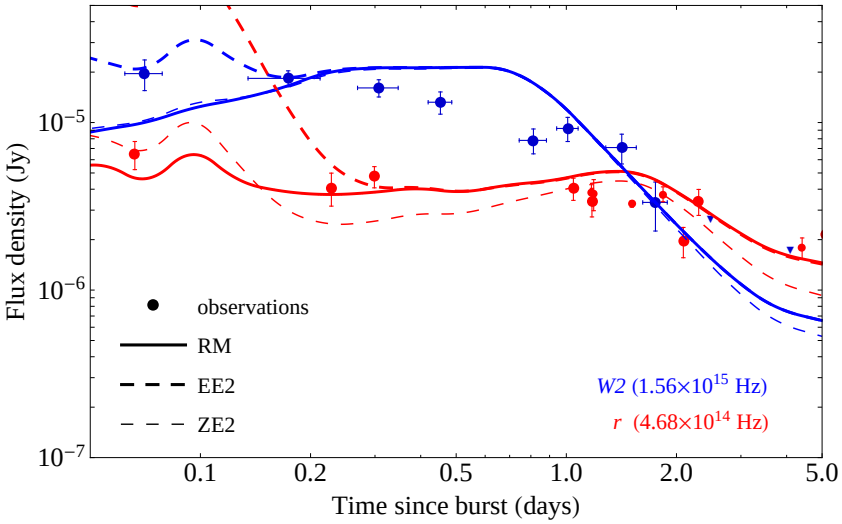

Figure 3.28: Synthetic LCs for different values of ϵ_e and ζ_e, respectively: 10^{-3} and 10^{-1} (RM, solid lines); 10^{-2} and 10^{-1} (EE2, thick dashed lines) and 10^{-3} and 10^{-2} (TE2, thin dashed lines). Observational data are marked with symbols (see Fig. 3.21).

here.

3.7.2.1 Non-thermal microphysical parameters

Fixing the hydrodynamical parameters used for the RM, we show how a change in the power-law index of the electron energy distribution affects the LCs in Fig. 3.27. Values up to $q \approx 2.6$ are compatible with the first 5 d of observations in the $W2$ band. However, a value $q = 2.3$ yields synthetic LCs closer to the observations in the r band. The $W2$-band flux remains unchanged until $\simeq 2$ d, independent of q, since in this band the thermal flux density is dominant at early times. At later times, smaller values of q tend to produce a flatter and slightly more luminous LC, but still compatible with the observational upper limits available after ~ 2 d.

Among the parameters used to model the synchrotron emission, ϵ_e is the one which affects most the emission in both the $W2$ and in the r bands (Fig. 3.28). We find that an increment of ϵ_e is reflected in the LC as a flux

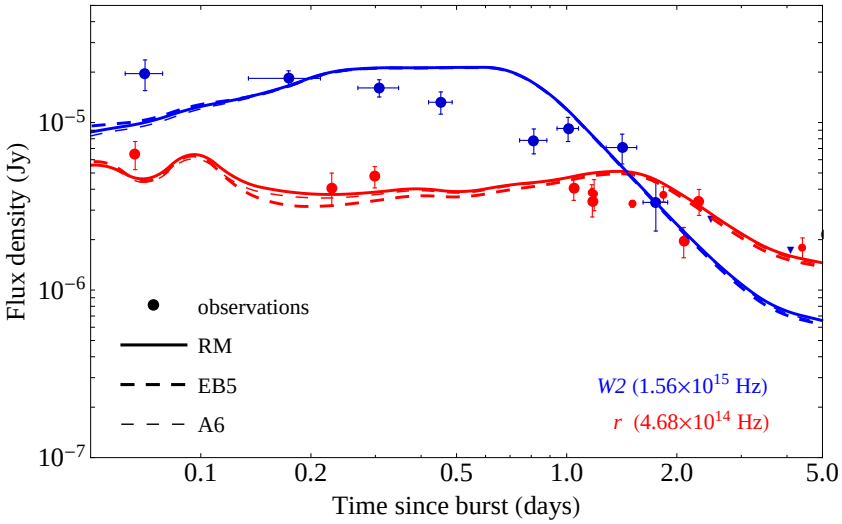

Figure 3.29: Synthetic LCs for different values of ϵ_B and $a_{\rm acc}$, respectively: 10^{-6} and 1 (RM, solid lines); 10^{-5} and 1 (EB5, thick dashed lines); 10^{-6} and 10^{6} (A6, thick dashed lines). Observational data are marked with symbols (see Fig. 3.21).

increase, especially at low frequencies and early times, which is incompatible with observations (see model EE2; Table 3.2). A noticeable effect is that the non-thermal emission in the $W2$ band becomes the dominant contribution to the total flux until $\simeq 0.2$ d, in contrast to the dominance of the thermal radiation in our RM (compare thick dashed and solid blue lines in Fig. 3.28). Decreasing $\zeta_{\rm e}$ by the same factor as $\epsilon_{\rm e}$ one obtains the same value for the effective fraction of the energy imparted to relativistic electrons, $\epsilon'_{\rm e}$, but the LCs are different. Decreasing $\zeta_{\rm e}$ (see model ZE2; Table 3.2) decreases the number of radiating electrons, yielding a higher flux at early times because there is more energy per electron. However, when the electrons have cooled at later times, the flux decreases compared to the reference case (which initially contains more electrons at lower energies).

In Fig. 3.29 we show the effect of changing ϵ_B in the RM. An increase by a factor of 10 of ϵ_B (which is on reach of our models; see Sect. 3.3.1.3) has almost no influence on the observed flux. In the same Fig. 3.29 we display the effect

of changing $a_{\rm acc}$. It is evident that the variation of $\gamma_{\rm max}$ (Equation (2.62)) of the particle distribution produced by the change in $a_{\rm acc}$ ($\gamma_{\rm max} \propto a_{\rm acc}^{-1/2}$) is insufficient to induce an observable variation on the global behaviour of the optical LCs. The reason for it is that the typical Lorentz factors contributing to the synchrotron emission in the $W2$ and r bands ($\sim 9\times10^3$ and $\sim 5\times10^3$, respectively) are smaller than $\gamma_{\rm max}$ when $a_{\rm acc}$ is either 1 ($\gamma_{\rm max} \sim 2\times10^7$) or 10^6 ($\gamma_{\rm max} \sim 2\times10^4$).

3.7.2.2 Isotropic energy of the jet, $E_{\rm iso}$

One of the parameters under consideration is the equivalent isotropic energy of the jet, for which we only have a lower observational limit. We have considered two different models with isotropic energies of 4×10^{53} (RM) and 2×10^{53} (E53), keeping $\theta_{\rm j} = 17^\circ$ constant. The change in $E_{\rm iso}$ causes important differences associated with the emission of non-thermal radiation, while the thermal contribution, which is dominant from $\gtrsim 0.2\,$d, is similar in both cases. More energetic jet models develop stronger bow shocks (i.e., stronger forward shocks) and, hence, the associated non-thermal emission is more powerful. In Fig. 3.30 we see that for the least energetic jet model, E53, the flux at early times is low compared with observations. A slightly larger value of $\epsilon_{\rm e}$ could increase the early time flux, so that the data could still be fitted with a larger non-thermal component until $\lesssim 0.15\,$d At later times it can be seen that the total emission is comparable to that of RM.

3.7.2.3 Half-opening angle, $\theta_{\rm j}$

For a fixed value of the equivalent isotropic energy of the jet, the true injected energy ($E_{\rm j}$) depends on the assumed half-opening angle of the jet. This means that for a constant energy per solid angle broader jets are more energetic: $E_{\rm j} = E_{\rm iso}(1-\cos\theta_{\rm j})/2$. In the model T14 the spectral inversion is produced about half a day later (thin dashed line in Fig. 3.30) than in RM. On the other hand, in the LC of T20 (thick dashed line in Fig. 3.30) the spectral inversion happens earlier than it does observationally (by almost half a day), and earlier

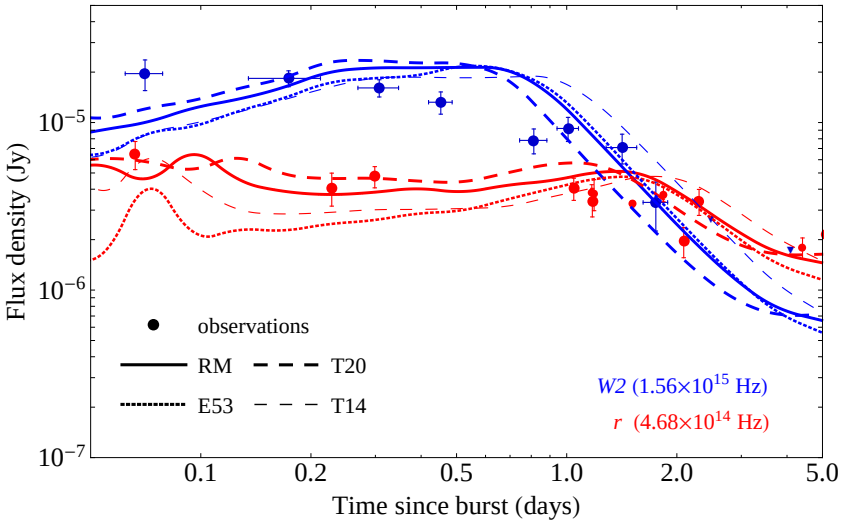

Figure 3.30: Synthetic LCs for different jet energies. Models RM (solid lines), E53 (dotted lines), T20 (thick dashed lines) and T14 (thin dashed lines) are depicted. Observational data are marked with symbols (see Fig. 3.21).

than in the RM. After the spectral inversion in the model with the largest half-opening angle, the decay rate of the flux is very similar to the RM. Our conclusion is that values $\theta_{\rm j} \simeq 17^\circ$ are those which reproduce the observations better.

3.7.2.4 CE-shell density contrast with respect to the external medium, $\rho_{\rm CE,sh}/\rho_{\rm ext}$

Assuming a fixed CE-shell geometry, a change of the rest-mass density of the shell, $\rho_{\rm CE,sh}$, yields an equivalent change in its total mass. We take moderate values for the CE-shell mass, $M_{\rm CE,sh} \sim 0.26,\ 0.14 M_\odot$. This corresponds to the rest-mass densities $\rho_{\rm CE,sh}/\rho_{\rm ext} = 1500$ (RM), 817 (D2), respectively, if the shell is uniform. We also consider model GS which incorporates a CE shell that has a rest-mass density decay as r^{-2} (see Table 3.1). We have tuned the rest-mass density at $R_{\rm CE,in}$ in order to have approximately the same mass in the CE shell of model GS as in the RM. In model GS the density jump across

the inner edge of the CE shell is about three times larger than in the RM, while at the outer edge of the CE shell the density jump is halved with respect to the RM. The change in the distribution of rest mass of the CE shell yields small differences in the $W2$- and r-band LCs of model GS (see Fig. 3.19). The observed flux in these two bands integrated up to the peak frequency in each band is $\gtrsim 10$ per cent larger than in the RM, and the peak at each frequency is shifted to a bit earlier times. After the maxima, the decay of the LCs is slightly faster than in the RM.

For model D2 the $W2$-band flux is halved with respect to that of the RM in the period under study (Fig. 3.31, blue solid and thick dashed lines). The response in the r band to changes in the CE-shell density is non-monotonic (Fig. 3.31, red solid and thick dashed lines). At early times ($t_{\rm obs} \lesssim 0.1$ d), when the flux is dominated by the non-thermal contribution, the observed emission grows in model D2 by a factor of 2 with respect to the RM. Afterwards it is smaller and does not fit the data very well. Therefore, a lower shell density causes the thermal flux to decrease. The reason for this behaviour is that different CE-shell densities will cause differences in the jet/shell interaction. The lower density CE shell allows the jet to travel through the funnel more easily, dragging less mass and breaking out of the shell outer radius at a higher speed. During this epoch the jet FS is still rather relativistic and, consistently, an afterglow-like emission dominates the observed flux. The opposite happens for a more massive CE shell, where the jet is slowed down much more and the afterglow-like emission is more suppressed.

3.7.2.5 CE-shell geometry

As we have already shown, most of the observed thermal radiation comes from the interaction region between the CE shell and the jet. In previous sections, we have argued that the jet/CE-shell interaction also produces the elimination of the RS and, furthermore, depending on the details of such interaction, the emission associated with shocks in that region may also yield a significant change in the observed flux at early times. Therefore, the exact properties of the shell and the funnel geometry can significantly influence both the thermal

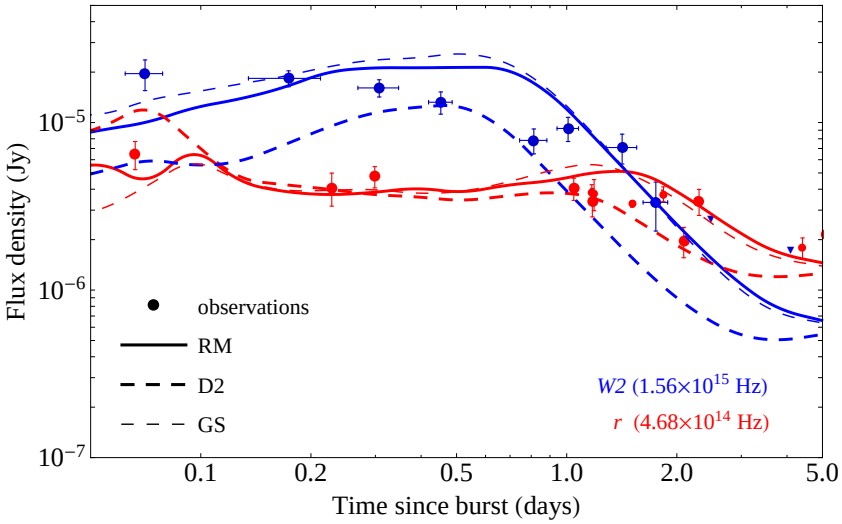

Figure 3.31: Synthetic LCs obtained varying the rest-mass density, $\rho_{\rm CE,sh}$, and geometry of the CE shell: RM (solid lines), D2 (thick dashed lines) and GS (thin dashed lines) models. Observational data are marked with symbols (see Fig. 3.21).

and the non-thermal emission signatures of our models.

We have tested three different CE-shell funnel geometries: two toroidal ones (RM and G3) and a simpler, linear geometry (G2) for the funnel (see Fig. 3.1). We use the same CE-shell density in these all three models. Therefore, the shell mass in the case of linear opening of the funnel (G2) is a bit smaller than in the RM, with a toroidal-like shell funnel, and this one is even smaller than in the model G3 with a more closed funnel. Fig. 3.32 shows that a toroidally shaped CE-shell geometry explains a bit better the observations. As in the case of reducing the CE-shell density (Sect. 3.7.2.4), reducing the amount of mass that the jet sweeps in the angular region $\theta_{\rm f,in} \leq \theta \leq \theta_{\rm j}$ results in a reduced jet/shell interaction and less flux at early times in $W2$ band. The r band is still dominated at early times by non-thermal radiation. The spectral inversion in G2 happens later than in RM due to the initially smaller jet/shell interaction, which delays the CE-shell effective ablation. This gives a later peak in $W2$ band and the flattening of the r band up to 5 d.

Model G3 is the one which has the largest mass of what we called the CE-early-interaction wedge. For this reason the jet/shell interaction is stronger initially (although non-thermal radiation is not dominant at the early stages of evolution) and the CE shell is ablated even sooner than in RM, giving an earlier peak of flux and an earlier reddening of the system (Fig. 3.32).

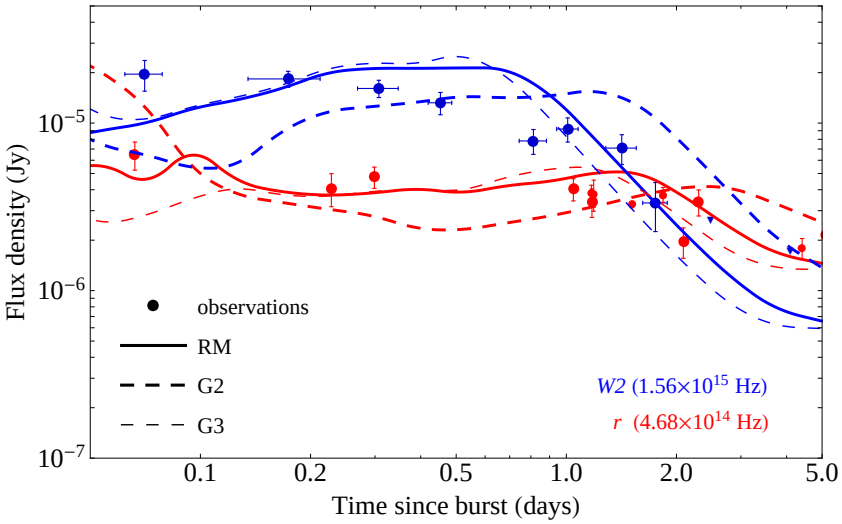

Figure 3.32: Synthetic LCs obtained varying the rest-mass density and geometry of the CE shell, $\rho_{\rm CE,sh}$: RM (solid lines), G2 (thick dashed lines) and G3 (thin dashed lines) models. Observational data are marked with symbols (see Fig. 3.21).

3.7.2.6 External medium

As we have already seen, the thermal emission does not depend on the EM structure. It is mainly produced by the jet/CE-shell interaction. However at later times ($t_{\rm obs} \gtrsim 3$ d), after the CE shell has been completely ablated, a flattening in the LC can be observed. This emission is associated with the thermal contribution of the bubble blown by the jet, whose expansion rate depends chiefly on the mass plowed by the FS from the EM. This emission is expected to be reduced in models with a low-density EM (e.g., in model M2). In our models with an EM with a declining rest-mass density and pressure

(S1 and S2) the mass of EM swept by the FS after the same time after the jet injection is smaller, in particular after a lab-frame time $T \gtrsim 0.6\,\mathrm{d}$ (see Fig. 3.4). Thus, the average rest mass of the cavity in models S1 and S2 is 5–10 times smaller than in the RM and, thereby, the thermal bremsstrahlung emissivity (proportional to the square of the rest-mass density) is much smaller. The consequence is that the synthetic LCs of models S1 and S2 do not tend to flatten after $t_{\mathrm{obs}} \gtrsim 3\,\mathrm{d}$, but decay with time as $\sim t_{\mathrm{obs}}^{-2.7}$ (Fig. 3.33).

The way in which the stratification of the EM affects the non-thermal emission is more complex. At late times, only the FS is still able to efficiently accelerate non-thermal electrons. The fraction of energy transferred to the electrons depends on the density of the external shock where they are injected. This density mostly depends on the EM conditions, so that at smaller density of the EM, one obtains a smaller density of the region shocked by the external shock, and consistently a smaller non-thermal flux density. All this causes the total emission at times $t_{\mathrm{obs}} \gtrsim 0.2\,\mathrm{d}$ to be dominated by the thermal emission, rather than by the FS. In the RM this situation may change after $t_{\mathrm{obs}} \gtrsim 5\,\mathrm{d}$, when the FS flux density becomes comparable to that of the expanding shell in the UVOIR bands (Fig. 3.21). This is not the case of model M2, in which a 10 times lower density in the EM results in a four times smaller flux than in the RM after 5 d (Fig. 3.33). At early times, the thermal emission flux density is basically the same in stratified and non-stratified models, since the CE shell is uniform in both cases, and the thermal emission is linked to the jet/CE-shell interaction (see Fig. 3.13). The non-thermal emission shows a rather different early evolution depending on the EM rest mass and pressure gradients. Our models S1 and S2 have a fiducial pressure, p_{ext}, 100 times larger than in the RM. While the pressure quickly decreases below that of the RM in model S2, the linear pressure decrease of model S1 makes that the environmental pressure in this model equals that of the uniform medium of the RM only a long time after the jet head has left the outer radial CE-shell boundary. Before this time, the jet of model S1 encounters an EM with a (much) larger pressure than that of the RM or the S2 models. In particular, this happens while the jet is still advancing along the funnel. As a consequence, the strength of both the FS and

the RS is larger in model S1 than in models RM and S2 and, hence, the non-thermal flux emitted by this model is larger. Conversely, the pressure along the funnel in model S2 is the smallest, thus the jet in this model develops the weaker (in relative terms) pair of FS and RS, resulting in the weakest early-time flux density of all three models.

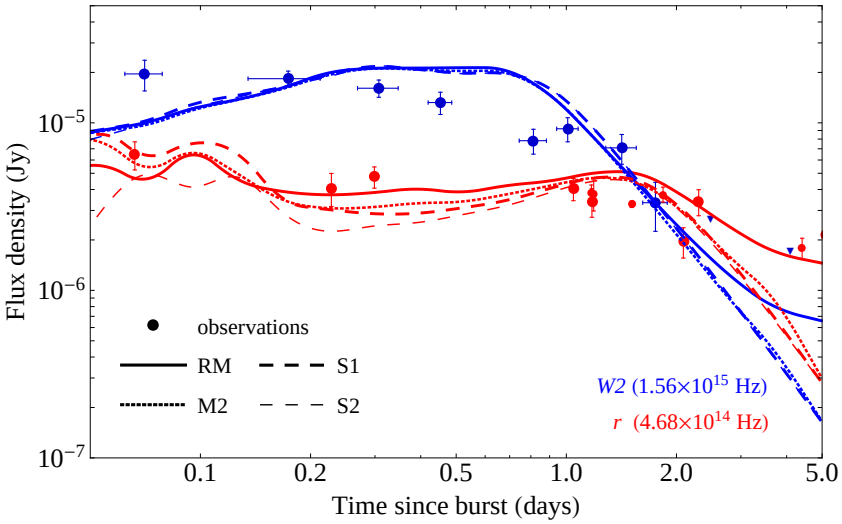

Figure 3.33: Synthetic LCs for different external media. We show two models with uniform media, RM (solid lines) and M2 (dotted lines), as well as two stratified media S1 (thick dashed lines) and S2 (thin dashed lines). The stratification of the EM is set in the in rest-mass density and pressure as $\propto r^{-1}$ (S1) and $\propto r^{-2}$ (S2). Observational data are marked with symbols (see Fig. 3.21).

The difference in strength of the forward and reverse shocks among models with different stratification of the EM also sets the times when the thermal flux becomes the dominant contribution to the observed emission. For model S2, the non-thermal flux density is always smaller than the thermal one, except at about $t_{\rm obs} \sim 0.1\,{\rm d}$, when they are comparable. For models RM, S1 and M2 the non-thermal flux density is larger than the thermal one until $t_{\rm obs} \sim 0.15\,{\rm d}$ (and comparable up to $\sim 0.3\,{\rm d}$; see Fig. 3.33 and compare with Fig. 3.14). Furthermore, it is worth to notice that the r-band flux of RM lies below of that of M2 and S1 models, in spite of the fact that the latter models a less

dense EM and, consistently, the number density of non-thermal particles in the FS is smaller. The larger flux then results from a larger Doppler boosting of the FS radiation, produced because the jet propagates faster in a lower density EM. In model S2, the initial extra Doppler boosting does not compensate the deficit in the emission, which results from the lowest number density among all models at hand. After the initial phase, the thermal emission quickly becomes dominant since the jet advances in a decreasing rest-mass density EM.

3.8 Resolution study

We have performed a resolution study in order to test the convergence of the morphological evolution of the outflows and select an adequate mesh spacing. We have tested three different sizes: $n_{\rm r} \times n_\theta = 2700 \times 135$ (low resolution), 5400×270 (standard resolution; employed in all the models listed in Table 3.1 which have a uniform medium) and 10800×540.

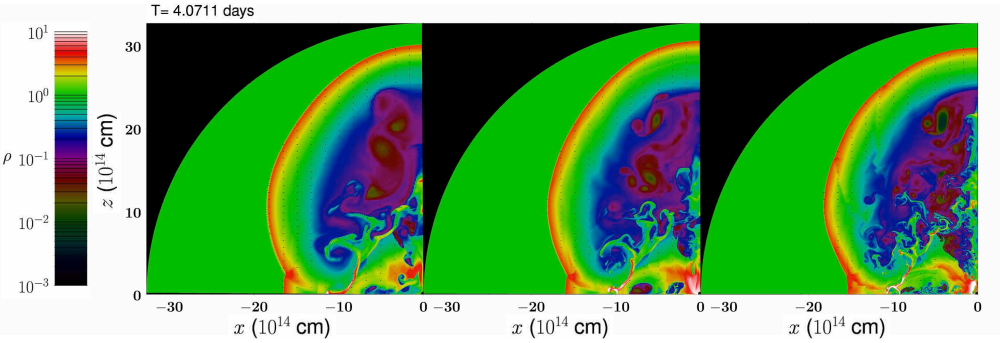

Figure 3.34: Snapshots, at the end of the simulation, of the same model with three different mesh sizes, $n_{\rm r} \times n_\theta = 2700 \times 135$ (left), 5400×270 (centre) and 10800×540 (right).

As we can see in Fig. 3.34 the morphological evolution of all three cases is reasonably similar; the jet head has reached the same position in the z-axis in all the cases. The transverse expansion of the outflow is also consistent. Obviously, the exact morphology of the turbulent internal part of the cavity is not the same, but the exact details of that region are irrelevant to shape

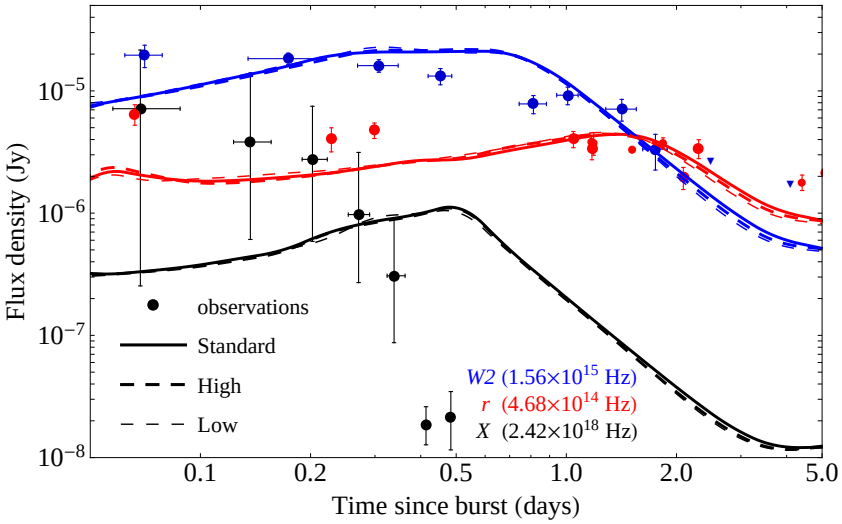

Figure 3.35: Light curves for the RM considering only the (thermal) bremsstrahlung-BB contribution, comparing the convergence of the results employing different mesh sizes, $n_{\rm r} \times n_\theta$: 5400×270 (standard; solid lines), 10800×540 (high; thick dashed lines) and 2700×135 (low; thin dashed lines).

either the non-thermal emission, dominated by the bow and reverse shocks, the properties of which are very similar in the standard and high-resolution runs, or the thermal emission, dominated by the jet/CE-shell interaction. To show that the thermal emission is roughly the same in all three cases we have explicitly computed the light curves due to thermal emission processes for the different resolutions (Fig. 3.35). The fact that the synthetic emission depends only weakly on the resolution is because the jet/CE-shell interaction region is sufficiently well resolved in all cases. Therefore, we are justified in choosing a mesh size $n_{\rm r} \times n_\theta = 5400 \times 270$ (standard resolution) for all our simulations, because it gives the best trade-off between resolution and computational cost.

3.9 Discussion and conclusions

In this work we provide a robust set of numerical models aiming to explain the bizarre phenomenology of GRB 101225A (in particular) and of the so-called

BBD-GRBs (in general).

The CB has been interpreted by T11 as resulting from the merger of a NS with the helium core of an evolved, massive star after a CE evolution. The key ingredient in that model is the ejection of the outer hydrogen layer of the secondary star, which adds a complex structure to the medium surrounding the progenitor system. Using the RHD code MRGENESIS, we have modelled via numerical two-dimensional, axisymmetric, special relativistic simulations the propagation of relativistic jets of different physical conditions through the outer layers of the secondary star and through the circumstellar medium, focusing on the jet/ejecta interaction dynamics. The ejecta are not the result of a self-consistent simulation of the merger of a NS with a He core. Instead, we parametrized the unbound CE matter as a shell that, by the time the ultrarelativistic jet catches up, has expanded out to $\gtrsim 10^{14}\,\mathrm{cm}$. To assess the reliability of our results we have performed a parametric scan of the most important physical properties of the jet (by varying $E_{\rm iso}$ and $\theta_{\rm j}$), of the CE shell (by varying its rest-mass density and its geometry), and of the circumburst medium (by considering either uniform or stratified cases).

Using a full radiative transport code, SPEV, we post-process the previous RHD models and we estimate their synthetic emission signature. We have made a proper comparison between the numerical models and the first 5 d of UVOIR and X-Ray Telescope (XRT) observations post-processing the RHD models with a full transport scheme considering thermal emission processes (free–free bremsstrahlung) and non-thermal (synchrotron) emission.

As anticipated by T11, there are three key elements that any theoretical model of the progenitor of the CB must explain: the persistent X-ray hotspot, the lack of a standard afterglow, and the UVOIR BB evolution. The current special RHD models provide a likely explanation for two of these features, namely, the origin of the thermal emission in the subclass of BBD-GRBs and the effective absence of a classical afterglow. As we have seen, all features result from the interaction between the jet and the CE shell ejected in the late stages of the progenitor system evolution.

Morphological evolution. All simulated jets and ejecta undergo a very similar dynamical evolution that can be divided up into three stages.

In the first phase, an ultrarelativistic jet is injected through a small nozzle at a distance $R_0 = 3\times10^{13}$ cm and freely expands until hitting the inner surface of the CE-ejecta shell.[9]

The second phase begins when the jet encounters the funnel in the ejecta. Since the ejecta have toroidal structure, with a funnel along the symmetry axis, and since the jet is broader than the ejecta funnel, a minor fraction of the jet (its central core) proceeds through the funnel. Simultaneously, the outer layers of the jet impact against the CE shell, much denser than the EM. Because the geometry of the CE shell is non-trivial, a number of oblique shocks result from the CE-shell/jet interaction. Simplifying the picture, we may say that two types of shocks form as a result of the interaction. They propagate at a certain angle with respect to the radial direction (i.e., with respect to the direction of propagation of the jet). Some of the shocks sweep the CE shell and heat it up, while other shocks move towards the jet axis and convert a fraction of the jet kinetic energy into thermal energy. Furthermore, the jet progressively displaces and pushes forward the fraction of the CE shell which is on its path. This is the mechanism by which the jet accumulates substantial baryonic mass, so that a very quick deceleration process begins. The jet injection lasts for ~ 3800 s, a time by which the head of the jet core breaks out of the outer boundary of the CE shell (located at $R_{\rm CE,out} \simeq 10^{14}$ cm). Although, for numerical reasons, the jet injection does not immediately cease at ~ 3800 s, after that time the amount of energy still injected is tiny (the jet luminosity decreases as t^{-4}).

In the third stage, the baryon-loaded, shock-heated jet inflates a cavity, which is initially prolate. The evolution after the first day enters into a quasi-self-similar regime, so that the aspect ratio (i.e., the cross-sectional to longitudinal bubble diameter ratio) grows monotonically. Extrapolating our results indicates that the shape of the cavity, propagating in a uniform, high-density

[9] This first stage is absent in model G0, where we do not set up any gap between the CE shell and the innermost radial boundary of our domain, in which case, the dynamics begins directly in the second phase we describe in the text.

EM, will be roughly spherical after 12–18 d. At this stage, the cavity expansion rate is monotonically decreasing. The speed of propagation of the outer edge of the bubble is mildly relativistic and decreases from $\simeq 0.9c$ (after $\simeq 0.1$ d) to subrelativistic values $\simeq 0.1c$ (after $\simeq 4$ d). Starting from the end of the second phase (roughly coincident with the time at which we stop the jet injection) the initial jet structure is progressively being disrupted and, after a few hours a jet beam cannot be identified any more. The cavity dynamics in this third evolutionary stage strongly depends on the EM characteristics. It is chiefly determined by the balance between the EM mass ploughed by the outermost (forward) shock, and the energy injected into the cavity by the jet. Within the first 4 d of evolution our models accumulate ~ 1–$2M_{\odot}$ from the EM (when it is assumed to be uniform and with a high density). Since the external shock is subrelativistic, it does not leave the typical fingerprint of a standard GRB afterglow. However, this shock has a non-negligible signature in the UVOIR bands (see below). During the third evolutionary stage, the CE shell is fully ablated by the shocks triggered during the second stage of evolution. These shocks transfer momentum to the CE shell and heat it up. After ~ 2 d, the whole CE shell is disrupted and has expanded significantly, lowering by a factor of 10–100 the rest-mass density of the region initially occupied by the CE shell.

On top of the basic evolutionary dynamics described above, we find a number of differences between models, especially during the first hours of evolution. The CE-shell/jet interaction is a non-linear process which depends on the jet energy and its angular extent. Broader jets increase the effective interaction region and incorporate more mass from the CE shell than narrow ones. More energetic jets blow the jet cavity faster, and ablate the CE shell earlier. Additionally, the jets propagating into lower density EM develop more prolate cavities. These tend to adopt a spherical shape later than those of the higher density external media. Another key factor shaping the CE-shell/jet interaction is the CE-shell funnel geometry. As stated above, our model of the CE ejecta stems from the results of past simulations. Here we have considered a simplified (linear) funnel structure and a (more elaborate) 'toroidal' funnel

geometry, where the funnel half-opening angle grows non-linearly from a minimum value at the radial inner face of the CE shell ($\theta_{\rm f,in}$) to a maximum one ($\theta_{\rm f,out}$; see Fig. 3.1). These two funnel geometries change substantially the amount of mass of the CE shell which is within reach of the relativistic jet (the angular region $[\theta_{\rm f,in}, \theta_{\rm j}]$, and the radial region $R_{\rm CE,in}$ to $R_{\rm CE,out}$. This region is very quickly incorporated into the jet beam and contributes to the early jet deceleration. Those shell geometries in which there is a large amount of rest mass close to the symmetry axis maximize the CE-shell/jet interaction and decelerate the jet beam more rapidly. Finally, reducing the rest-mass density of the CE shell the jet is decelerated more slowly, the CE shell is ablated sooner, and the average cavity rest-mass density is smaller. However, these effects do not translate into a very different bubble evolution because most of the cavity mass does not come from the CE shell, but from the EM, which is the same in most of the models we considered.

CE-shell/jet interaction: Thermal radiation & supression of classical afterglow. Apart from the jet/shell interaction dynamics, the landmark of this work is the identification of the regions where the emission is coming from. According to our model, the thermal signature in the CB and by extension in BBD-GRBs should be attributed to the interaction of an ultrarelativistic jet with a dense hydrogen shell in the vicinity of the progenitor star. We find that the UVOIR observations can be chiefly explained as radiation coming from the CE-shell/jet interaction region, rather than the surface of an expanding bubble as proposed in T11. The overall contribution of the expanding hot bubble to the total observed thermal flux is negligible during the first 4 d of evolution. This is especially true in the models with the lower rest-mass density in the EM. According to our models, the region from where most of the thermal emission comes from is much smaller ($\lesssim 5 \times 10^{13}$ cm) than the size of the cavity blown by the simulated jets (with a size that grows up to $\lesssim 10^{15}$ cm). Furthermore, the thermal emitting region in the UVOIR bands is a mixture of transparent and semitransparent regions.

From observations a spectral inversion in optical bands can be distinguished

between 1.5–2 d, also observed in our models. This spectral reddening is caused by the transition from an optically thick to an optically thin emitting regime, in which the W2-band flux density starts to decay much faster than that in the r band. The dynamical reason for such a transition is the complete ablation of the CE shell by the outward pushing ultrarelativistic jet. Indeed, model RM captures very precisely this transition and that has been one of the main reasons to choose it as a reference case.

Since the CE shell is cold and much denser than the jet, the jet/CE-shell interaction stimulates the thermal bremsstrahlung emission of the shocked CE shell, and we receive a long-lasting thermal emission that decays very quickly once the CE shell is fully disrupted by the jet and the system becomes transparent. The time it takes to disrupt the CE shell depends on the balance of several factors. Less massive shells (e.g., model D2) are more rapidly ablated and show a clear flux density deficit with respect to the observations and with respect to the RM. However, how the mass is distributed in the shell is also important. Shells that are more massive closer to the axis of the system (e.g. our model G3, where the funnel of the toroidal shell is narrower than in the RM) or wider jets (e.g., model T20, with a larger half-opening angle than the RM) tend to increase the strength of the jet/CE-shell interaction and they can also be disrupted faster. Since our models assume a geometry and a mass for the CE shell (rather than computing the CE-shell geometry as a result of the neutron star/He star merger), we can only qualitatively compare our results with the observations.

In a consistent simulation of the merger phase of a CE-binary system, the ejected CE shell will not have the sharp boundaries we are employing in our models to simplify the problem. Instead, we expect a relatively smooth transition between the He-core and the densest part of the CE shell. If the amount of mass in the region below the radius that we have named $R_{\rm CE,in}$ and the He-core is small compared with the mass between $R_{\rm CE,in}$ and $R_{\rm CE,out}$, there will not be appreciable differences in the overall thermal emission with respect to the models in this work (neither in the overall total emission). More notable differences may arise if the CE shell extends towards (much) larger

radii, since in this case, if we fix the CE-shell mass (and consistently, reduce the average shell density), the emitted thermal flux (proportional to $\rho^2_{\rm CE,sh}$) will be strongly suppressed. Furthermore, the spectral reddening of the models will happen at a different time than in our RM. For instance, in the case in which $R_{\rm CE,out}$ is larger than assumed in the RM, but the CE-shell mass is fixed, the spectral inversion will happen earlier than in our RM. Hence, to reproduce the spectral reddening at the right time after the burst, our models favour CE ejecta that do not travel much further away than $\sim 10^{14}\,$cm during the final inspiral in of the neutron star on to the He-core, if the mass of the CE shell is a fraction of a solar mass.

The lack of a classical afterglow (or the presence of a very faint one) also results from the jet/CE-shell interaction, which baryon loads the beam of the jet leading to a much faster deceleration than what one would expect in the case in which the EM of the GRB progenitor star would not harbour such an 'obstacle' for the jet propagation.

All these conclusions do not change if we consider a different EM, such as a more realistic stratification of the rest-mass density and of the pressure. Though the dynamical differences are apparent, the thermal emission does not differ much with respect to the corresponding models with a uniform EM. The reason is that, as stated above, the origin of the thermal emission is the jet/shell interaction, and, models having the same CE-shell and jet parameters yield very similar thermal light curves.

The agreement with observational data in the UVOIR bands is not optimal during the first $\simeq 0.2\,$d, in which we underpredict the observed flux by a factor of $\lesssim 3$. However, we have seen that the non-thermal contribution may account for the flux deficit at early times.

EM/jet interaction: Non-thermal radiation. Though it is true that we do not observe a classical afterglow signature, our jet models still develop a hot cavity bounded by a pair of forward and reverse shocks. We show that the FS synchrotron emission is very important to compensate for the thermal flux deficit at early times, particularly at low optical frequencies (r band). The

contribution of the non-thermal radiation in the X-ray band is very small and can be neglected for practical purposes. The emission of the RS is comparable to that of the FS during, approximately, the first $\sim 80\,\mathrm{min}$ of evolution. After that, it quickly decays because the RS is smeared out as a result of the jet/CE-shell interaction. This interaction generates a number of shocks which move almost perpendicularly to the jet propagation direction. Besides adding a minor contribution to the observed non-thermal flux density, such shocks cross the jet beam and eventually reach the jet axis. Along the way, they raise the rest mass and the entropy of the ultrarelativistic beam with the side effect that the jump in the hydrodynamical variables through the RS is basically cancelled.

The quantitative contribution of non-thermal (synchrotron) processes to the observed flux depends on the set of microphysical parameters adopted. In the present work, we have assumed somewhat low effective efficiencies for the RM, the one which accommodates better the observations. For the RM, having an isotropic equivalent energy $E_{\rm iso} = 4\times10^{53}\,\mathrm{erg}$, values of $\epsilon'_{\rm e} = \epsilon_{\rm e}/\zeta_{\rm e} \lesssim 0.1$ and $\epsilon_B = 10^{-5}$–10^{-6} are needed to not overpredict the UVOIR flux at early times. Larger efficiencies $\epsilon'_{\rm e} \simeq 0.1$ and $\epsilon_B \simeq 10^{-3}$ are also marginally compatible with observations if $E_{\rm iso} \simeq 10^{53}\,\mathrm{erg}$ (though the $W2$ band displays an obvious flux deficit in this case). We point out that technical difficulties prevent raising ϵ_B in our models. Values of ϵ_B in excess of 10^{-4} yield synchrotron cooling time-scales which are smaller than the typical time steps of our hydrodynamical models and cause order of magnitude errors in the estimation of the non-thermal flux density (particularly at high optical or X-ray frequencies).

In the present work, we have restricted the analysis to the case in which the microphysical parameters are uniform and time independent for all shocks. However, it seems quite plausible that the RS has a larger value of ϵ_B than the FS (see e.g., De Pasquale et al. 2015). Should that be the case, the RS signature might be more prominent during the first $\sim 0.06\,\mathrm{d}$. Values of the power-law index of the energy injection spectrum of the electrons, q, in excess of the reference value ($q = 2.3$), tend to reduce a bit the total flux density during the first $\simeq 0.6\,\mathrm{d}$ of evolution, making them less likely, unless we combine an

increase of q with a moderate increase in, e.g., $\epsilon_{\rm e}$.

Since the dominant thermal contribution in our models is not associated with the expanding cavity blown by the jet, and since the non-thermal emission produced by the FS (that strongly depends on the properties of the EM) is subdominant throughout most of the evolution, the exact structure of the EM does not show up until observing times $t_{\rm obs} \gtrsim 2\,{\rm d}$. By that time, the flux density decreases more shallowly in models with a uniform and high-density EM than in models with a density decaying or uniform low-density ones. In the uniform, high-density medium, at low optical frequencies (r band), the flux decays as $\propto t_{\rm obs}^{-1.4}$ between the second and the third day, while it does as $\propto t_{\rm obs}^{-1.9}$ in the $W2$ band. This trend should be compared to the decay $\propto t_{\rm obs}^{-2.7}$ in both S1 and S2 models where the rest-mass density and pressure decrease as r^{-1} and r^{-2}, respectively. Model M2 (uniform, low-density medium) shows a flux decay which lies between RM and models S1–S2 (although more similar to the latter ones). Remarkably, the time when the system becomes optically thin is also $t_{\rm obs} \simeq 1.5$–$2\,{\rm d}$. The transition to transparency depends only on the time it takes the jet to completely ablate the CE shell, which is largely independent of the EM if the CE-shell mass is fixed and its radial extension is not drastically changed. The differences in the emission at early times caused by the EM structure are much more dependent on the parameters of the set-up than, e.g., the time of transition to transparency and the typical location of the peak in different UVOIR bands.

We point out that using the same radial gradients as in our models S1 and S2, but a (much) larger initial rest-mass density, so that the Sedov length of models S1 and S2 was the same as that of the RM (i.e., similar to the set-up of De Colle et al. 2012) may have brought a stronger non-thermal emission. However, our choice for a reference model having a uniform environment is motivated by the fact that under the assumption that the progenitor system of BBD-GRBs were neutron star/He star mergers, the environment of the later may not develop the strong winds typical of massive stars with solar metallicity.

X-ray evolution. In the X-ray band, T11 conclude that $\sim$ 20 per cent of the flux can be attributed to a bright hotspot, radiating as a BB at a temperature $\simeq$ 1–1.5 keV until $\lesssim$ 0.34 d. The X-ray flux estimated from our models is marginally consistent with such an observational fit until $\lesssim$ 0.3 d. Furthermore, during that period of time the brightness temperature we infer from our models of the X-ray emission is $\sim$ 0.2 keV. However, we overpredict the duration of the X-ray emission, whose maximum happens in our models $\sim$ 0.5–0.7 d after the GRB. After $\simeq$ 0.3 d, our models overestimate X-ray flux. The main reason for the discrepancy is that the X-ray emission comes from a significant fraction of the CE-shell/jet interaction region. This region is much larger ($\lesssim 4 \times 10^{13}$ cm) than the size estimated for the X-ray hotspot in T11 ($\simeq 2 \times 10^{11}$ cm). However, our simulations indicate that radiative flux has a very strong dependence on the geometry and the density gradient of the CE-shell funnel. In particular, the 'toroidally' shaped funnel seems to reduce X-ray flux. Therefore, extrapolating our results, we suggest that an initially narrower funnel with a larger density would improve the results obtained in the X-ray band. Unfortunately, this would require substantially increasing the numerical resolution of our models close to the symmetry axis, and likely, extending the CE shell towards smaller radii. Both facts drastically reduce the time step with which we shall run our models and notably enlarge the execution time.

Distribution of total emission. For an observer looking head on at the event, the spatial distribution of the received radiation will evolve with time (Fig. 3.36). Initially, the thermal emission from the jet/CE-shell interaction region together with the non-thermal emission from the RS and the shocks resulting from the jet/CE-shell interaction will be concentrated around the centre of the observed region. In addition to these components, a comparable emission arising from the FS will be seen as limb brightened (Fig. 3.36, left). At these early times, the emission pattern will be 'core dominated'. As the CE shell is ablated by the jet, the core emission will weaken and, eventually, the residual thermal emission from the whole bubble and the non-thermal emission from the FS will be the only observable components, both of which will be limb

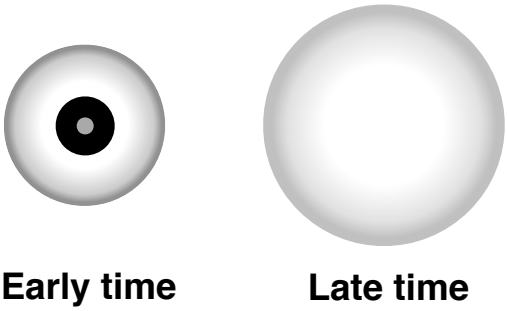

Figure 3.36: Schematic representation of the distribution of received radiation at early times (left) and at late times (right) for an observer viewing the event at 0°. The grey-scale is roughly associated with the flux density, black being the largest flux and lighter grey shades showing lower intensity values. The figure is not directly obtained from simulation data, though it is an attempt to sum up the general properties of most of the numerical models.

brightened. Thus, at late times we expect a 'limb-dominated' emission pattern. We predict that the change in time from core- to limb-dominated emission will most probably produce have a significant change in polarization.

Applicability of the model. The emission model of GRB 101225A is extended to the subclass of BBD-GRBs, i.e., GRBs with a prominent thermal component in their emission spectrum and likely associated to SN. In particular, the CB has been associated to a faint SN observed as a small bump in the optical LCs (T11). The NS/He merger is able to produce such a weak SN explosion since it may produce only a small amount of nickel-56. Exact calculations of this value have not been made for our particular event, however Cano et al. (2017) estimate a mass of $M_{\rm Ni} \sim 0.4 M_\odot$ which in principle is roughly larger than expected as it is compatible with more "standard" GRB/SN (e.g., SN 1998bw associated with GRB 980425 in which case it has been obtained, by means of a model, a nickel-56 mass of ~ 0.3–$0.5 M_\odot$, Mazzali et al. 2006, 2014). A proper estimate of the nickel-56 mass relies on the analysis (or even by comparison with other SNe) of the bolometric LC, however this is not avail-

able for the CB's SN so that only estimates by comparing a single band can be made (therefore, they should be taken with caution). The absolute magnitude in V band that was initially (i.e., for a redshift $z = 0.33$) calculated was $\mathcal{M}_V = -16.7$ mag (T11). When corrected for the new redshift ($z = 0.847$) this becomes $\mathcal{M}_V = -17.93$ mag (Pian, private communication), which is a magnitude fainter than that of SN 1998bw in the same band. For GRB 100316D/SN 2010bh, an event similar to the CB, estimations on the nickel-56 mass were done by comparing its bolometric LC peak with that of the SN 1998bw which is one order of magnitude larger, thus, indicating a nickel-56 mass of $\sim 0.12 M_\odot$ (Cano et al. 2011; Bufano et al. 2012). Based on these arguments, the mass on the CB's SN should not exceed $M_{\rm Ni} \lesssim 0.1 M_\odot$. On the other hand, Thöne et al. (2015) make a new estimate obtaining $\mathcal{M}_B = -19.4$ mag (in the B band) that, as they argue, makes the CB's SN more similar to SN 1998bw (in that sense, the nickel-56 mass estimated by Cano et al. 2017 would be consistent). All in all, our model could be applied also to afterglows of another (ultra-)long GRBs with faint as well as more luminous, standard SN, whatever its progenitor system.

Model restrictions & other alternatives. As a cautionary note, we want to outline that our models support the possibility that BBD-GRBs are the byproduct of NS/He mergers, but do not rule out other possible progenitor models for BBD-GRBs. Our models assume a specific distribution of rest mass in the EM surrounding the progenitor. NS/He mergers provide such structure naturally, but we may not discard the possibility that in single-star progenitor models (e.g., Nakauchi et al. 2013) the original massive star ejects mass non-isotropically. If this mass is preferentially ejected along the equatorial regions and leaves a relatively low-density funnel around the rotational axis of the system, we foresee that the jet/EM interaction would result in a dynamics qualitatively similar to the one described in this work. Hence, we also preview a non-trivial thermal signature in the latter case.

Our models accommodate better the observational data if the GRB-jet (true) energy is $\lesssim 10^{52}$ erg. According to Fryer et al. (2013), this places some

(soft) restrictions of the mass of the He cores that shall merge. For neutrino-powered jets, it would be requested that the He core mass be larger than $\sim 10 M_{\odot}$. However, if the jet is magnetically powered, the previous restriction is not so stringent in practice, since for He cores with masses $\gtrsim 3 M_{\odot}$ one may get a sufficient amount of energy.

The fact that our models with a large CE-shell mass ($M_{\rm CE,sh} \simeq 2.6 M_{\odot}$) is at odds with observations is suggestive of several possibilities: (1) that the secondary star of the merger has either a relatively small He-core mass, (2) that most of the envelope of the secondary has been ejected before the final CE phase begins, or (3) that the fraction of the CE participating in the thermal emission during the first 2 d is relatively minor compared with the rest of the (likely bound) CE interior to the CE shell. Elucidating which of these possibilities is more likely is not possible with our models, since they depend on the initial mass distribution in the envelope of the star, i.e., on the details of a region not included in our models.

Finally, we have to mention that our treatment of the emission has certain limitations. For instance, we do not include the Comptonization of the radiation flux though we plan to incorporate it in the near future. Also, our models would need a higher resolution to properly resolve the CE-shell funnel if the CE-shell innermost radius ($R_{\rm CE,in}$) was smaller. The interest of such a set up is that in T11, the X-ray emission of the standing hotspot is attributed to the shocked funnel, with a transversal size of a couple of solar radii ($\sim 10^{11}$ cm). In this work the cross-section of the funnel is $\simeq 8 \times 10^{11}$ cm, limited by the resolution we can have in the broad parametric scan of models we have performed. Hence, the X-ray synthetic LCs, though compatible with observations, display a clear excess of flux after $\simeq 0.3$ d. We will address this issue in the future with higher resolution models.

Chapter 4

On the breakout of GRB jets from massive stars

The current theory of stellar core collapse considers a variety of outcomes for the post-collapse evolution of the cores of massive stars ($M_{\rm ZAMS} \gtrsim 8\,M_\odot$). These outcomes are supported by a large number of observations of SN explosions, GRBs, their remnants, and the compact objects they leave behind. One of the possibilities involves the formation of a PNS, from which a shock wave is launched and fails to reach the outer layers of the star but stalls inside the core. Neutrino heating, hydrodynamic instabilities, and, likely, other mechanisms such as rotation and magnetic fields counteract the accretion of the surrounding shells increasing the mass of the PNS. The balance between these effects may lead to a SN explosion and the PNS at the centre gradually transforms into a NS. Alternatively, the PNS may grow beyond the maximum mass supported against self-gravity and, finally, collapse to a BH. The latter outcome is probably inevitable if the SN *fails* to blow up the stellar envelope.

The first scenario (SN explosion and NS formation) seems likely particularly for stars in the lower range of masses (for recent studies, see, e.g., O'Connor & Ott 2011; Janka 2012; Ugliano et al. 2012; Nakamura et al. 2015; Sukhbold et al. 2016; Bruenn et al. 2016), while we might encounter conditions favoring BH formation with or without SN explosion among stars with higher masses

(Obergaulinger & Aloy 2017). The former studies suggest a fairly complex dependence of the final outcome on the progenitor conditions rather than, e.g., a clear threshold at a certain mass.

There are several open questions concerning some GRBs associated to SNe, especially in the case of llGRBs (but not restricted to them). The atypical prompt emission, the origin of X-ray blackbody (BB) components, and the unusual X-ray afterglow are difficult to fit in terms of standard GRB theory. In light of the current observational data (see Sect. 1.2), it is still unclear whether progenitors of llGRBs are the same as that of LGRBs or whether these ultra-long llGRBs are members of a low-luminosity end of a continuum of collapsar explosions or, maybe, a different stellar endpoint. Answering these questions has important implications for high-mass stellar evolution, the connection between SNe and GRBs, and the low-energy limits of GRB physics, especially taking into account that llGRBs are likely more frequent than cosmological GRBs (see Sect. 1.3). The particularities of these bursts, the mounting amount of observations in many wavebands (in some cases), and the active debate they generate in the scientific community (see, e.g., Irwin & Chevalier 2016 for an excellent review) make these particular llGRBs very interesting targets for theoretical and numerical modeling. The latter is extremely challenging because of the disparity of length and time scales involved in the modeling.

Several SNe light curves (LCs) have been observed well before the SN lightcurve peak both in the UV/optical bands (Gezari et al. 2008, 2010; Soderberg et al. 2008). In several cases, GRB 060218/SN 2006aj (Campana et al. 2006), X-ray flash (XRF) 080109/SN 2008D (Soderberg et al. 2008) or GRB 100316D/SN 2010bh (Stamatikos et al. 2010; Chornock et al. 2010), observations reveal a relatively luminous XRF. The signal produced by GRB 060218/SN 2006aj and XRF 080109/SN 2008D have been considered by the astronomical community as prototypes of the signature left by a SN shock breakout. A number of theoretical models have addressed the early UV/optical post-breakout LC, on time-scales $\sim 1\,\mathrm{d}$ (Chevalier & Fransson 2008; Nakar & Sari 2010). The XRF is more challenging to model, since it shall include the properties of radiative shocks propagating through the density declining stellar envelope.

If the shock velocity is $\gtrsim 0.07c$, free–free emission will be unable to produce a sufficiently large photon number density to produce a BB spectrum (Katz et al. 2010). Hence, as pointed out by Balberg & Loeb (2011) any analysis of the breakout LC based on the assumption of local thermodynamic equilibrium and a BB spectrum may not reproduce the photon flux and spectrum emitted from the shock region during breakout.

In this chapter we aim to obtain an approximate radiative signature of the process of breakout of relativistic collimated jets out of the surface of compact progenitor stars. As a first approximation to the problem, we only consider the thermal emission produced by the jet/progenitor interaction. Even more, we restrict ourselves to the case in which thermal bremsstrahlung is the dominant emission process. Comptonization and pair creation are neglected in this simplified approach to the problem at hand. We do not restrict ourselves to the subset of nearby llGRBs, but instead we address the "generic" case of LGRBs in order to assess which are the observational properties to be expected in more standard GRBs also likely associated to SNe. We aim, in this way, to find observational features which could help distinguishing between collapsar and non-collapsar events and, to suggest potential observational signatures to be undertaken in suitable observational campaigns. As we shall see, we have only partly succeed in our goals due to the extremely large computational resources needed. Thus, we advance the reader that the contents of this chapter show our route towards our goal and the problems found along the way, being our conclusions in this field only preliminar.

Following the ideas of Nakar (2015), we work under the hypothesis that the stellar progenitor from which LGRBs and llGRBs are produced is the same originating Type Ic SN explosions. This means that we will consider compact stellar progenitors without a hydrogen envelope whose radius is smaller than 10^{11} cm. However, the outer stellar layers or the close circumstellar environment might be affected by different physical mechanisms, which drive a non-negligible fraction of the stellar mass towards the aforementioned locations.

The outline of the chapter is as follows. In Section 4.1, we explain the

details of our physical model. We describe the progenitor system (a Wolf-Rayet (WR) surrounded by an inflated envelope) and the setup of our SN ejecta and jet simulations. In Section 4.2, we study the hydrodynamic properties of both simulations of SN ejecta (Sect. 4.2.1) and jets (Sect. 4.2.2) propagating in the WR and the external medium. In particular we try to discern possible differences between those jet models in which a previous SN ejecta has been injected from those in which the SN is absent. We also discuss about the reservoir of energy in jets that could be converted into radiation (Sect. 4.2.3). In Section 4.3, we study the radiative evolution of our models. We show that the origin of the thermal radiation comes from the RS shock region. Afterwards, we compute LCs and spectra at the times following the break out of the star of the SN and jet models (Sect. 4.3.3). Due to some technical problems (Sect. 4.3.1), part of the results are provisional and have to be taken with some caution. In Section 4.4, we discuss our results, propose possible improvements in our models and present some conclusions of this on-going work.

4.1 The model

The signature of the jet breakout is likely driven by the hydrodynamic interaction of a collimated relativistic outflow with the outer stellar layers and/or the circumstellar medium. This problem can be decoupled from the precise central engine responsible for the energy input of the relativistic outflow which we therefore neglect in our models. Instead, we focus our modeling on the propagation of an already generated and collimated relativistic jet inside of a progenitor massive star whose zero-age main sequence (ZAMS) mass is $35 M_{\odot}$ (Sect. 4.1.1). For this purpose, we can excise the inner iron core of the massive star and map in our computational domain the remaining stellar progenitor as well as an assumed circumstellar medium. Physically, the outer layers of the star are in hydrostatic equilibrium and no causal connection exists between them and the core on time scales smaller than the free-fall time of each mass shell onto the core. Since our models need to be run for dynamical times comparable to the sound crossing time of the star, in order to keep our stellar

model in hydrodynamic equilibrium (especially to keep the surface of the progenitor star at rest) we include the effects of self-gravity in an approximated way (App. C).

In order to incorporate in our model the dynamics generated by an ongoing SN explosion, we add to our stellar progenitor a synthetic SN ejecta (Sect. 4.1.3) driven *ad hoc* by a *piston* mechanism (Sect. 4.1.3.1). We have performed simulations of SN ejecta propagating through the envelope of our stellar progenitor in 2D (not shown in this thesis). However, the ejecta in 2D become Rayleigh-Taylor unstable as they propagate through the stellar envelope (e.g., Arnett, Fryxell & Mueller 1989; Fryxell, Arnett & Mueller 1991; Mueller, Fryxell & Arnett 1991). A proper accounting for the instability growth requires extremely fine numerical resolution in reach only for AMR codes (e.g., Kifonidis et al. 2003). But even with the adequate numerical resolution the development of the instability along the symmetry axis of the star is affected by coordinate singularities close to that axis (see the numerical artifacts along the axis on fig. 13 of Kifonidis et al. 2003). As we aim to inject a jet through a nozzle centered at the symmetry axis of our computational domain, the interaction of the jet with the numerically driven structures close to the rotational axis would result in artificial dynamics in our jet/SN shock interaction models. To prevent such behaviour, we have simplified our set up reducing the SN ejecta propagation to a 1D, spherically symmetric problem. Beyond the simplified jet/SN ejecta interaction, the 1D ejecta modelling reduces considerably the computational cost associated to the calculation of its hydrodynamic evolution as it travels inside of the stellar envelope.

After letting the SN shock travel for some time, we map the 1D shock structure into our 2D computational domain. Certainly, we do not expect a SN shock launched in a fast rotating stellar progenitor (as the one at hand) to be perfectly isotropic. However, with the current approximation we may approximately explore the dynamical and observational imprint of a relativistic jet catching up with the SN shock. We point out that Nagakura et al. (2011) have also studied how the earlier emergence of a shock can influence the propagation and emission of a jet. In the work of Nagakura et al. an ongoing shock

arises naturally after gravitational collapse is stalled in the star envelope by the effect of centrifugal forces (i.e., it is not the SN shock resulting from the core collapse, which in Nagakura et al.'s model is assumed to have been swallowed by the central BH). Furthermore, we note, that the progenitor model employed in Nagakura et al. (2011) is not directly a progenitor resulting from a stellar-evolution code. Instead, the authors build their own rotating equilibrium configuration to closely mimic the density distribution of model 16TI from Woosley & Heger (2006). This model corresponds to a metal poor star that has a ZAMS mass of $16M_{\odot}$, and rotates rapidly.

As mentioned before, we assume that a relativistic jet has been already formed inside our inner boundary, which is located at $R_9 \sim 1$, where we express the radius in terms of $10^9\,\mathrm{cm}$, $r = R_9 10^9\,\mathrm{cm}$. This position has been chosen because it puts our inner boundary well outside the iron core and the surrounding matter that has fallen onto the hypermassive PNS by the time we start our simulations (see Obergaulinger & Aloy 2017). Consistently, we inject a conical flow through the innermost boundary of our computational domain in the medium left behind by the SN ejecta (Sect. 4.1.4). We explore the dependence of the jet breakout based on whether the SN ejecta is present or not (Sect. 4.2).

Finally, we compute in a postprocess phase the synthetic emission of the 2D hydro simulations solving the full radiative transport problem (Sect. 4.3). Since we employ the radiative transfer scheme as presented in Sect. 2.4 and throughly employed in Chap. 3, our numerical method for computing the expected observational signature of the shock breakout goes well beyond that of Nagakura et al. (2011).

4.1.1 The progenitor star

Initially the mass of collapsars was theoretically speculated to be in the range of $25 - 35M_{\odot}$ (MacFadyen & Woosley 1999). In recent observations of GRB/SN associations –as we have seen, collapsar candidates– it has been possible in some cases to establish an initial mass of the progenitor beyond this range, reaching values up to $\sim 40M_{\odot}$ (see, e.g., for GRB 980425/SN 1998bw; Naka-

mura et al. 2001, or for GRB 031203/SN 2003lw; Mazzali et al. 2006). On the other hand, GRB production seems to be also favored in models of rotating stars with masses between 40 and $60 M_{\odot}$ (Georgy et al. 2012).

As progenitor star we take the presupernova model 35OC of Woosley & Heger (2006), which corresponds to a $35 M_{\odot}$ main-sequence star. This model is one of the most massive stars evolved by Woosley & Heger (2006) that has enough rotational energy to be considered a GRB candidate. One reason for the high rotational energy is the weak mass loss the star suffers on the main sequence, which is partly due to its low metallicity (10% of solar). The star reaches core collapse as a WR star with a final mass of $28.07\,M_{\odot}$ and an iron core of $2.02\,M_{\odot}$. We note that Georgy et al. (2012) confirm the importance of rotation for the formation of WR stars and type Ib/c SNe. From the stellar evo-

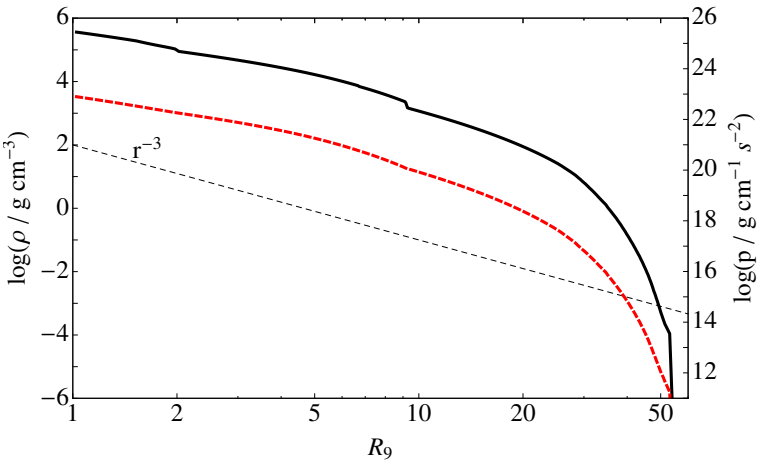

Figure 4.1: Rest-mass density (black solid) and pressure (red dashed) profiles of model 35OC (Woosley & Heger 2006). R_9 is the radius in units of 10^9 cm.

lution model 35OC we take the density (Fig. 4.1), pressure and radial velocity profiles, but we ignore the angular velocity profile for several reasons: (1) the rotational kinetic energy is very small in the layers of the star beyond 10^9 cm, and (2) in order to keep more easily the hydrodynamic equilibrium of the stellar model. The stellar radius of the 35OC model is $R_{\star} = 5.31 \times 10^{10}$ cm, i.e., it is a rather compact stellar progenitor. We have not considered the chemical

composition of the different layers, and thus, nuclear burning is not considered. This can affect slightly the outcome as pointed by Lazzati et al. (2012). For simplicity, the chemical composition in the star is assumed to be uniform and fixed by the ratio of relative abundance of hydrogen over heavier elements, $X_{\rm h}$. As the progenitor is expected to have lost all the hydrogen, we have adopted a very small value. In particular, we have taken $X_{\rm h} = 0.02$, found by Szécsi et al. (2015) at the end of evolution of their models of low-metallicity massive stars that evolve chemically-homogeneously (which are expected to end as fast rotating WRs). We note that their models are evolved, so far, only until the end of the main-sequence stage and this value may be closer to zero for models evolved up to the presupernova point. The same value of $X_{\rm h}$ is assumed in the external medium.

We map the model 35OC onto an initial radial grid composed of three uniform-spaced subgrids (Fig. 4.2), covering the range $[R_0, R'_{\rm out}] = [10^9, 2 \times 10^{12}]$ cm. The first radial subgrid has $n_{\rm r,1} = 1200$ zones and covers the range $[R_0, 6.1{\times}10^{10}\,{\rm cm}]$ (i.e., the resolution is $\Delta r_1 = 5{\times}10^7$ cm), while the second one has $n_{\rm r,2} = 9400$ zones and covers the range $(6.1{\times}10^{10}\,, 10^{12}]$ cm ($\Delta r_2 = 10^8$ cm) and the third one has $n_{\rm r,3} = 2500$ zones and covers the range $(1, 2] \times 10^{12}$ cm ($\Delta r_3 = 2 \times 10^8$ cm). Since our models need to be run for a rather long time, the set up flows may eventually reach the limit of the basic grid sketched above. When this happens, we extend the computational domain in the radial direction. The extension is done by adding chunks of external medium with the same resolution as in the third level (Δr_3). The three different resolution levels have been chosen in order to suitable resolve all the large gradients that may eventually show up in the stellar interior and its surface (first level) and in the external medium (second and third level). Obviously, in 1D we could employ much finer numerical grids. Nevertheless, much larger resolutions are not viable in the subsequent computational phase in 2D (Sect. 4.1.4). The resolution we have employed in our models is a trade off between what we would optimally need to attain a global convergence of the main morphological features of our jets (e.g., forward shock (FS) and reverse shock (RS) positions, widths of the cocoon, etc.) and what we can afford with the computational

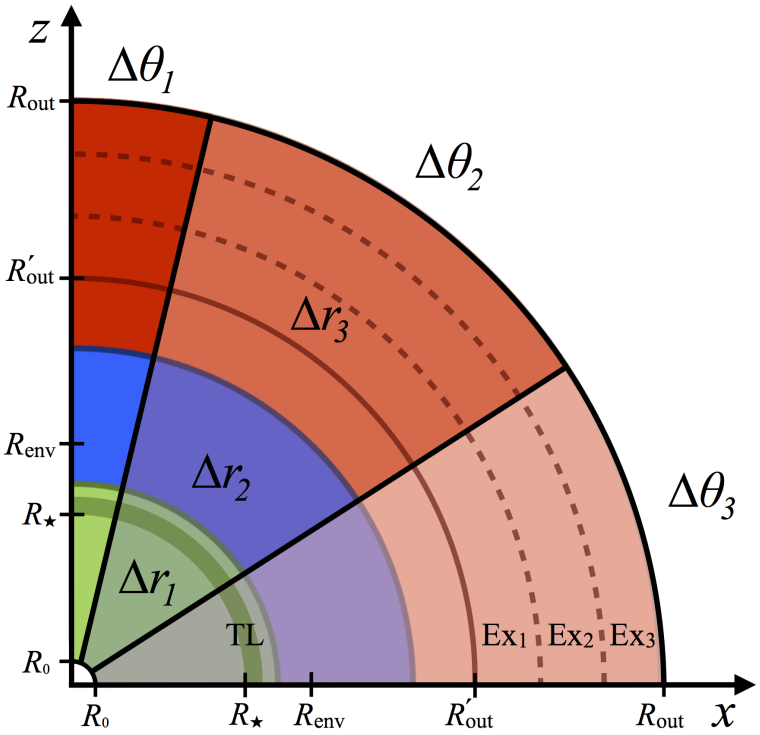

Figure 4.2: Sketch of the numerical grid. We use three subgrids with different levels of refinement along both radial (green, blue and red) and angular directions (dark to lighter colours). The stellar surface ($R_\star$), the transition layer (TL; dark green annulus; included in the first level of refinement of the radial grid), the envelope extension ($R_{\rm env}$) and the the initial ($R'_{\rm out}$) and final length of the radial grid ($R_{\rm out}$) after the inclusion of three extra chunks (denoted as 'Ex') are marked in the figure. Note that the sketch particularly describes the grid setup in model SH. For jet simulations the sketch is equally valid but R_0 should be replaced by $R_{\rm inj,j}$. Furthermore, we stress that $R'_{\rm out}$ and $R_{\rm out}$ have different values and that only two extra chunks, with a different extension than those in model SH, are added to the grid in jet models. See the text for more details. Figure is not to scale.

resources available. As we shall see, the resolution beyond 10^{12} cm (i.e., in the third coarser resolution level) has proven to be insufficient for a reliable estimation of the radiative signature ~ 0.6 s, in the worst case, after the jet

breakout. The mass beneath R_0 is $M_{\rm in} \approx 3.385 M_\odot$. We assume that this mass will collapse to form a PNS first and, eventually, to a BH (Cerdá-Durán et al. 2013).

4.1.2 External medium

The initial data of our simulations represent a stellar core at the onset of collapse. Although the stellar-evolution calculations the model is based on (Woosley & Heger 2006) include all important processes, the approximations required for following the evolution during the hydrostatic phases entail limitations in several aspects that are particularly relevant to the present study. Of those, we highlight the mass loss due to the intense winds driven by radiation pressure common to high-mass stars, which modify the environment of the star and may generate inflated envelopes or, in the most extreme cases, generate dense shells around the star.

From the physical and numerical modeling point of view, the rate of mass loss depends crucially on processes in the outer shells of the stars whose small length scales and short time scales impede a detailed modelling and which, therefore, are included in the models in a simplified, parametrized way. The parametrization can be calibrated by comparing the resulting stellar models to observations of stellar winds. For WR stars, commonly considered potential progenitors of GRBs and the focus of our work, mass-loss rates between $\dot{M} = 10^{-5}$ and $10^{-4}\, M_\odot\, {\rm yr}^{-1}$ have been inferred (for a review, see Crowther 2007). The gas injected in the wind surrounds the star in an expanding layer whose properties are not included in the stellar-evolution model but can be inferred from the models of Sanyal et al. (2015) displaying an inflated envelope of a mass $M_{\rm env} \sim 10^{-6}\, M_\odot$ with a roughly uniform density of $\rho_{\rm env} \gtrsim 10^{-10}\, {\rm g\, cm}^{-3}$.

Consistent with the low metallicity of the stellar progenitor model 35OC, Woosley & Heger (2006) assume that the mass loss rate for this model is a factor 10 smaller than "typical" for Type Ib SN. Indeed, this model has lost $\sim 7 M_\odot$ into the wind according to the stellar evolution calculation. Thus, we may consider that a mass loss rate consistent with the stellar progenitor at hand is $\dot{M} \simeq 10^{-7} \dot{M}_{-7}\, M_\odot\, {\rm yr}^{-1}$. The implication of such a low mass loss rate

is that the density of the wind right at the stellar radius should be

$$\rho_{\rm w} \sim 1.9 \times 10^{-11} {\rm g\,cm^{-3}} \dot{M}_{-7} v_{\rm w,100}^{-1} R_{\star,5.3\times10^{10}}^{-2}, \tag{4.1}$$

where we have assumed a typical wind speed of $v_{\rm w} = 100 v_{\rm w,100}\,{\rm km\,s^{-1}}$ and scaled the radius of the star as $R_\star = 5.3 \times 10^{10} R_{\star,5.3\times10^{10}}\,{\rm cm}$. This value is so low that the optical thickness of the wind is expected to be

$$\tau_{\rm w} \sim \int_{R_\star}^{\infty} \rho_{\rm w} (R_\star/r)^2 \kappa {\rm d}r = \rho_{\rm w} \kappa R_\star \simeq 0.2 \kappa_{0.2} \dot{M}_{-7} v_{\rm w,100}^{-1} R_{\star,5.3\times10^{10}}^{-1}, \tag{4.2}$$

where we have assumed a frequency independent opacity in the (hydrogen-free) wind $\kappa = 0.2\kappa_{0.2}\,{\rm cm^2\,g^{-1}}$. Hence, the wind in our progenitor model shall be optically thin. This is in clear contrast with the standard assumption that the wind surrounding typical Type Ic progenitors is optically thick (e.g., Li 2007; Balberg & Loeb 2011) and it may have large implications on the expected phenomenology.

The mass loss of massive stars can be studied not only during hydrostatic phases of stellar evolution, but also using observations of supernovae because the presence of either a uniform shell or a wind profile and their respective properties can modify the breakout of the SN shock and its radiative signature. The interpretation of the evolution of the observed radiation can be based on theoretical modelling of the shock breakout as done in early studies by Imshennik & Nadezhin (1989). Later, Matzner & McKee (1999) provided a thorough investigation of (spherical) shock propagation into a prescribed EM, and Calzavara & Matzner (2004) showed a method for inferring the properties of SNe from the breakout signal. Of more recent work, we particularly note the one by Moriya et al. (2015) that uses an EM based on the winds of WR stars.

The scatter in the mass-loss rates quoted for progenitors of Type Ic SN is quite large: $\dot{M} \simeq 5 \times 10^{-7} M_\odot\,{\rm yr^{-1}}$ for SN 2002ap (Berger, Kulkarni & Chevalier 2002), $\dot{M} \simeq 7.5 \times 10^{-6} M_\odot\,{\rm yr^{-1}}$ for SN 2003L (Soderberg et al. 2005), $\dot{M} \simeq 4 \times 10^{-7} M_\odot\,{\rm yr^{-1}}$ for SN 1998bw (Li & Chevalier 1999), $\dot{M} \simeq 3 \times 10^{-4} M_\odot\,{\rm yr^{-1}}$ for SN 2006aj (Campana et al. 2006). Also from the radio observations of the Type Ib SN 2008D, Soderberg et al. (2008) infer $\dot{M} \simeq$

$7 \times 10^{-6} M_\odot\,\mathrm{yr}^{-1}$ for its progenitor star. Even for the same SN event, different assumptions employed to explain the breakout signal of the shock may lead to estimate different mass-loss rates. For instance, for SN 2008D, Svirski & Nakar (2014) obtain $\dot{M} \simeq 10^{-4} M_\odot\,\mathrm{yr}^{-1}$, compared to a rate of $\dot{M} \simeq 7 \times 10^{-6} M_\odot\,\mathrm{yr}^{-1}$ (in agreement with the value inferred by Soderberg et al. 2008) obtained from a theoretical study of the generation of the wind (Sanyal et al. 2015).

As we have seen, observations and theory allow for a wide range of mass loss rates of stars prior to SN. In this work, we consider that an inflated envelope is generated at the surface of the WR. This envelope is not contained in the stellar evolution model of Woosley & Heger (2006). For this reason, we will in the following refer to this intermediate region at the border between the star proper and the interstellar medium as a part of the EM. As seen in different studies (see, e.g., Gräfener et al. 2012; Sanyal et al. 2015) the density profile in these envelopes remains roughly constant with a value $\rho_{\mathrm{env}} \sim 10^{-10}\,\mathrm{g\,cm}^{-3}$. The inflated envelope is mainly radiative and the gas pressure ($p_{\mathrm{bar}} \sim 10^3\,\mathrm{g\,cm}^{-1}\,\mathrm{s}^{-2}$, for a $23 M_\odot$ WR star; see fig. 2 of Gräfener et al. 2012) is dominated by the radiation pressure ($p_{\mathrm{rad}} \sim 10^6\,\mathrm{g\,cm}^{-1}\,\mathrm{s}^{-2}$). The estimated temperature is $T_{\mathrm{env}} > 10^4$ K at the surface of the envelope. Our EoS does not include the separated contributions of the radiation and baryonic pressure, but only the latter (see, e.g., Eq. (2.18)). This means that to obtain pressure values in the WR envelope $p \simeq p_{\mathrm{rad}}$ the temperature (as obtained from the *TM* EoS, i.e., $T = T_{\mathrm{bar}}$) in our model must be artificially risen. Although this temperature is considered in the hydrodynamics, we lately assume in our analysis that the temperature is obtained adding the two mentioned contributions in the total pressure. In the following we assume that the temperatures are the result of assuming that the barionic gas and radiation are in equilibrium. As we set up first temperature and then pressure in the envelope, and taking into account that the ambient pressure has a large influence on the jet dynamics, we have to find a compromise between two contending effects. First, we aim to set the highest possible pressure in order to get a value as close as possible to that of the model of $23 M_\odot$ of Gräfener et al. (2012). But on the other hand, we want to have a WR envelope cool enough to be distinguished from

the stellar surface. Thus, we fix $T_{\rm env} = 10^5\,{\rm K}$, which is more than one order smaller than the temperature in the surface of model 35OC ($T_\star \sim 2.7 \times 10^6$ K) but slightly larger than $T_{\rm env}$, giving us a value for the total pressure of $p_{\rm env} \sim 2.5 \times 10^5\,{\rm g\,cm^{-1}\,s^{-2}}$. With these values both the rest-mass density and pressure show strong jumps at the interface separating the star and the envelope. Thus, for reasons of numerical stability, we have implemented a transition layer consisting of 50 radial zones in the layer $[R_\star, 5.56 \times 10^{10}\,{\rm cm}]$ to smoothly connect these two regions (see Fig. 4.2).

The radial extent of the inflated envelope, $\Delta R_{\rm env} := R_{\rm env} - R_\star$, was found by Gräfener et al. (2012) to be a few stellar radii ($R_\star$), with higher values for higher stellar masses. Lacking detailed information for model 35OC, our choice of $\Delta R_{\rm env} = 2R_\star \approx 1.1 \times 10^{11}$ cm, is motivated by the fact that a much larger value would make the envelope optically thick, in conflict with the fact that stars that end as fast rotating WR stars may become transparent to UV radiation during main-sequence evolution (Szécsi et al. 2015).

From $R_{\rm env}$ outwards we assume that both density and pressure follow a wind profile, i.e., $p,\, \rho \propto r^{-2}$. Immediately outside of $R_{\rm env}$, i.e., in the interface that separates the inflated envelope with the wind-like medium, we fix $\rho_{\rm EM,0} = \rho_{\rm env}$ and $p_{\rm EM,0} = 2.5 \times 10^5\,{\rm g\ cm^{-1}\ s^{-2}}$ which, if only the gas pressure is considered to contribute in the total pressure, gives a constant temperature of $T_{\rm EM} = 4 \times 10^4\,{\rm K}$ in the whole medium. This temperature is consistent with values of $T_{\rm env}$ (Gräfener et al. 2012). The latter assumption is valid only if the radiation is decoupled from the gas, which it is true if the medium is transparent as it is in our case for $r \gtrsim R_{\tau=1} \simeq 4 \times 10^{11}\,{\rm cm}$. Below this distance the medium becomes optically thick and radiation can contribute to the total pressure, causing a drop in temperature to $T_{\rm EM,0} \sim 1.6 \times 10^4\,{\rm K}$ at $R_{\rm env}$.

We may estimate the optical depth of the WR envelope to be

$$\tau = \int_{R_\star}^{R_{\rm env}} \rho_{\rm env}\kappa + \int_{R_{\rm env}}^{\infty} \rho_{\rm env}\kappa \left(\frac{R_{\rm env}}{r}\right)^2 = 5.3\rho_{\rm env,-10}\kappa_{0.2}R_{\star,5.3\times10^{10}}, \quad (4.3)$$

which is compatible with the assumptions described above. In the latter formula $\rho = 10^{-10}\rho_{\rm env,-10}\,{\rm g\,cm^{-3}}$ and we took that $R_{\rm env} = 3R_\star$. The result can be compared with that shown in Eq. (4.2) where we assumed a low-density

wind placed in front of the WR.

For simplicity, in the rest of the chapter we will refer to the wind-like external medium as just the EM.

In all of our models, we assume the EM (including the envelope) to be at rest, which, strictly speaking, is inconsistent with a stellar wind. The typical speeds of the wind are, however, smaller than the velocities of the SN shock and the jets once they enter the EM. Hence, the profiles of density and pressure evolve only little on the time scales of the propagation of the ejecta, justifying this simplification.

4.1.3 Supernova ejecta

We have simulated the SN explosion as an spherical outflow by performing 1D simulations (model SH). The initialization of the grid is sketched in Sect. 4.1.1. For this simulation we have extended the numerical grid three times with chunks of size $\Delta R_{\rm patch} = 10^{12}\,{\rm cm}$ and $n_{\rm r,patch} = 5000$ up to a final distance $R_{\rm out} = 5\times10^{12}\,{\rm cm}$ (see Fig. 4.2). Thus, for model SH the total number of zones in the radial direction arrives to be $n_r = 30600$ by the end of the computed evolution.

The initialization of the SN ejecta is done using a piston-like model (Rosenberg & Scheuer 1973; Gull 1973) since energy, $E_{\rm SN}$, and mass, $M_{\rm SN}$, are carried by an spherical flow, which enters the numerical grid through the inner boundary, at a constant rate, until $t_{\rm SN} = 1\,{\rm s}$. The practical implementation of the piston model is detailed in Sect. 4.1.3.1. The stellar potential sets a minimum required amount of energy to launch any outflow at a distance R_0. We have checked that the binding energy of the matter on the numerical domain is $\gtrsim 5\times10^{50}\,{\rm erg}$, i.e., any successful SN must exceed this value, which is compatible with energies of typical SN. Thus, the total energy injected is $E_{\rm SN} = 10^{52}\,{\rm erg}$, which places this model in the HN realm, while the total mass injected by the piston mechanism through the innermost radial boundary has been fixed to $M_{\rm SN} = 0.1 M_\odot$[1]. This mass is removed from the excised mass

[1]This mass must not be confused with the mass of the SN ejecta, which is obviously much larger. It is only a practical way of setting up the properties of the piston mechanism.

enclosed below R_0. The reason for this operational procedure is to not modify the gravitational potential (and, hence, the equilibrium conditions) in the layers of the star beyond the SN shock. In case we do not apply this correction to $M_{\rm in}$, unwanted displacements of the outer progenitor mass shells (including the stellar surface) are generated. Once the constant injection phase is over, a quickly decaying mass and energy injection follows. After that, the inner boundary is open and copy conditions are set, allowing the inflow of material from the grid to the excised part. During this phase, we follow the evolution of $M_{\rm in}$, which is suitably updated to self consistently compute the gravitational potential.

See Table 4.1 for a summary of the parameters.

4.1.3.1 The 'piston' model

The 1D SN ejecta is injected from the start of the simulation until a final time of $t_{\rm SN}$ with a piston-like model in which we set both the energy and the mass fluxes, $\dot{E}_{\rm SN} = E_{\rm SN}/t_{\rm SN}$ and $\dot{M}_{\rm SN} = M_{\rm SN}/t_{\rm SN}$ respectively, across the innermost radius of our computational domain, R_0. After $t_{\rm SN}$, the energy and mass injection are not switch off abruptly but decay very rapidly with time ($\propto t^{-12}$). This fast injection decline is introduced for numerical convenience, since the gas behind the rear end of the SN ejecta is very rarefied. The gradient of, e.g., density between ejecta and the trailing matter is very steep for an instantaneous end of the injection, which can cause a failure of the simulation. This instability can be removed by a smooth transition at the end of the SN injection. The steep time decrease of the ejecta injection conditions has been tuned to keep injecting a negligible amount of energy and mass in the computational grid on the time scales of interest (a few seconds).

Taking units in which $c = 1$, the injection model is based upon the main assumption that $\Theta = p/\rho \ll 1$ (where p and ρ are the fluid pressure and density). This holds as long as $E_{\rm SN} \ll M_{\rm SN}c^2$, condition we guarantee setting up suitable values for the parameters $E_{\rm SN}$ and $M_{\rm SN}$. Using the *TM* EoS (Mignone & McKinney 2007), for low Θ the square of the speed of sound in

the medium, $c_{\rm s}$, (Eq. (2.37)) is

$$c_{\rm s}^2 = \frac{\Theta}{3h}\frac{5h-8\Theta}{h-\Theta} \approx \frac{5\Theta}{3h}\,, \tag{4.4}$$

and the enthalpy (Eq. (2.17)) is

$$h = \frac{5}{2}\Theta + \sqrt{\frac{9}{4}\Theta^2+1} \approx \frac{5}{2}\Theta + 1\,. \tag{4.5}$$

From energy and mass flux we get that

$$h\Gamma = 1 + \frac{\dot{E}_{\rm SN}}{\dot{M}_{\rm SN}c^2} = \xi\,. \tag{4.6}$$

Using the definition of the Mach number, $\mathcal{M} = v/c_{\rm s}$, with β the (radial) velocity of the fluid, the bulk Lorentz factor takes the form

$$\Gamma = 1/\sqrt{1-\mathcal{M}^2 c_s^2}\,. \tag{4.7}$$

Using Eqs. (4.4)–(4.7), we arrive at

$$\Theta = \frac{6(\xi^2-1)}{45+\xi^2(10\mathcal{M}^2-15)}\,, \tag{4.8}$$

which only depends on the parameters $\dot{E}_{\rm SN}$, $\dot{M}_{\rm SN}$ and $\mathcal{M}$ and always will be much smaller than 1. The Mach number is set to ensure that the shock is supersonic at injection, $\mathcal{M} = 2$.

Once Θ is computed we recover in the following order, h (Eq. (4.5)), $\Gamma = \xi/h$ (Eq. (4.6)), ρ (from the mass flux) and $p = \Theta\rho$. Note that $\xi \geq h$ must be fulfilled in order to assure that $\Gamma \geq 1$, i.e., it will be satisfied that

$$\Theta \leq \frac{2}{5}(\xi-1)\,. \tag{4.9}$$

4.1.4 Jet injection

The delay between a successful SN explosion and the subsequent generation of a relativistic jet from the central engine is not completely known. For the model 35OC, the General Relativistic Hydrodynamic core-collapse simulations

Table 4.1: Summary of some of the parameters of all models: dimensionality (Dim), isotropic equivalent energy ($E_{\rm iso}$), true energy (E),initial Lorentz factor (Γ), initial enthalpy (h), injection time ($t_{\rm inj}$), injection radius ($R_{\rm inj}$), inner mass below $R_{\rm inj}$ ($M_{\rm in}$) and time delay with respect to the SN ($t_{\rm del}$).

Model	SH	J0	J3-H	J3-L
Dim	1D	2D	2D	2D
$E_{\rm iso}$ (erg)	10^{52}	10^{54}	10^{54}	5×10^{53}
E (erg)	$E_{\rm iso}$	3×10^{50}	3×10^{50}	1.5×10^{50}
Γ	1.0315	5	5	5
h	1.0237	20	20	20
$t_{\rm inj}$ (s)	1	20	20	20
$R_{\rm inj}$	R_0	$2R_0$	$2R_0$	$2R_0$
$M_{\rm in}$ ($M_\odot$)	3.385	6.055	3.289	3.289
$t_{\rm del}$ (s)	–	–	3	3

of O'Connor & Ott (2011) predict BH formation times after core bounce in the range $[0.84, 2.7]$ s, depending on the nuclear EoS considered. These calculations were done including a simplified neutrino leakage scheme, unable to drive a SN explosion. More recently, Obergaulinger & Aloy (2017), including a much more elaborated neutrino transport method and magnetic fields as indicated by stellar evolution calculations, find that the BH formation time after bounce can be larger than the upper bounds estimated in O'Connor & Ott (2011). In some models it is even likely that a BH does not form at all. In the cases in which the BH forms, it is necessary to wait a bit more until energy can be efficiently extracted from the central engine, since an accretion disc must form, which may take a few seconds after the BH is formed. Furthermore, the ram pressure of the accreting matter will be too high to allow for jet launching until the polar regions accrete so much mass that their density decreases below $\sim 10^6\,{\rm g\,cm^{-3}}$ (MacFadyen & Woosley 1999). Altogether, the time elapsed between core bounce and jet formation is an uncertain quantity on the order of several seconds, as long as or even above $\sim$ 5–10 s. In this work, we consider a time delay between the SN and the jet of $t_{\rm del} = 3\,{\rm s}$ (model J3). For comparison

we note that the SN shock of model 35OC-RO of Obergaulinger & Aloy (2017) has already reached $\simeq 3\times10^9$ cm at 1.6 s after the core of model 35OC bounces, which is before BH formation.

As the jet injection radius is now fixed at $R_{\rm inj,j} = 2R_0$ and the SN ejecta was crossing this point at 0.8 s after its injection, we take the rest-mass density, pressure and radial velocity profiles of the SN ejecta after 3.8 s as initial conditions for the simulations with jets. We also consider the case in which no ejecta have not been injected previously (model J0).From this point on, we take the 1D profiles of model SH and remap them into a new 2D spherical grid, which has the same levels of resolution in the radial direction (see Sect. 4.1.1). However, for jet models the inner edge of the numerical grid has been set up to $R_{\rm inj,j}$ and the initial extent to $R'_{\rm out} = 1.5\times10^{12}$ cm (see Fig. 4.2), that gives a number of radial cells of $n'_r = 13080$. Jet simulations are more expensive because they are two-dimensional. Hence, we have only made two more extensions of the radial grid up to a final distance of $R_{\rm out} \simeq 2.5\times10^{12}$ cm (i.e., half of that in model SH), having a total number of radial cells $n_r = 18087$ for all our jet models. For that reason too, we have used chunks of size $\Delta_{\rm patch} \simeq 5\times10^{11}$ cm with the same resolution as in the third level. The angular grid is composed of $n_\theta = 264$ angular cells, distributed in also three uniform-spaced subgrids with different levels of resolution (Fig. 4.2), covering in total the range $[0°, 90°]$. The first level spans the range $[0°, 9°]$ where we use a number of angular zones $n_{\theta,1} = 81$, i.e., the angular resolution is $\Delta\theta_1 = 0°.\overline{1}$. The second level consists of $n_{\theta,2} = 153$ and goes up to 60° ($\Delta\theta_2 = 0°.\overline{3}$) and the third level of $n_{\theta,3} = 30$ and cover the remaining angular space up to 90° ($\Delta\theta_3 = 1°$).

In models J3 the inner mass enclosed below $R_{\rm inj,j}$ is basically $M_{\rm in}({\rm J3}) \simeq M_{\rm in} - M_{\rm SN} \approx 3.289 M_\odot$, since the SN ejecta cleans the region between R_0 and $R_{\rm inj,j}$. However, for model J0 the mass enclosed in this region has to be taken into account, giving an inner mass for model J0 of $M_{\rm in}({\rm J0}) \approx 6.055 M_\odot$.

In principle, the parameter space of possible injection conditions is very large. We can, however, exclude several of the more extreme parameters. On one hand, extremely large isotropic energies of more than 10^{55} erg are very unlikely. On the other hand, a lower limit on the injected energy comes from

the fact that we are interested in jets, for which supersonic propagation is required. That means that at the injection point the velocity of the jet's head must be larger than the speed of sound of the medium, i.e., $v_{\rm h} > c_s$. Following the prescriptions of Matzner (2003) and Bromberg et al. (2011b; see also Martí et al. 1997), the velocity of the jet's head can be approximated by

$$v_{\rm h} = \frac{v_{\rm j}}{1+\tilde{L}^{-1/2}}\,, \tag{4.10}$$

where

$$\tilde{L} \equiv \frac{\rho_{\rm j} h_{\rm j} \Gamma_{\rm j}^2}{\rho_{\rm a}} \simeq \frac{L_{\rm j}}{S_{\rm j}\rho_{\rm a} c^3}\,, \tag{4.11}$$

where $L_{\rm j}$ is the jet luminosity and $S_{\rm j}$ is the jet's cross section. The indices 'j' and 'a' refer to properties of the jet and the ambient medium, respectively. If the medium is very dense, as it is the case at the injection radius, $\sim 10^9\,{\rm cm}$, $\tilde{L} \ll 1$ and the jet Mach number must fulfill

$$\frac{v_{\rm h}}{c_s} \simeq \frac{\tilde{L}^{1/2}}{c_s} > 1 \tag{4.12}$$

From this condition, and using Eq. (4.4) and that $S_{\rm j} = \pi R_{\rm j}^2 \sin\theta_{\rm j}{}^2 \approx \pi R_{\rm j}^2 \theta_{\rm j}^2$, we estimate the minimum luminosity that a jet with a half-opening angle $\theta_{\rm j}$ (we have assumed that $\sin\theta_{\rm j} \ll 1$) must have at the injection point, $R_{\rm j} = R_{\rm inj,j}$. With typical values of $p_{\rm a} = 7.54\times10^{22}\,{\rm erg\,cm^{-3}}$ for the initial stellar profile at R_0, we find that the Mach number exceeds unity only if

$$L_{\rm j} \gtrsim 1.4\times10^{49} \left(\frac{R_{\rm j}}{10^9\,{\rm cm}}\right)^2 \left(\frac{\theta_{\rm j}}{2^\circ}\right)^2 \left(\frac{p_{\rm a}}{7.54\times10^{22}\,{\rm erg\,cm^{-3}}}\right) {\rm erg\ s^{-1}}\,. \tag{4.13}$$

To convert the previous jet intrinsic luminosity into an equivalent isotropic quantity we employ $L_{\rm iso,j} = 2L_{\rm j}/(1-\cos\theta_{\rm BO}) \simeq 4L_{\rm j}/\theta_{\rm BO}^2$. Likewise, we obtain an equivalent isotropic energy as $E_{\rm iso,j} = L_{\rm iso,j} \times (4/3)\, t_{\rm inj,j}$; where the factor 4/3 takes into account the shut down phase of the injection. In the previous expression $\theta_{\rm BO}$ corresponds to the opening angle of the jet *after* the jet break-out. According to Mizuta & Ioka (2013), $\theta_{\rm BO} \simeq 1/(5\Gamma_j)$. In our case, $\Gamma_j = 5$ and, therefore, we would obtain $\theta_{\rm B0} \simeq 2.3^\circ \simeq \theta_j$, in which case condition (4.13)

translates into:

$$L_{\rm iso,j} \gtrsim 3.6\times10^{52}\left(\frac{R_{\rm j}}{10^9\,{\rm cm}}\right)^2\left(\frac{\theta_{\rm j}}{2^\circ}\frac{2.3^\circ}{\theta_{\rm BO}}\right)^2\left(\frac{p_{\rm a}}{7.54\times10^{22}\,{\rm erg\,cm^{-3}}}\right)\,{\rm erg\,s^{-1}}\,, \tag{4.14}$$

and

$$E_{\rm iso,j} \gtrsim 9.6\times10^{53}\left(\frac{R_{\rm j}}{10^9\,{\rm cm}}\right)^2\left(\frac{\theta_{\rm j}}{2^\circ}\frac{2.3^\circ}{\theta_{\rm BO}}\right)^2\left(\frac{p_{\rm a}}{7.54\times10^{22}\,{\rm erg\,cm^{-3}}}\right)\left(\frac{t_{\rm inj,j}}{20\,{\rm s}}\right)\,{\rm erg}\,, \tag{4.15}$$

$t_{\rm inj,j}$ being the jet injection time.

Hence, if the results of Mizuta & Ioka (2013) hold, we do not expect any jets that manage to propagate supersonically in the presupernova model 35OC to fall into the category of llGRBs (see Sect. 1.3), unless the radiative efficiency in the $\gamma-$ray band, $\epsilon_\gamma = L_{\rm iso,\gamma}/L_{\rm iso}$, is very small ($\epsilon_\gamma \lesssim 10^{-4}$).

However, the set up of our models is quite different from that of Mizuta & Ioka (2013). For instance, we employ model 35OC as stellar progenitor, which is more extended and massive than model 16TI employed by the former authors. We consider much lower luminosity jets ($L_{\rm j} \gtrsim 1.5\times10^{49}\,{\rm erg\,s^{-1}}$) than Mizuta & Ioka (who use $L_{\rm j} = 10^{50}\,{\rm erg\,s^{-1}}$). We inject jets with an asymptotic Lorentz factor 100, while Mizuta & Ioka (2013) use a much larger value ($\simeq 538$). Another differences are the jet injection angle and time. Mizuta & Ioka (2013) use $\theta_{\rm j} \simeq 4.6^\circ$, and $t_{\rm inj,j} = 12.5\,{\rm s}$, while we use $\theta_{\rm j} \simeq 2^\circ$, and $t_{\rm inj,j} = 20\,{\rm s}$. Finally, the inference of the former authors on the jet opening angle is not time independent and they could depend to some extend on set up of the circumburst medium. As can be seen from their Fig. 9, there is some trend for the jet breakout angle to increase with time. With all these considerations in mind, we anticipate that the breakout opening angle of our models will be larger than predicted in Mizuta & Ioka (2013). Indeed, we expect $\theta_{\rm BO} \sim a/\Gamma_{\rm j}$, with $0.5 < a \lesssim 3$. This larger breakout angle translates into the following constrains on the isotropic luminosity and energy:

$$L_{\rm iso,j} \gtrsim 1.5\times10^{50}\left(\frac{R_{\rm j}}{10^9\,{\rm cm}}\right)^2\left(\frac{\theta_{\rm j}}{2^\circ}\frac{35^\circ}{\theta_{\rm BO}}\right)^2\left(\frac{p_{\rm a}}{7.54\times10^{22}\,{\rm erg\,cm^{-3}}}\right)\,{\rm erg\,s^{-1}}\,, \tag{4.16}$$

and

$$E_{\rm iso,j} \gtrsim 4.1{\times}10^{51} \left(\frac{R_{\rm j}}{10^9\,{\rm cm}}\right)^2 \left(\frac{\theta_{\rm j}}{2^\circ}\frac{35^\circ}{\theta_{\rm BO}}\right)^2 \left(\frac{p_{\rm a}}{7.54\times10^{22}\,{\rm erg\,cm^{-3}}}\right) \left(\frac{t_{\rm inj,j}}{20\,{\rm s}}\right) {\rm erg}\,, \tag{4.17}$$

Note that in the case in which the breakout opening angle grows well above the expectations of Mizuta & Ioka (2013), but as suggested by our models (see Sect. 4.2.2), with a radiative efficiency $\epsilon_\gamma \lesssim 0.05$ the jets here set up would have isotropic equivalent luminosities within the realm of llGRBs.

For a quantitative analysis, see Fig. 4.3, where we show the minimum energy that has to be injected for a jet to form as a function of radius. The blue line corresponding to 35OC confirms our previous result of a threshold of $E^{\rm thr}_{\rm iso,j} \sim 10^{54}\,{\rm erg}$ at a radius of $10^9\,{\rm cm}$. The only way around this restriction may be for the jet to be injected into a medium of a much lower density, which in this context can be achieved by having a SN shock wave propagating ahead of the jet. As we can see from Fig. 4.4, after the passage of the SN shock, the density is reduced below $\sim 3\times10^9\,{\rm cm}$, which allows for a smaller energy injection (Eq. (4.15)). Nevertheless, for models J3 (magenta line in Fig. 4.3) the energy threshold at $10^9\,{\rm cm}$ only reduces by around one order of magnitude with respect to model 35OC, still being in the energy range of standard GRBs. For comparison we have depicted the density profile of another GRB progenitor candidate, the presupernova model 16TI of Woosley & Heger (2006). For this model the energy threshold is smaller than that of the model 35OC above $10^8\,{\rm cm}$, e.g., by a factor 5 around $10^9\,{\rm cm}$. We have also included the density profile of the 2D presupernova model of Obergaulinger & Aloy (2017; orange line), evolved from the onset of core collapse in the progenitor 35OC until BH formation. By that time, the layers at the distance of our injection location are still unaffected by the dynamics of the core collapse and, thus, there is no difference in the energy requirements with respect to our progenitor model.

In consideration of the arguments in the previous paragraphs, we set isotropic equivalent energy of the jet, $E_{\rm iso,j}$, is fixed to $10^{54}\,{\rm erg}$ (models J0 and J3-H). From Fig. 4.3, we see that this value roughly corresponds to the threshold energy for model 35OC at $R_{\rm inj,j}$. Setting the half-opening angle of the jet to

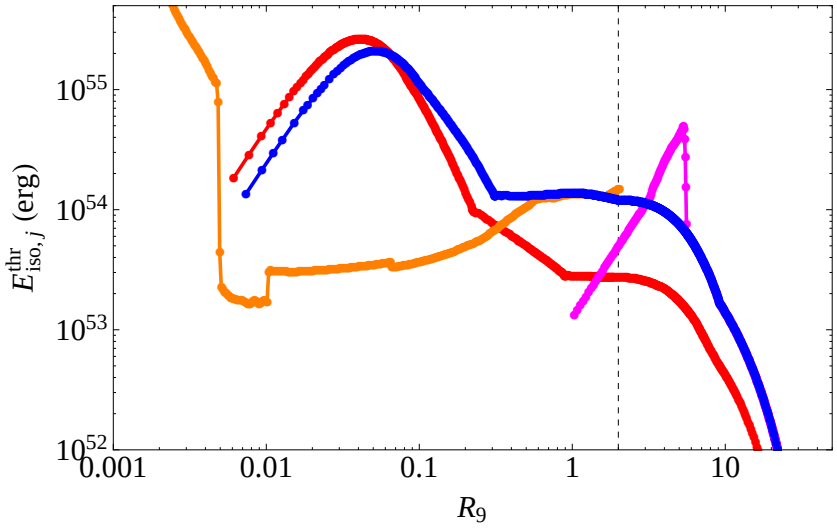

Figure 4.3: Threshold energies for different progenitor models: presupernova models 35OC (blue) and 16TI (red) of Woosley & Heger (2006), and models J3 of this work (magenta). We also include data computed for the density profile of one of the presupernova models of Obergaulinger & Aloy (2017), corresponding at the moment of BH formation after the core collapse of model 35OC (orange). The vertical dashed line shows the position of $R_{\rm inj,j}$

$\theta_{\rm j} = 2°$ the true jet energy is $E_{\rm j} = (1-\cos\theta_{\rm j})/2 \times E_{\rm iso,j} \simeq 3\times10^{50}\,{\rm erg}$. The jet is injected for $t_{\rm inj,j} = 20\,{\rm s}$, so that the isotropic luminosity of the jet is $L_{\rm iso,j} = 5\times10^{52}\,{\rm erg\,s^{-1}}$ and the true luminosity of the jet is $L_{\rm j} \simeq 1.5\times10^{49}\,{\rm erg\,s^{-1}}$. In order to reduce as much as possible the jet energy, we have run a model in the 'J3' series with $E_{\rm iso,j} = 5\times10^{53}\,{\rm erg}$ (model J3-L), which corresponds to the threshold energy at $R_{\rm inj,j}$ in model J3, where the SN shock has partly evacuated the injection region reducing the threshold energy. In all the models the initial jet Lorentz factor $\Gamma_{\rm j} = 5$ and enthalpy $h_{\rm j} = 20$ translate into an asymptotic Lorentz factor $\Gamma_{\infty,0} = h_{\rm j}\Gamma_{\rm j} = 100$. See a summary of the parameters of each model in Table 4.1.

For resolving the large gradients between the jet and the stellar profile, we have used the third-order spatial reconstruction scheme PPM (Colella & Woodward 1984).

4.2 Hydrodynamic evolution

4.2.1 SN ejecta

As pointed by Matzner & McKee (1999) a SN explosion goes through three different stages: (1) the blastwave stage, where the shock crosses the stellar interior (Chevalier 1976); (2) the 'rarefaction' stage, in which the shock breaks out the star and accelerates into the EM; and (3) the 'ejecta' stage, once the shock is not accelerated anymore and the material swept by it expands homogeneously with a velocity $v = r/t$. Matzner & McKee (1999) showed that the density and pressure profiles of the SN ejecta and the progenitor star have a close relationship, and depend mainly on whether the outer envelope of the progenitor is radiative or convective.

The dynamics of the ejecta can be described after they have left the star by self-similar solutions for the RS (Parker 1963) and the FS (Chevalier 1982). However, these solutions are valid only at larger distances from the stellar surface than the ones we are considering here. In our case, the low optical depth of the EM means that the SN flash signal is observed at the breakout from a distance relatively close to the star, i.e., at a time when the condition for the self-similarity solutions do not yet apply. Hence, we can only rely on numerical modelling for this part of the evolution.

In Fig. 4.4 we show different snapshots of the profiles within the progenitor for different time after the SN injection. The passage of the SN ejecta is critical for the progenitor star. The ejecta sweeps all the material from its innermost layers leaving behind a very different and less denser mass profile, which will make easier the jet propagation. All this material is piled up in the leading layer compressed by the FS, which travels outward non-relativistically (~ 10000 km s^{-1}) within the star. The thin layer spreads out as the FS of the SN advances quicker than its RS leaving a relatively dense inter-shock medium. This behaviour corresponds to the stage (1) described above (Matzner & McKee 1999; Chevalier 1976). The ejecta arrive at the stellar surface after ~ 35.5 s, with a velocity of $\lesssim 0.3c$ and accelerate up to $\sim 0.9c$ once they emerge out of the star and encounter the sharp drop in the hydrodynamic profiles (these dynamics

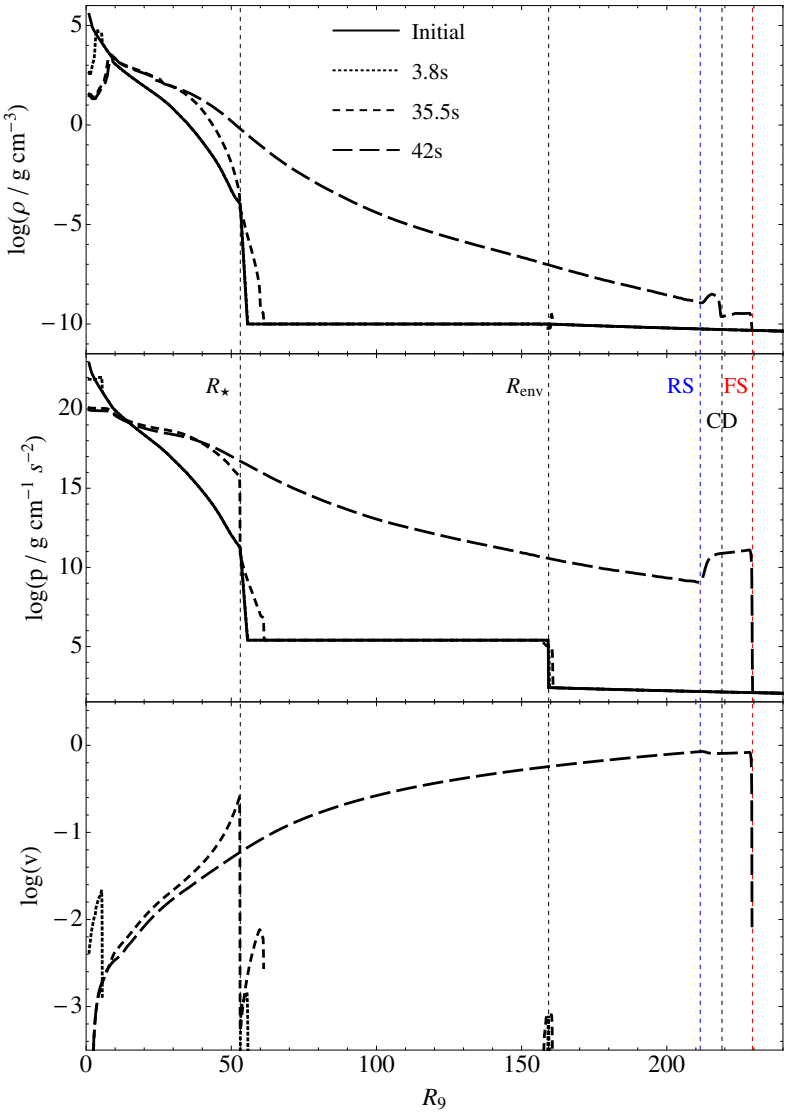

Figure 4.4: Rest-mass density (upper panel), pressure (center panel) and radial velocity (lower panel) profiles of a 1D SN shock with an energy $E_{\rm SN} = 10^{52}$ erg. The different line styles correspond to evolutionary times of 0 (initial), 3.8, 35.5 and 42 s after injection (see legend). Note that the lines corresponding to the initial model and to an evolutionary time of 3.8 s practically overlap everywhere in the upper and middle panels except at the innermost layers of the computational domain. $R_\star$ and $R_{\rm env}$ as well as the positions of the RS (blue), the CD (black) and the FS (red) at $t = 42$ s are marked.

corresponds to the stage (2) described above). As they propagate into the EM the ejecta decelerate: 4 minutes after the shock breakout the FS is located at $\sim 4.69 \times 10^{12}\,\mathrm{cm}$ (see Fig. 4.5) and their propagation velocity is $\sim 0.7c$. The latter evolutionary phase corresponds to the beginning of the stage (3) according to the classification of Matzner & McKee (1999).

As we see from Fig. 4.4 maintaining hydrostatic equilibrium is difficult in the stellar surface and therefore at the SN breakout point these layers have expanded radially up to a $\sim 13\%$, with a velocity $\lesssim 10^{-2}c$. Also a small expansion develops at $R_{\rm env}$. After the SN ejecta breaks out of the star, the typical FS-RS structure can be easily seen, e.g., in Fig. 4.4, upper and middle panels. There we observe at $\sim 9.4 \times 10^{10}\,\mathrm{cm}$ and at $\sim 1.18 \times 10^{11}\,\mathrm{cm}$ density and pressure jumps associated to the RS and FS, respectively.

Within the time of our simulation, the temperatures of both FS and RS drop by about an order of magnitude, being both in the interval $T \sim 10^6$–$10^5\,\mathrm{K}$ (see Fig. 4.5, lower panel). The evolution of temperature of both shock with time ($T \propto t^b$) shows that the RS decays a bit faster ($b = -0.72$) than that of the FS ($b = -0.71$) at the end of the simulation. We note that here the fluid temperature is computed assuming local thermodynamic equilibrium, i.e., $T = T_{\rm bar} = T_{\rm rad}$. This assumption may be violated as the ejecta becomes optically thin, in which case the temperature of the baryonic gas is underestimated. This happens in the FS when it becomes transparent at $t \simeq 50\,\mathrm{s}$. The RS starts to be transparent 4 seconds later, at $t \simeq 54\,\mathrm{s}$ (Fig. 4.5).

In Fig. 4.6 we draw the values of $x = 1 - R_{\rm RS}/R_{\rm FS}$ and

$$\chi_{\rm E} = \frac{\int_{R_{\rm RS}}^{R_{\rm FS}} p(r) r^2 dr}{R_{\rm FS}^3 x p_{\rm FS}}\,, \tag{4.18}$$

defined in Balberg & Loeb (2011). After 4 min $x \simeq 0.17$ and $\chi_{\rm E} \simeq 0.63$ and both parameters are almost constant in time (although they are still rising very slightly), which is a hint of being close to the self-similar regime,[2] but still not in it. In fact, from Fig. 4.5 (upper panel) we obtain that the FS radius evolves faster in time ($R \propto t^b$, with $b = 1.16$) than the one of the RS ($b = 1.14$).

[2]Balberg & Loeb (2011) obtained, for their particular case, a values of $x = 0.146$ and $\chi_{\rm E} = 0.9$ in the self-similar regime.

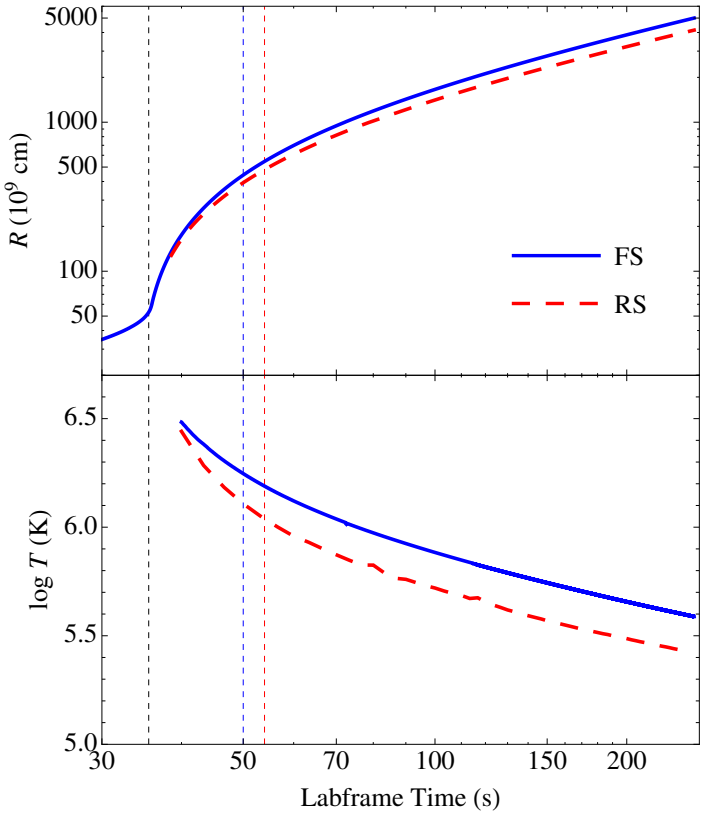

Figure 4.5: Upper panel: FS (blue solid) and RS (red dashed) location as a function of the lab-frame time. Lower panel: temperature evolution of the post-FS and -RS states. The vertical black dashed line denotes the breakout time. The blue and red vertical dashed lines denote the times at which the FS and RS, respectively, become optically thin. This happens when $R_{\rm FS} \sim 4.5 \times 10^{11}$ cm and $R_{\rm RS} \sim 4.9 \times 10^{11}$ cm.

4.2.2 Jet models

We can classify our jet models in two groups. The first group is formed by model J0, in which the jet propagates into the stellar mantle ahead of the SN ejecta (in particular, no SN is injected for this model). The second group includes the J3 series (models J3-H and J3-L) in which the SN ejecta have been injected preceding the jet. As we shall see, even a small delay between the SN and the jet can influence the dynamics of the latter as the SN ejecta

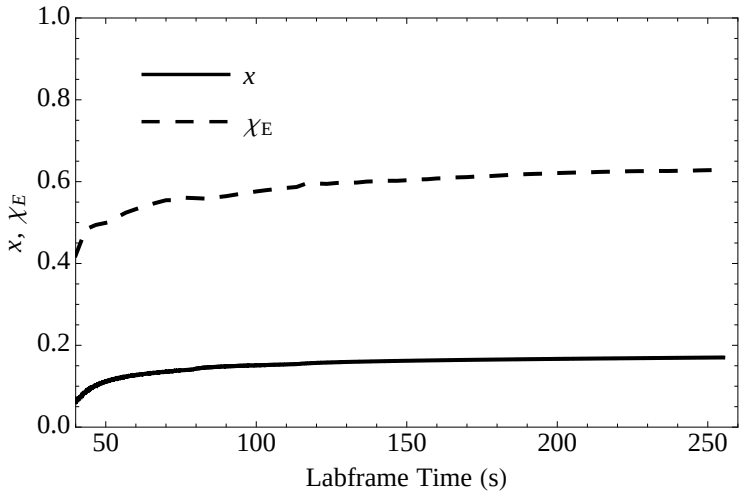

Figure 4.6: Time evolution, in the laboratory frame, of $x = 1 - R_{\rm RS}/R_{\rm FS}$ and $\chi_{\rm E}$.

Table 4.2: Breakout time in the laboratory frame ($t_{\rm BO}$) and in the observer's frame ($t_{\rm obs,BO}$), and time spent by the jet to overtake the FS of the SN ejecta ($t_{\rm j\to SN}$) and by the FS to approximately arrive to $R_{\tau=1}$ ($t_{\tau=1}$).

Model	$t_{\rm BO}$ (s)	$t_{\rm obs,BO}$ (s)	$t_{\rm j\to SN}$ (s)	$t_{\tau=1}$ (s)
SH	35.53	37.28	–	~ 50
J0	16.24	16.00	–	~ 28
J3-H	13.48	12.95	7.14	~ 25
J3-L	18.51	18.49	13.00	~ 30

modify the stellar profiles.

We can in principle use two definitions of jet breakout. An obvious choice is the moment when the jet leaves the stellar surface. However, at that moment, it may still be invisible to a distant observer because it is still hidden by the optically thick wind ahead of it. Therefore, the second way to define the breakout is given by the appearance of an electromagnetic signal as the jet emerges from the photosphere. We will refer to these two instants of breakout in the following as *hydrodynamic* and *electromagnetic* breakout, respectively. Without any qualifying adjective, we always refer to the hydrodynamic break-

out as the breakout for short. Table 4.2 shows the breakout times of all our models, measured both in the laboratory frame and the observer's frame (located a large distance from the star and observing the phenomenology by means of the photons arriving to him). To calculate the time in the observer's frame we have assumed that the progenitor system is located at a redshift of $z = 0.1$, which is typical for closeby GRB/SNe. We should note that in all the 'J' models the time of breakout (see Tab. 4.2) is measured with respect to the beginning of jet injection. To compare directly with model SH, one can assume that $t = 0\,\mathrm{s}$ in that model corresponds to the moment in which the FS of the SN ejecta is passing through $R_{\rm inj,j}$. Thus, to properly synchronize models with jets and without them, a time width of $\Delta t = 0.80\,\mathrm{s}$, for model J0, and $\Delta t = 3.80\,\mathrm{s}$, for models J3, should be added to the laboratory-frame breakout times. For the observer-frame times one should apply the correction $\Delta t_{\rm obs} = (\Delta t - (R_{\rm inj,j} - R_0)/c)(1+z)$. In Tab. 4.2 we see that $t_{\rm obs,BO} < t_{\rm BO}$ for the jet models, unlike it happens in model SH. In part, this is due to the fact that in $t_{\rm BO}$ the cosmological correction due to the redshift has been included. If this cosmological effect is neglected, i.e., for the case of an observer located right in front of the stellar surface, the corresponding breakout time in the observer's frame would be $t_{\rm det,BO}({\rm SH}) = t_{\rm obs,BO}({\rm SH})/(1+z) = 33.89\,\mathrm{s} < t_{\rm BO}$. The column of Tab. 4.2 tagged with $t_{\rm j\to SN}$ shows the time it takes a jet model to catch up with the preceding SN FS. As expected, the more energetic jet of model J3-H propagates faster through the medium left behind of the SN ejecta. It overtakes them in about half the time it takes the model J3-L to catch up with the SN FS.

In Fig. 4.7 we show 2D rest-mass density profiles at (hydrodynamic) breakout. We see how the base of the cocoon of the jet in model J0 is pinched due to the high rest-mass density and pressure in the stellar layer which extends up to $r = 9 \times 10^9\,\mathrm{cm}$ (see the drop in density in the stellar progenitor caused by an abrupt change in composition at such distance; Fig. 4.1). In models J3 the FS of the SN is already at distances much larger than this layer. Despite the SN explosion has lowered the density profile close to $R_{\rm inj,j}$, the jet changes its geometry because the pressure is still high up to this radius ($R_{\rm FS}$). Indeed,

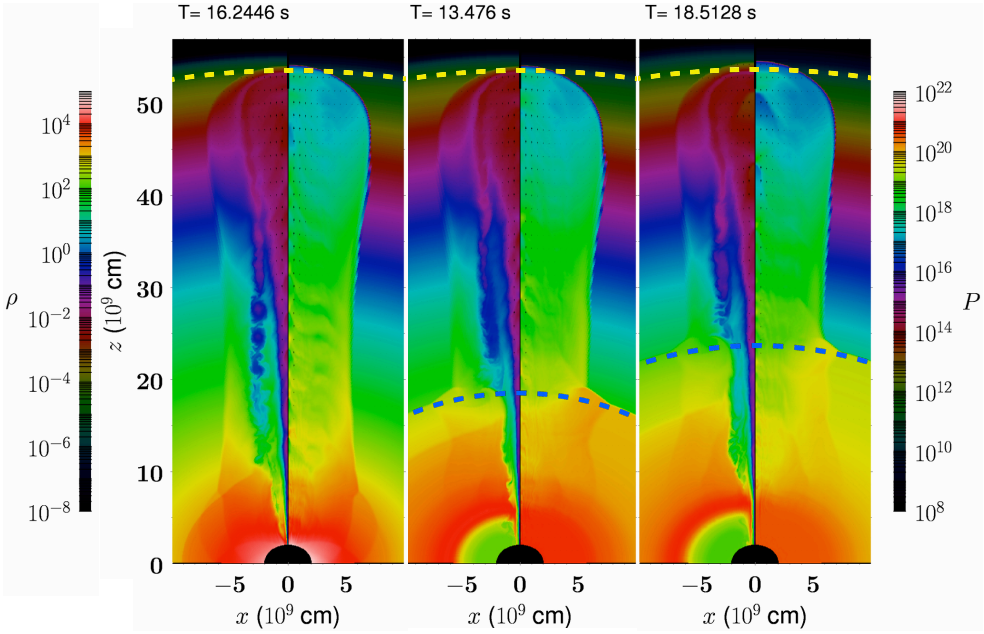

Figure 4.7: Snapshots of rest-mass density (left side of each panel) and pressure (right side of each panel) in the laboratory frame of models J0 (left panel), J3-H (central panel) and J3-L (right panel) at breakout from the stellar surface (times are annotated above each panel). The rest-mass density (palette on the left side of the figure) and pressure (palette on the right side of the figure) are in CGS units. $R_\star$ and $R_{\rm FS,SN}$ are marked with yellow and blue dashed lines, respectively.

the beams of all the jets of the J3 series remain highly collimated (being almost parallel to the z-axis) from their injection point up to slightly beyond the location of the $R_{\rm FS}$.

In Fig. 4.8 we show profiles of the rest-mass density, the Lorentz factor and the asymptotic Lorentz factor along the jet axis at breakout. The profiles of ρ and Γ are very variable, independently of whether the jet has interacted with the SN ejecta or not. We can, however, glimpse that the amplitude of the variations of ρ and Γ is larger in model J0 than in J3 models for distances $r \lesssim 3\times10^{10}$ cm. The oposite is true for distances above the latter approximated radial threshold. A more careful analysis of the reasons for these behaviour need of the study of the spectrogram of the jet profiles. This has not been

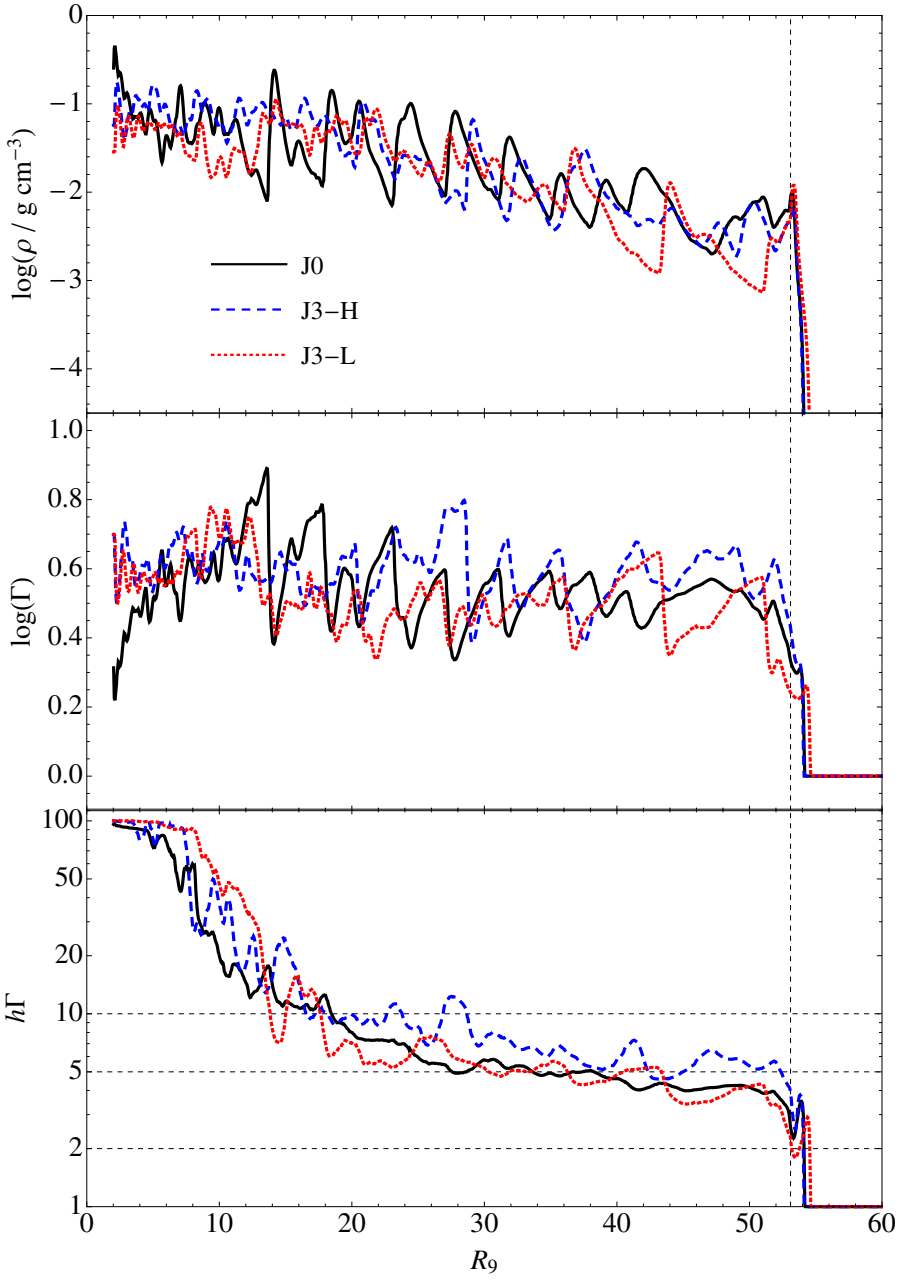

Figure 4.8: Rest-mass density (upper panel), Lorentz factor(mid panel) and $h\Gamma$ (lower panel) profiles along the axis of models J0 (black solid), J3-H (blue dashed) and J3-L (red dotted) taken once the jet's head reaches the original location of $R_\star$ (marked with a vertical dashed line).

done due to the time restrictions, but it is a matter of future work. The lower panel of Fig. 4.8 shows the profiles of Γ_∞. The most evident trend in the latter profiles is their non-monotonic decrease from its injection point to the jet's head, in contrast to the results of Mizuta & Ioka (2013). The reason why is not kept constant, even before the jet injection is over, may be due the interaction of the jet with the stellar mantle or the SN ejecta (among other factors; see Sect. 4.2.3 for more details).

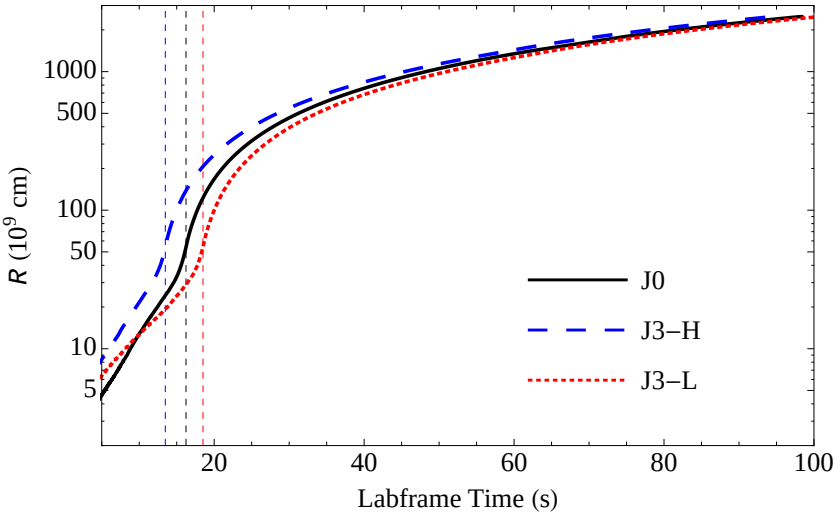

Figure 4.9: Time evolution, in the laboratory frame, of the location of the jet's head for model J0 (black solid), J3-H (blue dashed) and J3-L (red dotted). Using the same color scheme, $t_{\rm BO}$ for each model are marked with vertical dashed lines.

In Fig. 4.9 we show the propagation of the jet's head for all the models. Comparing models J0 and J3-H, both with the same jet energy, we observe that the jet which must propagate through the unperturbed progenitor (J0) takes longer to breakout than if the jet catches up with an energetic SN along the way (Tab. 4.2). The main reason for this is the reduced ram pressure model J3-H finds during its whole propagation. Furthermore, the SN ejecta drives the medium with a radial outwards velocity, in contrast to the fluid basically at rest found by the jet of model J0. As expected, models J3 are initially faster during the first seconds of the evolution (Fig. 4.9). Furthermore, the one of this

series with the largest initial jet energy (model J3-H) shows the fastest jet at the end of the simulation. However, the jet of model J3-L is overtaken by that of model J0 at $\sim 10\,\mathrm{s}$, and remains behind it during the rest of the evolution.

To study the different phases by of the evolution of the jet, we calculate the parameter (Martí, Müller & Ibáñez 1994)

$$\eta^* = \frac{\rho_\mathrm{j} h_\mathrm{j} \Gamma_\mathrm{j}^2}{\rho_\mathrm{EM} h_\mathrm{EM} \Gamma_\mathrm{EM}^2} \tag{4.19}$$

which is equivalent to the $\tilde{L}$ parameter of Matzner (2003) and Bromberg et al. (2011b), when the external medium is cold and at rest, as it is in our case. If $\eta^* < 1$ the jet's head is non-relativistic as it is the case when it is propagating within the stellar mantle (see Fig. 4.10). At the breakout all models show a fast rise in η^* while the jets become relativistic and enter the uncollimated regime ($\eta^* > \theta_\mathrm{j}^{-4/3} \simeq 88$; for a value of $\theta_\mathrm{j} = 2°$) once they propagate into the EM. This behaviour is consistent with that expected in GRB jets (Bromberg et al. 2011b). The sudden variations found in η^* after the breakout (Fig. 4.10) are of numerical origin. They are related to the technical difficulty in the localization of the post-FS state in our multidimensional simulations.

The mass enclosed below the innermost radial boundary in models where SN ejecta have been injected (J3) remains almost constant ($M_\mathrm{in} \sim 3.3 M_\odot$) through the whole hydro evolution. In those models, the accretion rate, through the inner radial boundary $\dot{M}_\mathrm{ac}$, starts around 10^{-5}–$10^{-4}\ M_\odot\ \mathrm{s}^{-1}$ ends with values of a few times $10^{-3}\ M_\odot\ \mathrm{s}^{-1}$. $\dot{M}_\mathrm{ac}$ is much larger for model J0 (the one without SN), where $\dot{M}_\mathrm{ac} \sim 1$–$0.1\ M_\odot\,\mathrm{s}^{-1}$ during the first 50 s of evolution to later decay to values of a few times $10^{-2}\ M_\odot\,\mathrm{s}^{-1}$. In this model the inner mass grows dramatically up to $26 M_\odot$ at the end of the simulation ($t \sim 100\,\mathrm{s}$). The absence of a rotating progenitor could explain this behavior. As observed by Nagakura et al. (2011), who build a rotating equilibrium model that resembles an stellar progenitor of Woosley & Heger (2006), including fast rotation in the envelope triggers a centrifugal shock in their models. It is, however, arguable whether this shock may really survive if a full General Relativistic treatment of the dynamics and the processes of nuclei photodissociation and neutrino losses are included (as the former authors recognize). In any case,

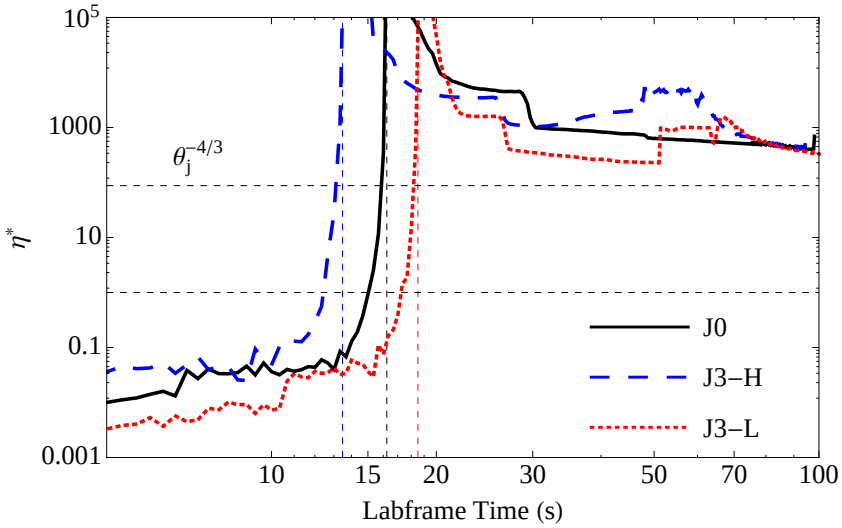

Figure 4.10: Time evolution, in the laboratory frame, of η^* for model J0 (black solid), J3-H (blue dashed) and J3-L (red dotted). Using the same color scheme, $t_{\rm BO}$ for each model are marked with vertical dashed lines. Values of $\eta^* = 1$, $\theta_{\rm j}^{-4/3}$ are marked with horizontal dashed lines.

the larger mass accretion rate of model J0 is associated to the larger rest-mass density (and also larger baryonic mass) close to the injection boundary in this model. If we compare the initial density profiles of J0 and, any other of the models in which a SN ejecta is present (Fig. 4.4 upper panel), it is evident that close $R_{\rm inj,j}$ the density of the initial progenitor (i.e., the density profile in which J0 shall evolve) is ~ 3 orders of magnitude larger than those of the rest of the models, in which the SN ejecta has cleaned the vicinity of the innermost radial boundary.

Finally, we discuss the post-breakout opening angle of the jet ($\theta_{\rm BO}$). We observe in Fig. 4.11 that in all models, after an initial transient phase in which $\theta_{\rm BO}$ cannot be reliably estimated, the jet opening angle decreases and settles to a value $\sim 9^\circ - 11^\circ$ in all jet cases. These values are $\gtrsim 5\theta_j$, i.e., substantially larger than the initial opening angle of the jet. The monotonical increase observed, e.g., in model J3-L $\sim 20\,$s post-breakout, is an artifact resulting from the operative criterion employed to measure it.

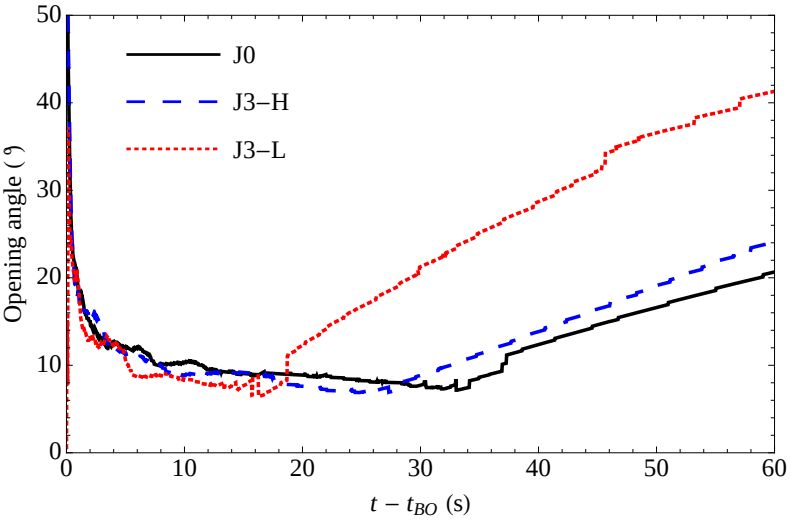

Figure 4.11: Time evolution, in the laboratory frame, of the opening angle of the jet after breakout for models J0 (black solid), J3-H (blue dashed) and J3-L (red dotted).

4.2.3 Energy reservoir for radiation

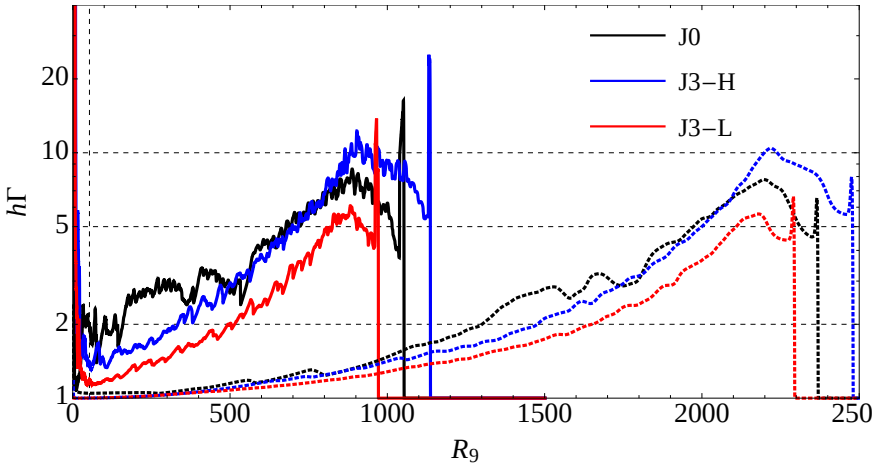

Figure 4.12: Profiles along the jet axis of $\Gamma_\infty = h\Gamma$ for models J0 (black), J3-H (blue) and J3-L (red) at $t = 50\,\mathrm{s}$ (solid) and $t = 94\,\mathrm{s}$ (dotted).

In Figs. 4.8 (bottom panel) and 4.12 we show the value of $\Gamma_\infty = \Gamma h$ along the axis of the jet. We see that before breakout Γ_∞ decreases in the jet from

its initial value at the injection point ($h_i\Gamma_i = 100$) to values of < 5 at the jet's head, but once the jet leaves the star, Γ_∞ starts to increase again.

This quantity should be conserved along a streamline but as we can see it quickly drops already within the star (Fig. 4.8). Mizuta & Ioka (2013) show that Γ_∞ remains constant up to the jet's head even at distances of 10^{11} cm. They contrast these results to the ones of Mizuta et al. (2011) where Γ_∞ decreases with radius. They attribute this decrease to the insufficient numerical resolution, leading to numerical diffusion at the jet head which causes excessive baryon-loading and thus reduces Γ_∞. Although our simulations use a coarser radial grid (Mizuta & Ioka used $\Delta_{\rm r,min} = 10^7$ and 5×10^6 in their two simulations), the angular resolution within the range $[0°, 9°]$ is much finer ($\Delta_\theta = 0°.1$) than the one used by Mizuta et al. (2011). In principle, the existence of a gravitational potential makes it necessary to add a correction for the gravitational energy in the evolution of Γ_∞, which therefore is no longer constant on a streamline. However, the correction is small and $\Gamma_{\infty,\rm pot} \simeq \Gamma_\infty e^{-M_{\rm in}/R_{\rm inj,j}} \simeq \Gamma_\infty$. Finally, another factor that may account for such a drop in Γ_∞ is that our jet injection only lasts for 20 s (the constant phase), in contraposition to that of Mizuta & Ioka (2013), which is set constant at all times. Furthermore our initial value of $\Gamma_{\infty_0} = 100$ is more than five times less and $R_\star$ also smaller, so that the jet/star interaction is much more critical in our case. However, we point to the jet interaction with the star or with the SN ejecta and the lose of collimation as the main cause for the deviation from uniform Γ_∞. In the case of J0 the density profile of the star, and in particular the one associated to the layer which extends up to $r = 9 \times 10^9$ cm, is the responsible of that (see in Fig. 4.8 how Γ_∞ drops by a factor of 5 up to this radius). For the series of models J3 we identify the shell in the post-FS region as the place where Γ_∞ starts its drop.

We calculate the thermal energy contained in the jet for different ranges of the asymptotic Lorentz factor, Γ_∞ (Fig. 4.13). This energy sets the total energy available to be converted to radiation (in practice, conversion to emission will proceed with an efficiency factor less than unity) and received by an observer. We assume here that the observer is facing the jet, i.e., $\theta_{\rm obs} = 0°$. Due to

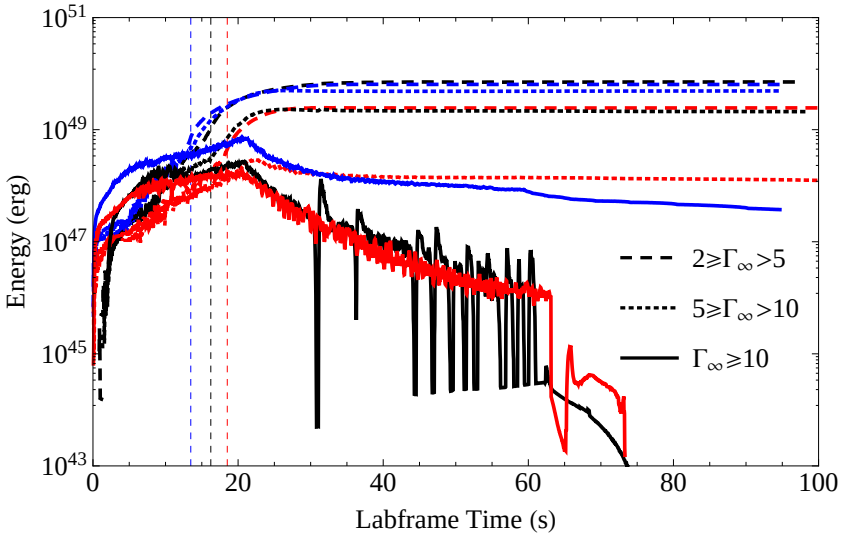

Figure 4.13: Time evolution, in the laboratory frame, of the energy stored in the jet material with $2 \leq \Gamma_\infty < 5$ (dashed), $5 \leq \Gamma_\infty < 10$ (dotted) and $\Gamma_\infty \geq 10$ (solid), which potentially could be radiated and observed by an observer located at $\theta_{\rm obs} = 0°$. Models J0 (black), J3-H (blue) and J3-L (red) are shown together with a vertical dashed line indicating the jet breakout time in each model.

the relativistic motion of the jet, radiation is collimated over a solid angle $\theta < 1/\Gamma$ and it is received by our observer if it has been emitted from an angular position $\theta_{\rm pos} \leq \theta$. Therefore, for the calculation we assume that only those jet elements with $\Gamma_\infty < 1/\theta_{\rm pos}$ contribute.

Fig. 4.13 shows that, for all the models, most of the energy, viz. 10^{49}–10^{50} erg, is stored in material with $2 \leq \Gamma_\infty < 5$ and that this amount is constant throughout most of the evolution until the end of the simulations. If this energy is released as radiation its contribution is, due to moderate Lorentz factor, expected as (soft) X-rays and lower energy radiation.

In the regime of $5 \leq \Gamma_\infty < 10$ we find a relatively large amount of material (though smaller than in the range $2 \leq \Gamma_\infty < 5$). This material is mostly found in regions closer to the jet head. The internal energy of all this material is in general smaller compared to the material within the Lorentz factor regime discussed above, except for the particular case of model J3-H, for which the

energies in both regimes are comparable. In model J0, we find a factor of ~ 3 less energy in this regime than at lower values of Γ_∞, while in J3-L this difference goes beyond 1 order of magnitude. Its emission is expected to come mostly from the post-FS region, as the jet becomes transparent. The higher Lorentz factor makes for a more energetic radiation than from the gas discussed above, leading to emission in the hard X-rays or even the γ-ray band.

The jet elements in the range $\Gamma_\infty \geq 10$ are expected to contribute to the γ-ray emission. As shown in Fig. 4.12, the jet's head and a small region behind it are the only places beyond $R_\star$ where the jet reaches such values of Γ_∞. Besides, as the time advances Γ_∞ decreases and eventually the jet's head material evolves towards $\Gamma_\infty < 10$. The rest of material, which is contributing to this regime is deep inside the star, close to the injection point. It may eventually convert its thermal energy into kinetic energy and leave the star (probably with a smaller Γ_∞). Figure 4.12 shows that the decay in Γ_∞ is abrupt from the injection point to the jet's head. As we see in Fig. 4.13 the behaviour of the energy curve follows mainly from the energy injection at the jet nozzle. At $t_{\rm inj,j} \simeq 20\,{\rm s}$ (time by which the constant energy injection phase ends) all models reach a peak n the intervals of Γ_∞ where $\Gamma_\infty > 5$. After that point the energy stored in matter with $\Gamma_\infty > 5$ decreases, since the injection stops and the jet loses its source of energy. At $\sim 60\,{\rm s}$ there is a sudden decay as the material close to $R_{\rm inj,j}$ no longer possesses such a high Lorentz factor, with the exception of J3-H (with $\sim 4 \times 10^{47}$ erg at the end of the simulation) in which there is still a small region in which $10 \leq \Gamma_\infty$. Due to its larger energy (with respect to J3-L) and the presence of the SN ejecta (compared to J0) the jet in this model retains larger values of Γ_∞. The jet cools progressively as the time goes on but, at the end of the simulation, this energy is almost comparable to that of model J3-L in the regime of $5 \leq \Gamma_\infty < 10$. Models J0 and J3-H show both internal energies between 10^{48}–$10^{46}\,{\rm erg}$, dropping below $10^{46}\,{\rm erg}$ at $t \simeq 60\,{\rm s}$ ($\sim 40\,{\rm s}$ after the breakout) and show more variability than model J3-H. Model J0 is not affected by SN ejecta and its variability is triggered by the star while the jet has to break through it, specially through the layer which extends up to $r = 9 \times 10^9\,{\rm cm}$. Although $E_{\rm iso,j}$ is two times smaller in J3-H,

the SN ejecta reduce the density into which the jet propagates during the first seconds. This effect makes the jet ballistic and less prone to instabilities.

4.3 Spectral evolution

To calculate the observed flux density of the radiation emitted in our simulations we postprocess the computed hydrodynamic models with SPEV. The breakout of GRB/SN jets is expected to contain an observable thermal component in addition to the non-thermal emission associated to particles accelerated at shocks.

In this section we only focus on thermal emission since it is, compared to synchrotron emission, less dependent on the (forward) shock position that can be misidentified after applying the fix up needed to overcome the problem associated to the diffusion of the FS (see Sect. 4.3.1). We also include Thomson absorption, $\alpha_\nu = 0.2(1 + X_\mathrm{h})\rho$, in the whole domain of the simulations since it can be dominant at large temperatures and densities.

Although the EoS used in our hydrodynamic simulations only considered the contribution of baryons, the temperature has been computed 'artificially' in SPEV assuming local thermodynamic equilibrium, i.e., $T = T_\mathrm{bar} = T_\mathrm{rad}$. As stated earlier in the chapter, this temperature is underestimated in optically thin regions where radiation is decoupled from the baryonic gas and only the latter contributes to the total pressure. Unlike we did in Chap. 3, this time we do not apply the temperature calculation in optically thin regions as explained in Sect. 2.4.3 in order to save computational time, and both the baryonic and radiation contributions are considered here in the whole physical domain.

4.3.1 Technical aspects

The postprocessing of the hydrodynamic models is particularly demanding, since we have to work in a large range of scales. On the one hand, we need to properly capture the jet propagation within the star. This means to resolve scales even smaller than $\sim 10^8$ cm which sets the resolution of our hydrodynamic models. Also, we want to capture properly the main episodes of jet

evolution, mainly those which occur very close to the breakout moment. The latter requires having a large number of hydrodynamic outputs spaced in time by, at most, a few milliseconds. Furthermore, we nave to cover a large radial extent, requiring a large number of grid cells and making the run computationally very expensive. This is because the jet moves relativistically and the length scale of our problem becomes quickly many orders of magnitude larger than the smallest scale used in the simulation. On the other hand, the relativistic motion of the jet head means that a given lab time interval corresponds to only a small interval in the observer frame (see, e.g., Fig. 2.1). Thus, computing the emission for as large a time as possible requires an even large hydrodynamic evolution in the lab frame. This increments enormously the number of needed hydrodynamic outputs.

We record the full 2D hydrodynamic state (i.e., rest-mass density, pressure, temperature and two velocity components) 30 times per second in the laboratory frame. Due to relativistic time delays, strongly dependent on the local fluid Lorentz factor, in order to produce a LC of a few seconds in the observer frame, we need to run our models for about 30 minutes in the laboratory frame. In practice, this amounts to save more than 50000 files per model (requiring $\sim 10\,\mathrm{Tb/model}$) in order to perform the post-processing evaluation of the emitted radiation. The recording frequency of 30 Hz of the hydrodynamic state is a trade off between what we can technically store and the optimal storing frequency ($\sim$ 1 model per hydrodynamic time step, resulting in a frequency of $1/\Delta t \sim 75\,\mathrm{Hz}$). In practice, the current recording frequency is good enough to obtain converged spectra and LCs at frequencies below hard X-rays. However, the accuracy of the results is degraded in the gamma-ray realm, where the variability timescales of the radiative processes are much shorter.

For the evaluation of the radiative signature we employ a virtual detector with ~ 1 pixels per each 10^9 cm.

We have assumed that the progenitor system is located at a redshift of $z = 0.1$ which is typical for nearby GRB/SNe. The spectra have been calculated using a resolution of 26 points logarithmically distributed in the frequency range of $[10^{13}$–$10^{19}]$ Hz. We show different LCs in the r band ($4.68 \times 10^{14}\,\mathrm{Hz}$),

the $W2$ band (1.56×10^{15} Hz) and the ones of *Swift*'s XRT (7.25×10^{16} Hz $< \nu < 2.42 \times 10^{18}$ Hz) and BAT (3.63×10^{18} Hz $< \nu < 3.63 \times 10^{19}$ Hz). In this way we cover a range of frequencies that go from the optical up to the γ-ray regime.

Our jets suffer of a bit of numerical diffusion when they cross the radius $r = 10^{12}$ cm where the radial grid resolution decreases. The most serious consequence of this extra diffusion is that a fraction of the shocked external medium propagates faster than the speed of light. At the time of computing the synthetic time evolution of the emission this is a drawback, since photons which have been emitted at the jet head can be overtaken by the jet itself. To avoid this we have implemented the following fix up. If the jet head propagates faster than or at the speed of light (i.e., $v_{\rm h} = \Delta R_{\rm h}/\Delta t \geq c$) between two consecutive hydrodynamic snapshots, the timestep between them is reset to $\Delta t_{\rm reset} = \Delta R_{\rm h}/v'_{\rm h}$, so that $v'_{\rm h}/c = \sqrt{1-(\Gamma_{\rm max}/\sqrt{2})^{-2}} < 1$. We have assumed that the jet head propagates at a velocity defined by the maximum Lorentz factor $\Gamma_{\rm max}$ found along its axis divided by a factor $\sqrt{2}$.

We have to take into account that the fix up modifies the mapping between given time intervals in the lab frame and the corresponding time intervals in the observer frame. On the other hand, the emission is also affected when the photosphere crosses the spherical surface located at $r \sim 10^{12}$ cm. The jump in resolution can lead to the misidentification of the photosphere, which produces artifacts in the computed LCs and spectra. For this reason we limit our study up to the time in which the photospheres in each of the jet models go into the coarser radial grid.

4.3.2 The emitting region

The left panels of Fig. 4.14 show the hydrodynamic profiles along the jet axis in the observer frame of model J3-L, for a given observation time after breakout. These profiles have been obtained by postprocessing the data with SPEV. Both curves in density and pressure are smooth in contrast with the hydrodynamic profiles in the laboratory frame (right) in which we observe small scale variability, caused by many weak shocks along the axis as a result of the jet in-

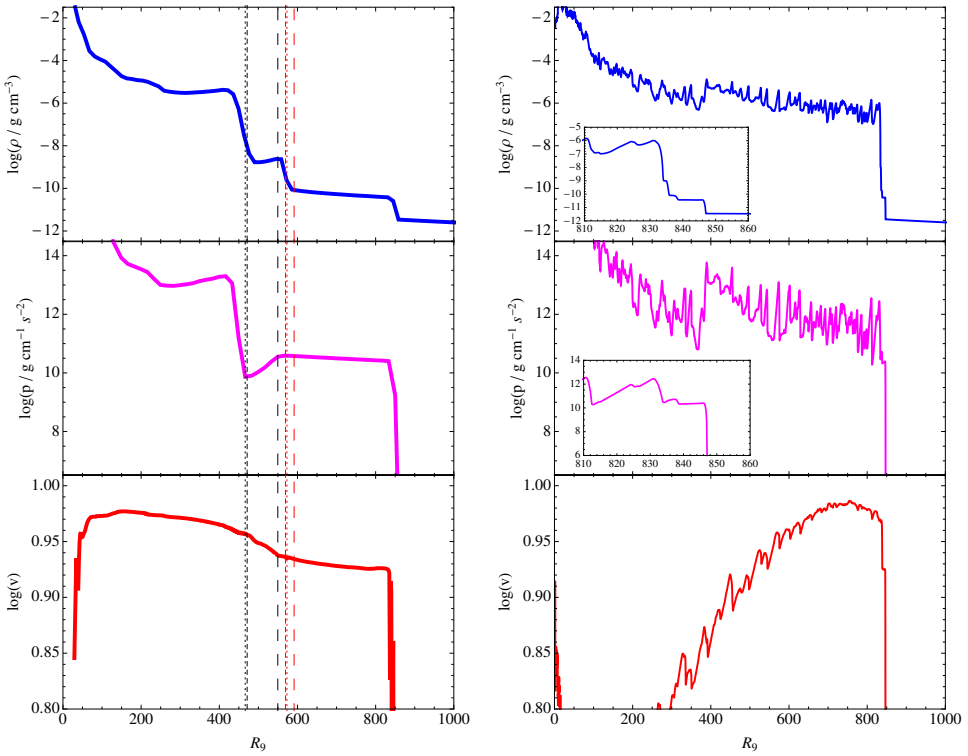

Figure 4.14: Observer- (left) vs. laboratory-frame (right) profiles along the jet axis of rest-mass density (top), pressure (center) and velocity (in units of c; bottom) of model J3-L. The observer-frame profile is taken at $t_{\rm obs} = 19.35\,{\rm s}$ after the observed breakout. The laboratory-frame profile at $t \simeq 45.7\,{\rm s}$. Vertical dashed lines in the left panels indicate the location of the surface where the optical depth is 10 (black) and 1 (red) for the different observing frequencies: $\nu_p = 3\times10^{15}\,{\rm Hz}$ (peak spectral frequency of model J3-L; short dashed), r band (long dashed) and XRT band (dotted). In the upper and middle right panels both insets show a zoom of the respective quantities around the head of the jet.

teraction with the SN ejecta and the progenitor star. As we can see, the shock structure is highly stretched in the observer-frame profiles in comparison with the lab-frame profile, evidencing the relativistic character of the source. The times of the observer-frame and lab-frame profiles were chosen such that the positions of the jet head in both frames roughly coincide. The density profile ends at $R_9 \sim 850$ with a steep decline that coincides with the position of the

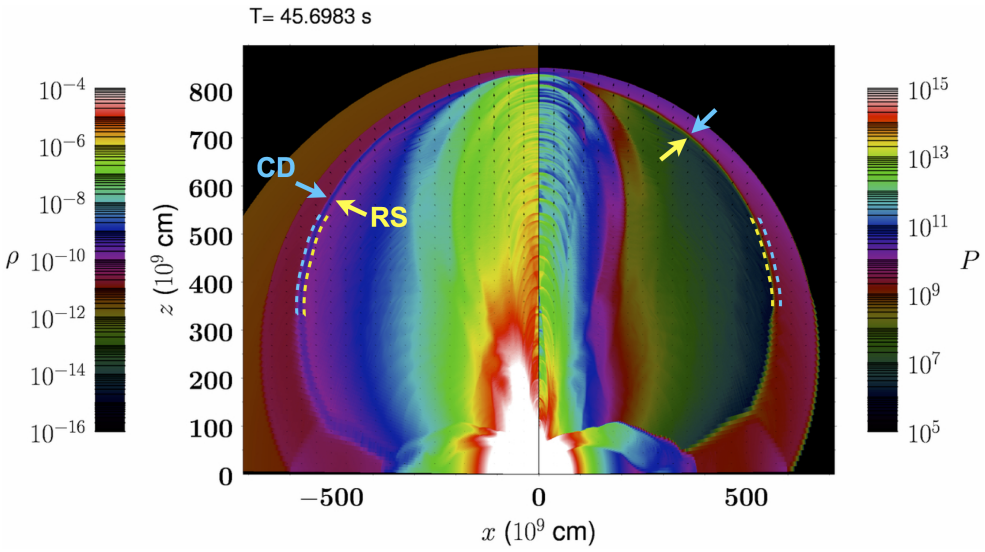

Figure 4.15: Snapshot at $t \simeq 45.7$ s of model J3-L. Rest-mass density (left) and pressure (right) are in CGS units. The contact discontinuity (CD; blue) and the reverse shock (RS; yellow) are marked with dashed lines. We have also denoted with arrows the extension of the post-RS state.

FS. In the left panels the contact discontinuity (CD) separating the shocked jet matter from the shocked external matter can be clearly identified, since pressure and velocity are continuous while density shows a jump of more than one order of magnitude. Furthermore, the CD coincides with the region in which the optical depth is equal to 1 at a frequency which falls between the peak spectral frequency of the event ($\nu_p = 3 \times 10^{15}$ Hz; see Sect. 4.3.3 for more details) and the XRT band in model J3-L. The RS is marked roughly by the line in which the optical depth at the peak spectral frequency (also the one in the XRT band) is equal to 10. To identify these regions in the lab-frame profiles we have to zoom in to properly distinguish them (see insets in the right panels of Fig. 4.14). The comparison with the structures seen on the left panels is not straight forward. The FS is located right at $R_9 \sim 847$, the CD at $R_9 \sim 835$ and the RS at $R_9 \sim 834$ (see insets)[3]. However, the identification of

[3]Another jump is seen in both the rest-mass density and pressure at $R_9 \sim 838$ whose formation we attribute to the interaction of the jet head with a very low-density external

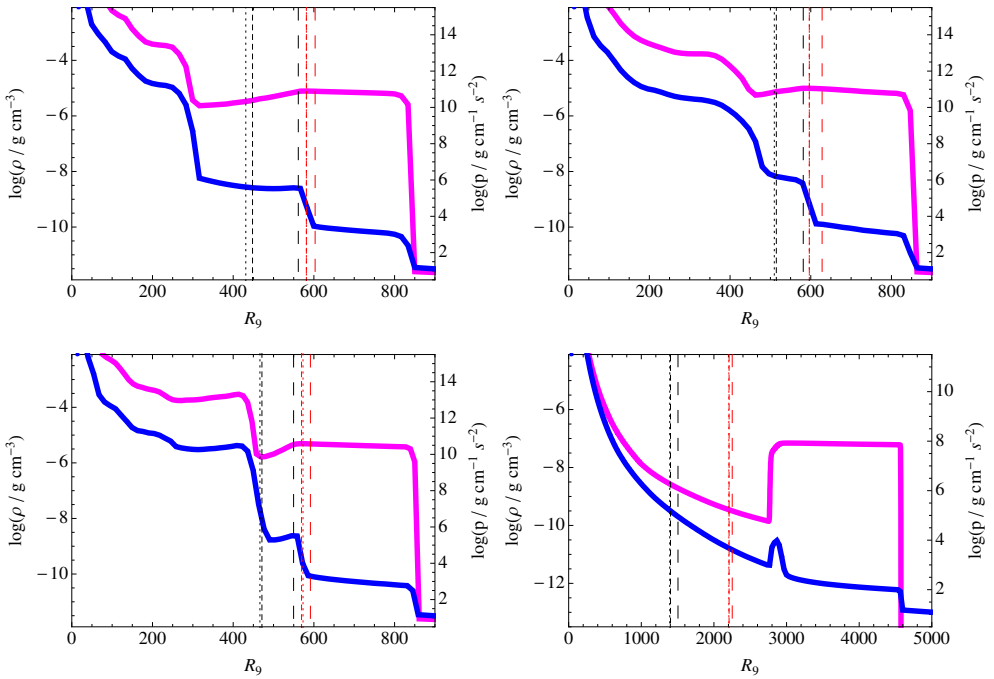

Figure 4.16: Rest-mass density (blue) and pressure (magenta) profiles along the jet axis for models J0 ($t_{\rm obs}$ = 16.4 s, i.e., $\Delta t_{\rm obs,BO}$ = 0.4 s; upper left), J3-H ($t_{\rm obs}$ = 13.35 s, i.e., $\Delta t_{\rm obs,BO}$ = 0.4 s; upper right) and J3-L ($t_{\rm obs}$ = 19.35 s, i.e., $\Delta t_{\rm obs,BO}$ = 0.86 s; lower left) and SH ($t_{\rm obs}$ = 90 s, i.e., $\Delta t_{\rm obs,BO}$ = 54.5 s; lower right) in the observer frame. $\Delta t_{\rm obs,BO}$ denotes the time elapsed since the breakout. Vertical dashed lines indicate the location of the surface where the optical depth is 10 (black) and 1 (red) for the different observing frequencies: ν_p of each model (short dashed), r band (long dashed) and XRT band (dotted).

the RS along the axis is not trivial since, although we see jumps in all the three quantities depicted in Fig. 4.14, the post-RS state does not resemble that seen, e.g., in model SH (see Fig 4.4; or alternatively see Fig. 4.16). Indeed, for the identification of the RS we need to resort to the 2D representation of the model (Fig. 4.15), since the morphology of the shocks is very different off-axis. In that picture, the off-axis locations of the RS and the CD are marked. As we show in Fig. 4.14 the position of the photosphere at the peak spectral frequency is

medium. This component is not yet identified in the observer-frame hydrodynamic profiles.

located roughly at the position of the CD and thus the thermal emission comes mainly from the shocked jet ejecta (more loosely speaking, from the RS region). Furthermore, we see that the photosphere at the peak spectral frequency basically coincides with that observed in the XRT band. The weak dependence of the photospheric location on frequency is a hint that the Thomson absorption is dominant in this range of frequencies. However in the r band the thermal bremsstrahlung absorption is comparable to that of Thomson as indicated by the fact that the photospheric radius is larger in this band. Also, the optical depth gradient becomes larger at r band so that the emitting region is a bit smaller at frequencies below the peak spectral frequency.

Another important consequence is that the stretching of the shock structure, because of the relativistic motion, limits the extension of the observed region during the first seconds after breakout. At the time of evolution shown in Fig. 4.14, the jets are opaque below the RS at all frequencies and the variable structure caused by the small shocks behind the it (seen in the laboratory-frame profiles) is hidden from observers during the first moments of observation. However it is expected to contribute to the variability of the LC later.

In Fig. 4.16 we show a comparison of model J3-L with the rest of the models. We have chosen the observer-frame profiles at that time where the jet head is, approximately, located at the same position in all the models. As can be seen the profiles of models J0 and J3-H are very similar to those shown for model J3-L, so all the discussion made for the latter model can be also applied to the former ones. The most remarkable exception is that model J0 shows a post-RS region ($250 < R_9 < 600$) more extended than models J3. In the lower right panel of the figure we also show a profile for model SH at 54.5 s after the breakout. In this case the shock structure is very similar to that in the laboratory frame (see Fig. 4.4) which results from the subrelativistic propagation of SN ejecta, as we already saw in Sect. 4.2.1.

In Fig. 4.17 we show the temperature and intensity evolution along the line of sight for the peak spectral frequency (close to the $W2$ band) in each of the jet models. The emission, as already stated, comes from regions below the photosphere which are moderately optically thick (to be precise from the

region between lines of $\tau = 1$ and $\tau = 10$ in Fig. 4.17), whose temperature is $T \gtrsim 10^6\,\mathrm{K}$. As shown in Fig. 4.18 the emission in the XRT and $W2$ bands comes from a similar volume (see also right panels on Fig. 4.17) in models J0 and J3-H, while in model J3-L the emitting region has a larger volume. In the BAT band (Fig. 4.18; left panel) the emission region it is clearly more concentrated around the axis of the jet. We also see that the $\gamma-$ray emission of model J3-H is more intense close to the symmetry axis than in the other two models.

Before proceeding to the next section we warn the reader that, as already mentioned, we are affected in the calculation of the emission by numerical diffusion in the hydrodynamic models. As we shall see in Sect. 4.3.3, the computation of the optical depth can be affected by it and for $\nu > \nu_p$ we can have contributions coming from regions below the RS (of larger density and emissivity) from the moment when the photosphere reaches the coarser radial grid, so that the emission can be overestimated.

4.3.3 Light curves and spectra

4.3.3.1 SN shock breakout

Shock breakout flashes were predicted by Colgate (1968, 1974) as a source for $\gamma-$ray bursts, which where undetected by that time. Since then, a large number of analytic and numerical studies of the SN shock emergence have been carried out. An exhaustive list of relevant contributions is beyond the scope of this thesis, but some of the most relevant works in the field are Klein & Chevalier (1978); Imshennik & Nadezhin (1988, 1989); Blinnikov & Postnov (1998); Ensman & Burrows (1992); Matzner & McKee (1999); Blinnikov et al. (2000); Tan et al. (2001); Nakar & Sari (2010, 2012).

As the SN goes off in an optically thick wind, the breakout is not immediately observed, and the XRF emerges only when the shock width in the wind becomes comparable to its distance from the circumstellar material photosphere (Li 2007; Balberg & Loeb 2011). Indeed, since the shock must progress through the wind until it becomes transparent, the flash is not only delayed,

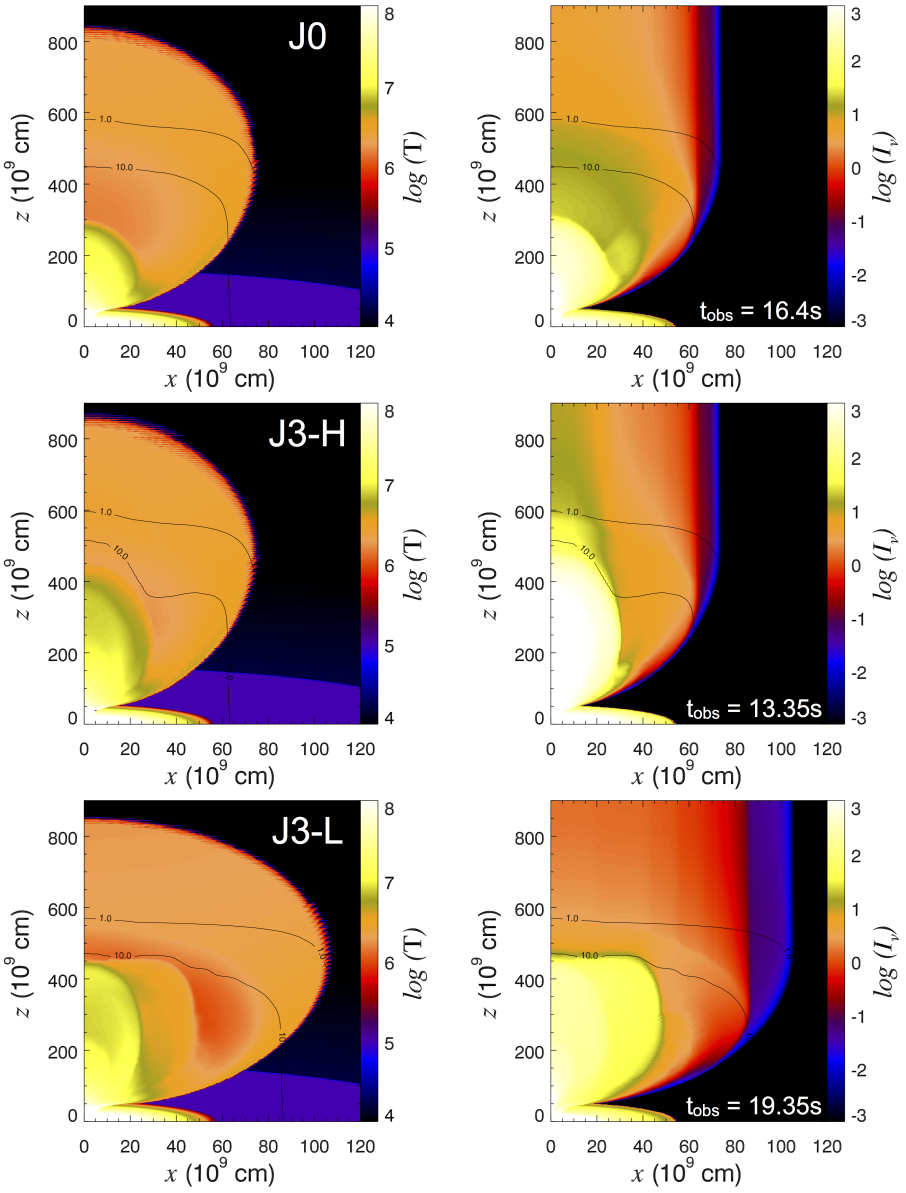

Figure 4.17: Snapshots of temperature (left) and specific intensity (right) of the thermal emission at the peak frequency of different models as seen in the observer frame. The observer is located in the vertical direction (towards the top of the page) at a viewing angle $\theta_{\rm obs} = 0°$. The emission is computed at the following observational times: $t_{\rm obs} = 16.4\,$s (J0; upper panels), 13.35 s (J3-H; center panels) and 19.35 s (J3-L; lower panels). Units are in CGS.

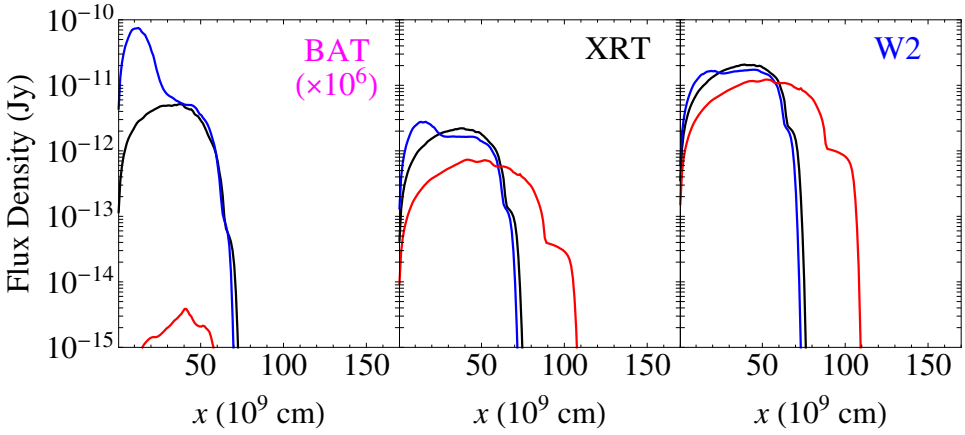

Figure 4.18: Distribution of flux in the 1D detector for models J0 (at $t_{\rm obs} = 16.4$ s; black), J3-H (at $t_{\rm obs} = 13.35$ s; blue) and J3-L (at $t_{\rm obs} = 19.35$; red) at different frequency bands.

but also happens when the fluid is cooler due to its adiabatic expansion. This may shift the signal towards the UV-band (see, e.g., Ofek et al. 2010).

In our models, the UV and optical spectral flux densities (F_ν; Fig. 4.19 top panel) are larger by 2 orders of magnitude than that of the X-rays. Computing the luminosity ($L_\nu \sim \nu F_\nu 4\pi D_L^2$; where $D_L = 463$ Mpc for a redshift $z = 0.1$) in the r, $W2$ and XRT bands (Fig. 4.19 bottom panel), we observe that the event is more luminous in X-rays than in the $W2$ band during the first 20 s. Furthermore, in the former band we find a peak already at ~ 6 s. The LC in both the r and $W2$ band peaks at about 26 s after breakout.

Up to ~ 10 s after the breakout the observed emission peak is located in the extreme UV band, but it shifts to the optical as the ejecta cool down (see how the blue and red lines intersect in Fig. 4.19 top panel). From that moment on up to the end of the simulation (~ 45 seconds later), we calculate the average spectral energy distribution (F_ν, Fig. 4.20 top panel) and average spectral luminosity (L_ν, bottom panel) of the SN. The spectrum is composed, roughly, of two power laws and a cutoff at X-rays, to each of the sides of the spectral peak which is located at the r band. The low- and high-energy tails below and above the spectral peak frequency have spectral indices of

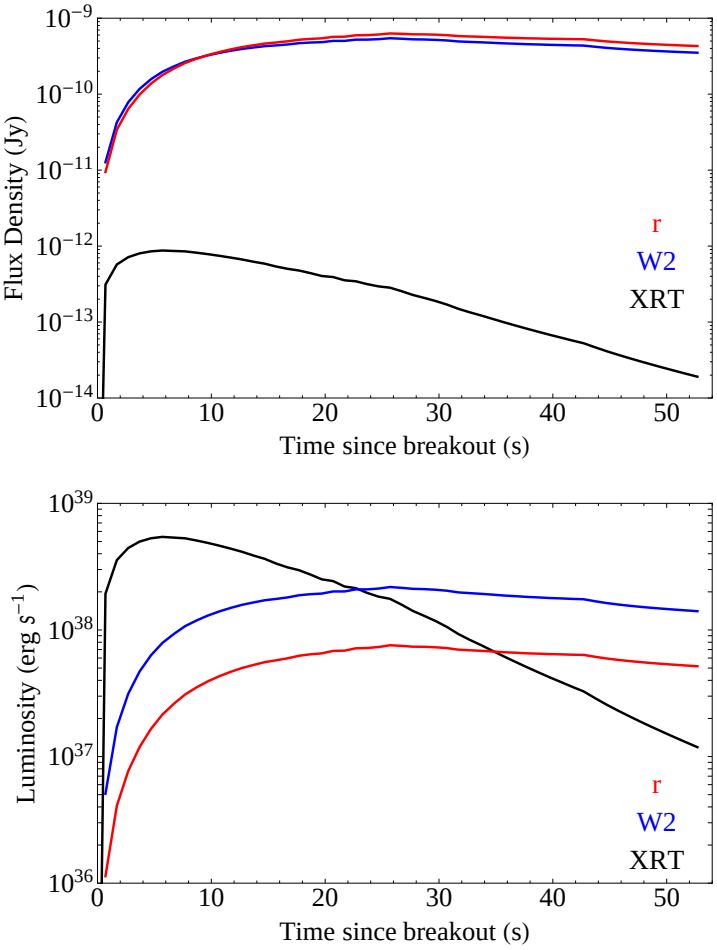

Figure 4.19: Time evolution of the flux density (F_ν; top) and luminosity (L_ν; bottom) of model SH for the following bands: r (red), $W2$ (blue) and XRT (black).

$b \sim 1.9$ and $b \sim -0.4$, respectively ($F_\nu \propto \nu^b$). Although we consider thermal bremsstrahlung emission, the spectrum does not exactly resemble to that of a BB because in our case Thomson absorption becomes dominant at the high-energy tail of the spectrum (recall that the larger is the frequency the smaller is the thermal-bremsstrahlung absorptivity, while the Thomson absorption is frequency independent).

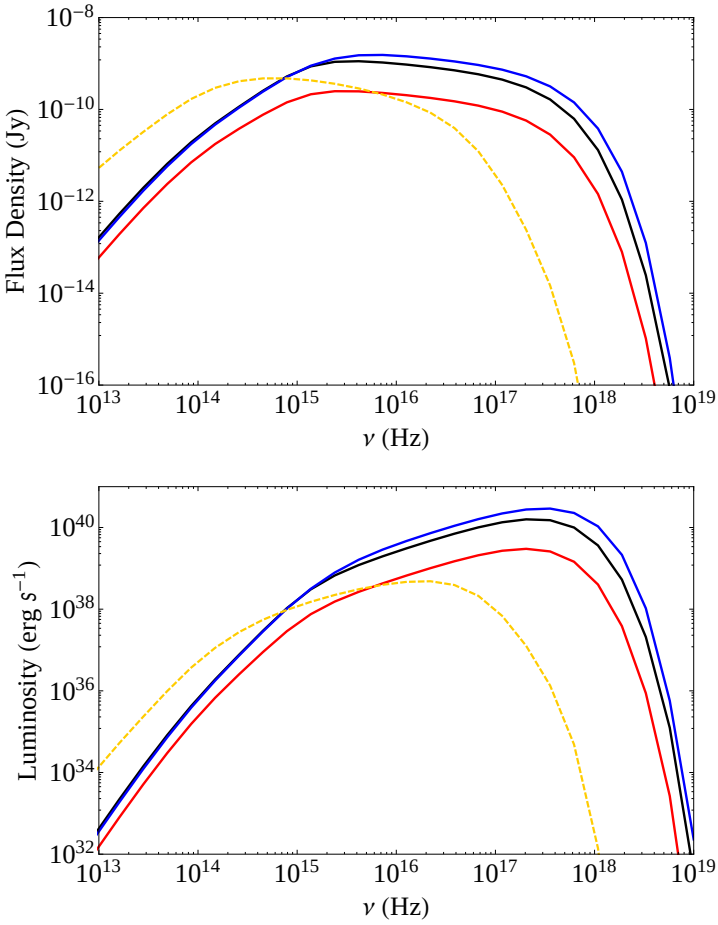

Figure 4.20: Average spectra in units of flux density (F_ν; top) and luminosity (L_ν; bottom) for models SH (yellow dashed), J0 (black), J3-H (blue) and J3-L (red).

4.3.3.2 Jet breakout

In Fig. 4.21 we show the time evolution of the flux density (top) and luminosity (bottom) in different emission bands for all the jet models. As it was stated at the beginning of the section, the emission of our jet models has to be taken with caution once the photosphere ($R_{\rm ph}$) reaches the coarser-resolution patch of the numerical grid where numerical diffusion affects the hydrodynamics (see Sect. 4.3.2). The region of confidence in our LCs is represented in Fig. 4.21

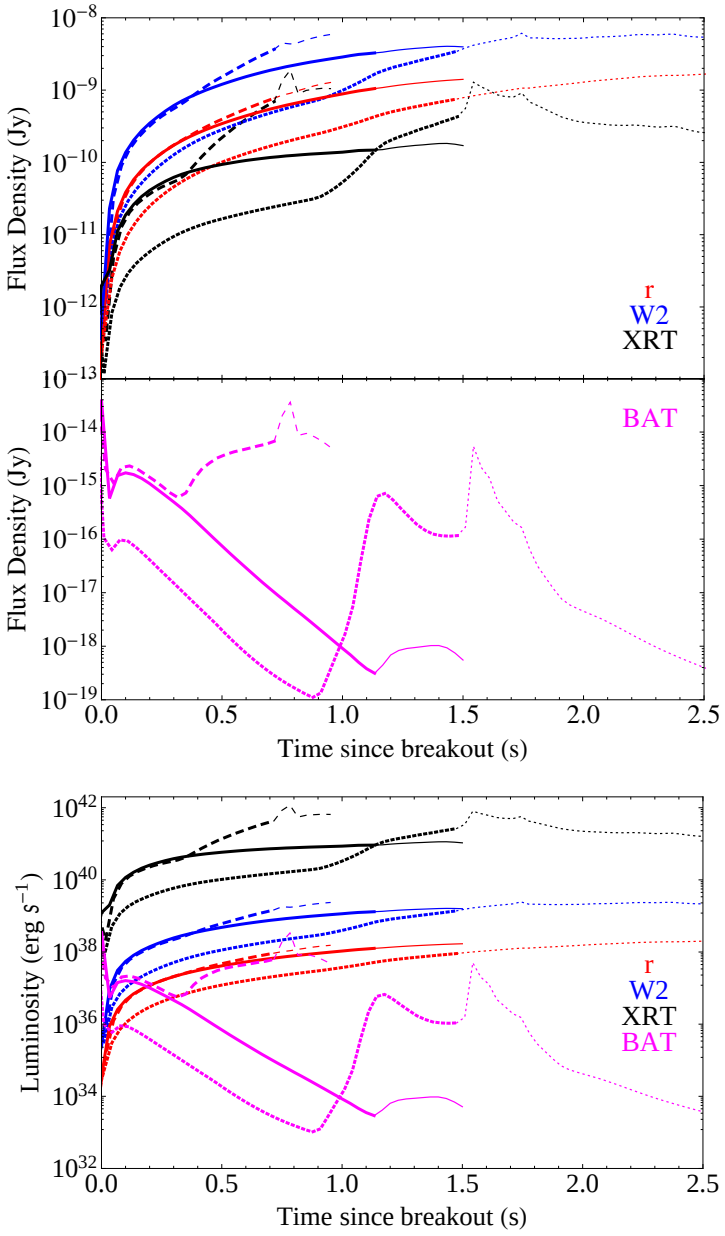

Figure 4.21: Time evolution of the flux density (F_ν; top) and luminosity (L_ν; bottom) of models J0 (solid), J3-H (dashed), J3-L (dotted) for the following bands: r (red), $W2$ (blue), XRT (black) and BAT (magenta). Thick lines represent the zone of confidence (mainly, when $R_{\rm ph} < 10^{12}$ cm). Thin lines have to be taken with caution.

with thick lines, and the regions that should be taken with caution with thin lines. In model J0 the confidence region ends at the time of a minimum in the BAT band ($\sim 1.1\,\mathrm{s}$ after breakout). In models J3 we have identified this first valley as the moment in which the jet head reaches the coarser grid at $10^{12}\,\mathrm{cm}$. However, we do not attribute the subsequent increase of flux in the BAT bands of models J3 (also a small increase can be observed in the $W2$ and XRT bands) to any issue related with numerical diffusion at this point because at this time the photosphere is still well below this region. Thus, we include this temporal region into our confidence region in models J3.

In Fig. 4.20, we show the average spectral energy distribution (top) and spectral luminosity (bottom). Because of the problems attached to the emission once $R_{\mathrm{ph}} > 10^{12}\,\mathrm{cm}$ and to make a direct comparison between models, the average has been performed only for 0.5 s: since 0.1 s up to 0.6 s after the breakout. This latter time corresponds to the time in which the photosphere of model J3-H (the one with the fastest jet) reaches the coarser radial grid. In general terms, the thermal spectra of all our jet models show many similarities between them, which make those models in which a SN explosion has been set up (J3) almost indistinguishable from that in which it has not (J0). The jet spectrum shows an overall flux density comparable to (though one order of magnitude larger than) that of the SN, but obviously, with a much more energetic tail extending up to the BAT band. In jet models the spectral peak is located in the UV regime rather than in the optical (top panel of Fig. 4.20; $\nu_{\mathrm{p}}(\mathrm{J0}) \sim 4 \times 10^{15}\,\mathrm{Hz}$, $\nu_{\mathrm{p}}(\mathrm{J3\text{-}L}) \sim 7 \times 10^{15}\,\mathrm{Hz}$ and $\nu_{\mathrm{p}}(\mathrm{J3\text{-}H}) \sim 3 \times 10^{15}\,\mathrm{Hz}$). The low-energy tails show indices of $b \simeq 1.8$ while the high-energy tails, which extend from the extreme UV up to the soft X-ray band, show indices of $b = -0.25$–-0.35 ($F_\nu \propto \nu^b$). Both indices are smaller, in absolute value, than those obtained in model SH.

4.4 Discussion and conclusions

The collapse of the inner core of low metallicity, fast-rotating, massive stars may produce the conditions to generate the central engine of a GRB as well

as a successful SN explosion. Our numerical models are set up assuming that unspecified processes (e.g., magnetohydrodynamic stresses or neutrino heating) have generated collimated outflows inside the core of the collapsed star. The propagation of a SN shock produces a drastic change in the structure of the star undergoing the SN explosion. As the SN ejecta sweep the stellar mantle, they modify the medium in which a GRB jet produced by the central engine shall propagate. We have justified that the delay between the generation of the SN ejecta and the trailing GRB jet should probably be of, at most, a few seconds on the basis of theoretical models and recent simulations of the formation of the central engine of GRBs (see, Chap. 1). However, since we expect the GRB jet be substantially faster than the SN ejecta, the former will eventually catch up the later, drill its way trough the expanding SN shocked layer and proceed later through the rest of the stellar progenitor (unless the jet/SN ejecta interaction catastrophically hinders the ulterior jet propagation).

The primary goal of the study undertaken in this chapter is exploring the effects that a SN shock preceding a GRB jet may imprint in the jet dynamics as well as in its radiative signature, specially after the jet breaks out from the surface of the progenitor star. For this reason, we restrict our study to the early phases of the propagation of a jet from stellar shells outside of the inner core to distances at which the jet may already be semitransparent to radiation. We furthermore point out that the phase we are interesting in here is to be distinguished from the supernova bumps, i.e., the SN signal observed in the lightcurves of several GRBs at late times, typically weeks after the GRB begins, and lasting for a much longer time. The energy source that powers them, the decay of ^{56}Ni, is also very different from that of the early emission here.

Since the first electromagnetic signal of a SN ejecta is produced at the time of the shock break out, we have devoted part of the chapter to test whether our SN models compare with observed phenomenology. Furthermore, we have guessed that the (relativistic) breakout of GRB jets from the surface of the progenitor star may share many dynamical similarities with the breakout of a SN shock if the latter is mildly relativistic. Mildly relativistic SN shocks could

happen in HNe events, in account of their large inferred kinetic energies.

Although they do not unambiguously point to a particular class of progenitors, observations put some constraints on the type of stars that might produce GRB/SN events. WR stars, likely hosts of Type Ib/c SN explosions, have been proposed as possible stellar progenitors of GRB/SNe. These massive stars are known to display episodes of mass loss through their surfaces. The shock breakout signal may be shaped by the structure of the circumstellar material in the vicinity of the stellar progenitor of the SN. In particular, the presence of stellar winds or envelopes inflated from the outer stellar layers may strongly influence the observational properties of the SN flash, since they may shift to distances (much) larger than the stellar radius the location of the photosphere. This appears to be the case of GRB 060218, whose SN shock seems to have reached transparency at distances $\sim 5.2 \times 10^{11}$ cm (Campana et al. 2006). Considering the compactness of the likely stellar progenitor of the former event (a WR star wit a radius $R_\star(\mathrm{SN2006aj}) \sim 4 \times 10^{11}$ cm), the SN shock of the former event must have broken up in the stellar wind surrounding the WR progenitor.

Setup. The simulations were performed with the relativistic hydrodynamics code MRGENESIS. We modelled the stellar gas and the circumstellar medium using the *TM* equation of state, which, while not accounting for the detailed chemical composition of the gas and for radiation, is a valid approximation in our case. In order to maintain the hydrostatic equilibrium of the star, we included its self-gravity. The numerical resolution is the result of a trade-off between the computational costs and several factors demanding large and fine grids. On the one hand, we need to resolve the small scales within the star to properly resolve the jet/star interaction. On the other hand, we need to go to larger length scales as we have to let the jet evolve up to very late times in the laboratory frame in order to capture its emission for times larger than a few tens of seconds. Our choice has been to use three different uniform-space subgrids in both radial and angular directions with different levels of refinement.

In this work, we have used as progenitor the presupernova model 35OC of Woosley & Heger (2006) which consists of a WR of $28M_{\odot}$ at the onset of explosion. The model is based on detailed, spherically symmetric stellar evolution calculations throughout the entire hydrostatic life time of the star, including the effects of rotation and magnetic fields in an approximate way. Mass loss is included in the models in a parametrized way without accounting for the detailed structure of the stellar winds beyond the surface of the star. Consequently, we have to set the profiles of density and temperature outside the star in such a way that they are consistent both with typical mass loss rates of this class of stars and with the properties of the GRB/SN progenitors we want to model. The former constraint leads us to consider winds that are fairly tenuous and (for numerical needs) hotter than physically expected. In spite of the low density of the medium surrounding the progenitor star, the latter translates into a circumstellar medium that has a moderate (Thomson) optical depth of a few. Our assumptions are consistent with the hypothesis of inflated envelopes around WRs such as the ones obtained by Sanyal et al. (2015). We point out that the latter element has not deserved sufficient attention in the literature in terms of the modification of the optical thickness of the external medium. The presence of these envelopes hides the stellar surface and pushes the (Thomson) photosphere to a few stellar radii.

The general scenario outlined at the beginning of this section regarding the GRB jet/SN ejecta interaction very likely applies to the 35OC stellar model. Detailed models of core collapse of this progenitor (Obergaulinger & Aloy 2017) show that a SN explosion may develop within less than a second after core bounce. While the shock wave propagates outwards, the conditions at the center might lead to the launching of a GRB jet after a further delay of the order of a few seconds. Our working hypothesis has been that jets interacting with SN ejecta inside of the stellar progenitor may leave an observational signature different to that of jets which propagate through the unmodified profile of the massive star. To more clearly distinguish what are the dynamical effects of the aforementioned hypothesis, we have set up 2D relativistic hydrodynamic models in which a jet overtakes a preexisting SN ejecta inside of the

presupernova model 35OC, models in which only a jet propagates in the star and, also, models where only a driven SN explosion takes place. In the first class of models, we varied the jet energy.

The simulations have been divided in two steps.

SN ejecta. First, we have computed the evolution of the SN performing 1D simulations of a spherical flow. Although SN explosions can be rather asymmetric within the star as shown by multimensional simulations (see, e.g., Kifonidis et al. 2003; Wongwathanarat et al. 2015), we assume that the explosion remains roughly spherical during the first moments of evolution. Furthermore, the main reason for running 1D simulations has been to speed up the computation of this ancillary step, which is necessary for generating the initial conditions for the axisymmetric continuation of the models. Another advantage of running this step in spherical symmetry is that we avoid the development of Rayleigh-Taylor instabilities that can be accentuated artificially around the symmetry axis of the system and distort the subsequent propagation of jets. The injection of the SN has been done *ad hoc* using a 'piston' model in the inner boundary of our numerical domain. The energy carried by the SN ejecta has been chosen in the HN energy regime, in concordance with those SN observer together with the GRB. Attempting to minimize the dimensionality of the parameter space that we shall explore, a single 1D SN set up has been later mapped in 2D to serve as background model on which a GRB jet is injected. Certainly, the properties of the injected SN ejecta may trigger different observational properties of both the SN shock breakout and of the GRB jet breakout. While the injected SN energy is constrained to be $E_{\rm SN} \sim 10^{52}\,{\rm erg}$ if we aim to produce a HN event, there is more freedom to fix the injected mass ($M_{\rm SN} = 0.1 M_\odot$ in our case). With the currently set values, a typical asymptotic speed of the SN ejecta would be $\beta_\infty \sim \sqrt{(2E_{\rm SN}/M_{\rm SN})} \simeq 0.3$. However, as we have seen the speed of propagation of the FS shock of the SN is much larger, displaying a maximum $\beta_{\rm FS} \sim 0.9$ by the time it reaches $R_\star$. This speed is larger than that obtained in previous papers (e.g., Nakar & Sari 2010; Balberg & Loeb 2011 and references therein). We may reduce that

propagation speed increasing $M_{\rm SN}$, something we consider as a future work. The relevance of the ejecta propagation velocity stems from two basic facts. On the first place, according to theoretical models (see the introduction of this chapter), the optical depth of the shock at breakout is $\sim \beta_{\rm FS}^{-1}$. For this reason, the radiation may escape the shocked SN ejecta. These shocks, termed radiation mediated shocks (e.g., Katz et al. 2010), display a dynamical behaviour which differs from the adiabatic shocks we simulate in our models. However, our numerical models incorporate (unavoidably) numerical diffusion at shock fronts. This numerical difusion smears the shock front over a few numerical cells, qualitatively mimicking the modification of the hydrodynamic profiles that radiation mediated shocks produce with respect to their adiabatic counterparts, at least in some regimes (Weaver 1976). In any case, the total optical depth of matter ahead of the shock is large up to distances $r \sim 10^{12}$ cm in our model. Thus, this radiation does not leak out of the progenitor immediately, but on the local diffusion timescale of the shells in which it propagates. This means that the approximations of our model may not allow us for an accurate description of the SN flash. On the second place, for $\beta_{\rm FS} > 0.2$ pair creation in the shock is relevant (Weaver 1976; Budnik et al. 2010; Katz et al. 2010). The creation of pairs in the high temperature precursor of a SN shock has two interesting consequences at least. First, they may act as a barrier preventing the post-shock radiation to leak out, thereby allowing the shock to propagate towards larger radii with, correspondingly, lower optical depth than would otherwise have been the case. Since our SN shocks are faster than the limit for pair creation mentioned above, by a fortunate coincidence, the creation of pairs may counteract the transfer of energy far ahead of the shock, making that the envisioned radiation mediated shocks behave in a qualitatively similar way as adiabatic ones. Second, they may yield a modification of the adiabatic index of the EoS. We partly incorporate these effects with our approximate *TM* EoS. However, future developments shall explicitly account for the effects of pairs on the EoS (e.g., similarly to Aloy et al. 2000 or with suitable variations thereof).

The SN ejecta has been evolved up to ~ 260 s after its injection. After ~ 100 s of evolution the parameter x has leveled off (Fig. 4.6), which is a hint

of the explosion entering the phase of self-similarity (stage (3) as described by Matzner & McKee 1999). However, the evolution is not self similar yet, as the FS radius still evolves with a slightly different temporal dependence than that of the RS. This also translates into different time evolutions of the FS and RS temperatures. Note that the shock temperature was calculated assuming thermodynamic equilibrium and this procedure can lead to underestimating the true temperature value once the ejecta become transparent. For the RS of the SN ejecta this happens when it reaches the photosphere, which is located at a distance $R_{\tau=1} \simeq 4 \times 10^{11}\,\mathrm{cm} > R_{\mathrm{env}}$. This moment can be considered as the 'true' breakout as seen in observations. As stated in the text we differentiate between the (*hydrodynamic*) breakout of the star (at $R_\star$) and the *electromagnetic* breakout (at $R_{\tau=1}$), the latter corresponding to the moment in which the radiation can first be seen by a distant observer. The temperature at the time in which the FS becomes transparent, i.e., when the *electromagnetic* breakout happens, is $T \sim 1.8 \times 10^6\,\mathrm{K}$. Balberg & Loeb (2011) estimate the BB temperature at breakout to be $T_{BB} \approx 2.64 \times 10^5 E_{\mathrm{rad},47}^{1/12} t_{\mathrm{diff},3}^{-5/12} \kappa_{0.2}^{1/6} (x/0.146)^{1/6} (\chi_{\mathrm{E}}/0.9)^{1/6}\,\mathrm{K}$. Li (2007) also estimates a somewhat lower breakout temperature $T_{\mathrm{BO}} \sim 0.8 \times 10^6 (R_\star/3R_\odot)\,\mathrm{K}$, which for a value of $R_\star = 0.74 R_\odot$ gives a value of $T_{\mathrm{BO}} \sim 1.6 \times 10^6\,\mathrm{K}$ in excellent agreement with our model.

Jets. After some time corresponding to a certain delay between the SN and the jet we have mapped the outcome of the 1D SN simulation onto a new 2D numerical grid where the jet simulations are carried out. The delay time between the SN and the jet formation has been chosen to be 3 s in our simulations. With the resolutions employed in this work we obtain that the total number of cells rises up to $\sim 5 \times 10^6$ cells in our 2D simulations, which has made very expensive the computation.

The jets are injected at the polar axis through the inner radial boundary situated at $R_{\mathrm{inj,j}} = 2 \times 10^9\,\mathrm{cm}$ with a half-opening angle of $\theta_{\mathrm{j}} = 2°$. For their parameters such as luminosity and Lorentz factor, we took into account the following considerations. In order for a jet, i.e., a supersonic flow to form at the

injection nozzle, the luminosity must be above a certain threshold depending on the conditions within the progenitor at the injection point. We have checked (not shown here for brevity) that jets with luminosities below the threshold of Eq. (4.14) failed in breaking out of the star. Two of our jet models (J0 and J3-L) have been chosen with luminosities only a bit above to threshold at $R_9 = 2$ in the presupernova model 35OC. In this point it is important to adress how the intrinsic jet luminosity thresholds we have obtained ($L_j \sim 10^{49}$ erg; Eq. (4.13)) translate into thresholds in the equivalent isotropic luminosity of the jets and, hence, on the expected $L_{\gamma,\mathrm{iso}}$. The key point here is what is the outflow opening angle after the jet breaks out of the surface of the star. Two basic possibilites have been considered: either the jet opening angle is basically the same as the initial jet opening angle or much larger than that. The former alternative follows from the results of Mizuta & Ioka (2013). The latter from our own results. Assuming that the outflow opening angle is θ_j, models J0 and J3-H have $E_{\mathrm{iso,j}} = 10^{54}$ erg (which gives an isotropic luminosity $L_{\mathrm{iso,j}} = 5 \times 10^{52}$ erg s^{-1}), while model J3-L $E_{\mathrm{iso,j}} = 5 \times 10^{53}$ erg ($L_{\mathrm{iso,j}} = 2.5 \times 10^{52}$ erg s^{-1}). We have tried to push down the previous values to bring them as close as possible to the observed range in llGRBs ($L_{\gamma,\mathrm{iso}} \sim 10^{46}$–$10^{48}$ erg), but as we have seen, values below a few times 10^{53} erg are impossible to obtain if we aim to launch a jet which is not chocked inside of the star (Fig. 4.3) in the typically assumed progenitors of GRBs. We note that the luminosities are still well above the corresponding energies observed in llGRBs. However, the hydrodynamic luminosities do not directly correspond to the γ- and/or X-ray radiation, since part of this energy may be still stored in the form of a thermal energy reservoir that can be released on longer time scales or converted to kinetic energy of the outflow. On the one hand, part of the injected energy can be dissipated by its interaction in the progenitor. Following the arguments of Mizuta & Ioka (2013) the energies considered here need a tiny efficiency factor for conversion of hydrodynamic energy into radiation, ϵ_γ, to lie in the low-luminosity regime. However, our setup is different from that of Mizuta & Ioka in many aspects. As a result, our jets develop opening angles after breakout $\theta_{\mathrm{BO}} \gg \theta_j = 2^\circ$, so that the luminosity condition relaxes to Eq. (4.16) (in that

equation we assumed $a \sim 3$). With all this assumptions in mind, acceptable efficiencies of $\epsilon_\gamma \sim 1\%$ for our jets could give rise to γ-ray luminosities in the range observed for the llGRB population. The duration of jet injection is another free parameter. It has been set to $t_{\rm inj,j} = 20\,{\rm s}$, which is more typical for standard long GRBs rather than for llGRBs, which show durations from hundreds to thousands of seconds. However, our choice has been triggered by the above luminosity restrictions. Noteworthy, the breakout times (especially the one measured for model J3, $t_{\rm BO}({\rm J3\text{-}L}) = 18.51\,{\rm s}$) are close to the injection time (i.e., $t_{\rm BO} \lesssim t_{\rm inj,j}$), so we are close to the regime in which the jet can fail in breaking out of the star as it chocked by the stellar envelope (Bromberg et al. 2011a).

In the analysis of jet models, we tried to figure out how the preexistence of the SN can influence the dynamics and emission of jets. At the time of jet injection the FS of the SN is located at $R_9 = 6$. Comparing models with the same energy (J0 and J3-H) we see that the jet of that model in which the SN is present (J3-H) propagates faster, and in consequence it breaks out of the star earlier. In this regard, the SN *helps* the jet to cross the regions close to $R_{\rm inj,j}$ as it reduces the density and the ram pressure of the gas into which the jet is injected. The jet of model J3-L, with two times less energy than that of J3-H, needs more time to catch up with the SN shock. It spends more than the half of its breakout time before overtaking the SN. Model J0 shows strong collimation due to the presence of a high-density layer up to $R_9 = 9$. By the time of jet injection in models J3 this layer has been swept by the SN ejecta, though the jets show even a higher degree of collimation than that of model J0 due to the high pressure in the regions shocked by the RS of the SN.

All three jet models follow the typical phases expect for GRB jets (Bromberg et al. 2011b). In the first phase, within the star, the jets are in the collimated, non-relativistic regime. Once they propagate into the external medium, they enter the relativistic, non-collimated regime and remain in it until the end of the simulation. In this last stage we have measured the internal energy stored by material with different Lorentz factors. This energy can be converted and released as radiation once the material becomes transparent. The jet material

is mostly found in the regime $\Gamma_\infty < 10$, with larger Lorentz factors only found in the jet head above $R_\star$. In all our models we measure internal energies of $\sim 10^{50}$ erg that might be converted into radiation mostly in the X-ray regime (consistently with the fact that our models aim to address llGRBs).

Spectral evolution. In the last part of this chapter we have studied the radiative evolution of our models with the SPEV code. Before discussing the results, we mention the limitations of our present analysis. Due to time limitations, we have assumed thermodynamic equilibrium in the whole domain. In consequence, the temperature is underestimated in optically thin regions. Furthermore, the computation of the thermal signature was affected by a few technical issues that have not been resolved by the time of presenting this thesis. We have figured out that the resolution employed in the third level of refinement of the radial direction is not good enough to properly resolve the jet head propagation and our jets suffer of numerical diffusion above 10^{12} cm. This numerical diffusion is not critical in the hydrodynamic part but eventually causes the head of the jet to propagate superluminally. This effect has terrible consequences at the time of computing the radiative signature with SPEV since photons emitted at later times can reach an observer earlier than photons emitted before them. To avoid this problem we reset the speed of jet head, v_h to a maximum value by modifying the time coordinate in the post-processing step whenever $v_\mathrm{h} > c$. Although this fixup successfully allowed us to compute the radiative evolution, the jump in resolution between the second and the third level in the radial direction can cause to misidentify the location of the emitting region around the photosphere. While the fixup yields a controlled error in the calculation of the thermal emission of the jet, it has a huge impact on the exact Lorentz factor of the FS of the jet. Since the FS is typically the origin of a sizable fraction of the non-thermal radiation in jet models (see previous chapter), we have not evaluated the synchrotron emission as we did in Chap. 3.

Converting the hydrodynamic profiles from the laboratory to the observer frame we have been able of identify the emitting region of our jet and SN

models. After roughly a tenth of seconds ($t_{\mathrm{obs},\tau=1} \approx (t_{\mathrm{j}\to\tau=1} - 4 \times 10^1 1/c + 2R_{\mathrm{inj,j}}/c)(1+z)$) we see that the jet FS becomes transparent, while the post-RS region does a few tenths of a second later. Indeed, the photosphere is identified at the CD for all our jet models at the end of the confidence zone (marked with thick lines in Fig. 4.21). For the calculation of the opacity we have included both thermal bremsstrahlung and Thomson contributions. The latter proves to be dominant in the jet head. Because of the relativistic motion of the jets, the hydrodynamic profiles show up very stretched in comparison with those in the laboratory frame. This effect leads to a very extended shock structure. It also makes the small-scale oscillations behind the RS largely disappear in the observer frame. For this reason, and because they are still behind the photosphere, these oscillations do not contribute to the variability of the emission. Conversely, since its velocity is subrelativistic the SN profile in the laboratory and in the observer frame is almost the same. At the end of the simulation the SN has already become transparent below its RS.

The times in which the FS and the RS of the SN become optically thin in the lab-frame time are separated by only $\Delta t \simeq 4\,\mathrm{s}$, which corresponds to a $\Delta t_{\mathrm{obs}} \approx 2(1+z)\,\mathrm{s}$ in the observer frame. The FS becomes transparent at $t \approx 50\,\mathrm{s}$ which corresponds to $t_{obs} \approx 40.5\,\mathrm{s}$, i.e., between the first 3–5 s after the hydrodynamic breakout in the observer frame (assuming $z = 0.1$) the FS and the RS become transparent for distant observer. In the first 3 seconds of evolution the observed flux shows its largest growth (Fig. 4.19). Although the SN LCs show later peak times in the bands studied here (around 26 s in the UV and optical bands), the one measured in the X-ray band shows a peak time of $\sim 6\,\mathrm{s}$ that could be related to the time in which the photosphere has receded from the FS up to the RS. However, the LCs show a smooth increasing trend up to the peak and do not show any feature that could be related with transition from the FS emission to the RS. This can be attributed to the combination of two effects. The first one arises from technical limitations. The displayed LCs are computed by evaluating models at discrete observer times, $T_n,\ n = 1, \ldots, n$. The interval between consecutive values $\Delta T_n = T_{n+1} - T_n$ is not necessarily uniform. The different time intervals can be tuned to have a

larger time resolution in regions of interest and lower time resolution once the LCs display smaller variability. In our models we set up the largest observing time resolution around the SN shock break out (when $\Delta T_n = 0.1\,\mathrm{s}$). About 3 seconds after the breakout we decrease the time resolution to $\Delta T_n = 1\,\mathrm{s}$. Unfortunately, the transition between FS dominated thermal emission and RS dominated thermal emission happens after we have changed to a coarser time resolution in the evaluation of the LCs. The second effect is of physical origin: variations happening on scales smaller than the angular time scale $\Delta T_{\rm ang} \sim R_\star/c \simeq 1.7\,\mathrm{s}$ are smoothed out due to the contributions arising from high-latitudes along the photosphere and emitted at later times.

It is evident from the luminosity evolution that our SN event is fainter (by about 3–4 orders of magnitude at the peak in the X-ray band) than estimated by, e.g., Ensman & Burrows (1992) for blue supergiant (BSG) stellar progenitors, or that computed by Nakar & Sari (2010) for WR progenitors. However, our values are closer to those of Tominaga et al. (2009), though the pre-SN star of these authors was a red supergiant (RSG). A number of reasons could be behind the discrepancy, specially the fact that our SN ejecta accelerates to velocities $\beta \sim 0.9$ once they emerge out of the star since it is still rather hot. Therefore, the SN shock should be more opaque to radiation due to the production of pairs. In future simulations, we may increase the mass injected by the piston model in the SN ejecta, which shall result into smaller propagation speeds of the SN shocks. Moreover, our progenitor model is substantially more massive and compact than any of the progenitors considered in the former references. Furthermore, observations of GRB/SNe seem to be rather heterogeneous in terms of, e.g, the typical peak luminosity. For instance, Bufano et al. (2011) show that SN 2010bh displayed a fainter absolute peak luminosity ($L_{\rm bol} \simeq 3\times10^{42}\,\mathrm{erg\,s^{-1}}$) than other members of the GRB/SN class. Certainly, this means that in the X-ray band, the luminosity of this SN could be close to what we have obtained in our models. We obtain a peak time in the X-ray band of $t_{\rm X,p} \sim 6\,\mathrm{s}$, very similar to that computed by Nakar & Sari (2010; $t_{\rm X,p} \sim 10\,\mathrm{s}$). Our value is slightly smaller probably because of our more compact WR progenitor. In any case, the peak of our luminosity is not in the

X-ray band, but rather in the extreme UV band.

As a consequence of the larger Lorentz factor of jet models, the interval of observed time ($\propto \Gamma^{-2}$) shortens significantly with respect of that obtained for the SN. Thus, computing longer LCs becomes extremely costly and we had to limit our results to relatively short periods. Even with a hydrodynamic evolution of $\sim 100\,\mathrm{s}$, we could only compute the emission for $2.5\,\mathrm{s}$ at most (in the case of model J3-L). In general, we have seen that this time is not enough to see many features in the optical, UV and X-ray LCs. During the computed time, the UV-to-X-ray LCs of jet models are still rising without having reached a maximum so far. Similarly, the γ-ray LC does not show any periodic variability. However, from the results shown here we can see that jet models are much more luminous than our SN in the XRT band (about $\sim$ 2–3 orders of magnitude) and have a comparable (but slightly larger) luminosity in the $W2$ band.

If we fix the same intrinsic jet luminosity (which is the case of models J0 and J3-H), from the inspection of their LCs at different wavelengths, we cannot differentiate models in which the SN is present from those in which the SN is absent. In part this is due to the fact that the time interval of confidence in our jet models after breakout is still too short. For this reason, ongoing simulations are set up to cover longer time scales. In spite of these results, we have seen that the presence of a previous ejecta in the progenitor notably influences the dynamics of jets within the stellar progenitor, and what it is more important, reduces the intrinsic luminosity threshold to inject jets that may break out of the stellar surface. Thus, it is easier to produce low-luminosity jets if a SN shock has previously propagated within the star. However, in those cases where the jet forms the SN shock signal can be highly absorbed and outshone by the jet emission during the first stages of evolution.

Our jet models display a large (kinetic plus thermal) enery reservoir after breakout. From the analysis of the asymptotic Lorentz factor in the whole cavity blown by the different jets, we foresee that the high-energy transients we may produce will be more similar to XRFs than to GRBs. Indeed, our jet events display peak specific luminosity in the extreme UV band, rather than

in the X-ray band, and clearly a fainter γ-ray luminosity ($\sim$ 2–4 orders of magnitude smaller than in the X-ray band).

Future development. Due to time limitations and technical problems during its development, the current study of the radiative evolution of our models has to be taken as preliminary. More in depth analysis of the models, including new ones, will be done in the future. It would be particularly interesting to study a wide range of parameters such as smaller intrinsic luminosities, longer injection times, different jet injection half-opening angles, etc., and study both their effects on the hydrodynamic evolution and the emission properties. Also the influence of the circumstellar medium, especially the inflated envelope, has to be tested in more detail, e.g., assuming different initial conditions or a larger extension. In our study the surface of $\tau = 1$ is located at 4×10^{11} cm but for more massive winds in WRs this surface can be even larger, causing a larger delay in the *electromagnetic* breakout.

Also, the inclusion of other radiative processes such as synchrotron or inverse Compton can be relevant in the present study. However, while the latter is assumed to produce small contributions at the optical and UV regimes, the former can be important or even dominant at early times. Since the density of the post-FS region decays as the jet propagates into the external medium, its synchrotron emission is expected to decrease. Finally, another area for improvement might be the development of numerical methods that reduce the diffusion across the jet head in order to limit the propagation speed to the physically allowed range. All these improvements and further analysis should permit us to compute reliable LCs and spectra at and after breakout.

Appendix A

Shock detection and divergence in polar coordinates

In MRGENESIS the calculation of the numerical fluxes is split in "sweeps" along the coordinate directions. In each of these sweeps, one dimensional problems are solved and, indeed, the reconstruction of the primitive variables is purely one-dimensional. This makes it unfeasible to evaluate properly the jump condition of a shock which is not propagating into a single direction. In particular, the divergence of the velocity cannot be evaluated at once if the velocity has more than one component. For such reason, when we consider polar coordinates, instead of imposing that $\nabla \mathbf{v} < 0$, we make the approximation of splitting the two contributions of the divergence and evaluate each of them independently in each of the sweeps.

The divergence of $\mathbf{v}$ in polar coordinates is

$$\nabla \mathbf{v} = \nabla_r v_r + \nabla_\theta v_\theta = \frac{1}{r^2}\partial_r r^2 v_r + \frac{1}{r\sin\theta}\partial_\theta v_\theta \sin\theta. \tag{A.1}$$

Discretizing for each of the directions, the velocity $\mathbf{v} = (v_r, v_\theta)$ in cell (i, j) must fulfill that

$$\nabla_r v_r \leq 0 \tag{A.2}$$

in the radial sweep, and

$$\nabla_\theta v_\theta \leq 0 \tag{A.3}$$

in the angular sweep.

Therefore, a shock is detected in cell $(i,\ j)$ if both conditions are fulfilled together with the pressure jump condition (Eq. (2.31)).

Appendix B

Correction of the Gaunt factor table

The Maxwellian (thermally) averaged free–free Gaunt factor, $\bar{g}_{\rm ff}(\nu, T)$, was obtained by interpolating from the values obtained numerically by Sutherland (1998). We have noted that these values are presented in the wrong way in his table 2 as the labels for the parameters $\log \gamma^2$ and $\log u$ (defined as x in this thesis) are transposed. The online version of the table[1] also contains this typo on the labels. As we have used such a table in Cuesta-Martínez et al. (2015a) and Cuesta-Martínez et al. (2015b) without taking into account this error, the Gaunt factor was always considered wrongly. For such reason, we have recalculated and updated in this thesis all LCs and spectra.

Furthermore, we have not only corrected this error but we have used a new table of thermally averaged free–free Gaunt factors (for $Z = 1$, and including relativistic Gaunt factors) produced by van Hoof et al. (2014; 2015; who also realized the mistake made by Sutherland 1998) in which they cover a wider range in both parameter directions $\log \gamma^2$ (from -6 to 10) and $\log u$ (from -16 to 13).

In this Appendix, a comparation of the corrected (using the tables of van Hoof et al. 2014, 2015) and the erroneous results (using a transposed version

[1] 'gffgu.dat' in http://www.mso.anu.edu.au/∼ralph/freefree.html

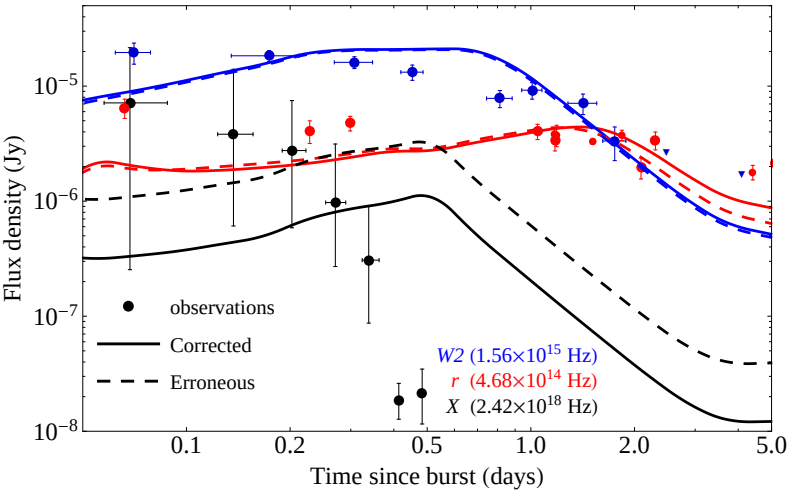

Figure B.1: Light curves for the RM considering only the (thermal) bremsstrahlung-BB contribution. Both optically thick (solid lines) and thin (dashed lines) LCs are plotted. For the X-ray band (black lines), the optically thin and thick LCs coincide, since the X-ray emitting region is optically thin.

of Sutherland's table) is shown. In Figure B.1 we show corrected (only thermal) LCs of our reference model (RM) compared to the erroneous ones from Cuesta-Martínez et al. (2015a). The error made in the r and $W2$ band is almost imperceptible since the ratio of fluxes is ~ 1. This is consistent with the fact that in the optical bands the Gaunt factor approaches unity and, as the conditions of our models sample the central regions of the interpolation table, the error made by omitting the transposition is less accentuated. However we would like to stress that after ~ 1.5 days, once the system becomes optically thin, the r-band flux is now a bit larger compared with the erroneous calculation. The biggest mistake comes in the X-ray band where we see that the discrepancy between the two calculations is a factor of ~ 3, confirmed also with the X-ray emission of the rest of the computed models (Fig. 3.20; compare with figure 20 of Cuesta-Martínez et al. 2015a).

Although all the LCs and spectra have been updated, Figs. 3.12, 3.17 and 3.23 have not been corrected in time, and it has been stressed in the caption

of each figure that a factor of 3 should apply in those panels referring to the X-ray emission.

The non-thermal emission remains unaltered. On the one hand, the error made in the optical bands is tiny and thermal absorption of non-thermal radiation does not change the final outcome. On the other hand, we saw in Cuesta-Martínez et al. (2015a) that both the non-thermal emission and thermal absorption in the X-ray band are negligible.

So, once seen that the new corrected optical LCs have barely changed, we can assure that our main conclusions remain valid despite the fact of having used a wrong Gaunt factor in Cuesta-Martínez et al. (2015a,b). In fact, the optical bands accomadate better to observations. However, all the discussion related with the thermal X-ray emission has been slightly modified in Chap. 3 respect to that in Cuesta-Martínez et al. (2015a,b).

Appendix C

Gravitational potential

Gravitational effects may become relevant if the deeper regions of the star are included in the model. Nevertheless, in order to reach hydrostatic equilibrium in the star, we need to introduce self-gravity for balancing the pressure gradient, especially at the stellar surface. This is especially true if the time over which we compute the models is comparable or larger than the sound crossing time of the stellar radius.

We have included in MRGENESIS a Newtonian gravitational potential, Φ, in order to account for self-gravity. Although our code is relativistic, we have chosen a Newtonian potential for simplicity, but including some relativistic corrections as considering in the source term $\rho_{\rm eff} := (\rho h \Gamma^2 - p/c^2)$ instead of $\rho_{\rm eff} := \rho$ alone. We note that a similar approach has been followed by Nagakura et al. (2011). Since we do not account for general relativity effects, the metric remains unchanged and, therefore, the influence of the potential only appears as an additional source term in the equations of the RHD (2.5). The new source term looks $\mathbf{S}_{\rm new} = \mathbf{S}_{\mathbf{U}} + \mathbf{S}_{\rm pot}$, where $\mathbf{S}_{\mathbf{U}}$ refers to Eq. (2.14) and $\mathbf{S}_{\rm pot}$ denotes the source vector due to the inclusion of the Newtonian potential. In

2D spherical coordinates ($c = G = 1$):

$$\mathbf{S}_{\rm pot} = \begin{pmatrix} 0 \\ -(\rho h\Gamma^2 - p)\dfrac{\partial \Phi}{\partial r} \\ -\dfrac{1}{r}(\rho h\Gamma^2 + \tilde{S}^r\tilde{v}^r)\dfrac{\partial \Phi}{\partial \theta} \\ -\rho h\Gamma^2\left(\tilde{v}^r\dfrac{\partial \Phi}{\partial r} + \dfrac{\tilde{v}^\theta}{r}\dfrac{\partial \Phi}{\partial \theta}\right) \end{pmatrix}, \tag{C.1}$$

where the components of the vectors appearing in the previous equation are expressed in the orthonormal spherical basis and, thus, we distinguish them from the orthogonal spherical basis by adding a "tilde" the the former ones. Once the potential source term is volume-averaged, we get

$$\tilde{\mathbf{S}}_{\rm pot} = \frac{1}{\Delta V}\int_V \mathbf{S}_{\rm pot}\ {\rm d}V = \begin{pmatrix} 0 \\ -(\rho_{i,j} h_{i,j}\Gamma^2_{i,j} - p_{i,j})\,\tilde{S}^r_{0,{\rm pot}} \\ -(\rho_{i,j} h_{i,j}\Gamma^2_{i,j} + \tilde{S}^r_{i,j}\tilde{v}^r_{i,j})\,\tilde{S}^\theta_{0,{\rm pot}} \\ -\rho_{i,j} h_{i,j}\Gamma^2_{i,j}\,(\tilde{v}^r_{i,j}\tilde{S}^r_{0,{\rm pot}} + \tilde{v}^\theta_{i,j}\tilde{S}^\theta_{0,{\rm pot}}) \end{pmatrix}, \tag{C.2}$$

being

$$\begin{aligned} \tilde{S}^r_{0,pot} =& \frac{3}{\Delta r^3}\Big[(\Phi_{i+1/2,j} r^2_{i+1/2} - \Phi_{i-1/2,j} r^2_{i-1/2}) - \Phi_{i,j}\Delta r^2\Big] \\ \tilde{S}^\theta_{0,pot} =& -\frac{3}{2}\frac{\Delta r^2}{\Delta r^3 \Delta\cos\theta}\Big[(\Phi_{i,j+1/2}\sin\theta_{j+1/2} - \Phi_{i,j-1/2}\sin\theta_{j-1/2}) - \Phi_{i,j}\Delta\sin\theta\Big], \end{aligned} \tag{C.3}$$

where in a given cell (i, j) the potential has to be known also at the cell boundaries $i + 1/2$, $i - 1/2$, $j + 1/2$ and $j - 1/2$. For uniformly spaced grids we make the simple assumption that

$$\Phi_{i+1/2,j} = \frac{1}{2}(\Phi_{i+1,j} + \Phi_{i,j}) \tag{C.4}$$

$$\Phi_{i+1/2,j} = \frac{1}{2}(\Phi_{i,j} + \Phi_{i-1,j}). \tag{C.5}$$

and the same is done for the interface values in the j-direction.

The Poisson's equation,

$$\Delta\Phi = 4\pi\rho_{\rm eff} \tag{C.6}$$

defines the behaviour of the potential, Φ, and its dependence on the mass distribution. To find the solution of this equation, we have used specific libraries that contain the mathematical tools for solving elliptic equations (as Poisson's) by giving prooper boundary conditions. For our convenience, we do not solve directly for the potential $\Phi = \Phi(r,\theta)$ but a modified potential $\Phi'(r,\theta) = \Phi(r,\theta) + M_{\rm in}/r$, where $M_{\rm in}$ is the excised mass below R_0. Neumann conditions for the potential are imposed at R_0, $\frac{\partial\Phi'}{\partial r}|_{R_0} = 0$, and Dirichlet conditions at the end of the grid, $\Phi'(R_f,\theta) = -M_T/R_f$. The total mass within the grid, M_T, excludes the excised mass $M_{\rm in}$. Once Φ' is calculated, we only have to subtract in the radial direction the quantity $M_{\rm in}/r$ to recover the real potential, Φ.

The potential is recalculated after a number of iterations equal to multiples of n_r. The reason is that $n_r\Delta t$ corresponds to the light crossing time[1] in the grid and the potential is updated before any perturbation can cross the whole numerical grid. Between two consecutive calculations it is very likely that the inner mass has changed due to a non-zero mass flux across R_0 (interface 1/2). This flux can supply a non-negligible amount of mass to the enclosed mass $M_{\rm in}$, making it necessary to consider it in order to properly recompute the potential. Whether or not such a contribution is included can strongly influence the dynamics, specially in those regions close to R_0. The total incoming mass, calculated as $\Delta M_{\rm in} = -\sum_j F_{1/2,j} S_{1/2,j}$, is evaluated in every time step in the same manner as for the conserved variables, i.e. it is updated in each of the Runge-Kutta steps (Eq. (2.27)). In the latter formula $F_{1/2,j}$ is the mass flux per unit surface between cells $(0,j)$ and $(1,j)$ [2] and $S_{1/2,j} = 4\pi(-\Delta\cos\theta)R_0^2$ is the surface of the respective boundary located at R_0. After the end of the time loop $\Delta M_{\rm in}$ is removed from the grid and incorporated to the inner mass.

[1] In the ideal case with a Courant-Friedrichs–Lewy condition of CFL = 1.

[2] The '$-$' is put in order to define positive $\Delta M_{\rm in}$ as the mass flux is negative if goes from the grid to the region below R_0.

Bibliography

ALMA Partnership et al., 2015, ApJL, 808, L1

Aloy M. A., Ibáñez J. M., Martí J. M., Müller E., 1999, ApJS, 122, 151

Aloy M. A., Müller E., Ibáñez J. M., Martí J. M., MacFadyen A., 2000, ApJL, 531, L119

Aloy M. A., et al., 2013, in Pogorelov N. V., Audit E., Zank G. P., eds, Astronomical Society of the Pacific Conference Series Vol. 474, Numerical Modeling of Space Plasma Flows (ASTRONUM2012). p. 33

Amati L., et al., 2002, A&A, 390, 81

Anderson M., Lehner L., Megevand M., Neilsen D., 2010, PRD, 81, 044004

Arnett D., Fryxell B., Mueller E., 1989, ApJL, 341, L63

Atteia J.-L., et al., 1987, ApJS, 64, 305

Badjin D. A., Blinnikov S. I., Postnov K. A., 2013, MNRAS, 432, 2454

Balberg S., Loeb A., 2011, MNRAS, 414, 1715

Band D., et al., 1993, ApJ, 413, 281

Barkov M. V., Bisnovatyi-Kogan G. S., 2005a, Astronomy Reports, 49, 24

Barkov M. V., Bisnovatyi-Kogan G. S., 2005b, Astronomy Reports, 49, 611

Barkov M. V., Komissarov S. S., 2010, MNRAS, 401, 1644

Barkov M. V., Komissarov S. S., 2011, MNRAS, 415, 944

Baumgarte T. W., Shapiro S. L., Shibata M., 2000, ApJL, 528, L29

Belczynski K., Bulik T., Fryer C. L., 2012, High Mass X-ray Binaries: Future Evolution and Fate, arXiv:1208.2422

Beloborodov A. M., 2010, MNRAS, 407, 1033

Berger E., 2014, Annu. Rev. Astron. Astrophys., 52, 43

Berger E., Kulkarni S. R., Chevalier R. A., 2002, ApJL, 577, L5

Birkl R., Aloy M. A., Janka H.-T., Müller E., 2007, A&A, 463, 51

Bisnovatyi-Kogan G. S., Timokhin A. N., 1997, Astronomicheskij Zhurnal, 74, 483

Blackman E. G., Yi I., 1998, ApJL, 498, L31

Blandford R. D., McKee C. F., 1976, Physics of Fluids, 19, 1130

Blandford R. D., Payne D. G., 1982, MNRAS, 199, 883

Blandford R. D., Znajek R. L., 1977, MNRAS, 179, 433

Blinnikov S. I., Postnov K. A., 1998, MNRAS, 293, L29

Blinnikov S., Lundqvist P., Bartunov O., Nomoto K., Iwamoto K., 2000, ApJ, 532, 1132

Bloom J. S., Djorgovski S. G., Kulkarni S. R., 2001, ApJ, 554, 678

Böttcher M., Dermer C. D., 2010, ApJ, 711, 445

Bošnjak Ž., Daigne F., Dubus G., 2009, A&A, 498, 677

Bromberg O., Nakar E., Piran T., 2011a, ApJL, 739, L55

Bromberg O., Nakar E., Piran T., Sari R., 2011b, ApJ, 740, 100

Bromberg O., Nakar E., Piran T., Sari R., 2012, ApJ, 749, 110

Bromberg O., Nakar E., Piran T., Sari R., 2013, ApJ, 764, 179

Bruenn S. W., et al., 2016, ApJ, 818, 123

Bucciantini N., Quataert E., Arons J., Metzger B. D., Thompson T. A., 2007, MNRAS, 380, 1541

Bucciantini N., Quataert E., Arons J., Metzger B. D., Thompson T. A., 2008, MNRAS, 383, L25

Bucciantini N., Quataert E., Metzger B. D., Thompson T. A., Arons J., Del Zanna L., 2009, MNRAS, 396, 2038

Budnik R., Katz B., Sagiv A., Waxman E., 2010, ApJ, 725, 63

Bufano F., Benetti S., Sollerman J., Pian E., Cupani G., 2011, Astronomische Nachrichten, 332, 262

Bufano F., et al., 2012, ApJ, 753, 67

Burrows D. N., et al., 2005, Science, 309, 1833

Bykov A. M., Meszaros P., 1996, ApJL, 461, L37

Calzavara A. J., Matzner C. D., 2004, MNRAS, 351, 694

Campana S., et al., 2006, Nature, 442, 1008

Cano Z., et al., 2011, ApJ, 740, 41

Cano Z., Wang S.-Q., Dai Z.-G., Wu X.-F., 2017, Advances in Astronomy, 2017, 8929054

Cavallo G., Rees M. J., 1978, MNRAS, 183, 359

Cerdá-Durán P., DeBrye N., Aloy M. A., Font J. A., Obergaulinger M., 2013, ApJL, 779, L18

Chevalier R. A., 1976, ApJ, 207, 872

Chevalier R. A., 1982, ApJ, 258, 790

Chevalier R. A., 2012, ApJL, 752, L2

Chevalier R. A., Fransson C., 2008, ApJL, 683, L135

Chornock R., et al., 2010, Spectroscopic Discovery of the Broad-Lined Type Ic Supernova 2010bh Associated with the Low-Redshift GRB 100316D, arXiv:1004.2262

Cobb B. E., Bailyn C. D., van Dokkum P. G., Natarajan P., 2006, ApJL, 645, L113

Colella P., Woodward P. R., 1984, Journal of Computational Physics, 54, 174

Colgate S. A., 1968, Canadian Journal of Physics, 46, S476

Colgate S. A., 1974, ApJ, 187, 333

Cook G. B., Shapiro S. L., Teukolsky S. A., 1994, ApJ, 424, 823

Costa E., et al., 1997, Nature, 387, 783

Coward D. M., 2005, MNRAS, 360, L77

Crowther P. A., 2007, Annu. Rev. Astron. Astrophys., 45, 177

Cucchiara A., et al., 2011, ApJ, 736, 7

Cuesta-Martínez C., Aloy M. A., Mimica P., 2015a, MNRAS, 446, 1716

Cuesta-Martínez C., Aloy M. A., Mimica P., Thöne C., de Ugarte Postigo A., 2015b, MNRAS, 446, 1737

Cui X.-H., Liang E.-W., Lv H.-J., Zhang B.-B., Xu R.-X., 2010, MNRAS, 401, 1465

de Ugarte Postigo A., et al., 2011, A&A, 525, A109

Dai Z. G., Zhang B., Liang E. W., 2006, GRB 060218/SN 2006aj: Prompt Emission from Inverse-Compton Scattering of Shock Breakout Thermal Photons, arXiv:astro-ph/0604510

Daigne F., Mochkovitch R., 1998, MNRAS, 296, 275

De Berredo-Peixoto G., Shapiro I. L., Sobreira F., 2005, Modern Physics Letters A, 20, 2723

De Colle F., Ramirez-Ruiz E., Granot J., Lopez-Camara D., 2012, ApJ, 751, 57

De Pasquale M., et al., 2015, MNRAS, 449, 1024

DeBrye N., Cerdá-Durán P., Aloy M. A., Font J. A., 2013, General Relativistic Simulations of the Collapsar Scenario, arXiv:1310.6223

Donat R., Marquina A., 1996, Journal of Computational Physics, 125, 42

Eichler D., Livio M., Piran T., Schramm D. N., 1989, Nature, 340, 126

Eldridge J. J., Fraser M., Smartt S. J., Maund J. R., Crockett R. M., 2013, MNRAS, 436, 774

Ensman L., Burrows A., 1992, ApJ, 393, 742

Evans P. A., et al., 2014, MNRAS, 444, 250

Fan Y.-Z., Zhang B.-B., Xu D., Liang E.-W., Zhang B., 2011, ApJ, 726, 32

Fox D. W., et al., 2003, Nature, 422, 284

Frail D. A., Kulkarni S. R., Nicastro L., Feroci M., Taylor G. B., 1997, Nature, 389, 261

Frail D. A., et al., 2001, ApJL, 562, L55

Fryer C. L., 1999, ApJ, 522, 413

Fryer C. L., Woosley S. E., 1998, ApJL, 502, L9

Fryer C. L., Woosley S. E., Heger A., 2001, ApJ, 550, 372

Fryer C. L., Rockefeller G., Young P. A., 2006, ApJ, 647, 1269

Fryer C. L., Belczynski K., Berger E., Thöne C., Ellinger C., Bulik T., 2013, ApJ, 764, 181

Fryxell B., Arnett D., Mueller E., 1991, ApJ, 367, 619

Galama T. J., et al., 1998, Nature, 395, 670

Galeazzi F., Kastaun W., Rezzolla L., Font J. A., 2013, PRD, 88, 064009

Gao H., Lei W.-H., Zou Y.-C., Wu X.-F., Zhang B., 2013, New Astron. Rev., 57, 141

Gehrels N., et al., 2004, ApJ, 611, 1005

Gehrels N., Ramirez-Ruiz E., Fox D. B., 2009, Annu. Rev. Astron. Astrophys., 47, 567

Gendre B., et al., 2013, ApJ, 766, 30

Georgy C., Ekström S., Meynet G., Massey P., Levesque E. M., Hirschi R., Eggenberger P., Maeder A., 2012, A&A, 542, A29

Gezari S., et al., 2008, ApJL, 683, L131

Gezari S., et al., 2010, ApJL, 720, L77

Ghirlanda G., Ghisellini G., Lazzati D., 2004, ApJ, 616, 331

Ghisellini G., Ghirlanda G., Nava L., Celotti A., 2010, MNRAS, 403, 926

Giannetti A., Brand J., Massi F., Tieftrunk A., Beltrán M. T., 2012, A&A, 538, A41

Giannios D., Spruit H. C., 2007, A&A, 469, 1

Giannios D., Mimica P., Aloy M. A., 2008, A&A, 478, 747

Goodman J., 1986, ApJL, 308, L47

Gräfener G., Owocki S. P., Vink J. S., 2012, A&A, 538, A40

Granot J., Sari R., 2002, ApJ, 568, 820

Granot J., Piran T., Sari R., 2000, ApJL, 534, L163

Greiner J., et al., 2015, Nature, 523, 189

Guetta D., Della Valle M., 2007, ApJL, 657, L73

Guetta D., Granot J., 2003, MNRAS, 340, 115

Guetta D., Granot J., Begelman M. C., 2005, ApJ, 622, 482

Gull S. F., 1973, MNRAS, 161, 47

Hascoët R., Daigne F., Mochkovitch R., 2013, A&A, 551, A124

Heger A., Fryer C. L., Woosley S. E., Langer N., Hartmann D. H., 2003, ApJ, 591, 288

Hjorth J., 2013, Philosophical Transactions of the Royal Society of London Series A, 371, 20120275

Hjorth J., Bloom J. S., 2012, The Gamma-Ray Burst–Supernova Connection, Chapter 9 in "Gamma-Ray Bursts", Cambridge Astrophysics Series 51, eds. C. Kouveliotou, R. A. M. J. Wijers and S. Woosley, Cambridge University Press (Cambridge). pp 169–190, doi:10.1017/CBO9780511980336.010

Hjorth J., et al., 2003, Nature, 423, 847

Holland S. T., et al., 2010, ApJ, 717, 223

Horváth I., 1998, ApJ, 508, 757

Horváth I., 2002, A&A, 392, 791

Imshennik V. S., Nadezhin D. K., 1988, Soviet Astronomy Letters, 14, 449

Imshennik V. S., Nadezhin D. K., 1989, Astrophysics and Space Physics Reviews, 8, 1

Irwin C. M., Chevalier R. A., 2016, MNRAS, 460, 1680

Ito H., Matsumoto J., Nagataki S., Warren D. C., Barkov M. V., 2015, ApJL, 814, L29

Ivanova N., et al., 2013, A&ARv, 21, 59

Iwamoto K., et al., 1998, Nature, 395, 672

Iwamoto K., et al., 2000, ApJ, 534, 660

Jackson J. D., 1962, Classical electrodynamics. Wiley, New York

Janka H.-T., 2012, Annual Review of Nuclear and Particle Science, 62, 407

Janka H.-T., Langanke K., Marek A., Martínez-Pinedo G., Müller B., 2007, Phys. Rep., 442, 38

Kaneko Y., Preece R. D., Briggs M. S., Paciesas W. S., Meegan C. A., Band D. L., 2006, ApJS, 166, 298

Kaneko Y., et al., 2007, ApJ, 654, 385

Kaplan J. D., Ott C. D., O'Connor E. P., Kiuchi K., Roberts L., Duez M., 2014, ApJ, 790, 19

Kardashev N. S., 1962, SvA, 6, 317

Katz B., Budnik R., Waxman E., 2010, ApJ, 716, 781

Kifonidis K., Plewa T., Janka H.-T., Müller E., 2003, A&A, 408, 621

Klebesadel R. W., Strong I. B., Olson R. A., 1973, ApJL, 182, L85

Klein R. I., Chevalier R. A., 1978, ApJL, 223, L109

Königl A., 2004, in Feroci M., Frontera F., Masetti N., Piro L., eds, Astronomical Society of the Pacific Conference Series Vol. 312, Gamma-Ray Bursts in the Afterglow Era. p. 333, arXiv:astro-ph/0302110

Kouveliotou C., Meegan C. A., Fishman G. J., Bhat N. P., Briggs M. S., Koshut T. M., Paciesas W. S., Pendleton G. N., 1993, ApJL, 413, L101

Kumar P., Barniol Duran R., 2009, MNRAS, 400, L75

Kumar P., Panaitescu A., 2003, MNRAS, 346, 905

Kumar P., Zhang B., 2015, Phys. Rep., 561, 1

Kumar P., Hernández R. A., Bošnjak Ž., Duran R. B., 2012, MNRAS, 427, L40

Lamb D. Q., Donaghy T. Q., Graziani C., 2004, New Astron. Rev., 48, 459

Lattimer J. M., Prakash M., 2001, ApJ, 550, 426

Lazzati D., Begelman M. C., 2010, ApJ, 725, 1137

Lazzati D., Morsony B. J., Begelman M. C., 2009, ApJL, 700, L47

Lazzati D., Morsony B. J., Blackwell C. H., Begelman M. C., 2012, ApJ, 750, 68

Lazzati D., Morsony B. J., Margutti R., Begelman M. C., 2013, ApJ, 765, 103

LeVeque R. J., 1992, Numerical Methods for Conservation Laws, 2nd edn. Lectures in mathematics - ETH Zürich, Birkhäuser, doi:10.1007/978-3-0348-8629-1

Leismann T., Antón L., Aloy M. A., Müller E., Martí J. M., Miralles J. A., Ibáñez J. M., 2005, A&A, 436, 503

Levan A. J., et al., 2014, ApJ, 781, 13

Leventis K., van Eerten H. J., Meliani Z., Wijers R. A. M. J., 2012, MNRAS, 427, 1329

Li L.-X., 2007, MNRAS, 375, 240

Li Z.-Y., Chevalier R. A., 1999, ApJ, 526, 716

Li L., et al., 2012, ApJ, 758, 27

Liang E., Zhang B., Virgili F., Dai Z. G., 2007, ApJ, 662, 1111

Lodato G., Rossi E. M., 2011, MNRAS, 410, 359

López-Cámara D., Morsony B. J., Begelman M. C., Lazzati D., 2013, ApJ, 767, 19

López-Cámara D., Morsony B. J., Lazzati D., 2014, MNRAS, 442, 2202

Lyutikov M., Blandford R., 2003, Gamma Ray Bursts as Electromagnetic Outflows, `arXiv:astro-ph/0312347`

MacFadyen A. I., Woosley S. E., 1999, ApJ, 524, 262

MacFadyen A. I., Woosley S. E., Heger A., 2001, ApJ, 550, 410

MacLeod M., Goldstein J., Ramirez-Ruiz E., Guillochon J., Samsing J., 2014, ApJ, 794, 9

Maeda K., Nomoto K., 2003, ApJ, 598, 1163

Margutti R., et al., 2013, ApJ, 778, 18

Margutti R., et al., 2015, ApJ, 805, 159

Martí J., Müller E., 1996, Journal of Computational Physics, 123, 1

Martí J. M., Müller E., Ibáñez J. M., 1994, A&A, 281, L9

Martí J. M., Müller E., Font J. A., Ibáñez J. M. Z., Marquina A., 1997, ApJ, 479, 151

Matzner C. D., 2003, MNRAS, 345, 575

Matzner C. D., McKee C. F., 1999, ApJ, 510, 379

Mazets E. P., et al., 1981, Astrophys. Space Sci., 80, 119

Mazzali P. A., et al., 2006, ApJ, 645, 1323

Mazzali P. A., McFadyen A. I., Woosley S. E., Pian E., Tanaka M., 2014, MNRAS, 443, 67

Medvedev M. V., 2006, ApJL, 651, L9

Medvedev M. V., Loeb A., 1999, ApJ, 526, 697

Meegan C. A., et al., 1995, ApJL, 446, L15

Melandri A., et al., 2014, A&A, 565, A72

Meszaros P., Rees M. J., 1997, ApJL, 482, L29

Metzger M. R., Djorgovski S. G., Kulkarni S. R., Steidel C. C., Adelberger K. L., Frail D. A., Costa E., Frontera F., 1997, Nature, 387, 878

Metzger B. D., Thompson T. A., Quataert E., 2007, ApJ, 659, 561

Metzger B. D., Giannios D., Thompson T. A., Bucciantini N., Quataert E., 2011, MNRAS, 413, 2031

Mignone A., McKinney J. C., 2007, MNRAS, 378, 1118

Mignone A., Plewa T., Bodo G., 2005, ApJS, 160, 199

Mimica P., 2004, PhD thesis, Max-Planck-Institut für Astrophysik

Mimica P., Aloy M. A., 2012, MNRAS, 421, 2635

Mimica P., Aloy M. A., Müller E., Brinkmann W., 2004, A&A, 418, 947

Mimica P., Aloy M. A., Müller E., Brinkmann W., 2005, A&A, 441, 103

Mimica P., Aloy M. A., Müller E., 2007, A&A, 466, 93

Mimica P., Giannios D., Aloy M. A., 2009a, A&A, 494, 879

Mimica P., Aloy M.-A., Agudo I., Martí J. M., Gómez J. L., Miralles J. A., 2009b, ApJ, 696, 1142

Mimica P., Giannios D., Aloy M. A., 2010, MNRAS, 407, 2501

Mizuta A., Aloy M. A., 2009, ApJ, 699, 1261

Mizuta A., Ioka K., 2013, ApJ, 777, 162

Mizuta A., Yamasaki T., Nagataki S., Mineshige S., 2006, ApJ, 651, 960

Mizuta A., Nagataki S., Aoi J., 2011, ApJ, 732, 26

Modjaz M., Liu Y. Q., Bianco F. B., Graur O., 2016, ApJ, 832, 108

Moriya T. J., Sanyal D., Langer N., 2015, A&A, 575, L10

Morrison I. A., Baumgarte T. W., Shapiro S. L., 2004, ApJ, 610, 941

Morsony B. J., Lazzati D., Begelman M. C., 2007, ApJ, 665, 569

Morsony B. J., Lazzati D., Begelman M. C., 2010, ApJ, 723, 267

Mueller E., Fryxell B., Arnett D., 1991, A&A, 251, 505

Mukherjee S., Feigelson E. D., Jogesh Babu G., Murtagh F., Fraley C., Raftery A., 1998, ApJ, 508, 314

Nagakura H., Ito H., Kiuchi K., Yamada S., 2011, ApJ, 731, 80

Nagakura H., Suwa Y., Ioka K., 2012, ApJ, 754, 85

Nagataki S., Takahashi R., Mizuta A., Takiwaki T., 2007, ApJ, 659, 512

Nakamura T., Mazzali P. A., Nomoto K., Iwamoto K., 2001, ApJ, 550, 991

Nakamura K., Takiwaki T., Kuroda T., Kotake K., 2015, Publications of the Astronomical Society of Japan, 67, 107

Nakar E., 2015, ApJ, 807, 172

Nakar E., Sari R., 2010, ApJ, 725, 904

Nakar E., Sari R., 2012, ApJ, 747, 88

Nakauchi D., Kashiyama K., Suwa Y., Nakamura T., 2013, ApJ, 778, 67

Narayan R., Paczynski B., Piran T., 1992, ApJL, 395, L83

Nousek J. A., et al., 2006, ApJ, 642, 389

O'Connor E., Ott C. D., 2011, ApJ, 730, 70

Obergaulinger M., Aloy M., 2017, MNRAS, 469

Ofek E. O., et al., 2010, ApJ, 724, 1396

Paczynski B., 1986, ApJL, 308, L43

Paczyński B., 1998, ApJL, 494, L45

Paczynski B., Rhoads J. E., 1993, ApJL, 418, L5

Page K. L., et al., 2011, MNRAS, 416, 2078

Panaitescu A., Mészáros P., Burrows D., Nousek J., Gehrels N., O'Brien P., Willingale R., 2006, MNRAS, 369, 2059

Park I. H., et al., 2013, New Journal of Physics, 15, 023031

Parker E. N., 1963, Interplanetary dynamical processes.

Passy J.-C., et al., 2012, ApJ, 744, 52

Paul J., Wei J., Basa S., Zhang S.-N., 2011, Comptes Rendus Physique, 12, 298

Pe'er A., 2008, ApJ, 682, 463

Pe'er A., 2015, Advances in Astronomy, 2015, 907321

Pe'er A., Mészáros P., Rees M. J., 2006, ApJ, 652, 482

Pendleton G. N., et al., 1996, ApJ, 464, 606

Pian E., et al., 2006, Nature, 442, 1011

Piran T., 1999, Phys. Rep., 314, 575

Piro L., et al., 1999, ApJL, 514, L73

Popham R., Woosley S. E., Fryer C., 1999, ApJ, 518, 356

Produit N., et al., 2005, Nuclear Instruments and Methods in Physics Research A, 550, 616

Quataert E., Shiode J., 2012, MNRAS, 423, L92

Racusin J. L., et al., 2009, ApJ, 698, 43

Ramirez-Ruiz E., Celotti A., Rees M. J., 2002, MNRAS, 337, 1349

Rees M. J., Meszaros P., 1992, MNRAS, 258, 41P

Rees M. J., Meszaros P., 1994, ApJL, 430, L93

Rees M. J., Mészáros P., 2005, ApJ, 628, 847

Ricker P. M., Taam R. E., 2012, ApJ, 746, 74

Rosenberg I., Scheuer P. A. G., 1973, MNRAS, 161, 27

Rybicki G. B., Lightman A. P., 1979, Radiative Processes in Astrophysics. Wiley-Interscience, New York, doi:10.1002/9783527618170

Sakamoto T., et al., 2004, ApJ, 602, 875

Sakamoto T., et al., 2006, ApJL, 636, L73

Santana R., Barniol Duran R., Kumar P., 2014, ApJ, 785, 29

Sanyal D., Moriya T. J., Langer N., 2015, in Hamann W.-R., Sander A., Todt H., eds, Wolf-Rayet Stars: Proceedings of an International Workshop held in Potsdam, Germany, 1-5 June 2015. Edited by Wolf-Rainer Hamann, Andreas

Sander, Helge Todt. Universitätsverlag Potsdam, 2015., p.213-216. pp 213–216, arXiv:1508.06055

Sari R., Piran T., 1995, ApJL, 455, L143

Sari R., Piran T., 1999a, ApJL, 517, L109

Sari R., Piran T., 1999b, ApJ, 520, 641

Sari R., Piran T., Narayan R., 1998, ApJL, 497, L17

Sari R., Piran T., Halpern J. P., 1999, ApJL, 519, L17

Savaglio S., Glazebrook K., Le Borgne D., 2009, ApJ, 691, 182

Shapiro P. R., Knight J. W., 1978, ApJ, 224, 1028

Shemi A., Piran T., 1990, ApJL, 365, L55

Shibata M., Baumgarte T. W., Shapiro S. L., 2000, PRD, 61, 044012

Shu C.-W., Osher S., 1988, Journal of Computational Physics, 77, 439

Sironi L., Spitkovsky A., 2011, ApJ, 726, 75

Soderberg A. M., Kulkarni S. R., Berger E., Chevalier R. A., Frail D. A., Fox D. B., Walker R. C., 2005, ApJ, 621, 908

Soderberg A. M., et al., 2006, Nature, 442, 1014

Soderberg A. M., et al., 2008, Nature, 453, 469

Sparre M., et al., 2011, ApJL, 735, L24

Stamatikos M., Sakamoto T., Starling R. L. C., Oates S. R., Barthelmy S. D., Burrows D. N., Roming P., Gehrels N., 2010, GCN Report, 278

Starling R. L. C., et al., 2011, MNRAS, 411, 2792

Starling R. L. C., Page K. L., Pe'Er A., Beardmore A. P., Osborne J. P., 2012, MNRAS, 427, 2950

Sukhbold T., Ertl T., Woosley S. E., Brown J. M., Janka H.-T., 2016, ApJ, 821, 38

Sutherland R. S., 1998, MNRAS, 300, 321

Svirski G., Nakar E., 2014, ApJL, 788, L14

Szécsi D., Langer N., Yoon S.-C., Sanyal D., de Mink S., Evans C. J., Dermine T., 2015, A&A, 581, A15

Tabik S., Romero L. F., Mimica P., Plata O., Zapata E. L., 2012, Computer Physics Communications, 183, 1937

Tagliaferri G., et al., 2005, Nature, 436, 985

Tan J. C., Matzner C. D., McKee C. F., 2001, ApJ, 551, 946

Taub A. H., 1948, Physical Review, 74, 328

Tchekhovskoy A., McKinney J. C., Narayan R., 2008, MNRAS, 388, 551

Tchekhovskoy A., Narayan R., McKinney J. C., 2011, MNRAS, 418, L79

Terman J. L., Taam R. E., Hernquist L., 1995, ApJ, 445, 367

Thompson C., 1994, MNRAS, 270, 480

Thompson T. A., Chang P., Quataert E., 2004, ApJ, 611, 380

Thöne C. C., et al., 2011, Nature, 480, 72

Thöne C. C., de Ugarte Postigo A., Fryer C. L., Kann D. A., 2015, in Massaro F., Cheung C. C., Lopez E., Siemiginowska A., eds, IAU Symposium Vol. 313, Extragalactic Jets from Every Angle. pp 396–397, doi:10.1017/S1743921315002604

Tikhomirova Y. Y., Stern B. E., 2005, Astronomy Letters, 31, 291

Toma K., Ioka K., Sakamoto T., Nakamura T., 2007, ApJ, 659, 1420

Tominaga N., Blinnikov S., Baklanov P., Morokuma T., Nomoto K., Suzuki T., 2009, ApJL, 705, L10

Ugliano M., Janka H.-T., Marek A., Arcones A., 2012, ApJ, 757, 69

Usov V. V., 1992, Nature, 357, 472

van Eerten H. J., Wijers R. A. M. J., 2009, MNRAS, 394, 2164

van Hoof P. A. M., Williams R. J. R., Volk K., Chatzikos M., Ferland G. J., Lykins M., Porter R. L., Wang Y., 2014, MNRAS, 444, 420

van Hoof P. A. M., Ferland G. J., Williams R. J. R., Volk K., Chatzikos M., Lykins M., Porter R. L., 2015, MNRAS, 449, 2112

van Paradijs J., et al., 1997, Nature, 386, 686

Vedrenne G., Atteia J.-L., 2009, Gamma-Ray Bursts: The Brightest Explosions in the Universe. Springer Praxis Books, doi:10.1007/978-3-540-39088-6

Vietri M., Stella L., 1998, ApJL, 507, L45

Vietri M., Stella L., 1999, ApJL, 527, L43

Villasenor J. S., et al., 2005, Nature, 437, 855

Wang X.-Y., Li Z., Waxman E., Mészáros P., 2007, ApJ, 664, 1026

Wang X.-G., et al., 2015, ApJS, 219, 9

Waxman E., Mészáros P., Campana S., 2007, ApJ, 667, 351

Weaver T. A., 1976, ApJS, 32, 233

Wheeler J. C., Yi I., Höflich P., Wang L., 2000, ApJ, 537, 810

Wongwathanarat A., Müller E., Janka H.-T., 2015, A&A, 577, A48

Woosley S. E., 1993, ApJ, 405, 273

Woosley S. E., Bloom J. S., 2006, Annu. Rev. Astron. Astrophys., 44, 507

Woosley S. E., Heger A., 2006, ApJ, 637, 914

Woosley S. E., Heger A., 2012, ApJ, 752, 32

Xu M., Nagataki S., Huang Y. F., Lee S.-H., 2012, ApJ, 746, 49

Yonetoku D., Murakami T., Nakamura T., Yamazaki R., Inoue A. K., Ioka K., 2004, ApJ, 609, 935

Zhang W., Fryer C. L., 2001, ApJ, 550, 357

Zhang B., Mészáros P., 2001, ApJL, 552, L35

Zhang B., Yan H., 2011, ApJ, 726, 90

Zhang W., Woosley S. E., MacFadyen A. I., 2003a, ApJ, 586, 356

Zhang B., Kobayashi S., Mészáros P., 2003b, ApJ, 595, 950

Zhang W., Woosley S. E., Heger A., 2004, ApJ, 608, 365

Zhang B., Fan Y. Z., Dyks J., Kobayashi S., Mészáros P., Burrows D. N., Nousek J. A., Gehrels N., 2006, ApJ, 642, 354

Zhang B.-B., et al., 2011, ApJ, 730, 141

Zhao Y.-N., Shao L., 2014, ApJ, 789, 74